

MICRO MOTION STAGES WITH FLEXURE HINGES - DESIGN AND CONTROL

By
MERVE ACER

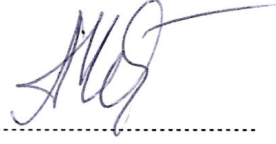
Submitted to the Graduate School of Engineering and Natural Sciences
in partial fulfillment of
the requirements for the degree of
Doctor of Philosophy

SABANCI UNIVERSITY
Spring 2012

MICRO MOTION STAGES WITH FLEXURE HINGES - DESIGN AND CONTROL

APPROVED BY:

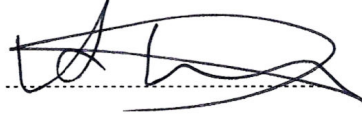
ASIF ŞABANOVIÇ
(Dissertation Advisor)



ALİ KOŞAR
(Dissertation Co-Advisor)



ATA MUĞAN



BURÇ MISIRLIOĞLU



GÜLLÜ KIZILTAŞ ŞENDUR



DATE OF APPROVAL:

08/05/2012

© Merve Acer 2012
All Rights Reserved

MICRO MOTION STAGES WITH FLEXURE HINGES - DESIGN AND CONTROL

Merve ACER

Mechatronics Engineering, PhD. Thesis, 2012

Thesis Supervisor: Prof. Dr. Asif ŞABANOVIĆ

Thesis Co-Supervisor: Asoc. Prof. Dr. Ali KOŞAR

Keywords: Compliant Mechanisms, Flexure Based Mechanisms, Parallel Mechanisms, Flexures, Compliance Calculations, Sliding Mode Control, Disturbance Observer, Piezoelectric Actuators

ABSTRACT

The developments in micro and nano technologies brought the need of high precision micropositioning stages to be used in micro/nano applications such as cell manipulation, surgery, aerospace, micro fluidics, optical systems, micromachining and microassembly etc. Micro motion stages with flexible joints called compliant mechanisms are built to provide the needed accuracy and precision. This thesis aims to build compliant planar micro motion stages using flexure hinges to be used as micropositioning devices in x-y directions by applying new control methods. First 3-RRR planar parallel kinematic structure is selected which is also popular in the literature. Then the mechanism is developed to have a new structure which is a 3-PRR mechanism. The necessary geometric parameters are selected by using Finite Element Analysis (FEA). The displacement, stress and frequency behaviors of the mechanisms are compared and discussed. Modeling of the flexure based mechanisms is also studied for 3-PRR compliant stage by using Kinetostatic modeling method which combines the compliance calculations of flexure hinges with kinematics of the mechanism.

Piezoelectric actuators and optical 2d position sensor which uses a laser source are used for actuation and measurement of the stages. After the experimental studies it's seen that the results are not compatible with FEA because of the unpredictable errors caused by manufacturing and assembly. We have succeeded to eliminate those errors by implementing a control methodology based on Sliding Mode Control with Disturbance Observer which is also based on Sliding Mode Control using linear piezoelectric actuator models. Finally, we have extracted experimental models for each actuation direction of the stage and used those models instead of piezoelectric actuator models which lowered our errors in the accuracy of our measurement and ready to be used as a high precision micro positioning stage for our micro system applications.

ESNEK BAĞLANTI ELEMANLI MİKRO HAREKET PLATFORMLARININ TASARIMI VE KONTROLÜ

Merve ACER

Mekatronik Mühendisliği, Doktora Tezi, 2012

Tez Danışmanı: Prof. Dr. Asif ŞABANOVIÇ

Tez Yardımcı Danışmanı: Doç. Dr. Ali KOŞAR

Anahtar Kelimeler: Esnek Bağlantılı Mekanizmalar, Paralel Mekanizmalar,
Komplians Hesaplamaları, Kayan Kipli Kontrol, Bozan Etmen Gözleyicisi

ÖZET

Mikro ve Nano teknolojilerindeki gelişmeler yüksek hassasiyetli mikro konumlandırma platformlarının hücre manipülasyonu, ameliyatlar, uzay sistemleri, mikro akışkan sistemler, optik sistemler, mikro işleme ve mikro montaj gibi mikro/nano uygulamalarda kullanımı için tasarımını gerektirmiştir. Esnek bağlantı elemanlı mikro hareket platformları gerekli doğruluk ve hassasiyeti sağlamak için geliştirilmiş mekanizmalardır. Bu tezde yeni kontrol metotları uygulayarak düzlemsel esnek bağlantı elemanlı mikro hareket platformlarının x-y yönlerinde mikro konumlandırma düzeneği olarak kullanılması amaçlanılmıştır. İlk önce literatürde de çokça kullanılmış olan 3-RRR düzlemsel paralel kinematik yapı seçilmiştir. Daha sonra mekanizma geliştirilmiş ve yeni bir yapıya sahip olup 3-PRR mekanizma haline gelmiştir. Gerekli geometrik parametreler sonlu elemanlar analizi ile seçilmiştir. Mekanizmaların yer değişimi, stres ve frekans davranışları karşılaştırılıp tartışılmıştır. Ayrıca 3-PRR esnek bağlantı elemanlı mekanizmanın modellenmesi de esnek bağlantı elemanlarının komplians hesaplarını mekanizmanın kinematığı ile birleştiren kinetostatik modelleme metodu kullanılarak yapılmıştır. Platformların tahriki için piezoelektrik eyleyiciler, ölçümü için

de lazer bir kaynak kullanan optik 2 boyutta pozisyon sensörü kullanılmıştır. Deneysel çalışmalardan sonra görülmüştür ki deneysel sonuçlar sonlu elemanlar analizinin sonuçları ile imalat ve montajdan dolayı ortaya çıkan, öngörülemeyen hatalardan dolayı uyuşmamaktadır. Bu hataları, kayan kipli kontrol ile doğrusal piezoelektrik eyleyici modeli kullanarak yine kayan kipli kontrolle oluşturulmuş bozan etmen gözleyicisi kontrol metodu uygulayarak elemeyi başardık. Son olarak, her tahrik yönü için platformun deneysel modelini çıkardık ve bu modelleri piezoelektrik eyleyici modelleri yerine kullanarak pozisyon kontrol hatamızı kullandığımız ölçüm sisteminin hassasiyetine indirgedik ve platformumuzu mikro sistem uygulamaları için yüksek hassasiyetli bir mikro konumlandırma platformu olarak kullanılabilir haline getirdik.

“To Selma and Kadri Acer”

ACKNOWLEDGEMENTS

I would like to express my gratitude to my advisor, Professor Asif Şabanoviç. I would like to thank him not for only completion of this thesis but also his support in my life, his patience and encouragement.

I am deeply grateful to Professor Ata Muğan for his sincere support during my academic education. I have furthermore to thank my dissertation committee Professors: Ali Koşar, Güllü Kızıldaş Şendur and Burç Mısırlıođlu for correcting my mistakes and sharing their valuable ideas.

I would also like to thank my only true and childhood friends M. Beril Alpagut and F. Zeynep Temel for their great support when I'm discouraged during my PhD.

Finally, I would like to express my gratitude to my parents Selma and Kadri Acer for their unlimited support, without them I wouldn't be able to get my PhD.

This research was supported by Tubitak Bideb 2211: domestic doctorate scholarship programme and the Yousef Jameel scholarship.

TABLE OF CONTENTS

1	Introduction	1
1.1	Micropositioning	1
1.2	Background and Motivation	5
1.3	The Goal and Objectives	7
1.3.1	Design of Compliant Stage	8
1.3.2	Modeling of Compliant Stage	9
1.3.3	Control of Compliant Stage	10
1.4	Organization of the Thesis.....	10
2	Literature Review	12
2.1	Designing of Compliant Stages	12
2.1.1	Mechanisms.....	13
2.1.2	Actuators	19
2.1.3	Measurement	20
2.2	Modeling of Compliant Positioning Stages.....	21
2.3	Control of Compliant Positioning Stages	23
2.4	Our Contribution to The Literature	25
3	Designing of The Planar Micro motion Stage.....	26
3.1	Limitations in Design of Compliant Stages.....	26
3.1.1	Range.....	26
3.1.2	Sensitivity to Parasitic Motions	27
3.1.3	Stress Distribution.....	27
3.1.4	Number of DOFs.....	28
3.2	Designed Planar Parallel Compliant Stages	28
3.2.1	3-RRR Compliant Stage.....	31
3.2.2	3-PRR Compliant Stage	33
3.3	Finite Element Analysis of Compliant Stages.....	36
3.3.1	Determining the type of the flexure	37

3.3.2	Determining the proper “b” and “t” parameters.....	39
3.3.3	FEA of 3-RRR Compliant Mechanism.....	44
3.3.3.1	Free 3-RRR Compliant Mechanism.....	44
3.3.3.2	Constrained 3-RRR Compliant Mechanism	48
3.3.4	FEA of 3-PRR Compliant Mechanism	54
3.3.4.1	Free 3-PRR Compliant Mechanism.....	54
3.3.4.2	Constrained 3-PRR Compliant Mechanism.....	59
3.4	Comparison of 3-RRR and 3-PRR Mechanism.....	64
3.5	Conclusion and Comments.....	67
4	Compliance Modeling of The Flexure Hinges	69
4.1	Basic concepts of circular flexure hinges	70
4.2	Compliance Calculation Methods	71
4.3	Numerical of Circular Flexure Hinge.....	74
4.3.1	Boundary Conditions	74
4.3.2	Meshing.....	76
4.4	Results and Comparison of The Methods.....	76
4.5	Conclusion and Comments.....	81
5	Kinetostatic Modeling of 3-PRR Compliant Mechanism	83
5.1	3-PRR Kinetostatic Modeling	84
5.1.1	Derivation of $C_{o,Fo}$	86
5.1.2	Derivation of $C_{o,Fin}$ and $C_{in,Fo}$	94
5.1.3	Derivation of $C_{in,Fin}$	97
5.1.4	The Jacobian matrix of 3 PRR compliant mechanism:.....	97
5.2	The Results and Comparison with FEA	97
5.3	Dynamics of the Compliant Mechanisms.....	101
5.4	Conclusion and Comments.....	104
6	Experimental Setup and Performance Results	105
6.1	The Experimental Setup	105
6.1.1	Manufactured Compliant Mechanisms	106
6.1.2	Designed and Manufactured Other Mechanical Parts.....	107
6.1.3	Piezoelectric Actuators.....	111
6.1.4	Measurements, Amplifiers and Control Unit.....	112
6.2	3-RRR Performance Results.....	116
6.3	3-PRR Performance Results	121

6.4	Comparison of 3-RRR and 3-PRR Compliant Mechanisms	126
6.5	Comparison with FEA	126
6.5.1	3-RRR Compliant Mechanism	127
6.5.2	3-PRR Compliant Mechanism	128
6.6	Conclusion and Comments	130
7	Piezoelectric Actuator Modeling And Control	132
7.1	Modeling of Piezoelectric Actuators	133
7.1.1	Hysteresis Model	134
7.1.2	Simulation of the Model	135
7.2	Sliding Mode Control with Disturbance Observer	137
7.2.1	Sliding Mode Observer for PEA	138
7.2.2	Position Control with Sliding Mode Control	141
7.3	Implementation of Position Control with Disturbance Observer for PEA	142
7.3.1	Position Control of PEA Without Observer	143
7.3.2	Position Control of PEA With Observer	144
7.4	Conclusion and Comments	146
8	Position Control Of Compliant Mechanisms	147
8.1	Position Control of 3-RRR Mechanism	148
8.2	Position Control of 3-PRR Mechanism	153
8.2.1	Position Control with Piezoelectric Actuator Models	153
8.2.2	PID Control Results	154
8.2.3	Open Loop Control with PEA Models	156
8.2.4	Closed Loop Control	158
8.2.4.1	Non-Redundant Control Results	158
8.2.4.2	Redundant Control Results	160
8.2.5	Experimental Modeling of 3-PRR Compliant Mechanisms	163
8.2.5.1	Position Control Results with Experimental Models	165
8.3	Conclusion and Comments	168
9	Conclusion And Future Work	170
9.1	Contributions	174
9.2	Future Work	175
10	References	178

LIST OF FIGURES

Figure 1.1 Laser micro machining unit [3].	1
Figure 1.2 Micro manipulation unit [4].	2
Figure 1.3 High Precision mechanism design methodology selections.	2
Figure 1.4 Kinematic structures.	4
Figure 1.5 A deformed flexure.	5
Figure 1.6 Misalignment of actuators with the compliant stage.	7
Figure 1.7 Stress-Strain curve [9].	8
Figure 2.1 Designing of compliant stages.	12
Figure 2.2 Serial compliant stages.	13
Figure 2.3 Lever mechanism based XY planar parallel compliant stages [20-21].	14
Figure 2.4 XY compliant stages based on 5 bar mechanism [25].	14
Figure 2.5 XY compliant stage based on parallelogram structures [19].	15
Figure 2.6 Planar XY nanopositioning system [15].	15
Figure 2.7 3 DOF planar parallel compliant mechanisms.	16
Figure 2.8 (a) Spatial Flexure Hinge, (b) Single Axis Flexure Hinge	17
Figure 2.9 Spatial compliant stages.	17
Figure 2.10 XYZ nanopositioning stage [46].	18
Figure 2.11 6 DOF compliant mechanism having 2 parallel kinematic structures [37].	18
Figure 2.12 (a) HexFlex in macro scale, (b) HexFlex in micro scale [45].	19
Figure 2.13 (a) 1 DOF model, (b) 2 DOF model.	21
Figure 2.14 Element definition of a flexible beam.	22
Figure 2.15 (a) Flexible beam with end moment, (b) The PRBM model [58].	23
Figure 3.1 Amplification mechanism (5 bar).	27
Figure 3.2 Triangular stage with actuating forces.	29
Figure 3.3 (a) 3-RRR kinematic structure, (b) 3-PRR kinematic structure.	30
Figure 3.4 Limbs with right circular flexure hinges.	30
Figure 3.5 3-RRR compliant stage with circular flexure hinges.	31

Figure 3.6 3-RRR compliant mechanism displacements.....	32
Figure 3.7 3D appearance of 3-RRR compliant mechanism.	32
Figure 3.8 2D appearance of 3-RRR compliant stage and its dimensions.	33
Figure 3.9 3-PRR compliant stage with circular flexure hinges.....	34
Figure 3.10 3-PRR compliant mechanism displacements.....	34
Figure 3.11 3D appearance of 3-PRR compliant mechanism.....	35
Figure 3.12 2D appearance of 3-PRR compliant stage and its dimensions.....	35
Figure 3.13 Analyzed flexure hinges.....	38
Figure 3.14 Boundary conditions of analyzed flexures.....	38
Figure 3.15 Stress distributions of flexure hinges.....	39
Figure 3.16 Boundary conditions of compliant mechanisms.....	40
Figure 3.17 3-RRR compliant mechanisms stress and displacement results.....	41
Figure 3.18 3-PRR compliant mechanisms stress and displacement results.....	43
Figure 3.19 (a) Boundary conditions of free 3-RRR mechanism, (b) Meshed 3-PRR mechanism.....	45
Figure 3.20 Center displacements for free 3-RRR compliant mechanism.....	46
Figure 3.21 a. Maximum displacement results free 3-RRR compliant mechanism.....	48
Figure 3.22 Boundary conditions of constrained 3-RRR compliant mechanism.....	49
Figure 3.23 Center displacements for constrained 3-RRR compliant mechanism.....	51
Figure 3.24 Maximum displacement results constrained 3-RRR compliant mechanism.	53
Figure 3.25 Mode shapes of 3-RRR compliant mechanism.....	54
3.26 (a) Boundary conditions of free 3-PRR mechanism, (b) Meshed 3-PRR mechanism.....	55
Figure 3.27 a. Center displacements for free 3-PRR compliant mechanism.....	56
Figure 3.28 Maximum displacement results of free 3-PRR compliant mechanism.....	58
Figure 3.29 Boundary conditions of constrained 3-PRR mechanism.....	59
Figure 3.30 Center displacements of 3-PRR compliant mechanism.....	61
Figure 3.31 Maximum displacement results for constrained 3-PRR compliant mechanism.....	63
Figure 3.32 Mode shapes of 3-PRR compliant mechanism.....	64
Figure 3.33 Assigned points for triangular stage.....	66
Figure 3.34 Direction of forces results for compliant mechanisms.....	67
Figure 4.1 Circular flexure hinge and its PRBM.....	70

Figure 4.2 Flexure hinge coordinate frame [70].	71
Figure 4.3 Applying moment (M_z).	75
Figure 4.4 Applying translational force (F_y).	75
Figure 4.5 Applying longitudinal force (F_x).	75
Figure 4.6 The meshed part analyzed using finite element method.	76
Figure 4.7 $\Delta\alpha_z/M_z$ compliance results for varying width “b”.	77
Figure 4.8 $\Delta x/F_x$ compliance results for varying width “b”.	78
Figure 4.9 $\Delta y/F_y$ compliance results for varying width “b”.	78
Figure 4.10 $\Delta\alpha_z/M_z$ compliance results for varying shortest distance “t” of the flexure.	79
Figure 4.11 $\Delta y/F_y$ compliance results for varying shortest distance “t” of the flexure.	80
Figure 4.12 $\Delta y/F_y$ compliance results for varying shortest distance “t” of the flexure (zoomed around $t=1.1$ mm).	80
Figure 4.13 $\Delta x/F_x$ compliance results for varying shortest distance “t” of the flexure.	81
Figure 5.1 Assigned coordinate frames and acting forces/moments.	85
Figure 5.2 Measurements of a PRR link.	85
Figure 5.3 Boundary conditions of 3-PRR compliant mechanism for FEA.	100
Figure 5.4 The mass-spring model of compliant mechanism.	102
Figure 6.1 Full experimental setup photos.	106
Figure 6.2 Manufactured compliant mechanisms using wire EDM.	107
Figure 6.3 Miniature translation stages for piezoelectric actuator positioning.	108
Figure 6.4 Designed parts for the assembly of the setup.	109
Figure 6.5 Assembling of manufactured parts of experimental setup.	110
Figure 6.6 Measurement part.	111
Figure 6.7 Piezoelectric actuator.	112
Figure 6.8 Dual position sensor on PCB.	112
Figure 6.9 Mounted dual position measurement with laser source.	113
Figure 6.10 Laser calibration setup.	114
Figure 6.11 (a) Filtered output Y voltage, (b) Filtered output X voltage.	114
Figure 6.12 Strain gauge amplifier output voltages of PEA.	115
Figure 6.13 Connections of dSPACE with measurements and amplifiers.	116
Figure 6.14 Motion vectors of PEAs in 3-RRR compliant mechanism.	116
Figure 6.15 3-RRR compliant mechanism experiment displacement results when only 1 PEA is assembled.	118

Figure 6.16 3-RRR compliant mechanism experiment displacement results for all PEAs are assembled.....	119
Figure 6.17 Workspace of 3-RRR compliant mechanism.....	120
Figure 6.18 Motion vectors of PEAs in 3-PRR compliant mechanism.....	121
Figure 6.19 3-PRR Compliant mechanism experiment displacement results when only 1 PEA is assembled.....	122
Figure 6.20 3-PRR Compliant mechanism experiments for all PEAs are assembled.	124
Figure 6.21 Workspace of 3-PRR compliant mechanism.....	125
Figure 6.22 Comparison of experimental and FEA results or 3-RRR compliant mechanism.....	128
Figure 6.23 Comparison of experimental and FEA results or 3-PRR compliant mechanism.....	130
Figure 7.1 Piezoelectric actuator model [74].....	133
Figure 7.2 Hysteresis loop and its parameters [77].	134
Figure 7.3 Block diagram of PEA model with hysteresis.....	136
Figure 7.4 The displacement result of simulated PEA.	137
Figure 7.5 The input piezo voltage result of simulated PEA.....	137
Figure 7.6 Block diagram of disturbance observer with sliding mode controller.	139
Figure 7.7 Simulation results for sliding mode observer of PEA.....	141
Figure 7.8 Block diagram of position control with sliding mode controller.	142
Figure 7.9 The Setup for implementation of position control of PEA.	142
Figure 7.10 Results of position control of PEA without observer.....	144
Figure 7.11 Results of position control of PEA with observer.....	146
Figure 8.1 Motion vectors of 3-RRR compliant mechanism.....	148
Figure 8.2 Block diagram of the position control of compliant mechanism.	149
Figure 8.3 Position control results of 3-RRR compliant mechanism.	151
Figure 8.4 x and y position results when the Radius of reference circle is 30 μm	152
Figure 8.5 Position control results for references having different frequencies.....	153
Figure 8.6 Motion vectors of 3-PRR compliant mechanism.	154
Figure 8.7 Block diagram of the PID position control of compliant mechanism.....	155
Figure 8.8 Results of PID position control for 3-PRR compliant mechanism.....	156
Figure 8.9 Open loop control block diagram.....	157
Figure 8.10 Results of open loop control for 3-PRR compliant mechanism.....	157
Figure 8.11 (a) 2 PEAs are activated, (b) 3 PEAs are activated.....	158

Figure 8.12 . Position control results of 3-PRR compliant mechanism for non-redundant case.....	159
Figure 8.13 Control inputs for non-redundant case.	159
Figure 8.14 Position control results of 3-PRR compliant mechanism for redundant case.	160
Figure 8.15 Control inputs for redundant case.	161
Figure 8.16 Position control results of 3-PRR compliant mechanisms with tuned parameters.....	162
Figure 8.17 Step responses with 5 μ m steps in x and y directions using position control with PEA models.	163
Figure 8.18 Experimental models and experiments results for step responses 3-PRR compliant mechanism.	165
Figure 8.19 Sliding mode position control with experimental model based disturbance observer.....	166
Figure 8.20 Position control using experimental models results of 3-PRR compliant mechanism.	167
Figure 8.21 Step responses with 5 μ m steps in x and y directions using position control with experimental models.....	168
Figure 9.1 Design path of compliant mechanisms.....	177

LIST OF TABLES

Table 3.1 The dimensions of 3-RRR compliant mechanism	33
Table 3.2 The dimensions of 3-PRR compliant mechanism	36
Table 3.3 Material properties of AL 7075	37
Table 3.4 FEA results for flexure hinges	39
Table 3.5 Results for varied “t” and “b” parameters for 3-RRR compliant mechanism	40
Table 3.6 Results for varied “t” and “b” parameters for 3-PRR.....	42
Table 3.7 Results of maximum displacement and stress of free 3-RRR compliant mechanism	48
Table 3.8 Results of maximum displacement and stress of constrained 3-RRR compliant mechanism	53
Table 3.9 Results of maximum displacement and stress of free 3-PRR compliant mechanism	59
Table 3.10 Results of maximum displacement and stress of constrained 3-PRR compliant mechanism	63
Table 3.11 Free and constrained compliant mechanism displacement results comparison.....	65
Table 4.1 Material properties of AL7075	74
Table 4.2 Compliance results of FEA and 4 kinds of analytic calculation methods	76
Table 4.3 Compliance errors of analytic methods compared to FEA.....	77
Table 5.1 Material and Geometric Properties of Circular Flexure Hinges.....	98
Table 5.2 Calculated In-Plane Compliances of Circular Flexure Hinges.....	98
Table 5.3 Link Length of 3-PRR Compliant Mechanism.....	98
Table 5.4 Compliance Results for 3-PRR Compliant Mechanism	99
Table 5.5 The C_oF_{in} compliance matrix results of FEA and kinetostatic method.....	100
Table 5.6 Jacobian matrix results of FEA and kinetostatic method	100
Table 5.7 % errors of computed C_oF_{in}	101
Table 6.1 Piezoelectric Actuator Datasheet Properties.....	111

Table 6.2 Workspace actuation and results of 3-RRR compliant mechanism.....	120
Table 6.3 Workspace results.....	125
Table 6.4 % errors compared to FEA for 3-PRR.....	127
Table 6.5 % errors compared to FEA for 3-PRR.....	129
Table 7.1 Material properties of PZT	134
Table 7.2 PSt 150/5/60 VS10 Piezoelectric actuator parameters	136
Table 8.1 Nominal parameters of PSt 150/5/40 VS10 Piezoelectric Actuator.....	150
Table 8.2 The control parameters of 3-RRR mechanism	150
Table 8.3 Tuned SMC disturbance observer and SMC position controller parameters	161
Table 8.4 Estimated transfer functions parameters.....	164
Table 8.5 Errors in x and y direction for 3-PRR compliant microposition stage with different control types	169

TABLE OF SYMBOLS

F_1	Acting force 1
F_2	Acting force 2
F_3	Acting force 3
C	Center point of triangular stage
u_1	Center displacement 1
u_2	Center displacement 2
u_3	Center displacement 3
t	the shortest distance between the circumferences of two notches
b	the overall thickness
R_i	Circular flexure hinge's radius (i representing the number)
L_i	Link lengths (i representing the number)
σ_{\max}	Maximum stress
α	Angle of displacement u_1
β	Angle of displacement u_2
γ	Angle of displacement u_3
x_c	Center displacement in x direction
y_c	Center displacement in y direction
P_1	Point 1 at the edge of the triangular stage
P_2	Point 2 at the edge of the triangular stage
P_3	Point 3 at the edge of the triangular stage
u_{F1}	Direction of force 1
u_{F2}	Direction of force 2
u_{F3}	Direction of force 3
F_x	Longitudinal force
F_y	Translational force
M_z	Moment in z axis
$\Delta x/F_x$	Translational compliance in x direction

$\Delta y/F_y$	Translational compliance in y direction
$\Delta\alpha_z/M_z$	Rotational compliance about z direction
$\Delta\alpha_x/M_x$	Rotational compliance about x direction
$\Delta\alpha_y/M_y$	Rotational compliance about y direction
$\Delta z/F_z$	Translational compliance in z direction
E	Moduus of elasticity
G	Shear modulus
ν	Poisson's ratio
u_i	Linear displacement at point i
θ_i	Angular deformation at point i
F_i	Force at point i
M_i	Moment at point i
U	Total strain energy
$U_{bending}$	Bending strain energy
$U_{shearing}$	Shearing strain energy
U_{axial}	Axial strain energy
$U_{torsion}$	Torional strain energy
{.}	Vector
[.]	Matrix
\mathbf{U}_o	Output displacement matrix
\mathbf{U}_{in}	Input displacement matrix
\mathbf{F}_o	Output force matrix
\mathbf{F}_{in}	Input force matrix
\mathbf{C}	Compliance matrix
$\mathbf{C}_{o,Fo}$	Compliance matrix that relates output forces with output displacements
$\mathbf{C}_{o,Fin}$	Compliance matrix that relates input forces with output displacements
$\mathbf{C}_{in,Fo}$	Compliance matrix that output forces with input displacements
$\mathbf{C}_{in,Fin}$	Compliance matrix that input forces with input displacements
\mathbf{C}_{hi}	Output compliances for flexure hinges
$\begin{bmatrix} \Delta\alpha_z \\ M_z \end{bmatrix}_i$	Rotational compliance about z direction for flexure hinge i

$\left[\frac{\Delta y}{F_y}\right]_i$	Translational compliance in y direction for flexure hinge i
$\left[\frac{\Delta x}{F_x}\right]_i$	Translational compliance in x direction for flexure hinge i
$\Delta \alpha_j^i$	The rotational displacement of ith flexure hinge about z axis at point “j”
Δy_j^i	The translational displacement about y-axis of ith flexure hinge at point “j”
Δx_j^i	The translational displacement about x-axis of ith flexure hinge at point “j”
T_i	Transformation matrices
K_i	Stiffness for each actuation direction i
f	Frequency
v	voltage
v_h	hysteresis voltage
v_p	Input piezo voltage
T	Ectromechanical transformation ratio
q	Total charge
q_p	Charge transduced due to mechanical motion
H	Hysteresis function that depends on q
m_p	Equivalent mass
c_p	Equivalent damping
k_p	Equivalent stiffness
F_c	Control force
F_{dis}	Disturbance force
ρ	Density
η	Viscosity
m_n	Nominal mass
c_n	Nominal damping
k_n	Nominal stiffness
T_n	Nominal ectromechanical transformation ratio
u	Displacement
v_{obsc}	Observer control input

v_{in}	Plant control input voltage
\hat{u}	Estimated displacement
σ	Sliding manifold
C_{obs}	Observer control parameter
D_{obs}	Observer control parameter
K_{obs}	Observer control parameter
dT	Sampling time interval
e	Error
\hat{e}	Estimated error
C_x	Position control parameter
D_x	Position control parameter
K_x	Position control parameter
θ_i	Angles of displacement vectors $i=1,2,3$
x_{ref}	Reference position in x direction
y_{ref}	Reference position in y direction
Amp	Amplitude
A	Transformation matrix which relates the motions u_1, u_2 and u_3 to x-y motion of the end-effector
K_p	Proportional control parameter
K_i	Integral control parameter
K_d	Derivative control parameter
$G(s)$	Transfer function
T_{pi}	Transfer function parameters $i=1,2,3$

TABLE OF ABBREVIATIONS

EDM	Electrical Discharge Machining
CNC	Computer Numerical Control
PZT	Piezoelectric
SMA	Shape Memory Alloy
DC	Direct Current
AC	Alternating Current
LVDT	Linear Variable Differential Transformer
RRR	Three Revolute Joint Link
PRR	One Prismatic Two Revolute Joint Link
PRBM	Pseudo Rigid Body Model
FEA	Finite Element Analysis
CCD	Charge Coupled Device
PSD	Position Sensitive Device
DOF	Degree Of Freedom
PEA	Piezoelectric Actuator
PI	Proportional Integral
PID	Proportional Integral Derivative
SMC	Sliding Mode Control
DOB	Disturbance Observer
DAC	Digital to Analog Converter
ADC	Analog to Digital Converter
SISO	Single Input Single Output

1 INTRODUCTION

1.1 Micropositioning

In modern technology, positioning of necessary parts became very important for micro/nano applications such as cell manipulation, surgery, aerospace, micro fluidics, optical systems, micromachining and microassembly etc. [1-2]. As a result of these developments in micro and nano technologies high precision positioning devices with controlled motions at sub-micron and even at nano level is needed. A laser micromachining unit in Microsystem Laboratory of Sabanci University is shown as an example in Figure 1.1. This system needs a micropositioning mechanism to focus the laser on the specimen precise enough to cut a circle in desired dimensions. Another example shown in Figure 1.2 is a micro manipulation unit, which needs to have high precision positioning stages for handling and manipulating the micro particles which are visualized via microscope.

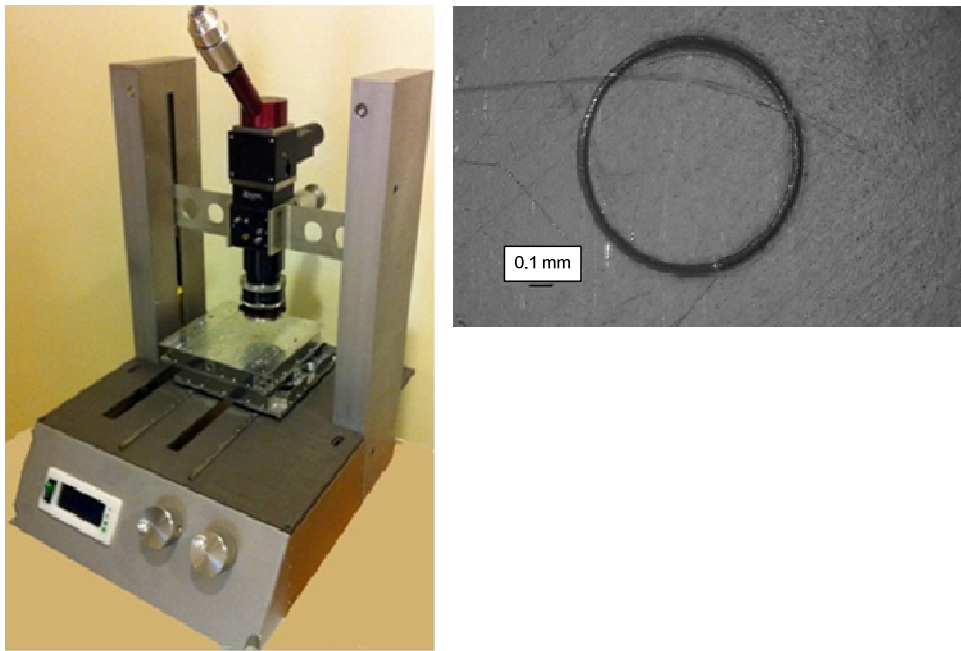


Figure 1.1 Laser micro machining unit [3].

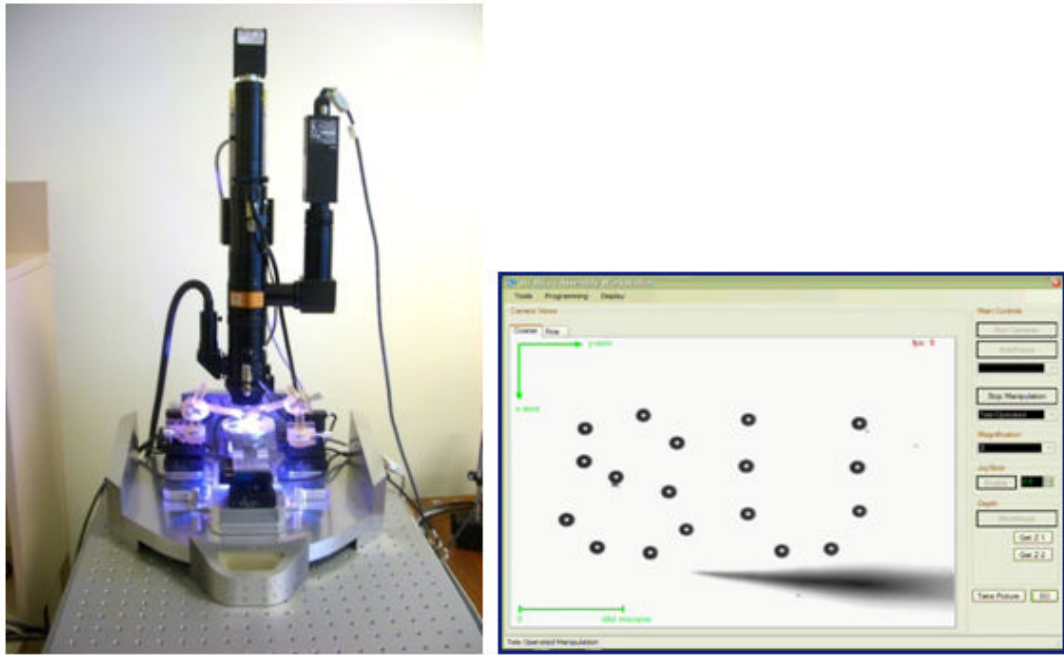


Figure 1.2 Micro manipulation unit [4].

The resolution of positioning, the range of application, the velocity, the needed number of degrees of freedom, the dimensions and the cost of these positioning mechanisms are the significant parameters of necessary applications to be fulfilled [5]. Thus, high precision positioning devices needs different methodologies which are simple enough for design and are composed of selection of kinematics, materials, actuation, measurement and control as shown in Figure 1.3.

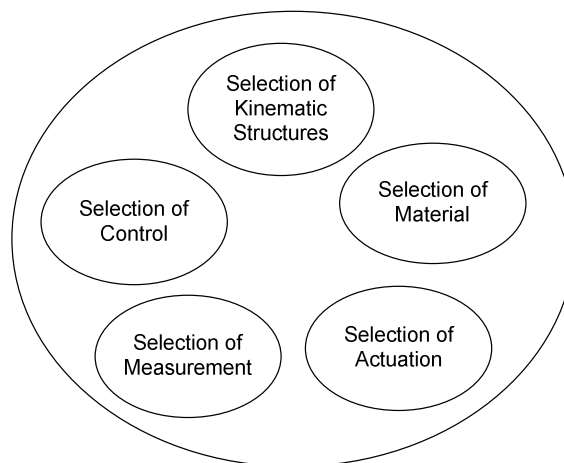


Figure 1.3 High Precision mechanism design methodology selections.

Kinematic structures are divided into two groups namely, serial and parallel kinematic structures. Serial kinematic structures are composed of serial links connected with active joints (actuated joints) as shown in Figure 1.4a and while parallel kinematic structures have separate and independent links actuated from the fixed base, which are connected with passive joints (not actuated joints) to the end effector and working in parallel as shown in Figure 1.4b. Serial kinematic structures provide large workspace. However, they have many disadvantages such as error accumulation, carry the weight of the actuators, having low stiffness and occupy big space.

Workspace is limited for micropositioning so that parallel kinematic structures are mostly chosen. They have the following advantages:

- No error accumulation: They average out the error coming from the links and joints. . As a result, the errors are not accumulated unlike in serial kinematic structures.
- Easy to shrink: Micropositioning stages should be small enough to be used in applications. Parallel kinematic structures are a good choice since they can be shrunk easily because of their compact structure.
- High stiffness: They increase the stiffness due to their closed kinematic chains and reduce the effects of off-axis forces. They can also work in high bandwidths.
- Reducing the moment of inertia: The actuators can be fixed on a base such that the actuators are not carried in the mechanism. The end effector, links and joints masses are also shared by each kinematic chain so that the moment of inertia is reduced and this leads to high dynamics (speeds and accelerations) and allowance of working in high bandwidths.
- Providing symmetrical structure: This also provides high dynamic performance. The end effector is balanced by the system which leads to smoother motion.

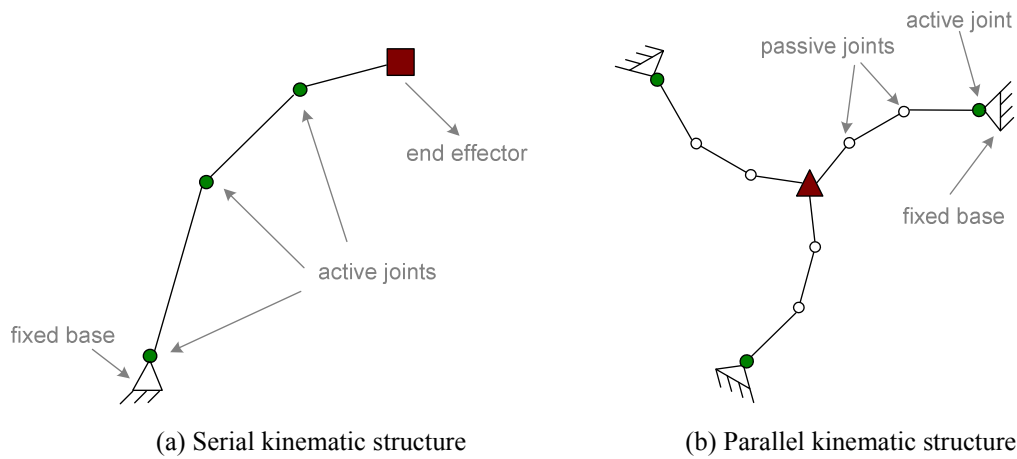


Figure 1.4 Kinematic structures.

Material selection is important for having a high precision stage. The material should be light enough to be used in fine positioning applications on the top of a coarse positioning stage. It should be convenient for high precision manufacturing techniques like wire electrical discharge machining (Wire EDM), laser cutting, water jet cutting, CNC milling etc. It should be resistive enough for fatigue, temperature, humidity etc., which are determined by the working conditions of the stage. Mostly in applications titanium, titanium alloys aluminum, silicon based materials, teflons etc. are used as stage materials [6].

Miniature actuators and compatible actuators are needed for micro-motion stages. Mainly two types of actuation are used in these fields, which are actuators working with fields and actuators working by changing their shapes. The first type of actuators uses the field of electrostatic, magnetostatic and electro-dynamic (DC servo motor, AC servo motor, stepper motor, coil motors etc.) fields, whereas the second type of actuators (piezoelectric (PZT), shape memory alloy (SMA), thermal actuators, ultrasonic etc.) are using the strain in the material that can be converted to force [7].

Position measurement is another important selection for micro positioning stages because it determines the performance of the stage. The resolution of the measurement system should be in sub-micron even in nano levels to render the measurement small enough to be compatible with the stage. Laser position sensors, capacitive sensors, eddy current sensors, inductive sensors (LVDT), high accuracy encoders are generally used in micropositioning [5].

Finally, for the control selection, advanced motion control techniques are used in micro positioning stages. The proposed control techniques filter the disturbances like

nonlinearities, hysteresis, friction, environmental effects out of the system and provide smooth, precise and robust enough motion to be used in micro manipulation applications.

1.2 Background and Motivation

The need of increased accuracy and precision requires the development of design and control methods simple enough that can be used in engineering practice. Traditional rigid body mechanisms do not provide needed accuracy and precision for micro scale applications. Instead, high precision mechanisms with flexible joints are designed in which flexible joints transfer necessary motion or force in the mechanism. The desired motion is provided with the deflection of these flexible joints also called in the literature as “flexures” which have limited rotation capability determined by their material properties as shown in Figure 1.5. According to N. Lobontiu, a mechanism which is composed of at least one component that is sensitive to deformation compared to the other rigid links called “compliant mechanism” [8].

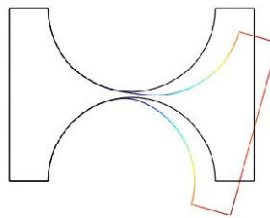


Figure 1.5 A deformed flexure.

Compliant mechanisms have many advantages for being used as high precision positioning stages. Firstly, they introduce no backlash and wear problem, also there is no need of lubrication. Displacements are smooth and continuous at all levels and small displacements up to $0.01 \mu\text{m}$ can be provided by the flexures. If the material is still under elastic region, there is no hysteresis in their motion. Under this condition, they provide submicron accuracy. If the mechanism is designed as a symmetric structure, it will be insensitive to temperature changes. Moreover, they reduce the weight of the stage, which is another important factor to be used in micro applications, where light weight is needed. Compliant mechanisms mostly designed as monolithic structures, which give them the advantage of being shrunk and making the system compact

enough. Final big advantage of compliant mechanisms is to be cheaper than the high precision mechanisms that use conventional rigid joints because of the manufacturing costs.

As mentioned earlier mostly parallel kinematic structures are used for micro positioning stages because of their advantages. However, parallel kinematic structures also have important disadvantages such as having limited workspace and dexterity, non-linear kinematics, difficult calculation of forward kinematics. But, these drawbacks are not problems for flexure based (compliant) mechanisms because the motions are in micro scale range and due to the resulting small flexure displacements the kinematics can be assumed as linear in the workspace range. The repeatability of these structures is eliminated with flexures because there is no backlash, friction problem in the joints as in rigid mechanisms [6].

In the 1970s, compliant mechanisms have been started to be designed. Since then, researches have tried to give solutions to the problems such as modeling, manufacturing, control etc. that compliant mechanisms have because of the flexible joints. Flexible joints have several advantages for high precision mechanisms as well as, some challenges and disadvantages [8]. The biggest challenge is analyzing and designing the high precision mechanisms with flexible joints because both mechanism analysis and synthesis methods of flexible elements should be known. Furthermore the interaction between rigid and flexible members should be also understood. If the flexure is forced to provide large deflections linearized equations cannot be used. Nonlinear equations, which are caused by the large deflections of the flexible joints due to their geometric nonlinearities, should be taken into account. Because of these designing difficulties many mechanisms with flexible joints were designed by trial and error in the past, which could be only used in very simple systems performing simple tasks. If flexure provides small deflections linear equations can be acceptable so that theories have been developed to simplify the analysis and design methods of mechanisms with flexible joints. However, they still have limitations and are more complicated than the theories applied to rigid body mechanisms.

Manufacturing and assembling of compliant mechanisms with the actuators and fixed base are also important problems for micro positioning applications. If the dimensions of flexures and the links have errors in manufacturing and there are misalignments in the assembly of the compliant mechanisms shown in Figure 1.6, the

provided motion of compliant mechanism will totally be different than the expected performance obtained from the modeling and design process.

Fatigue is another important problem for the mechanisms with flexible joints different from rigid body mechanisms, because the flexible joints are loaded cyclically when the mechanism is operated. Thus, it is important to design those flexible elements having a sufficient fatigue life to perform their functions appropriately in the mechanism.

A flexible joint cannot produce a continuous rotational motion unlike in pin joints since their motion is limited by the strength of the material of the flexible joints. These joints could also remain under stress for long periods of time or their material could creep or have stress relaxation at elevated temperatures.

In summary, compliant mechanisms based on flexures have many advantages for micro positioning but they have some drawbacks that should be taken into account while using implying that there are still active research topics about them are going on.

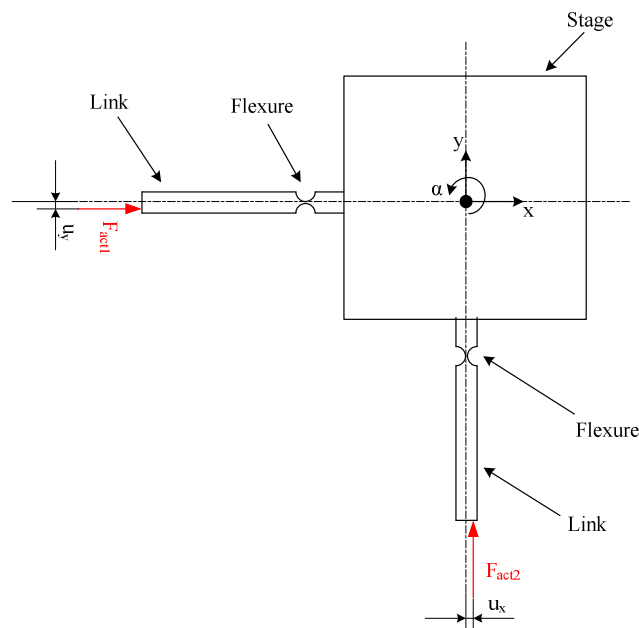


Figure 1.6 Misalignment of actuators with the compliant stage.

1.3 The Goal and Objectives

The goal of this thesis is to design a compliant mechanism that can be used as fine X-Y positioning stage for micro scale applications that is designed in our Microsystems Laboratory. This research aims to eliminate the unpredictable errors in design,

manufacturing and assembly by designing a control methodology which is our main contribution.

The objectives of this work can be classified into three groups, namely, design, modeling and control of compliant stages.

1.3.1 Design of Compliant Stage

The design procedure of the compliant stage is based on selecting a rigid kinematic structure and using flexure hinges instead of rigid joints to mimic the behavior of the mechanism. We have designed two types of planar parallel compliant stages which have 3-RRR (Three revolute jointed) and 3-PRR (One prismatic- two revolute jointed) kinematic structures. In the design process we have used Finite Element Analysis (FEA) to determine the behaviors of the mechanisms. The important points that are taken into account while designing the compliant stages are stated as follows:

- **Range of motion:** Flexible structures motions are limited due to stress and strains in their material. The designed flexible joint can bend until the yield stress of its material is reached. Beyond yield stress the deformation in the joint becomes plastic, which renders the behavior of the joint unpredictable.

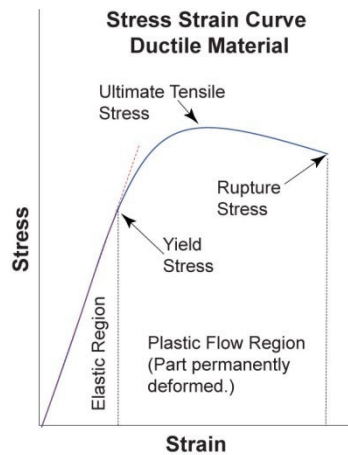


Figure 1.7 Stress-Strain curve [9].

- **Parasitic motion:** Parasitic motion is the unwanted motion of the flexible joint, which could associated with the observations that as for the notch type flexures the center of rotation are not fixed with respect to the links it connects and as for the translational flexures the axis of the motion can deviate from its straight line

motion. These parasitic motions can be eliminated by using symmetric structures while designing the flexible joints.

- **Off-axis stiffness:** Most of the flexures have low stiffness value also in directions, which are not the desired ones and causes parasitic motions for compliant mechanisms. Thus, increased off axis stiffness is needed when designing the flexures.
- **Stress Concentration:** Reduced stress in the flexure is preferable because it affects the life of the flexure. The flexures like spherical notch type ones have reduced cross sections, which cause high stresses on their reduced cross sectional area.
- **Compactness:** The flexible joints should be compact enough to be miniaturized.

1.3.2 Modeling of Compliant Stage

The model of a compliant mechanism should be simple enough to calculate the behavior of the flexible joints and accurate enough to be used as a tool for design. Modeling of Compliant mechanisms is the major problem while designing because of the non linear terms coming from the flexibility of the link which is dependent on both time and position of the links. The combination of the dynamics of the flexible parts of the mechanism and the parts which can be assumed as rigid bodies is also a different problem to make a whole dynamic analysis having both rigid and flexible parts.

Pseudo-Rigid-Body-Model (PRBM) [6] in which flexible joints are treated as torsional springs and the compliant mechanism is treated as an ordinary rigid body mechanism is mainly used for the simplicity of calculation. By using this technique we can easily use our knowledge about rigid mechanisms modeling. The calculation of spring stiffnesses of the flexure hinges determines the precision of the model so we have compared different types of calculation methods in the literature with Finite Element Analysis results to select the most proper calculation. After selecting the calculation methods we have implemented Kinetostatic Modeling technique for our newly designed 3-PRR compliant mechanism which combines the kinematics and statics of the mechanism by using the compliances of flexible joints.

1.3.3 Control of Compliant Stage

The position control of compliant mechanisms is needed to be used as positioning stages in Microsystem applications. The unwanted motions due to manufacturing and assembly errors can be eliminated by designing a control methodology based on observers. The main issues should be taken into account while controlling a flexible mechanism is stated as follows:

- The dimension scale is the main difference between classical robotic control and high precision robotic control. The mechanical system sensitivity to perturbation is bigger because of the controlled system has smaller weight.
- The displacement scales are also different, which means that a stage moving for 1ms at a speed of 1mm/sec (which is a low speed for classical robots) would make a displacement of 1 μm , which is a big displacement for high precision robots.
- The number of degrees of freedom of the manipulator and the number of available control inputs are not compatible so that we need to make a transformation between the joint and control spaces.
- There are oscillatory motions in the mechanism and to model the structural oscillations additional passive modes should be introduced, which makes the order of the dynamics higher.

The unwanted motions of the mechanisms are examined experimentally. We have observed that the kinematics calculated with the kinetostatic model and finite element analysis doesn't match with experimental results because our mechanism and setup is not ideal so with the computed models we can't achieve appropriate results with open loop position control methods so we have asked that can we fix these problems with a different control methodology based on Sliding Mode Control with Disturbance Observers to eliminate the unwanted motions.

1.4 Organization of the Thesis

The thesis structure is organized as follows: Section 2 presents a literature review about designed compliant mechanisms used as micropositioning stages, modeling types and used control methods. In Section 3 designed compliant stages are introduced and

Finite Element Analysis of these mechanisms with discussions of comparison of the stages is presented. The compliance modeling techniques of the flexure hinges that are used in design are compared and the important geometric parameters of flexure hinges are discussed in Section 4. Kinetostatic Modeling technique is applied for newly designed compliant mechanism and results are compared with Finite Element Analysis in Section 5. Experimental setup and experimental results for the behavior of the mechanism in terms of actuation and displacement are shown in Section 6. Piezoelectric Actuator modeling and its position control are done in Section 7. The position control of compliant stages by using piezoelectric actuators are implemented and discussed in Section 8. Finally, in Section 9 an overall conclusion is made and contributions of this work are stated.

2 LITERATURE REVIEW

Compliant mechanisms have been used in many studies for micro/nano positioning during the last decade. Generally, parallel kinematic structures have been selected for the design of compliant mechanisms. Different techniques have been developed to eliminate the drawbacks of compliant mechanisms caused by flexible joints. An overview of these techniques, which are based on designing, modeling and control, will be presented in this section.

2.1 Designing of Compliant Stages

The design of a compliant positioning mechanism (Figure 2.1) is composed of selection of the mechanism, materials and manufacturing techniques. In addition of the selection of measurement type, actuation is also another important concept of designing a compliant stage. These selections mostly depend on the applications, in which compliant stages will be used. In this part, the common selections in the literature will be presented.

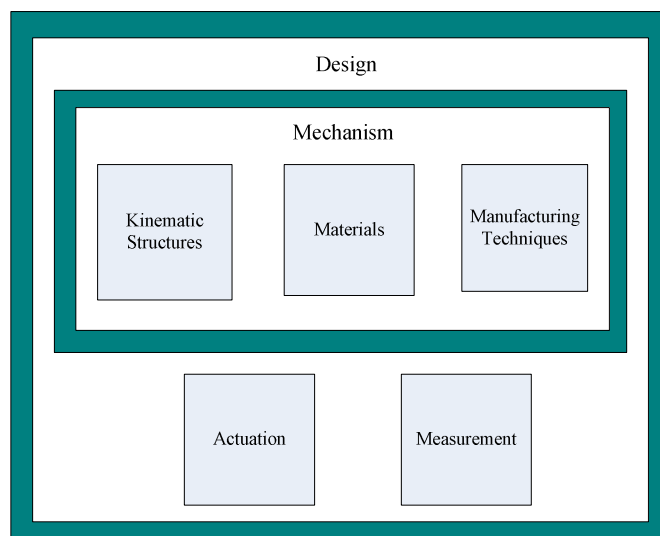


Figure 2.1 Designing of compliant stages.

2.1.1 Mechanisms

First compliant micro motion stage has been designed in 1978 by Scire and Teague for electron microscope probe application which has 1 degree of freedom (DOF) and composed of flexure hinges [10]. Thereafter, many compliant stages have been designed. Mostly parallel kinematic structures have been chosen for the kinematic structure of the mechanisms because of the advantages discussed in Section 1.1 whereas serial kinematic structures have also been used for micro positioning as shown in Figure 2.1. Two DOF x-y positioning stages with serial kinematics have been used in [11] which is used for scanning tunneling microscopes. Another two DOF x-y positioning stage is designed in [12]. A three DOF serial compliant stage is also designed in [13] for the alignment of optical device in x, y and z axes (Figure 2.2b).

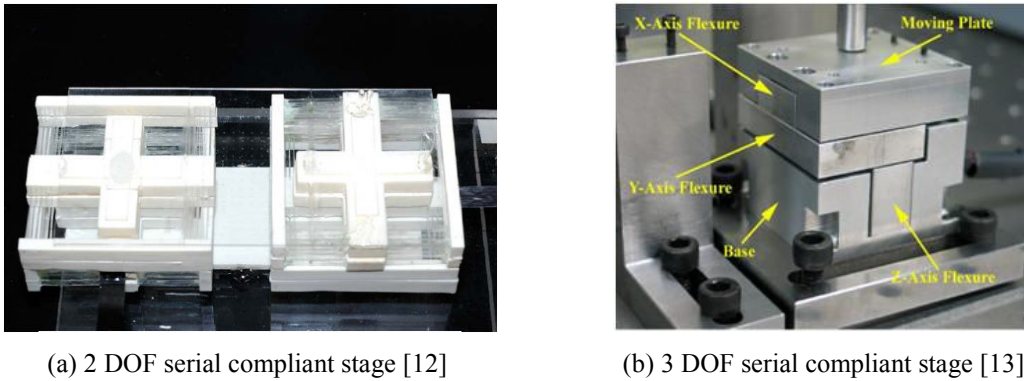


Figure 2.2 Serial compliant stages.

Various types of parallel kinematic structures have been used while designing compliant positioning stages in the literature. These structures are based on popular rigid body parallel mechanisms. We can classify those mechanisms as planar and spatial mechanisms. Planar compliant stages are the ones which can provide displacement on a plane. Many 2 DOF planar parallel compliant mechanisms have been studied in [14-24]. The common problems of these stages are parasitic motions and the limited range of the motion of these stages. Amplification mechanisms have been designed to improve the range of motion of these stages. Lever mechanisms shown in Figure 2.3 are the simplest amplification mechanisms which have been designed and analyzed in [20] and [21].

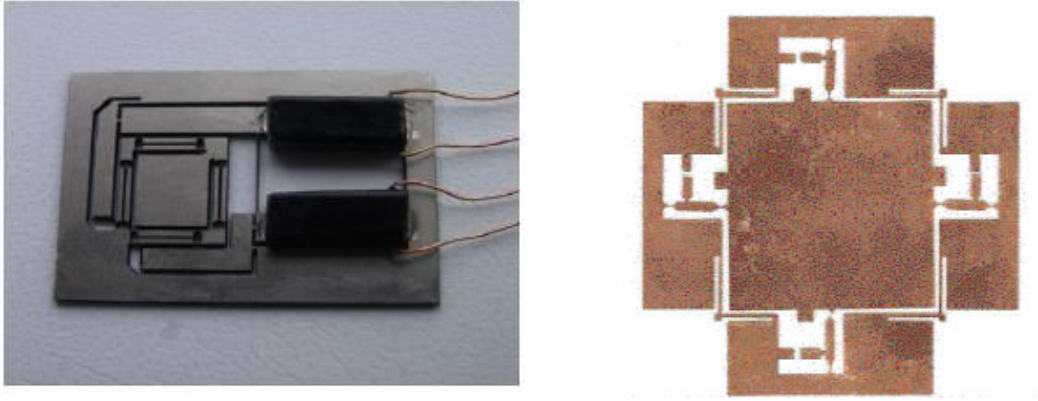


Figure 2.3 Lever mechanism based XY planar parallel compliant stages [20-21].

More complicated amplification mechanisms such as 5 bar mechanisms shown in Figure 2.4 have been used to overcome the unwanted (parasitic) motions by using parallelogram hybrid flexure structures in [14] and [17]. In addition a new amplification mechanism based on symmetric 5 bar topology has also been designed in [25].

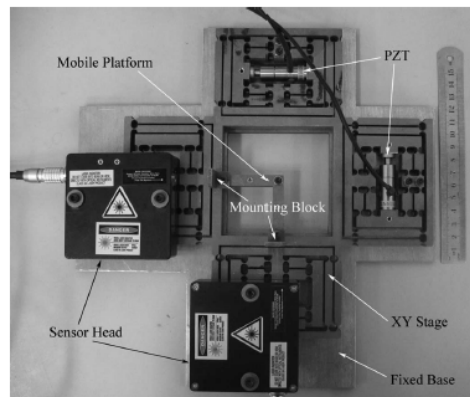
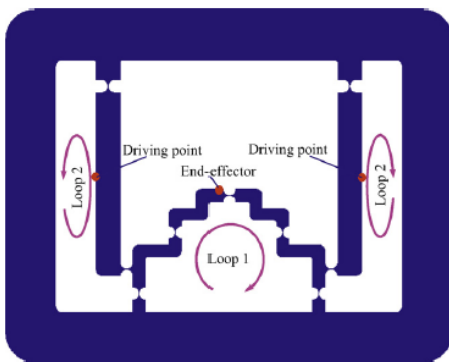


Figure 2.4 XY compliant stages based on 5 bar mechanism [25].

Double parallelogram structures having one DOF have been developed and used as constraint elements to design XY flexure mechanisms as shown in Figure 2.5 [19]. The choice of constraint patterns and degree of the symmetry determined the performance of the stage.

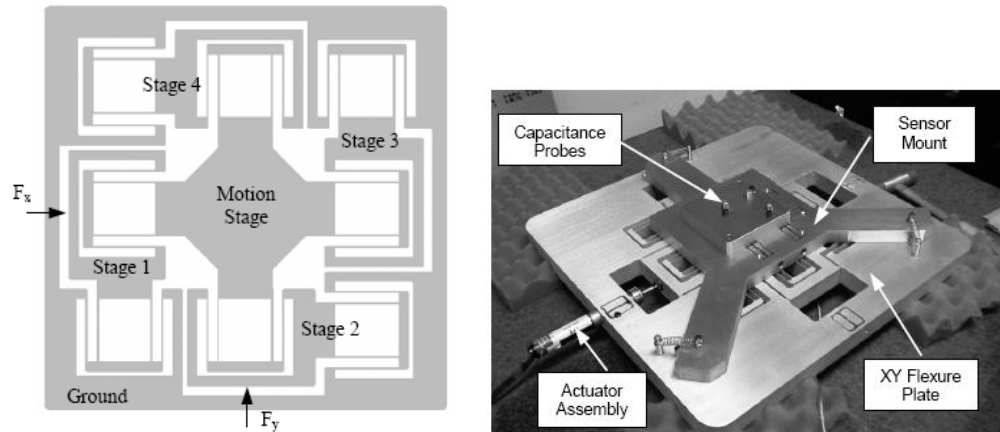


Figure 2.5 XY compliant stage based on parallelogram structures [19].

A high bandwidth XY Nanopositioning stage based on parallelogram structures have been design by Polit at al. shown in Figure 2.6 [15]. The stage is composed of a double clamped beam and a parallelogram hybrid flexure which is a module designed to be used in high-bandwidth needed applications. Compliant beams and circular flexure hinges were used as flexible joints.

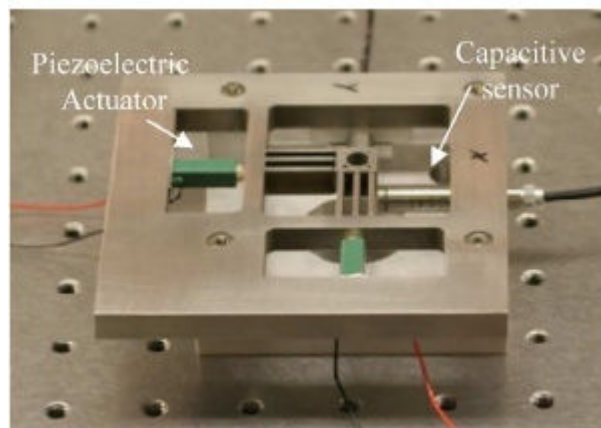
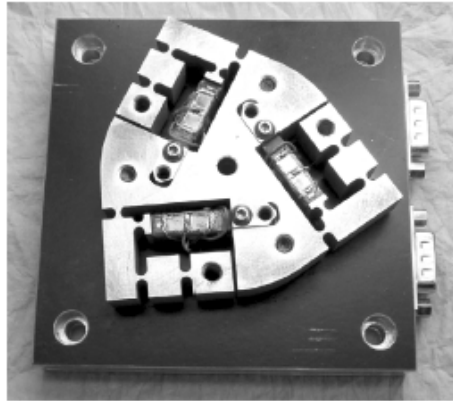


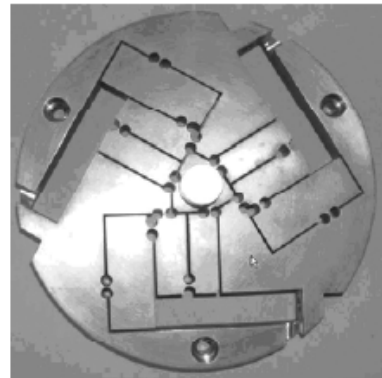
Figure 2.6 Planar XY nan positioning system [15].

Three DOF planar parallel structures have been developed for providing translation in x and y axes and rotation about z axis. These mechanisms are mostly based on triangular stages that have 3-RRR (three revolute joint) structure as showed in Figure 2.7a [26-32]. A triangular platform is actuated by three linkages which are at the corners of the stage. Each chain is composed of 3 revolute joints in a serial arrangement. The end-effector has translation motion along x-y direction and a rotation about the x axis. This type of parallel kinematic structure amplifies the motion of the actuators. The revolute joints were replaced with flexure hinges which were designed according to the

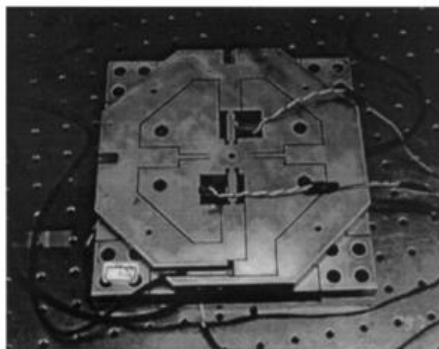
desired parallel kinematic performance. Other types of x - y - θ planar compliant structures with amplification beams as shown in Figure 2.7b and 2.7c have also been designed in [33] and [34]. A very compact x - y - θ planar compliant mechanism which is actuated by one actuator is studied in [35]. The compact stage can be seen in Figure 2.7d.



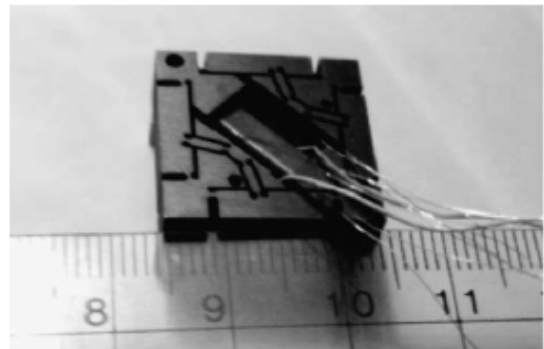
(a) 3 RRR compliant mechanism [27]



(b) 3RRR with amplification levers compliant mechanism [34]



(c) XYθ planar compliant mechanism [33]



(d) XYθ planar single actuated mechanism [35]

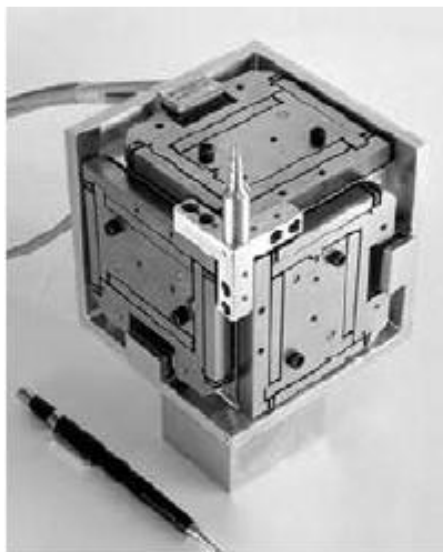
Figure 2.7 3 DOF planar parallel compliant mechanisms.

Spatial positioning stages by using compliant structures have been designed in [36-51] for XYZ motion. Spherical notch type flexures (shown in Figure 2.8a) which enable the links to have the motion capability in spatial directions have been used for designing a spatial compliant mechanism [47, 49-51] whereas, planar mechanisms with single axis flexure hinges (shown in Figure 2.8b) have been also used by placing the mechanisms in such a way that it has spatial motion capability [38, 42,45-46, 52]. There are also spatial compliant mechanisms that use both single axis and spatial axis flexures together [37, 39].

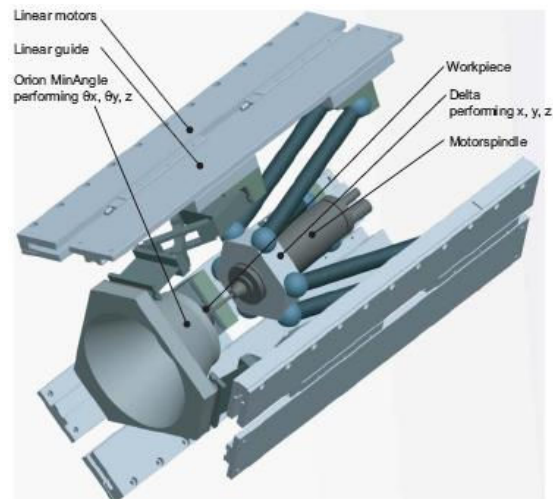


Figure 2.8 (a) Spatial Flexure Hinge, (b) Single Axis Flexure Hinge

Stewart platforms have been designed as compliant mechanisms by replacing the joints with spatial flexure hinges [43]. Delta robot have also been used to mimic the parallel kinematic structure shown in Figure 2.9a [40] and a parallel kinematic structure with designed flexible joints has been developed to be used with a Delta robot as shown in Figure 2.9b [41] which would enable an additional mechanism for delta to have ultra precision.



(a) Delta 3 stage [40]



(b) The orion minangle mechanism [41]

Figure 2.9 Spatial compliant stages.

A triangular stage having nano positioning in X-Y and Z axes have been developed by Q Yao et al. [46]. A triangular stage is the end effector which is connected by 3 independent kinematic chains in parallel as shown in Figure 2.10. Each kinematic chain is composed of two parallelogram four bar mechanisms which maintains the movements of the connector always parallel to the base.

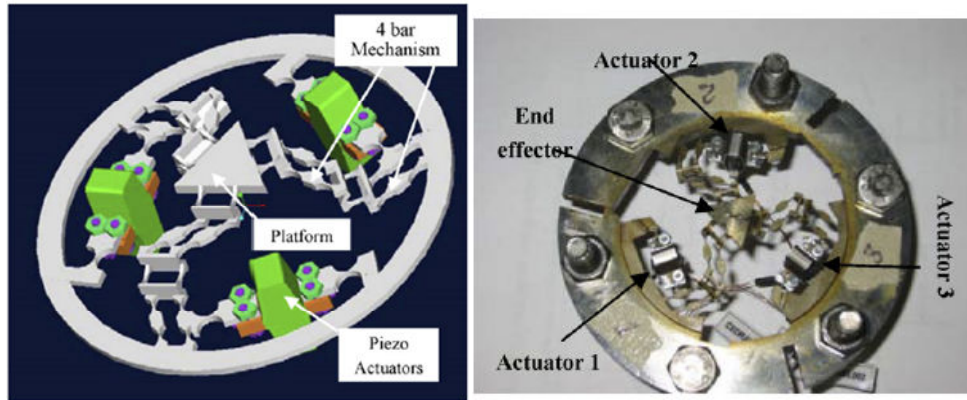


Figure 2.10 XYZ nanopositioning stage [46].

A 6 DOF compliant mechanism has been developed by combining two types of parallel kinematic structures in [37]. A 3-RPS (revolute-prismatic-spherical) mechanism is designed for the upper stage and a 3-RRR mechanism is designed for the lower stage as presented in Figure 2.11.

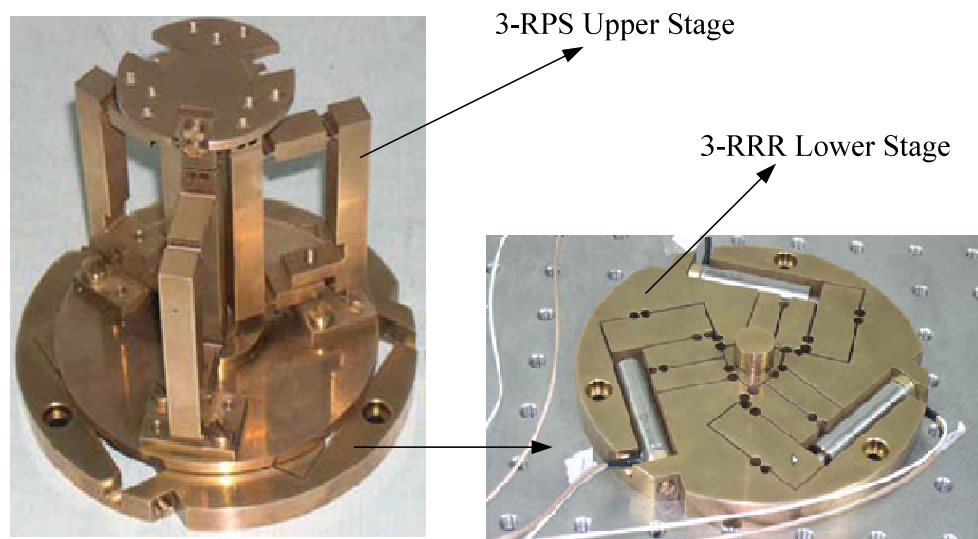


Figure 2.11 6 DOF compliant mechanism having 2 parallel kinematic structures [37].

Planar parallel kinematic structure called “HexFlex” is designed in [38,45] for out of plane motion of the end effector of the stage. Beam structures are used as flexible joints and they are actuated in such a way that the end effector of the stage has the motion capability on out of plane. The mechanism shown in Figure 2.12a is in macro scale and the mechanism shown in Figure 2.12b is in micro scale.

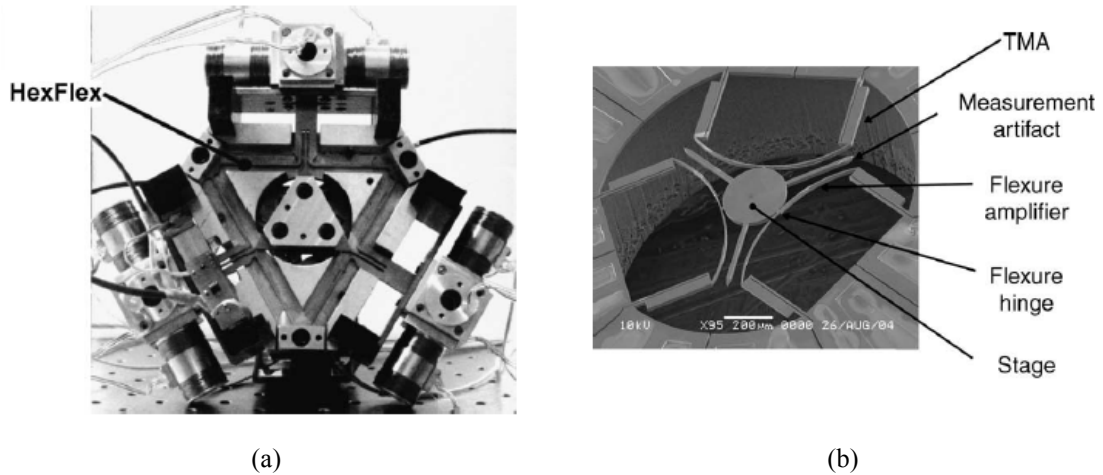


Figure 2.12 (a) HexFlex in macro scale, (b) HexFlex in micro scale [45].

Generally Aluminum is used as major material because it provides enough flexibility by having low Elastic Modulus (Young's Modulus). Wire Electro Discharge Machining (Wire EDM) technique is used for manufacturing and gives the advantage of manufacturing of thin members in mechanisms. Stainless steel especially spring steel to have lower elastic modulus has also been used in some applications [15, 25, 53, 49, 26]. Shape memory alloys (SMA) have been used in [51] to have angular deflections of $\pm 30^\circ$ which leads to provide larger workspace for compliant mechanisms. CuAlNiFe single crystal SMA was selected because of its allowance of machinability. Silicon based mechanisms have been designed and manufactured by using MEMS fabrication techniques in [16, 38, 54]. The mechanisms made with silicon are in micro scale and their motions are smaller than the mechanisms with Aluminum, Steel or SMA. Copper have been used in [21] by using lithography technique for manufacturing. A material called VeroWhite have been used in [47] to fabricate the mechanism by using a rapid prototyping machine called Objet to reduce the cost of fabrication and allow to manufacture more complex structures.

2.1.2 Actuators

Piezoelectric actuators commonly used for actuation of compliant mechanisms because of their several advantages like being compact, providing continuous and small motion with good displacement accuracy and having high frequency response. Other available actuators that have been used in the literature for driving the compliant mechanisms are Electromagnets [40, 45, 53], Electrostatic comb drives [54], Thermal

actuators [38], RC Servo actuators [12], DC Motors [41-55]. Electrostatic comb drives and thermal actuators are preferred in micro scale compliant mechanisms in which the actuators can be built in by MEMS fabrication methods. DC motors and RC Servo actuators seems bulky for these types of mechanisms because they are not compact.

2.1.3 Measurement

Measurement is important for the accuracy of the compliant positioning stages. It mainly determines the performance of the stage. Mostly non-contact displacement sensors with providing high resolution measurement are preferred for compliant mechanisms. Capacitive sensors are the most common ones which measures the displacement by using the electrical property of capacitance between two conductive surfaces. Small sensing surfaces are enough to measure the displacements with sub-nanometer resolutions.

Eddy current sensors have also been used in [27] and [31] which are also noncontact sensors with high resolution capability. They are based on magnetic fields. An alternating current is created in the sensing coil which creates an alternating magnetic field with causes small currents in the target material. They are less expensive than capacitive sensors but large gap between the sensor and the target is needed which require space for the compliant mechanism system.

Optical position sensors are also another choice for compliant mechanisms non-contact displacement measurement [23, 36, 40, 42, 47, 49]. It converts the light rays into electronic signals by using an electronic module called position sensitive device (PSD) which is analog or charge coupled device (CCD) which is digital. They can measure in one or two dimensions. Mostly the light source is laser but it can also be infrared laser source. Their range of measurement is bigger than capacitive or eddy current sensors.

Vision is another option for position measurement which is used in [12, 35, 38]. It mainly depends on the camera that we use and mostly microscopes are used for small range of motion detections.

2.2 Modeling of Compliant Positioning Stages

The need of modeling of compliant mechanisms is very important because the design and control procedure of compliant mechanisms was performed with trial error methods in the past which is not efficient technique. There are mainly four kinds of modeling methods of flexible links:

- mass-damper-spring model
- finite element method
- pseudo rigid body method
- assumed mode method

Mass-damper-spring model in Figure 2.13 uses mass damper spring constants for parameter identification of compliant systems. The results of this method are not good when compared with the experimental results and the mode behaviors of the flexible links cannot be analyzed with this method [56]. Mass-spring model with piezoelectric actuator linear model embedded is used in [17] for position control of a 5 bar flexure based mechanism.

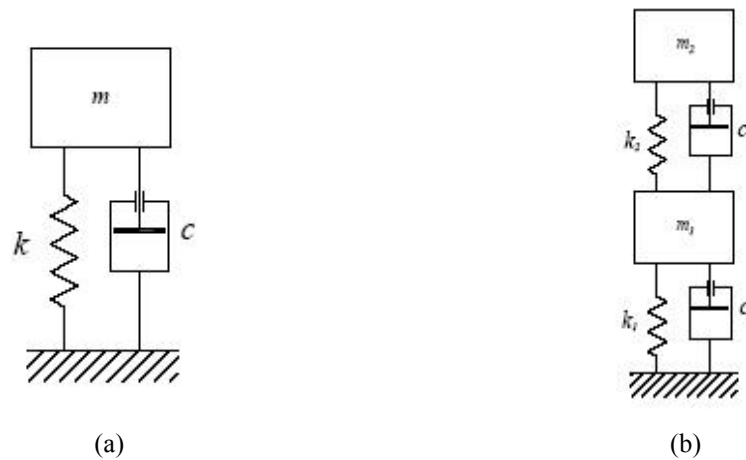


Figure 2.13 (a) 1 DOF model, (b) 2 DOF model.

Finite element method in Figure 2.14 is a systematic dynamic analysis of flexible mechanisms which is based on formulation of natural frequencies, modes, dynamic response, frequency characteristics and sensitivity analysis for flexible links [57]. Natural frequencies and modes are calculated by using undamped dynamic equations. The time response of the dynamics is calculated by a linear interpolation technique to approximate axial deformations and third order interpolation is used to approximate the bending deformation. The transfer function of the system is used to find the frequency

characteristic which is called modal testing theory. The transfer function of the system where force is the input and the displacement is the output is calculated by using Fast Fourier transformation algorithm. Finally the sensitivity of a certain parameter on the mechanism is calculated to see the affect on the natural frequency and vibration modes of the flexible links [57].

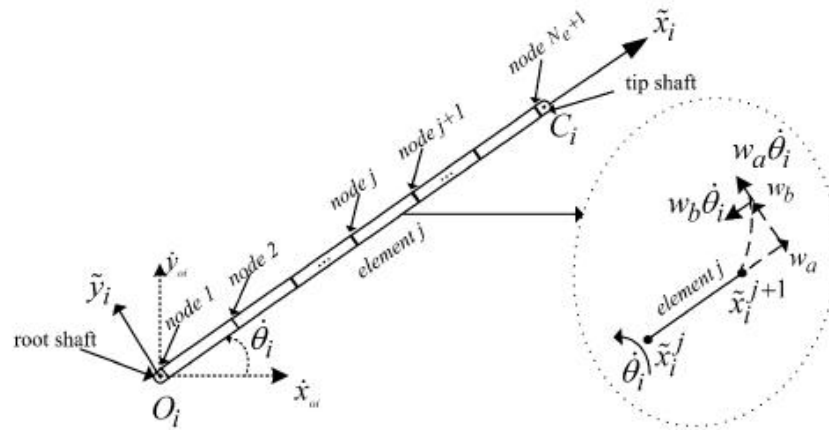


Figure 2.14 Element definition of a flexible beam.

Pseudo rigid body model (PRBM) shown in Figure 2.15 is a method which treats flexible mechanisms as rigid body mechanisms. It is a simple method because the flexible elements are represented by torsional springs at the pin joints with a massless rigid body [58]. The dynamics of the compliant mechanism is calculated by representing the flexible links with two torsional springs and one mass. This dynamics based on PRBM is called pseudo rigid body model dynamics (PRBMD). Kinetic and potential energies of the system are calculated with Lagrange's equations and a second order differential equation is derived. A generalized mass is represented in the kinetic energy of the system and potential energy of the system is calculated by deriving the dynamics spring constants for both end-force and end-moment load. The PRBMD results are compared with finite element analysis and it's seen that it can be used for modeling instead of FEA [58]. The dynamics of a four bar link is calculated in [59], while a micro half pantographs dynamics is calculated and it was observed that the method could be effectively used for the design of the compliant mechanism. PRBM makes calculating the compliant mechanism dynamics easier but the main disadvantage is that PRBM method does not take modes of the flexible elements into account. Thus it is suitable for a single configuration modeling. Loop closure theory has also been developed by using PRBM which is an effective kinematic model and incorporates the

complex number method to model the mechanism [30, 60]. A loop equation is calculated for each closed loop of the mechanism. The closed loop equations are expressed in terms of real and imaginary parts producing 2 equations per loop. Unknowns are found by solving the equations. Constant jacobian theory is also based on PRBM which calculates the jacobian of the mechanism which relates the input positions to output positions of the mechanism by using kinetostatic model [31-32, 61]. Kinetostatic model combines the kinematics and statics of the mechanism by using compliance calculations of the flexible joints.

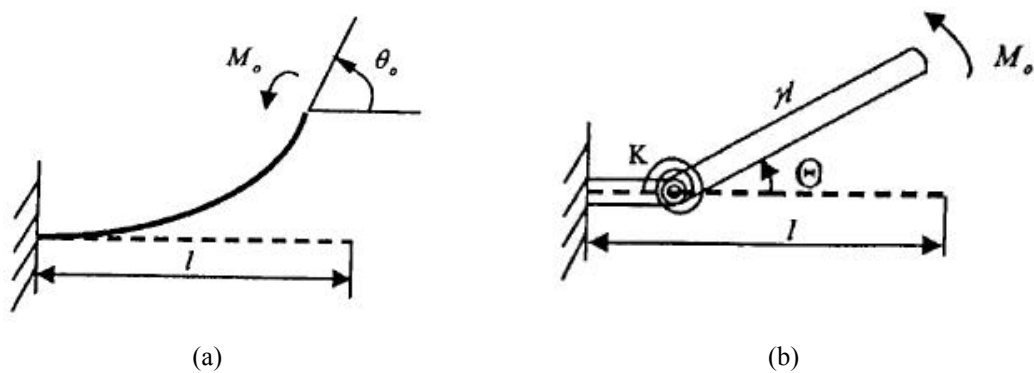


Figure 2.15 (a) Flexible beam with end moment, (b) The PRBM model [58].

Assumed mode method calculates the dynamics of the flexible mechanisms by using Euler Bernoulli beam equations. Firstly, the kinematic analysis of the mechanism is reformed, after the dynamics of the flexible links is considered and combined with the constraint equations. The constraints and the beam dynamics can be combined by using Lagrange equations and Lagrangian multipliers [62]. Craig Bampton method and other methods can be used to reduce the order of the dynamic model to compute the dynamics more efficiently.

2.3 Control of Compliant Positioning Stages

The position tracking control of the compliant micro motion stages is very important because of the high performance requirements in high precision applications. The structural flexibility of the mechanisms is a challenge. While the flexible joints and links give many advantages for high precision motion, they also easily generate oscillations at the tips of the links during the motion. There are also nonlinearities and

hysteresis in the system due to the behavior of the flexible joints/ links and used actuators like piezoelectric actuators. The motions are also maximum in micron range which makes it a little more difficult to control due to limited computation time, accuracy of sensors and makes the system more sensitive to perturbations when compared to general controlled mechanisms in macro range. The relation between the joint space and the task space is also important in terms of providing the desired motion to the end effector.

The main control problems of the flexible mechanisms can be stated as follows:

- The regulation of the end effector position.
- End effector rest motion at a fixed time.
- Tracking of a desired angular trajectory in joint space.
- Tracking of a desired end-effector trajectory in the operational space.

There are different kinds of control methodologies implemented for position control of micro motion compliant stages in the literature. PI control have been used for making the position control of the end-effector of a 3-RRR compliant mechanism in [31] with an individual feedback control of compensating the positions in x and y axis with using another PI control. The individual feedback is changed to PID control for compensating the inverse position Jacobian matrix having not only x-y motion but also rotation about z axis of the mechanism in [27, 32]. The used Jacobian matrix gives the relation between the joint-space (piezoelectric actuator) and task-space (end-effector). Both end-effector measurement and piezoelectric actuators position measurements are taken for the control of the mechanism. In [40] a control algorithm is designed by using a PID controller with state observer and a feedforward term based on a second order model determined experimentally. Servo switch feedback controller is used in [33] to compensate the backlash caused by the hysteresis and drift.

H. C Liaw and B. Shirinzadeh have been worked on different control methodologies for making the position control of a flexure based 4 bar mechanism which provides in one axis motion (1 DOF). An enhanced adaptive motion tracking control methodology providing 0.11 μm tracking error is designed based on a sliding control scheme to eliminate the uncertainties in the system such as hysteresis effect, external disturbances, nonlinearities [63]. Then they have implemented a neural network motion tracking control methodology to provide the unknown lumped system parameters, nonlinearities and disturbances [64]. The control methodology has succeeded to have 0.16 μm tracking error. Lastly they have tried another control

methodology with the same 4 bar mechanism which is robust generalized impedance control having 0.088 μm tracking error [65].

Yangmin Li and Qingsong Xu have also been developed the position control methodologies of compliant mechanisms having more than 1 DOF. A designed piezo-driven XY compliant micro positioning stage based on integrated parallel decoupled and stacked kinematic structure has been controlled by using the inverse of Bouc-Wen hysteresis model for the feed forward combined with a PID feedback control [66]. 0.51 μm tracking error for a circular path is achieved with this controller. Then they have proposed another type of control methodology which is sliding mode control with perturbation estimation featuring a PID-type sliding surface and adaptive gains for the motion tracking control of the mechanism [67]. They have improved their position tracking when compared to PID control. A totally decoupled piezo-driven XYZ compliant micropositioning stage is designed by using the same parallel compound structures. Modified Prandtl-Ishlinskii model is used for the hysteresis modeling and the inverse hysteresis model feedforward and feedback control scheme is implemented to the stage for making the position control in 3-DOF [52].

2.4 Our Contribution to The Literature

We have designed a new type of planar parallel compliant mechanism based on 3-PRR kinematic structure and we have shown that we can use compliant mechanisms that are roughly designed and manufactured if we have proper position control methodology. The designed stage has a lot of errors when the results of Finite element model compared to the experimental results. So we have implemented Sliding Mode Control with Disturbance Observer based on again Sliding Mode Controller using the Piezoelectric actuators linear model to eliminate the unknown, unpredictable motions of the compliant stage which is a new control methodology to the literature. We have also improved this control methodology by using the experimentally determined models instead of Piezoelectric actuator models for every motion direction.

3 DESIGNING OF THE PLANAR MICRO MOTION STAGE

This section presents the design procedure that is used for designing a X-Y micromotion compliant stage. In Section 3.1 the important points in design is discussed. In Section 3.2 the selected kinematic structure links are presented. In Section 3.3 the planar compliant mechanisms are designed and compared.

3.1 Limitations in Design of Compliant Stages

The performance criteria of the compliant stages is based on the range, parasitic motion, stress distribution and how many DOFs they can provide. In this section these concepts is discussed while designing the compliant stages.

3.1.1 Range

The range of the compliant micro positioning stages depends on the bending allowance of flexible joints and the generated force capability of the actuator that is used.

Compliance of the flexure hinges determines the capacity of rotation of the flexure hinges which affects the range of the compliant stage. The most important property is the Young's modulus of the material of the flexure hinge that determines the capacity of rotation. The width and the smallest thickness of the flexure hinge also determine the angular range of the flexure hinge. The compliance of the flexure is inversely proportional to the Young's modulus of the material which means that if the Young's modulus of the material is small the compliance is high so that the flexibility of the flexure will be high. Similarly if the minimum thickness and the width of the flexure is small the compliance is high.

The actuators are also important for determining the range. Mostly the selected actuator is piezoelectric actuator which is suitable for compliant stages because of their following advantages of providing:

- Smooth and continuous motion,
- Motion in microns even nano ranges,
- Design embedded in the stage which gives the possibility of compactness,
- Enough force to push or pull the flexible parts of the mechanism.

The major disadvantage of piezoelectric actuators is their limited maximum stroke so that designing an amplification mechanism to amplify the stroke of the piezoelectric actuator is necessary. In the market there are piezoelectric actuator cases with amplification mechanisms. However, to lower the cost of the actuators amplification mechanisms can be embedded to the compliant stage. Generally lever mechanisms, parallelogram mechanisms as shown in Figure 3.1 are used for this purpose.

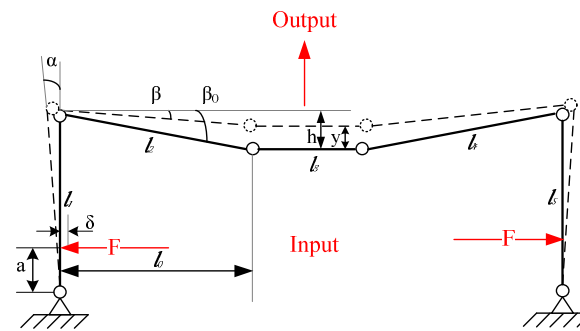


Figure 3.1 Amplification mechanism (5 bar).

3.1.2 Sensitivity to Parasitic Motions

Parasitic motions are the unwanted motions for our compliant stages when actuating forces are applied. Thus, the compliance out of drive axis should be as low as possible so that the mechanism would behave stiffer in those unwanted motion axes more discussion needed

3.1.3 Stress Distribution

Stress distribution is another important subject while designing a compliant stage because it determines the performance of the mechanism. If the stress of the flexible joint is maximized in a smaller zone the mechanism will behave more rigid like because

the flexible joint will bend almost from a point which gives the ability of mimic the rigid joints.

3.1.4 Number of DOFs

According to the application the number of degree of freedoms changes. The kinematic structure is selected due to the selected number of DOFs. Appropriate flexible structures should be designed in order to be replaced instead of rigid joints and provide the necessary movements in the kinematic structures.

Single axis flexures are suitable for rigid joints like bearings, which only have a single drive axis, whereas multi axis flexures are suitable for spherical joint type joints which can bend in multiple axes.

3.2 Designed Planar Parallel Compliant Stages

The designed micromotion compliant positioning stage should give solutions to the limitations that are mentioned in the previous section. According to those limitations if we summarize the mechanism should be stiff enough in the unwanted axes, amplify the range of the input actuation and give us opportunity to be controlled easily.

Our limitations are:

- The mechanism should provide $40\ \mu\text{m} \times 40\ \mu\text{m}$ x-y planar motion because our piezoelectric actuators have $40\ \mu\text{m}$ maximum stroke.
- The mechanism should be controlled easily to be used as a micro positioning stage.
- While the mechanism should be flexible enough to provide the necessary range for positioning it should also be stiff enough not to go under plastic region under the actuating forces.
- We have a limited manufacturing capability so the mechanism parameters and the experimental setup should be designed with interaction of the manufacturers.

We have first selected our stage to be a planar parallel mechanism because of the advantages of parallel kinematic structure that has been discussed in Section 1.1. The moving platform of the stage which is also called as the end-effector of the parallel

mechanism is selected to be a triangular stage. The actuating forces (F_1 , F_2 and F_3) of the triangular stage will come from the edges of the triangle as shown in Figure 3.2. If the forces are coinciding at the center of the stage can only move in a plane (on x and y axes) but if the forces are not coinciding at the center the stage can rotate about z axis.

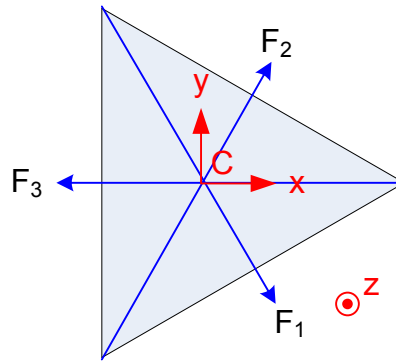


Figure 3.2 Triangular stage with actuating forces.

We will use the stage for x-y positioning and we have selected a mechanism having 3 actuation points so we will use the mechanism as a redundant mechanism although it might have a rotation capability. This redundancy will give us the advantage of increasing the workspace of the mechanism which is limited by the parallel kinematic structure and the deformation behavior of the flexible joints that will be used. Another advantage of redundancy is that it improves the dexterity of the mechanism which is the ability of the mechanism to arbitrarily change its position in arbitrary directions and it is an important subject for design and position control of the mechanisms.

We have selected our kinematic structure which has 3 kinematic chains connected to a triangular stage. The selected kinematic structure for the design of compliant stage is planar parallel structure which is composed of three RRR (3 revolute joints) limbs as shown in Figure 3.3a. This structure is popular for positioning applications because of the advantages of having a compact shape, amplifying the input actuation displacement and decouples the stiffness between the actuators. Decoupling is a very important role for control which gives the advantage of controlling the actuators separately so we can use 3 independent single input single output (SISO) controllers for each actuation direction of the triangular stage. We have improved the 3-RRR kinematic structure by replacing the active revolute joints with the prismatic joints and used three PRR (1 prismatic- 2 revolute joint) as shown in Figure 3.3b. The new structure is a 3-PRR kinematic structure. We will expect from 3-PRR mechanism to improve the stiffness of

the mechanism and the stress distribution which will improve the workspace and be stiffer to the parasitic motions.

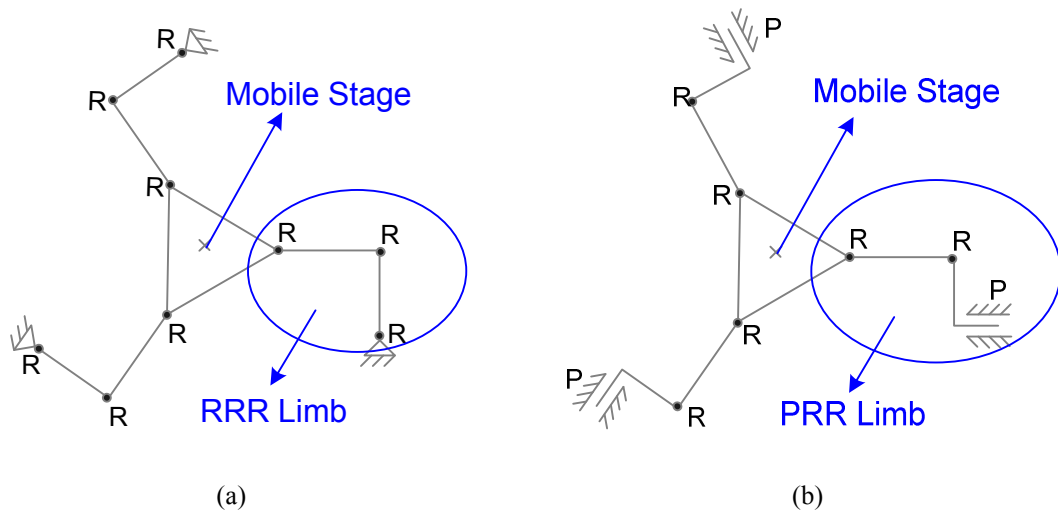


Figure 3.3 (a) 3-RRR kinematic structure, (b) 3-PRR kinematic structure.

Right circular notch flexure hinges are used for the revolute joints of the mechanisms and linear spring parallelogram flexible joints with right circular notch flexure hinges are used for the prismatic joints in 3-PRR kinematic structure which improves the stiffness in unwanted axis to eliminate the unwanted motions and it distributes the stress on the mechanism which improves the workspace of the mechanism. The reasons of choosing right circular notch flexure hinge will be discussed in section 3.3.1.

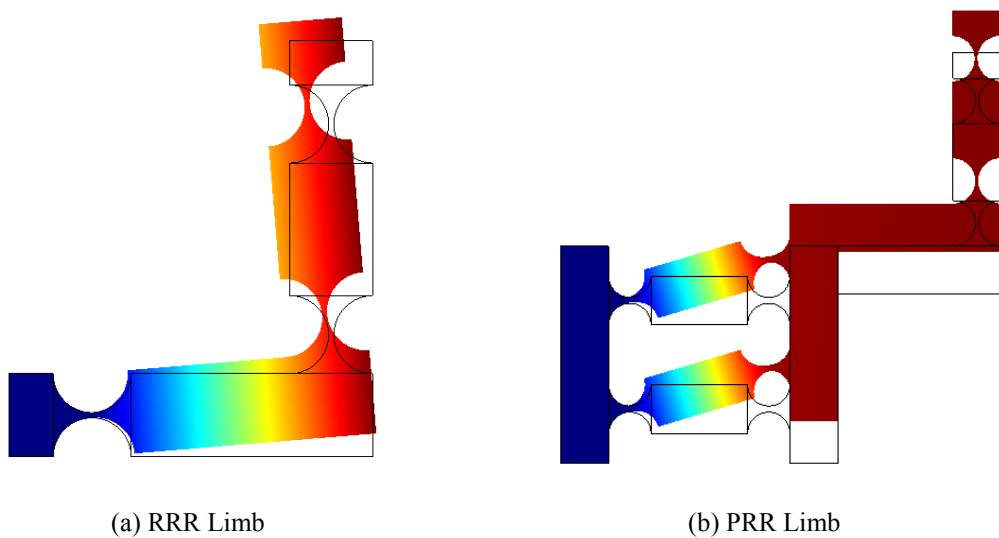


Figure 3.4 Limbs with right circular flexure hinges.

RRR limb is designed by the selected right circular flexure hinges representing the revolute joints as in Figure 3.4a. Simple linear spring structure based on right circular flexure hinges are used for prismatic joint of PRR limb as in Figure 3.4b. These designed compliant limbs are connected to the triangular stages and casing structures are also designed around the 3-RRR and 3-PRR compliant structures in order to be fixed to a setup and manufacture easily. The limbs and flexures parameters are picked by performing Finite Element Analysis to provide our limitations.

3.2.1 3-RRR Compliant Stage

3-RRR compliant mechanism is designed by using circular notch flexure hinges as shown in Figure 3.5. As mentioned earlier circular notch hinges are picked as revolute joints because they relieve the undesired stress on the beams and they can keep their position of rotation center stable so they are less sensitive to parasitic motions than the beam shaped flexures. The stage is actuated by driving a kind of lever mechanisms with piezoelectric actuators. The end-effector of the mechanism is a triangular stage which connects the three RRR links and has motion x-y directions and a rotation about z-axis.

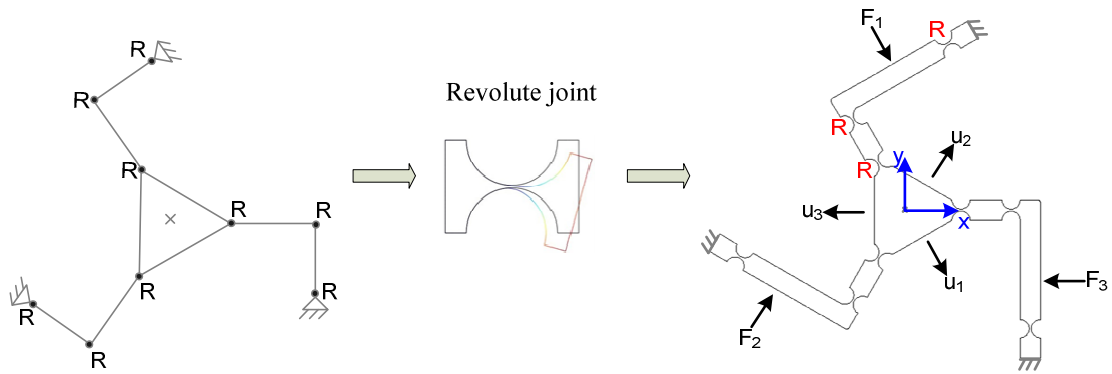


Figure 3.5 3-RRR compliant stage with circular flexure hinges.

Although the mechanism has 3 dof (x-y and rotation about z axis) we will deal only with the x-y motion of the stage. As mentioned earlier we will use the redundancy of the mechanism to increase the range of the stage and dexterity. The mechanism can be driven as illustrated in Figure 3.6. The RRR links are actuated by forces F_1 , F_2 and F_3 to create the displacements of u_1 , u_2 and u_3 respectively. By the combination of the “u” displacements desired x-y motion of the triangular stage can be generated.

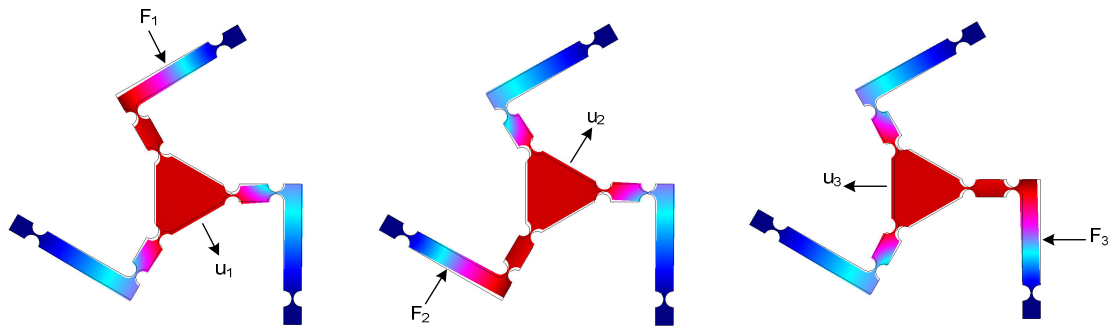


Figure 3.6 3-RRR compliant mechanism displacements.

An equilateral hexagonal case is designed for being easy for manufacturing and assembling of the compliant manufacturing with a designed base and actuators. The complete 3D design of compliant 3-RRR mechanism is shown in Figure 3.7. Holes are drilled for assembling the shaft of the piezoelectric actuators correctly. The most important geometric parameters are the shortest distance between the circumferences of two notches, “ t ”, and the overall thickness of the stage, “ b ” because they mostly determine the performance of the compliant mechanism. The discussion about “ b ” and “ t ” parameters will be done upcoming section 3.3.1. All necessary selected geometric parameters are shown in Figure 3.8 and Table 3.1. The hexagonal case has an outer circle tangent to it with a diameter of “ L_2 ”. All circular flexure hinges have the same radius, “ R ”. The triangular stage has an inner circle tangent inside the triangle with a radius of “ L_6 ”. All other parameters are the same just mirrored every 120° about z axis. These parameters are selected according to our limitations as mentioned before by using the Finite Element Analysis. The behavior of the mechanism will be explained in the next section.

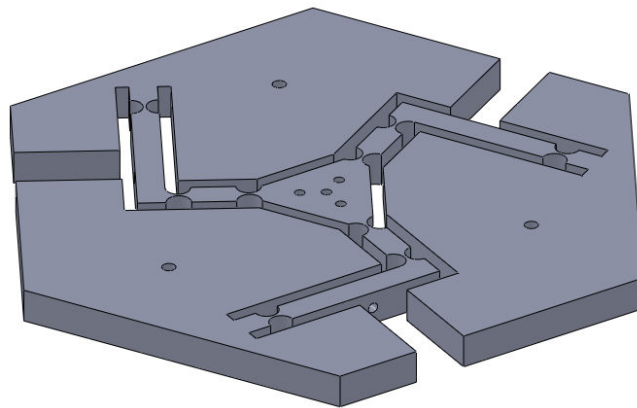


Figure 3.7 3D appearance of 3-RRR compliant mechanism.

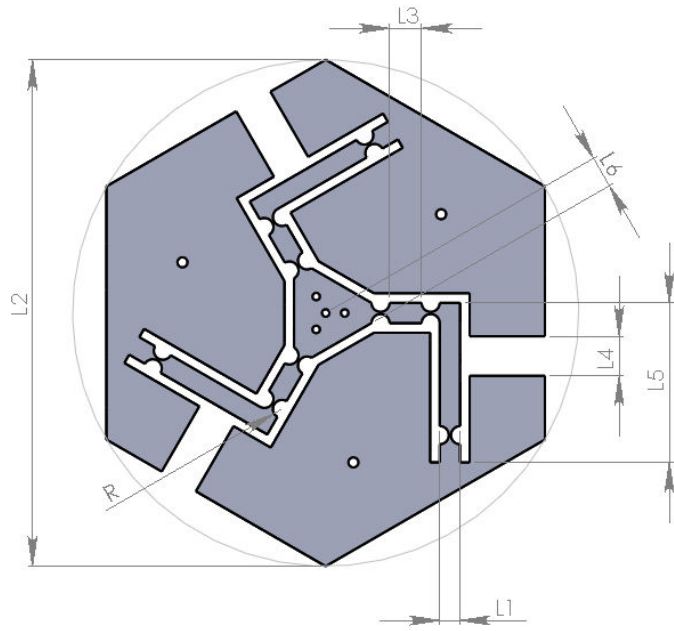


Figure 3.8 2D appearance of 3-RRR compliant stage and its dimensions.

Table 3.1 The dimensions of 3-RRR compliant mechanism

Geometric Parameters	Dimensions [mm]
t	0.8
b	10
R	3.6
L_1	8
L_2	200
L_3	12.6
L_4	15.6
L_5	63
L_6	12.5

3.2.2 3-PRR Compliant Stage

3-PRR compliant mechanism using circular notch hinges as shown in Figure 3.9. Simple linear spring structures based on circular flexure hinges are used for prismatic joints. Those linear springs have large compliance in actuation direction and small compliance in lateral direction so they can be used as joints for providing linear motion.

The stage is actuated by driving the prismatic joints with piezoelectric actuators. The end-effector of the mechanism is a triangular stage which connects the three PRR links and has motion x-y directions and a rotation about z-axis.

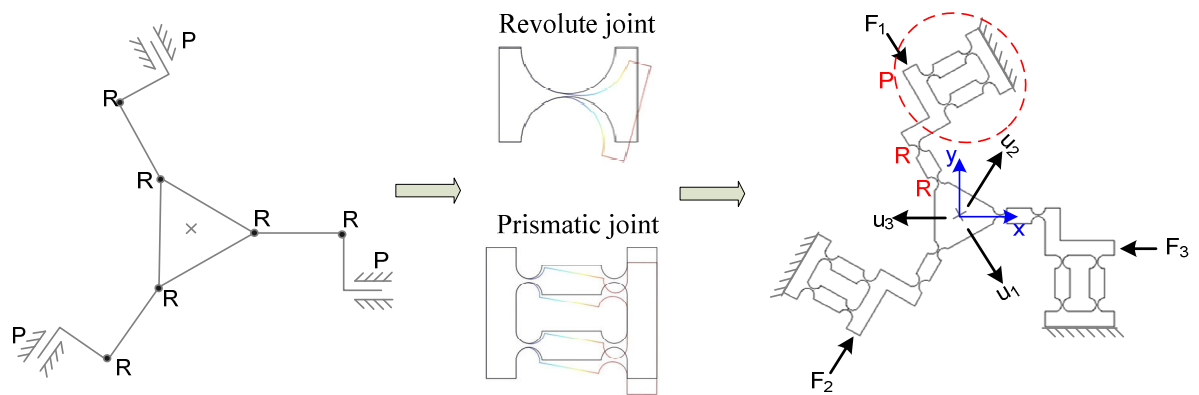


Figure 3.9 3-PRR compliant stage with circular flexure hinges.

As in 3-RRR compliant mechanism we will deal only with the x-y motion of the stage although it has a rotation motion about z axis. We will use the redundancy of the mechanism to eliminate the undesired motions and increase the range of the stage. The mechanism can be driven as illustrated in Figure 3.10. The prismatic joints are actuated by forces F_1 , F_2 and F_3 to create the displacements of u_1 , u_2 and u_3 respectively. By the combination of the “u” displacements desired x-y motion of the triangular stage can be generated.

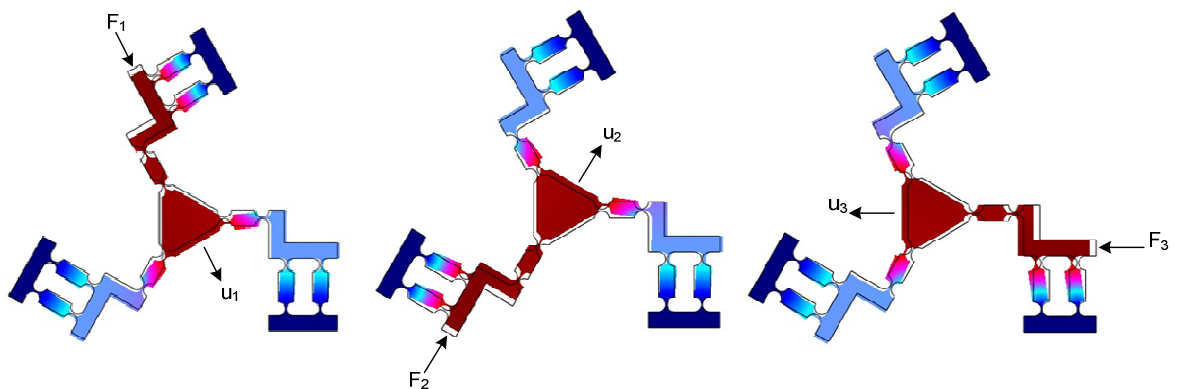


Figure 3.10 3-PRR compliant mechanism displacements.

Also an equilateral hexagonal case shown in Figure 3.11 is designed outside the mechanisms range so that it can be fixed to the experimental setup properly. In order to assemble the piezoelectric actuators correctly holes are drilled. Like in 3-RRR compliant mechanism the most important geometric parameters which are the shortest distance between the circumferences of two notches, “ t ”, and the overall thickness of the stage, “ b ” will be discussed in upcoming section 3.3.1. The selected geometric properties are presented in Figure 3.12 and Table 3.2. The mechanism is symmetric in every 120° about z axis. These parameters are selected according to our limitations as mentioned before by using the Finite Element Analysis. The behavior of the mechanism will be explained in the next section.

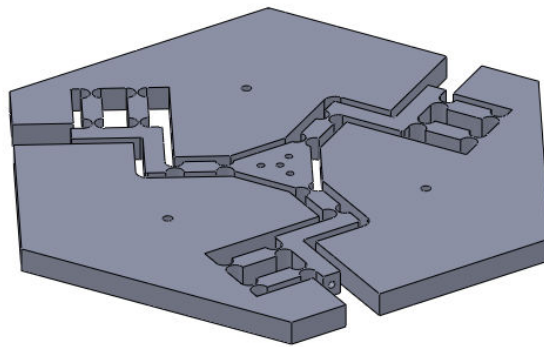


Figure 3.11 3D appearance of 3-PRR compliant mechanism.

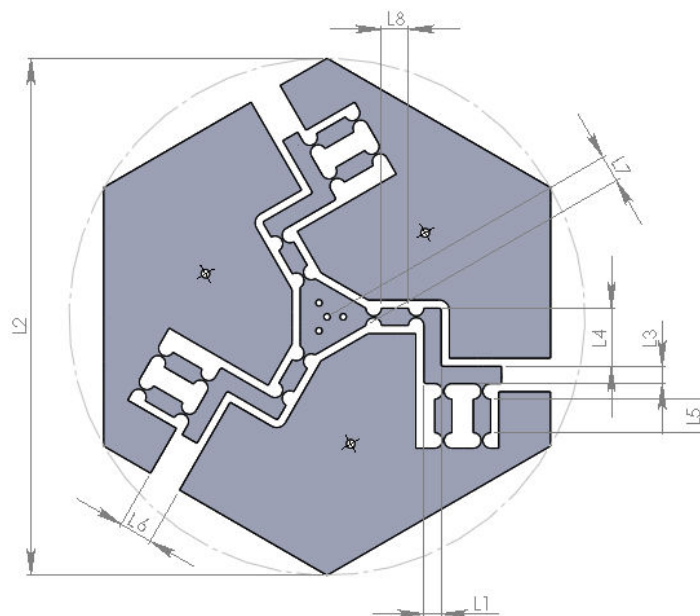


Figure 3.12 2D appearance of 3-PRR compliant stage and its dimensions.

Table 3.2 The dimensions of 3-PRR compliant mechanism

Geometric Parameters	Dimensions [mm]
t	0.8
b	10
R	3.6
L ₁	8
L ₂	240
L ₃	8
L ₄	27
L ₅	15.6
L ₆	15.6
L ₇	25
L ₈	12.6

3.3 Finite Element Analysis of Compliant Stages

Finite element analysis software called COMSOL is used for analyzing the behaviours of 3-RRR and 3-PRR compliant micro motion stages. The analyses are done in 2D Plane Stress structural mechanics module instead of 3D because of being faster. 3D analysis are also started to be done but the results are the same as 2D solutions so we went on with 2D finite element analysis. Plane stress elements which have 2 DOF have been used for meshing. 2D triangular plane stress elements are preferred for predicting the stiffness values of a flexure hinge instead of plane strain elements because Schotborgh [68] has proved that plain stress elements make safer estimations. Mapped meshing technique is used to control the distribution of number of elements. The number of elements is increased on the boundaries which are near the hinge until the results are converged to some number. Those places are important because they will have the most stresses.

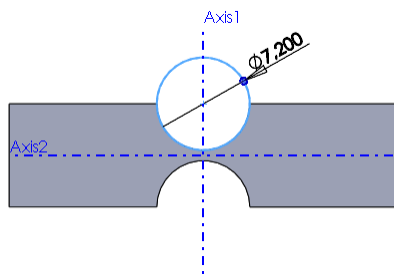
The material that is used in the analyses is Aluminum 7075 which is suitable for compliant mechanisms and the necessary material parameters are shown in Table 3.3.

Table 3.3 Material properties of AL 7075

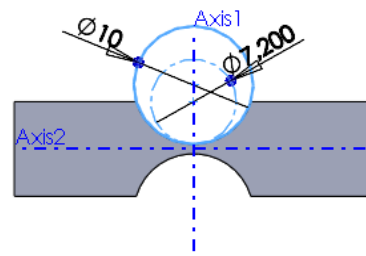
Young's (Elastic) modulus	71.7e9 [Pa]
Poisson's ratio	0.33
Thermal expansion coeff.	23e-6 [1/K]
Density	2810 [kg/m ³]
Yield Strength	503 [MPa]

3.3.1 Determining the type of the flexure

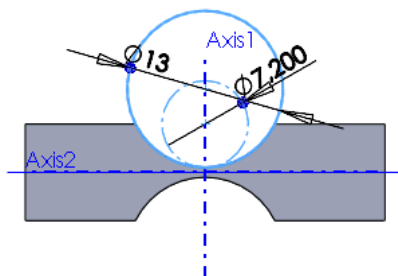
Flexure hinges that are used for revolute joints are analyzed by FEA in COMSOL and right circular notch flexure hinges are chosen because they provide the most accurate motion when compared to other types of flexures. Different types of circular flexure hinges having their center positioned on the edge of the link or on different positions away from the link as shown in Figure 3.13. The circular flexure that has its center placed on the link is called right circular flexure hinge (Figure 3.13a) and the others called elliptical flexure hinges.



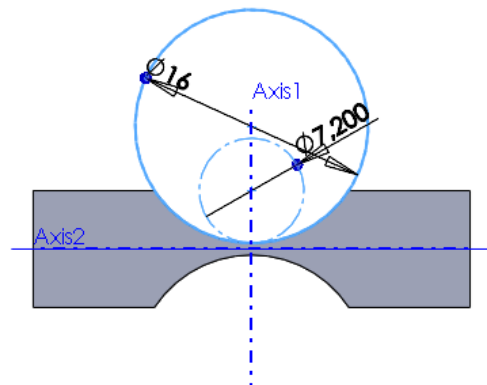
(a) Right Circular



(b) Elyptical 1



(c) Elyptical 2



(d) Elyptical 3

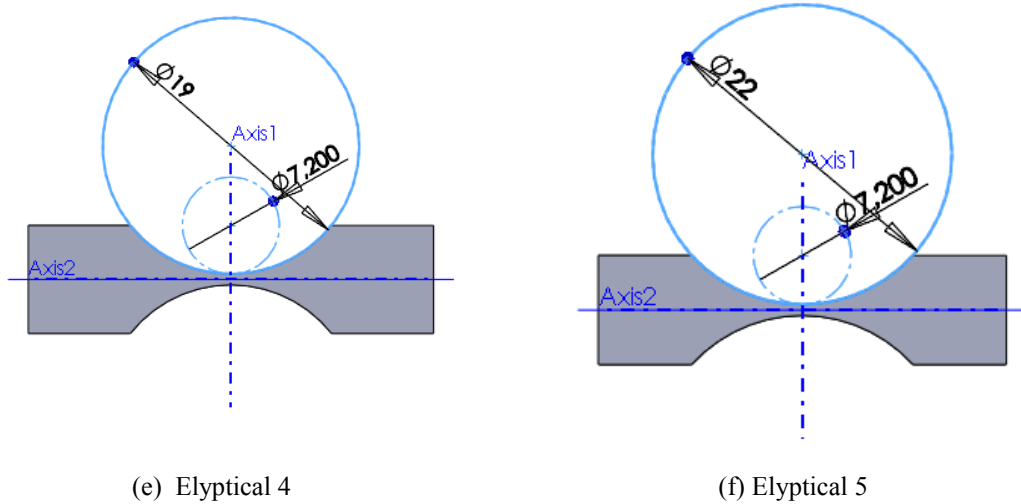


Figure 3.13 Analyzed flexure hinges.

While making the stress analysis of the flexures the right edge of the link is fixed and 1N force in $-y$ direction is applied at the free end of the link as shown in Figure 3.14. The measured displacement is the point where force is applied. The results are presented in Table 3.4.

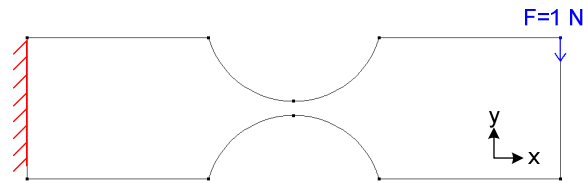


Figure 3.14 Boundary conditions of analyzed flexures.

The stress distributions of the flexures shown in Figure 3.13 respectively are presented in Figure 3.15. The stress distribution is almost at the center (the thinnest part) of the flexure (Figure 3.15a) which is a small zone. Elliptical flexures (Figure 3.15b, c, d, e and f) have distributed stress which makes its behavior nonlinear and open to parasitic motions. The right circular flexure hinges center of rotation is almost constant at any time so they mimic the rigid joints better than the other flexible joints. They are the least flexible ones when we examine the results in Table 3.4 but according to our available piezoelectric actuators this is not a problem for us so because of the importance of elimination of parasitic motions right circular flexure hinges are selected for our mechanisms. Detail information has also been given in [69] for comparing the performance of different kinds of flexures and they recommend right circular flexure

hinges for applications requiring not more than 100 μm of displacement and small output force which are the cases for our application.

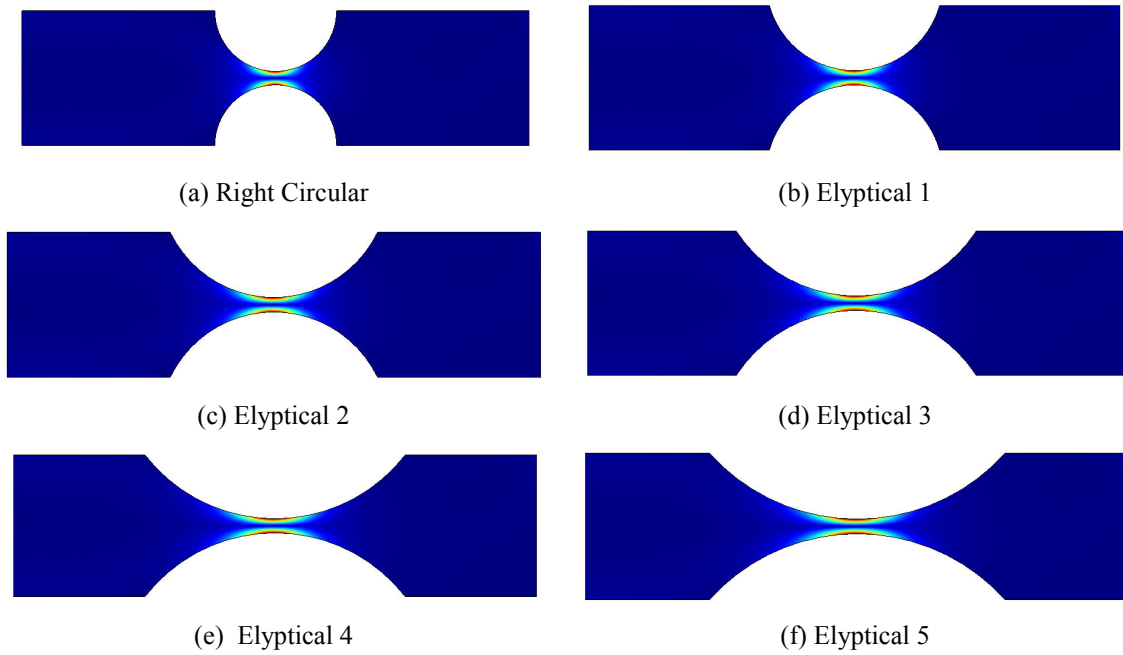


Figure 3.15 Stress distributions of flexure hinges.

Table 3.4 FEA results for flexure hinges

Flexure Type	Max. Stress [MPa]	Displacement in y direction [μm]
Right Circular	14.686	-15.8406
Elyptical 1	14.531	-18.3667
Elyptical 2	14.434	-20.7408
Elyptical 3	14.388	-22.8815
Elyptical 4	14.355	-24.848
Elyptical 5	14.334	-26.678777

3.3.2 Determining the proper “b” and “t” parameters

The overall thickness of the stage in z direction “b” and the shortest distance between the circumferences of two notches, “t”, are the most important parameters for the performance of the compliant mechanisms. The range and the maximum stress

determine the value of these parameters. The boundary conditions of 3-RRR and 3-PRR compliant mechanisms are shown in Figure 3.16. The boundaries numbered as 1, 2 and 3 have been fixed and 1 N force is applied at point 4. Maximum Von Mises stress values and the displacements at the center of the stage, C, are determined. “t” and “b” parameters are varied and same analysis is run for every parameter change and the results are presented in Table 3.5 for 3-RRR mechanism and Table 3.6 for 3-PRR mechanism.

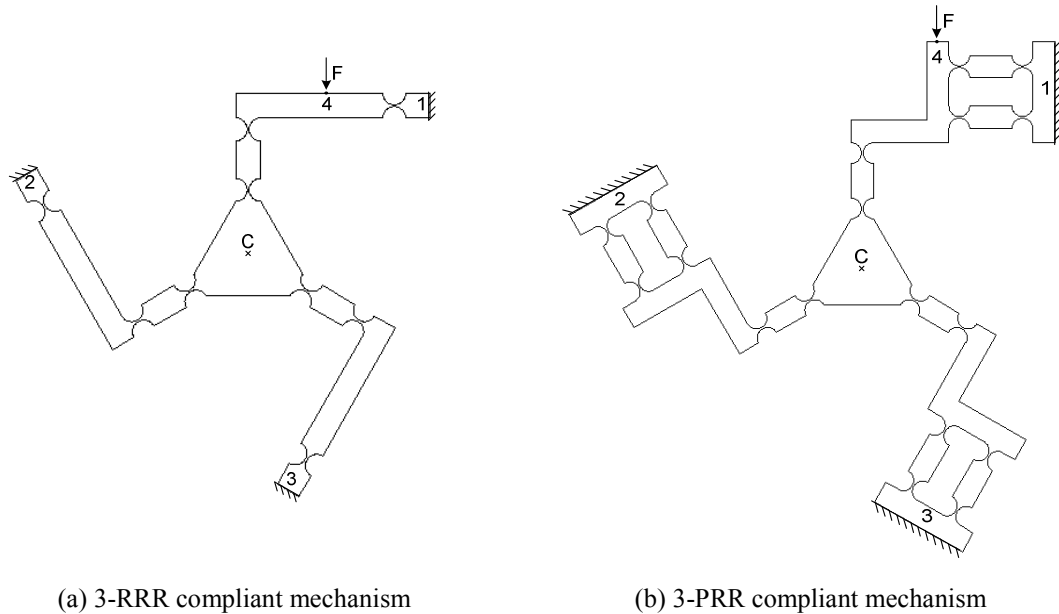
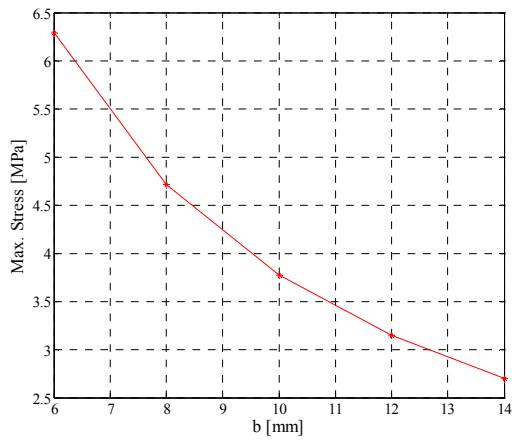


Figure 3.16 Boundary conditions of compliant mechanisms.

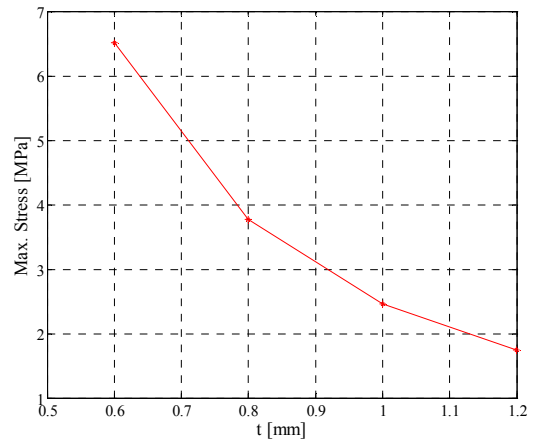
Table 3.5 Results for varied “t” and “b” parameters for 3-RRR compliant mechanism

t [mm]	b [mm]	σ_{\max} [MPa]	Displacement in C [μm]
0.6	6	15.573467	10.855
0.6	8	11.6801	8.141
0.6	10	9.34408	6.513
0.6	12	7.786734	5.428
0.6	14	6.674343	4.652
0.8	6	7.835496	6.288
0.8	8	5.876622	4.716
0.8	10	4.701297	3.773
0.8	12	3.917748	3.144

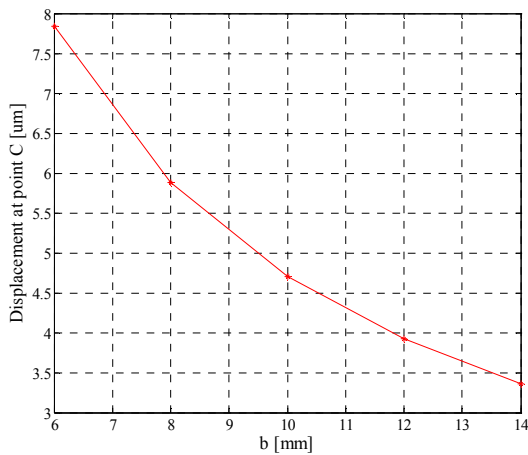
0.8	14	3.35807	2.695
1	6	4.636894	4.097
1	8	3.47767	3.073
1	10	2.782136	2.458
1	12	2.318447	2.048
1	14	1.98724	1.756
1.2	6	3.045671	2.901
1.2	8	2.284253	2.176
1.2	10	1.827403	1.741
1.2	12	1.522836	1.451
1.2	14	1.305288	1.243



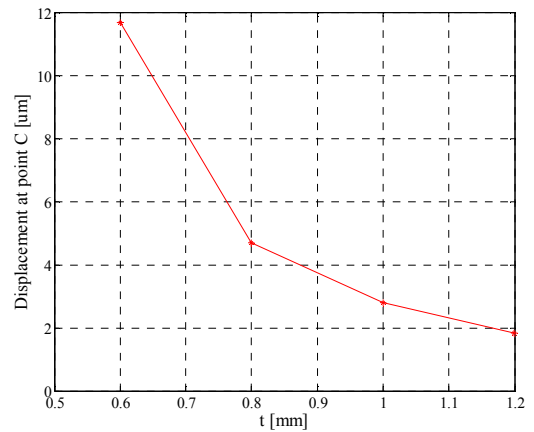
(a) Stress results for constant $t=0.8$ mm



(b) Stress Results for constant $b=10$ mm



(c) Displacement Results for constant $t=0.8$ mm

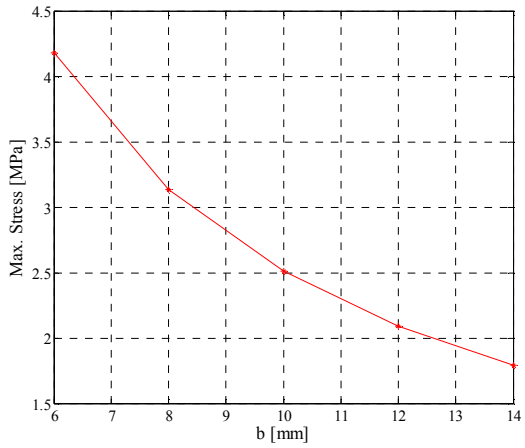


(d) Displacement Results for constant $b=10$ mm

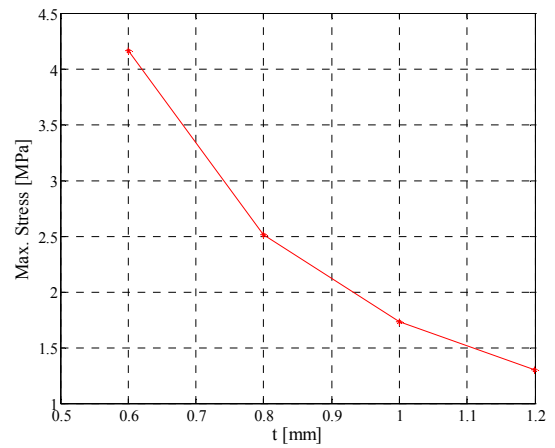
Figure 3.17 3-RRR compliant mechanisms stress and displacement results.

Table 3.6 Results for varied “t” and “b” parameters for 3-PRR

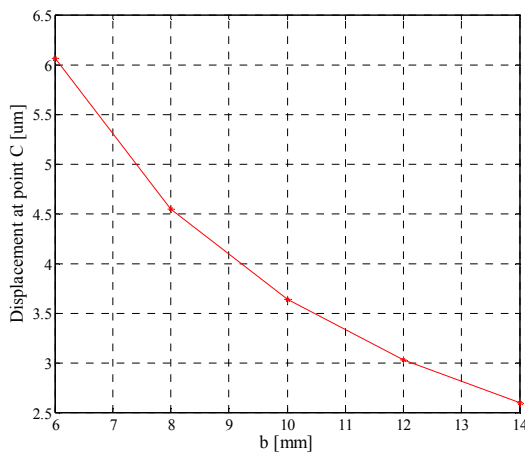
t [mm]	b [mm]	σ_{\max} [MPa]	Displacement in C [μm]
0.6	6	12.15538	6.94
0.6	8	9.116535	5.205
0.6	10	7.293228	4.164
0.6	12	6.07769	3.47
0.6	14	5.209448	2.974
0.8	6	6.060402	4.18
0.8	8	4.545302	3.135
0.8	10	3.636241	2.508
0.8	12	3.030201	2.09
0.8	14	2.597315	1.791
1	6	3.547774	2.883
1	8	2.660831	2.162
1	10	2.128665	1.73
1	12	1.773887	1.442
1	14	1.520475	1.236
1.2	6	2.299334	2.16
1.2	8	1.7245	1.62
1.2	10	1.3796	1.296
1.2	12	1.149667	1.079
1.2	14	0.985429	0.925



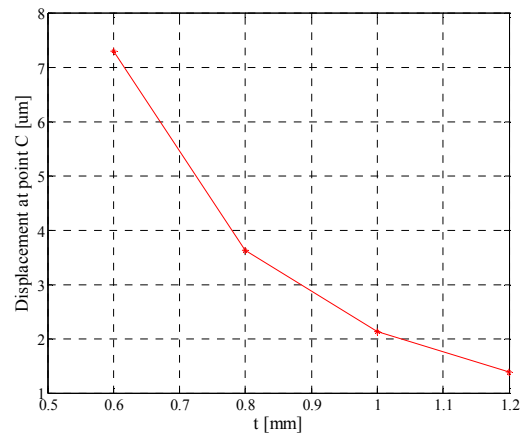
(a) Stress results for constant $t=0.8$ mm



(b) Stress Results for constant $b=10$ mm



(c) Displacement Results for constant $t=0.8$ mm



(d) Displacement Results for constant $b=10$ mm

Figure 3.18 3-PRR compliant mechanisms stress and displacement results.

According to the results for 3-RRR and 3-PRR compliant mechanisms presented respectively in Table 3.4 and Table 3.5 when “ t ” is constant the maximum stress and the displacement is increasing while “ b ” is decreasing. In Figures 3.17a, 3.17c for 3-RRR and in Figures 3.18a and 3.18c for 3-PRR it’s observed that the relationships between “ b ” values and the maximum stress or displacement are asymptotical. Similarly when “ b ” is constant the maximum stress and the displacement are increasing while “ t ” is decreasing. And in Figures 3.17b, 3.17d for 3-RRR and in Figures 3.18b and 3.18d for 3-PRR it’s observed that the relationships between “ t ” values and the maximum stress or displacement are asymptotical. So the “ t ” and “ b ” values should be small enough to let the flexures bend enough to provide necessary displacements for the triangular stage and should be big enough to have maximum stresses low in order not to be in danger of being in the plastic region. When the analysis and the manufacturing capabilities are taking into account “ t ”, is selected as 0.8 mm and which is the minimum achievable

thickness while manufacturing with Wire EDM technique if the material is Aluminum 7075 which is a relatively soft material but has enough flexibility for providing motion. The overall thickness of the stage, “b”, is selected as 10 mm to have lower stress values and provide easier manufacturing processes.

3.3.3 FEA of 3-RRR Compliant Mechanism

3.3.3.1 Free 3-RRR Compliant Mechanism

3-RRR Compliant mechanism is analyzed by examining the behavior of the mechanism by applying forces as piezoelectric actuators individually without having other piezoelectric actuators connected.

The necessary boundary conditions of the mechanism shown in Figure 3.19a are set as:

- The boundaries 4, 5 and 6 are fixed.
- 1, 2 and 3 points are assigned for point load representing the piezoelectric actuator forces.
- A point called C is assigned for examining the end effector displacement.

2D triangular plane stress elements are used for the meshing of the 3-RRR Compliant mechanism as shown in Figure 3.19b. After many iterations to find a convergence, the number of elements is set as 7844 elements and number of degrees of freedom is 33574.

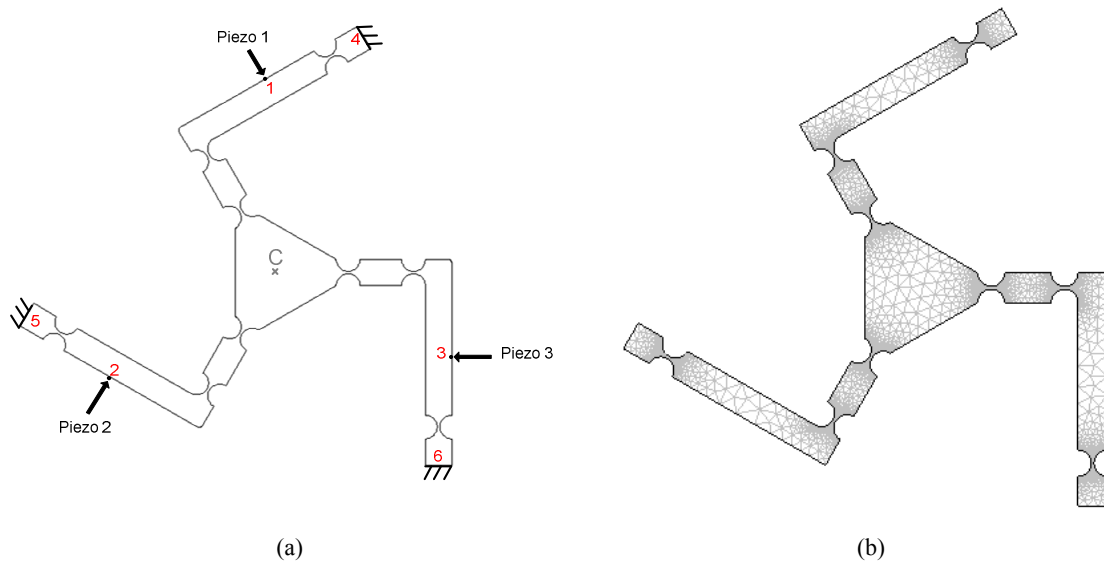
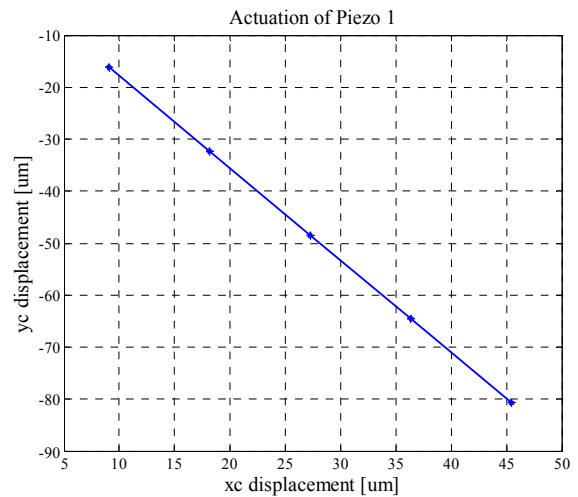
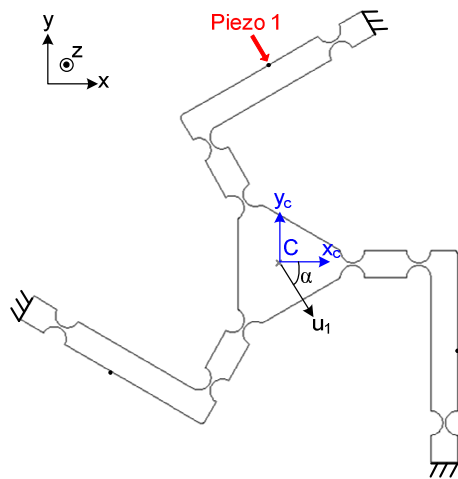
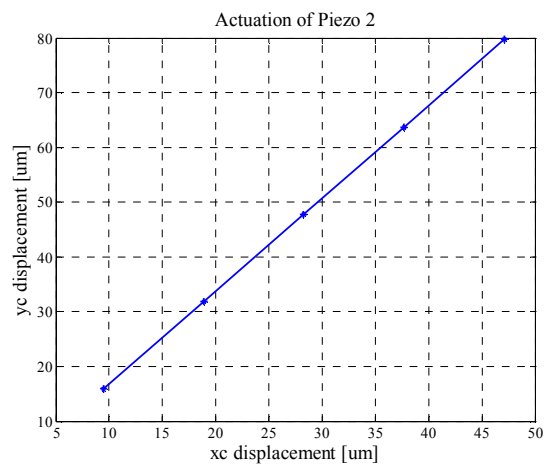
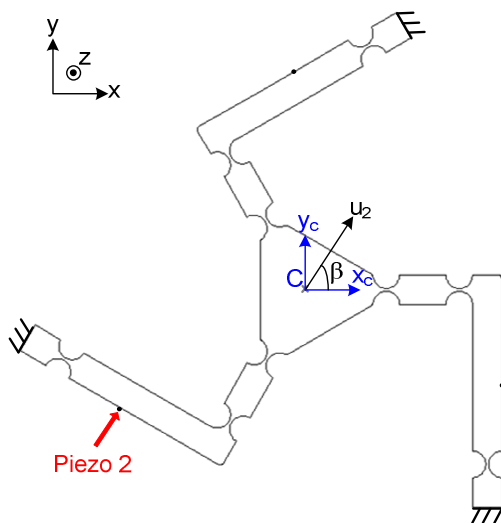


Figure 3.19 (a) Boundary conditions of free 3-RRR mechanism, (b) Meshed 3-PRR mechanism.

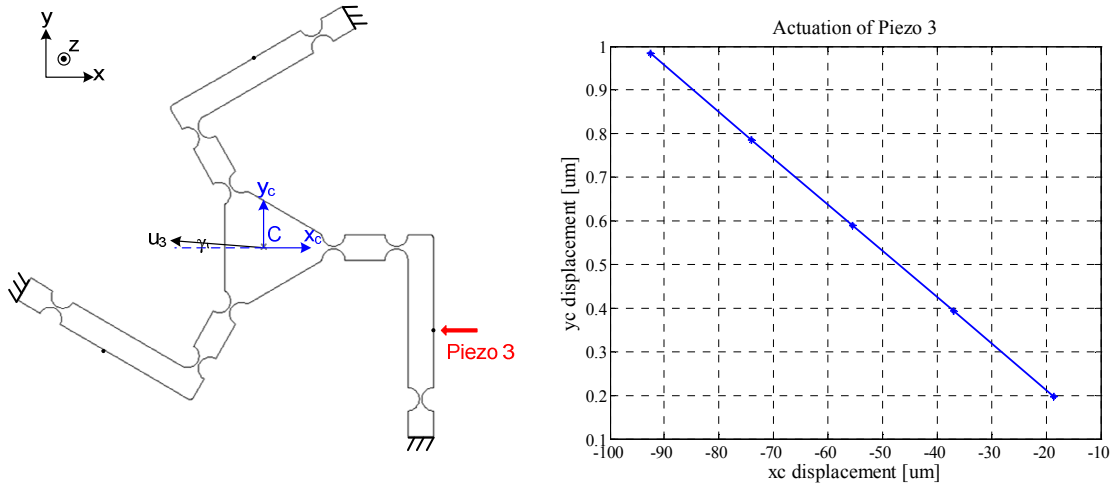
4N, 8N, 12N, 16N and 20N forces are applied as point forces respectively for representing the piezoelectric actuations. When only Piezo 1 is actuated the displacement vector of the center point C is presented as u_1 vector with the angle of α as shown in Figure 3.20a, when only Piezo 2 is actuated the displacement vector of the center point C is presented as u_2 vector with the angle of β as shown in Figure 3.20b and lastly when only Piezo 3 is actuated the displacement vector of the center point C is presented as u_3 vector with the angle of γ as shown in Figure 3.20c. The results of displacements at point C for piezo actuations are also shown in Figure 3.20 as displacement plots in x direction, x_c , versus displacements in y direction, y_c for every force applied in every case.



(a) Piezo 1 is actuated for free 3-RRR compliant mechanism



(b) Piezo 2 is actuated for free 3-RRR compliant mechanism

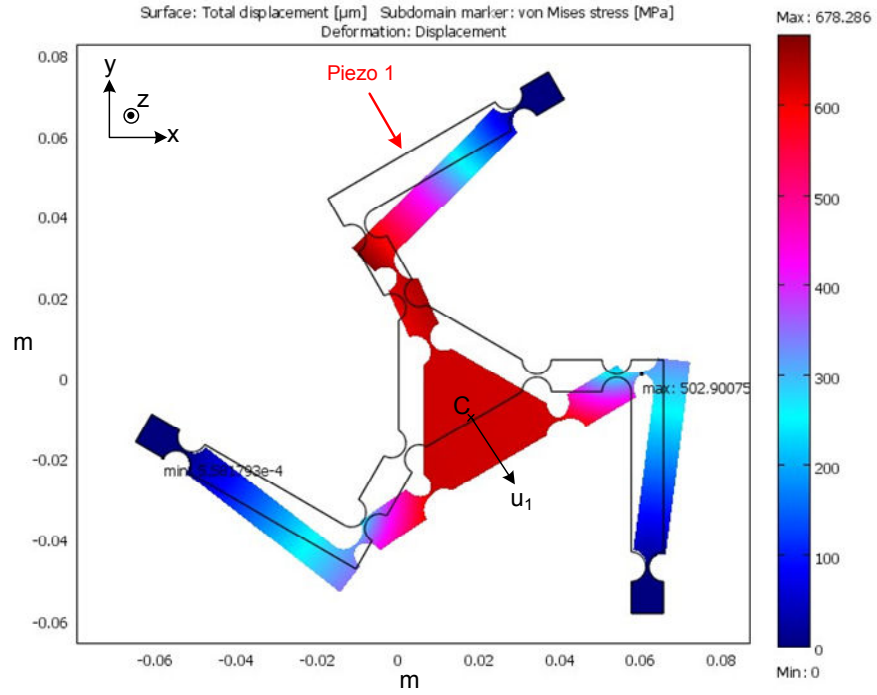


(c) Piezo 3 is actuated for free 3-RRR compliant mechanism

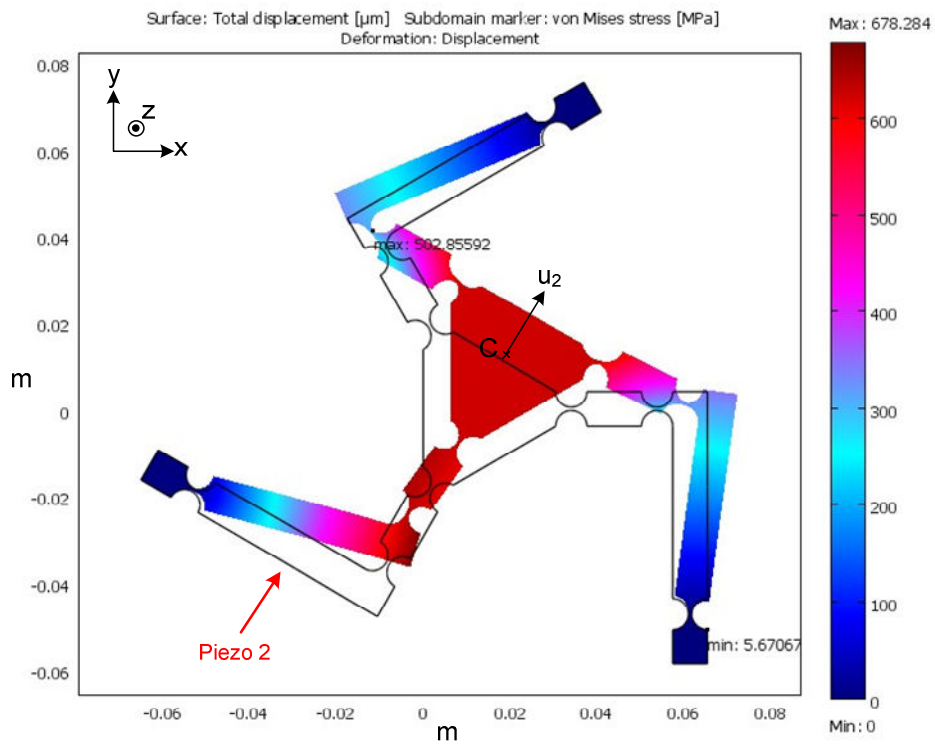
Figure 3.20 Center displacements for free 3-RRR compliant mechanism.

The result plots of displacements at the center point C presented in Figure 3.20 show that when only Piezo 1 is applied to the mechanism, the center of the mechanism has displacements in u_1 direction which has 60.61° angle (α) with the x axis. When only Piezo 2 is applied to the mechanism, the center displacements are in the direction of u_2 which has an angle (β) of 59.39° with the x axis and finally when only Piezo 3 is applied to the mechanism the center displacements are in u_3 direction which has an angle (γ) of 0.61° with the x axis.

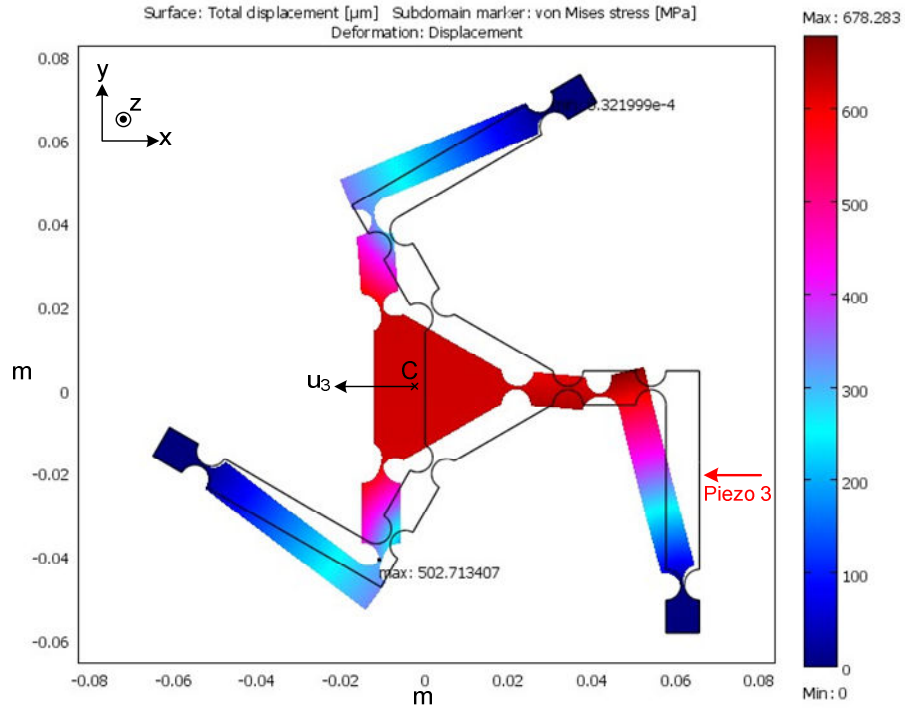
The workspace of the free 3-RRR compliant mechanism is analyzed by increasing applied force each actuation point until the maximum stress which is on the flexures thinnest thickness is close to the yield stress of AL 7075. Von Misses yield stress is used for comparing the yield stress of the material. The result figures of the simulations which are scaled to 20:1 are shown in Figure 3.19 and the results are presented for each piezoelectric actuation in Table 3.7. Results show us that for free 3-RRR compliant mechanism the maximum force can be applied is 137.5 N and the maximum center displacements in u_1 , u_2 and u_3 directions are $625.8 \mu\text{m}$.



(a) Piezo 1 actuation in free 3-RRR compliant mechanism



(b) Piezo 2 actuation in free 3-RRR compliant mechanism



(c) Piezo 3 actuation in free 3-RRR compliant mechanism

Figure 3.21 a. Maximum displacement results free 3-RRR compliant mechanism.

Table 3.7 Results of maximum displacement and stress of free 3-RRR compliant mechanism

Actuator	Max. Stress [MPa]	Max. Force Applied [N]	Max. Input Total Displacement [μm]	Max. Center Total Displacement [μm]
Piezo 1	502.9	137.5	405.542	625.873
Piezo 2	502.856	137.5	405.541	625.872
Piezo 3	502.713	137.5	405.540	625.871

3.3.3.2 Constrained 3-RRR Compliant Mechanism

3-RRR Compliant mechanism is analyzed by examining the behavior of the mechanism by applying forces as piezoelectric actuators individually with having other piezoelectric actuators connected. So a prescribed displacement constraint is added for

each link where piezoelectric actuators are assembled and block the displacement backwards.

The necessary boundary conditions of the mechanism shown in Figure 3.20 are set as:

- The boundaries 4, 5 and 6 are fixed.
- 1, 2 and 3 points are assigned for point load representing the piezoelectric actuator forces.
- 7, 8 and 9 points are added to have boundaries from 1 to 7, 2 to 8 and 3 to 9 (green lines) for the prescribed displacement that mimics the piezoelectric actuators connection and constrain the 3-RRR mechanism
- A point called C is assigned for examining the end effector displacement.

2D triangular plane stress elements and same amount of meshing elements as in free 3-RRR compliant mechanism analysis is used.

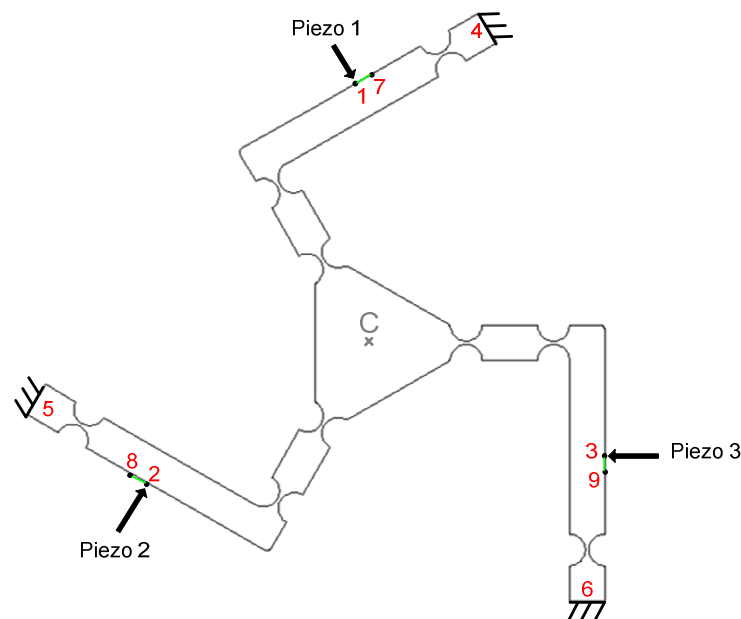
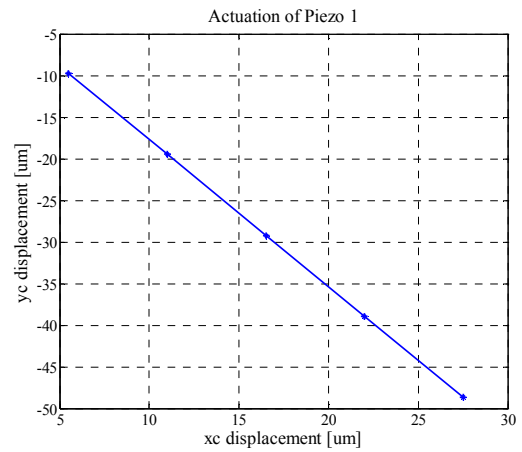
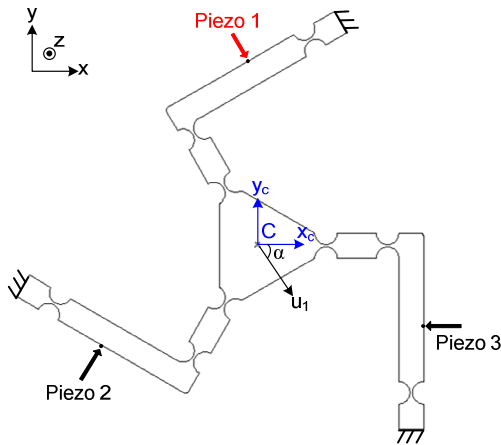


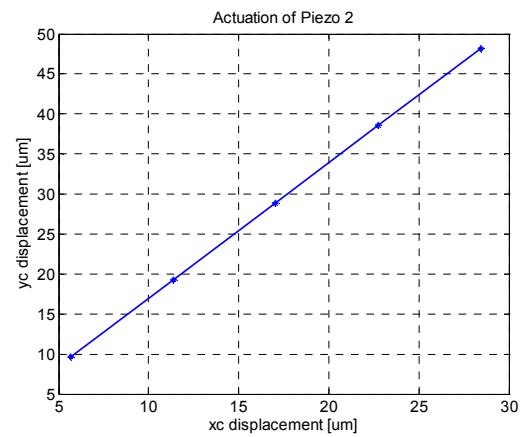
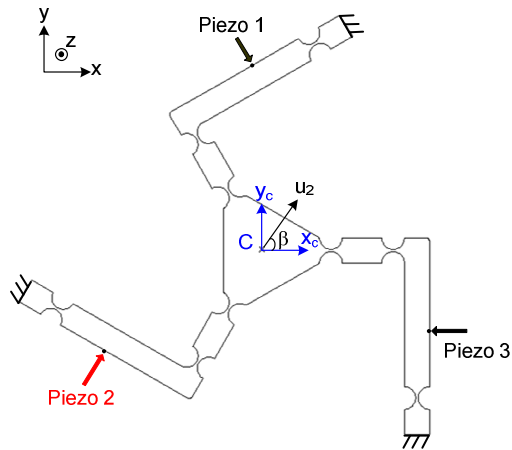
Figure 3.22 Boundary conditions of constrained 3-RRR compliant mechanism.

55N, 110N, 165N, 220N and 275N forces are applied as point forces respectively for representing the piezoelectric actuation. The red colored piezos represents the actuated piezoelectric actuators while the other piezoelectric actuators are just attached and constrained the mechanism. When only Piezo 1 is actuated the displacement vector of the center point C is presented as u_1 vector with the angle of α as shown in Figure 3.23a, when only Piezo 2 is actuated the displacement vector of the center point C is

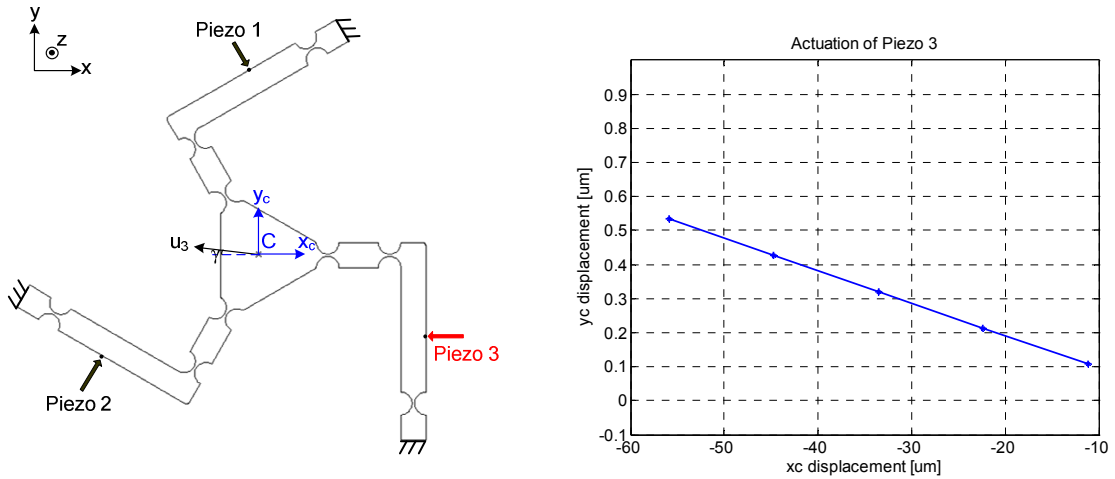
presented as u_2 vector with the angle of β as shown in Figure 3.23b and lastly when only Piezo 3 is actuated the displacement vector of the center point C is presented as u_3 vector with the angle of γ as shown in Figure 3.23c. The results of displacements at point C for piezo actuations are also shown in Figure 3.23 as displacement plots in x direction, x_c , versus displacements in y direction, y_c for every force applied in every case.



(a) Piezo 1 is actuated for constrained 3-RRR compliant mechanism



(b) Piezo 2 is actuated for constrained 3-RRR compliant mechanism

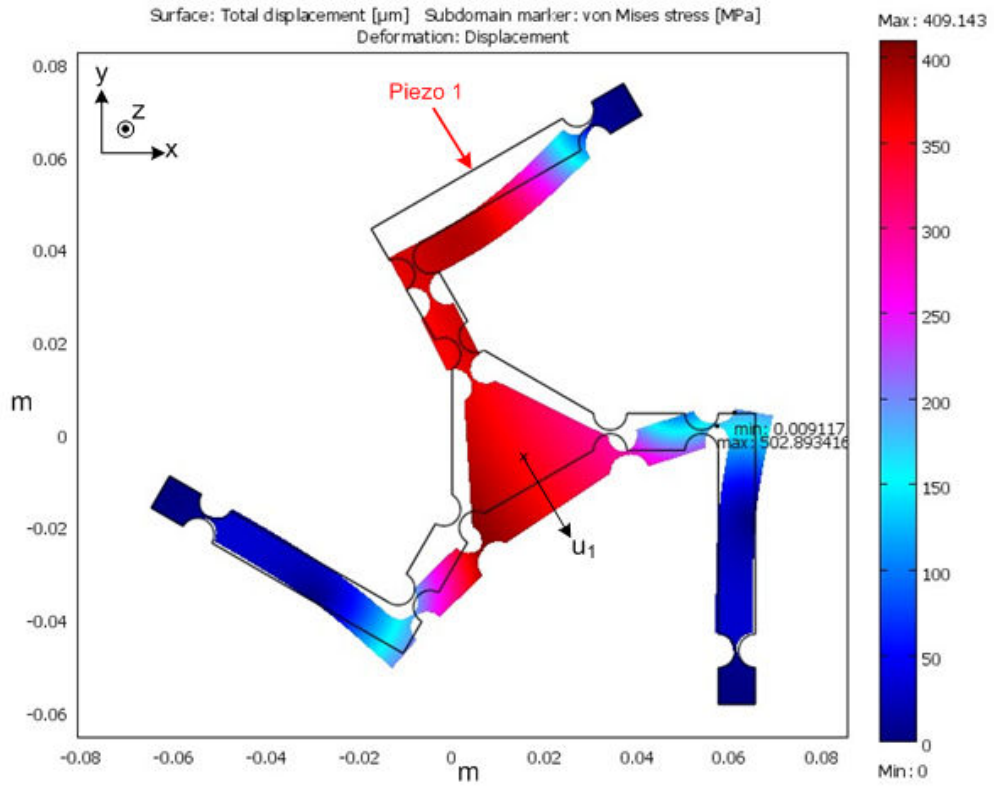


(c) Piezo 3 is actuated for constrained 3-RRR compliant mechanism

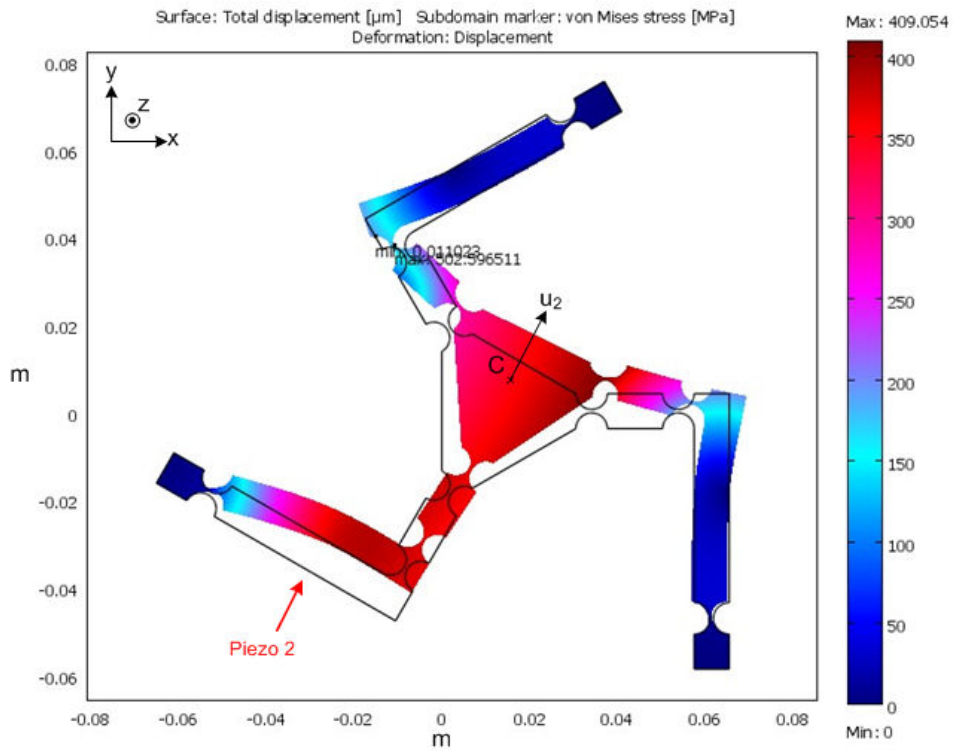
Figure 3.23 Center displacements for constrained 3-RRR compliant mechanism.

According to the plots presented in Figure 3.23 when only Piezo 1 is applied to the mechanism, the center of the mechanism has displacements in u_1 direction which has 60.52° angle (α) with the x axis. When only Piezo 2 is applied to the mechanism the center displacements are in the direction of the u_2 has an angle (β) of 59.46° with the x axis and finally when Piezo 3 is applied to the mechanism the center displacements are in u_3 direction which has an angle (γ) of 0.55° with the x axis.

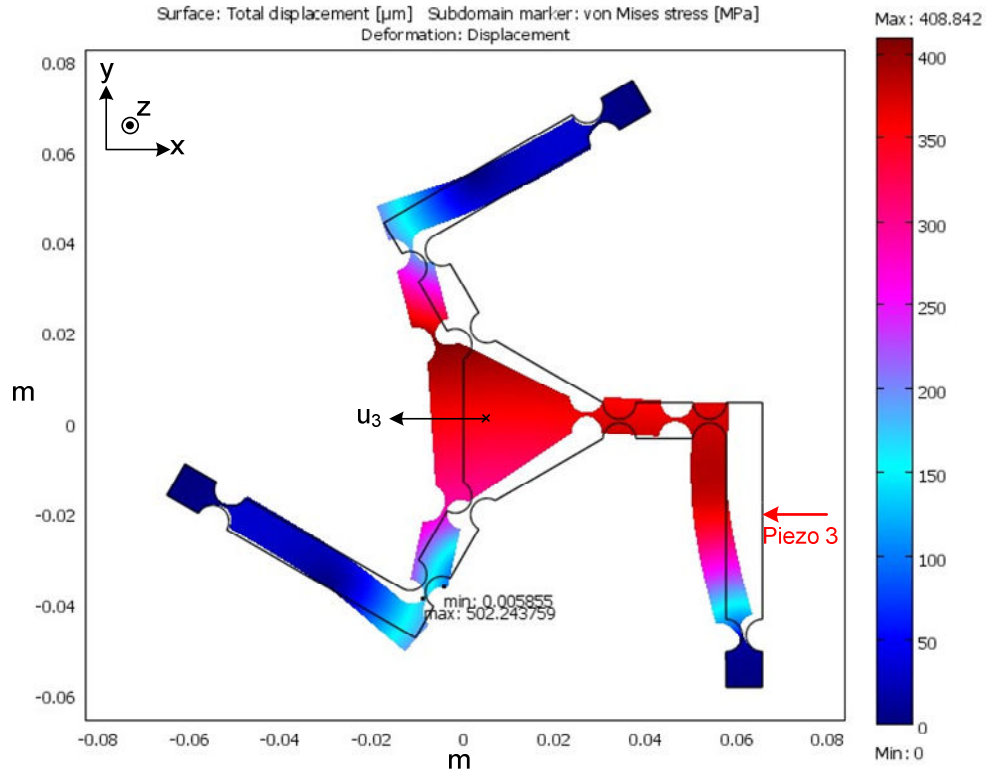
The result figures of the workspace analysis of the constrained 3-RRR compliant mechanism are shown in Figure 3.24. They are scaled to 20:1 and the results are presented for each piezoelectric actuation in Table 3.5. Results show us that for free 3-RRR compliant mechanism the maximum force can be applied is 1730 N and the maximum displacements in u_1 , u_2 and u_3 directions are almost $352 \mu\text{m}$.



(a) Piezo 1 actuation in constrained 3-RRR compliant mechanism



(b) Piezo 2 actuation in constrained 3-RRR compliant mechanism



(c) Piezo 3 actuation in constrained 3-RRR compliant mechanism

Figure 3.24 Maximum displacement results constrained 3-RRR compliant mechanism.

Table 3.8 Results of maximum displacement and stress of constrained 3-RRR compliant mechanism

Actuator	Max. Stress [MPa]	Max. Force Applied [N]	Max. Input Total Displacement [μm]	Max. Center Total Displacement [μm]
Piezo 1	502.893	1730	378.219	352.463
Piezo 2	502.597	1730	378.186	352.393
Piezo 3	502.244	1730	378.120	352.184

The resonance frequency of the stage is examined by making the modal analysis with FEA. First three natural frequencies are taken into account for the analysis and the mode shapes are illustrated in Figure 3.25. The first two natural frequencies are 314.852667 Hz and 314.853875 Hz. They are almost identical and their mode shapes are translations on x-y plane as presented in Figure 3.25a and in Figure 3.25b respectively. Third mode shape is rotational as seen in Figure 3.25c which has a natural

frequency of almost 3.76 times the translational ones (1181.244804 Hz). The results show us that the designed 3-RRR compliant mechanism can be used in high frequency operations where micromotion positioning is needed.

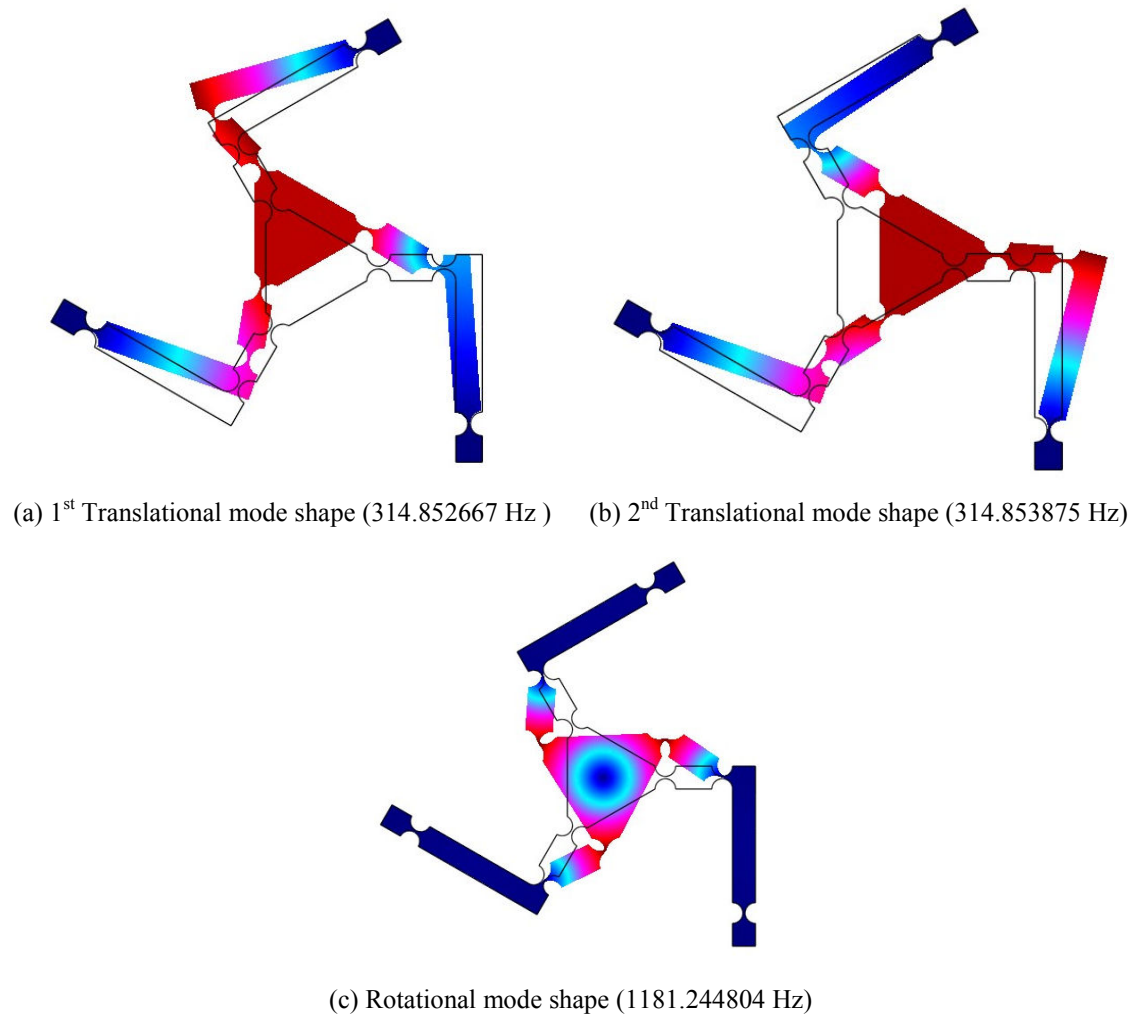


Figure 3.25 Mode shapes of 3-RRR compliant mechanism.

3.3.4 FEA of 3-PRR Compliant Mechanism

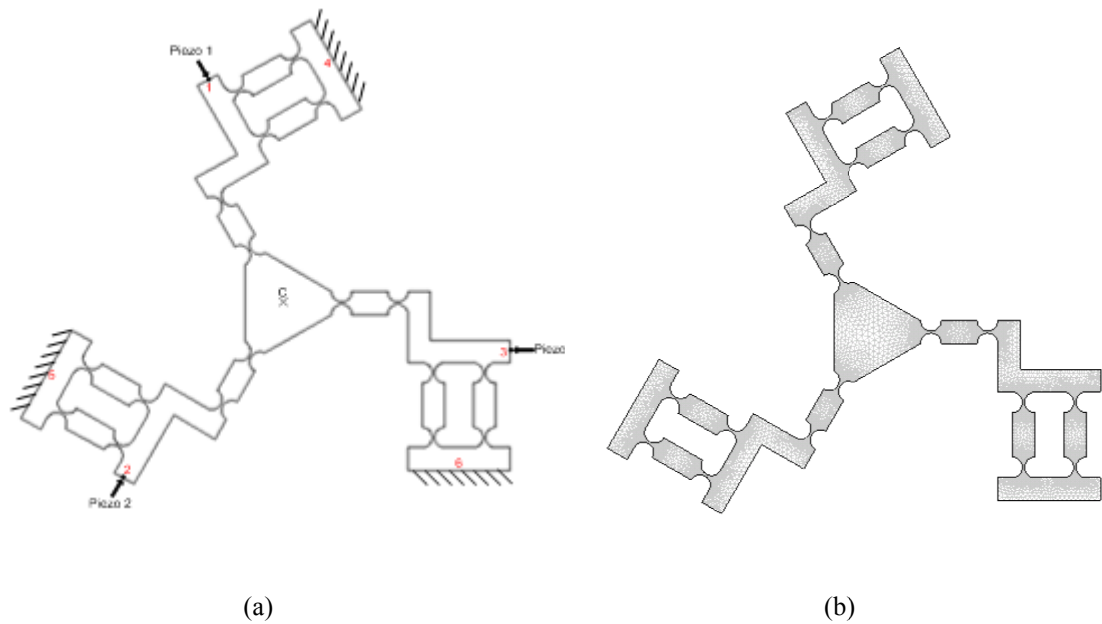
3.3.4.1 Free 3-PRR Compliant Mechanism

The behavior of the 3-PRR compliant mechanism is analyzed by applying piezoelectric actuators generated forces individually without having other piezoelectric actuators assembled to the mechanism.

According to Figure 3.26a the necessary boundary conditions that helps to mimic the behavior of free 3-PRR free compliant mechanism are set as:

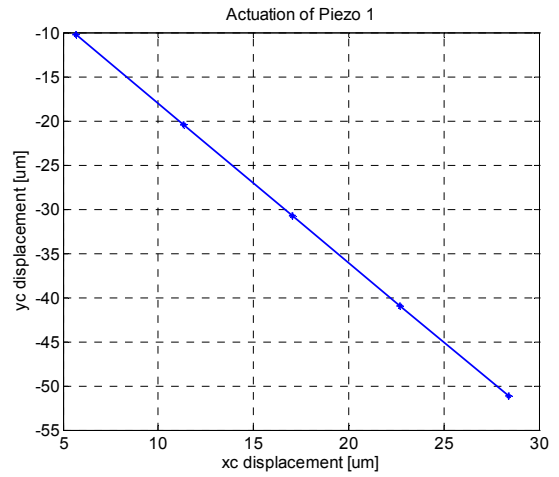
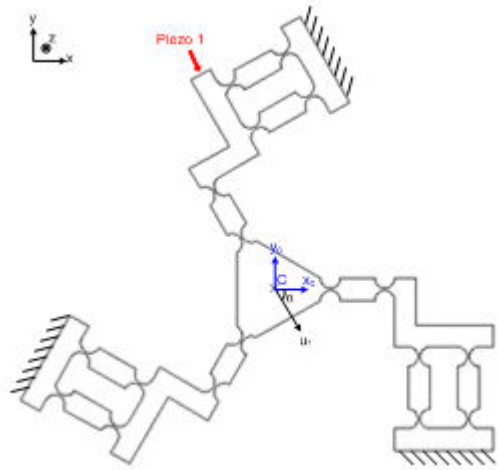
- The boundaries 4,5 and 6 are fixed.
- 1, 2 and 3 points are assigned for point load representing the piezoelectric actuator forces.
- A point called C is assigned for examining the end effector displacement.
-

2D triangular plane stress elements are used for the meshing of the 3-PRR compliant mechanism as shown in Figure 3.26b. A lot of iterations have been made to find a convergence value and the number of elements is set as 18548 elements and number of degrees of freedom is 78448.

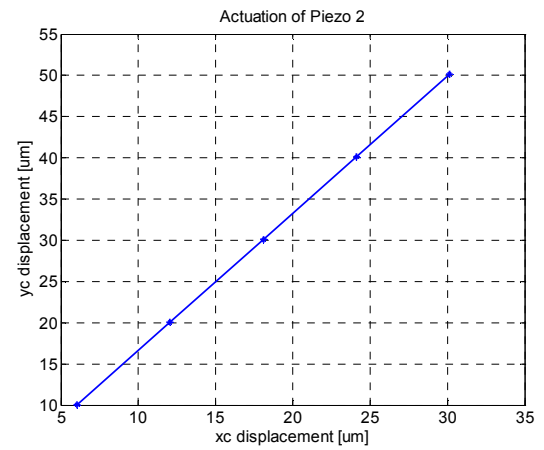
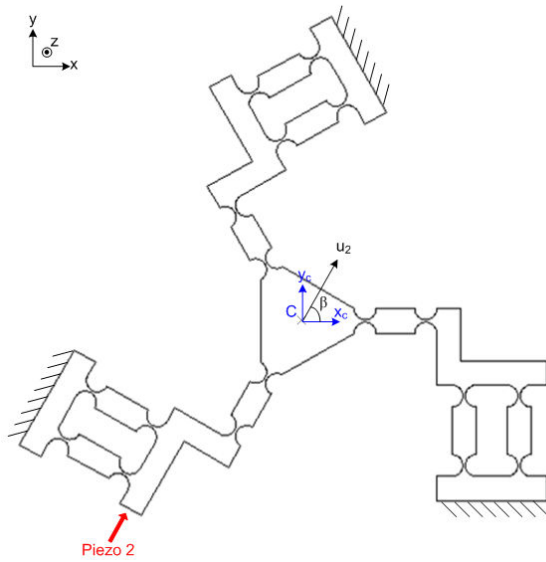


3.26 (a) Boundary conditions of free 3-PRR mechanism, (b) Meshed 3-PRR mechanism.

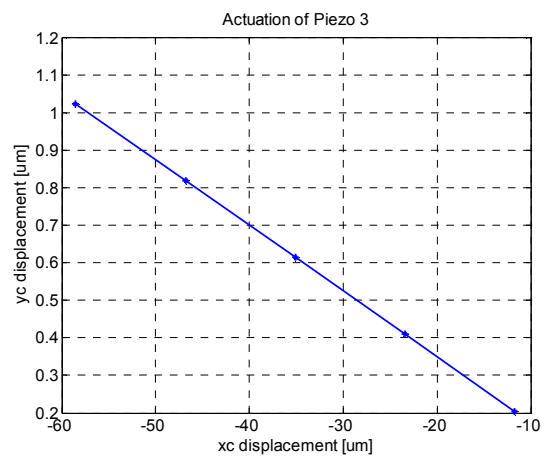
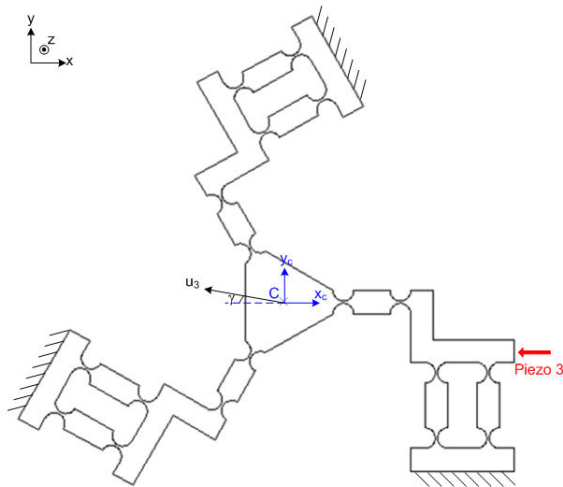
3N, 6N, 9N, 12N and 15N forces are applied as point forces respectively for representing the piezoelectric actuations. When only Piezo 1 is actuated the displacement vector of the center point C is presented as u_1 vector with the angle of α as shown in Figure 3.27a , when only Piezo 2 is actuated the displacement vector of the center point C is presented as u_2 vector with the angle of β as shown in Figure 3.27b and lastly when only Piezo 3 is actuated the displacement vector of the center point C is presented as u_3 vector with the angle of γ as shown in Figure 3.27c. The results of displacements at point C for piezo actuations are also shown in Figure 3.27 as displacement plots in x direction, x_c , versus displacements in y direction, y_c for every force applied in every case.



(a) Piezo 1 is actuated for free 3-PRR compliant mechanism



(b) Piezo 2 is actuated for free 3-PRR compliant mechanism

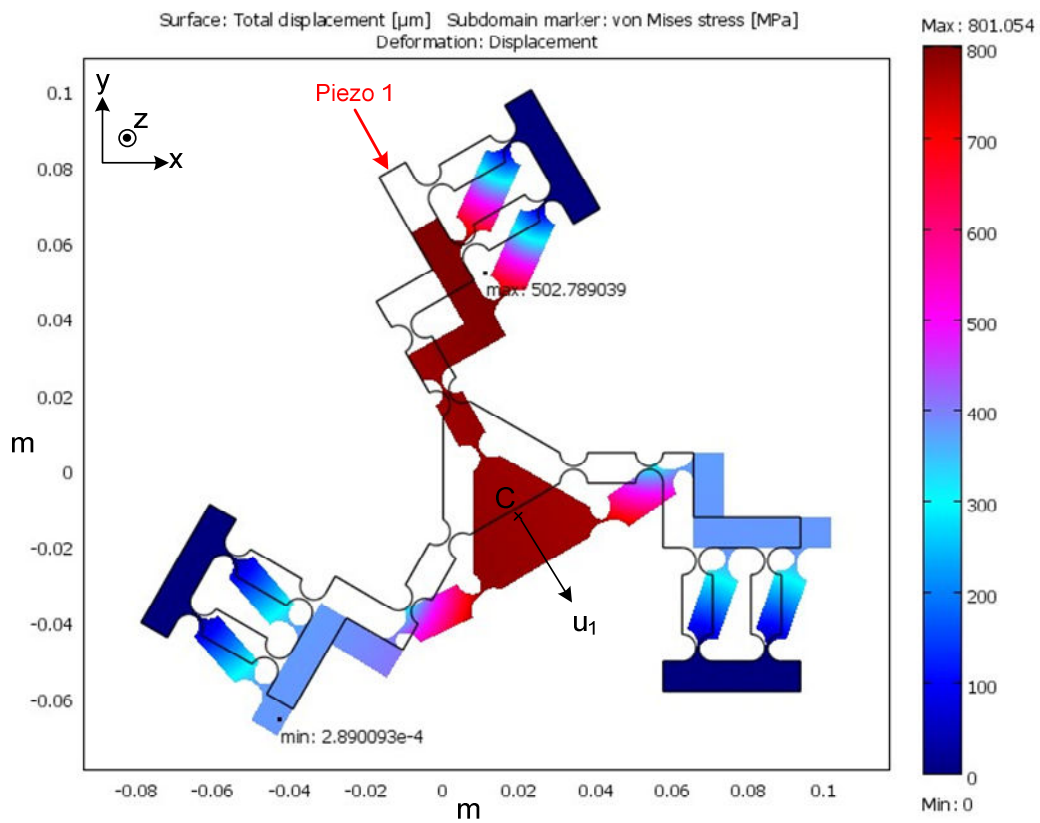


(c) Piezo 3 is actuated for free 3-PRR compliant mechanism

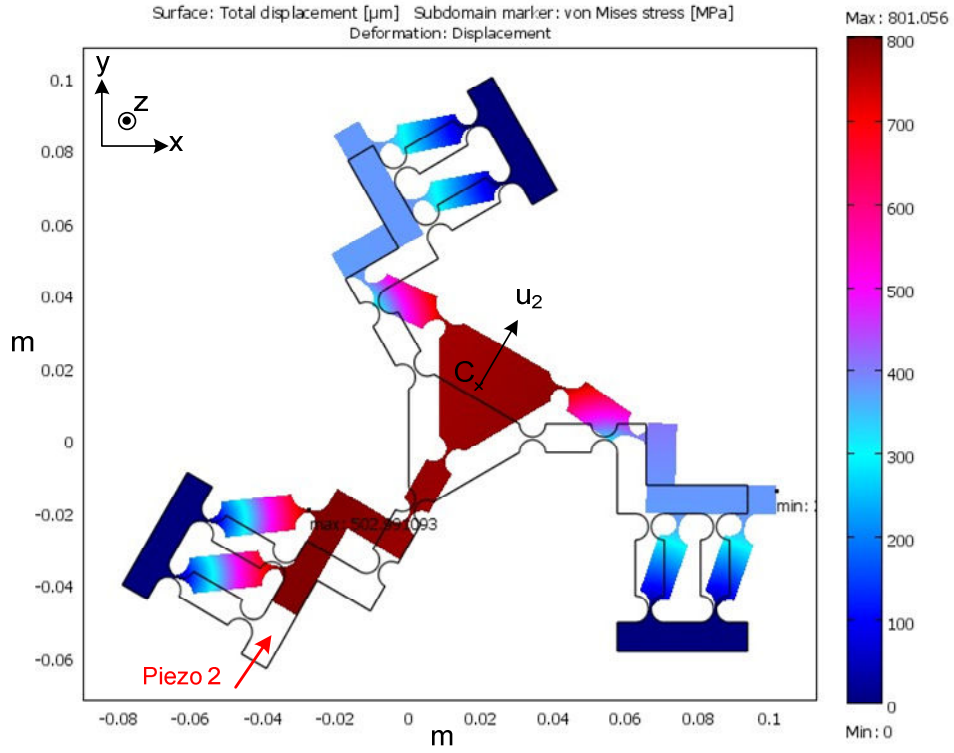
Figure 3.27 a. Center displacements for free 3-PRR compliant mechanism.

According to the plot presented in Figure 3.27 when only Piezo 1 is applied to the mechanism, the center of the center of the mechanism has displacements in u_1 direction which has 61° angle (α) with the x axis. When only Piezo 2 is applied to the mechanism the direction of u_2 has an angle (β) of 58.99° with the x axis and finally when Piezo 3 is applied to the mechanism the center displacements are in u_3 direction which has an angle (γ) of 1° with the x axis.

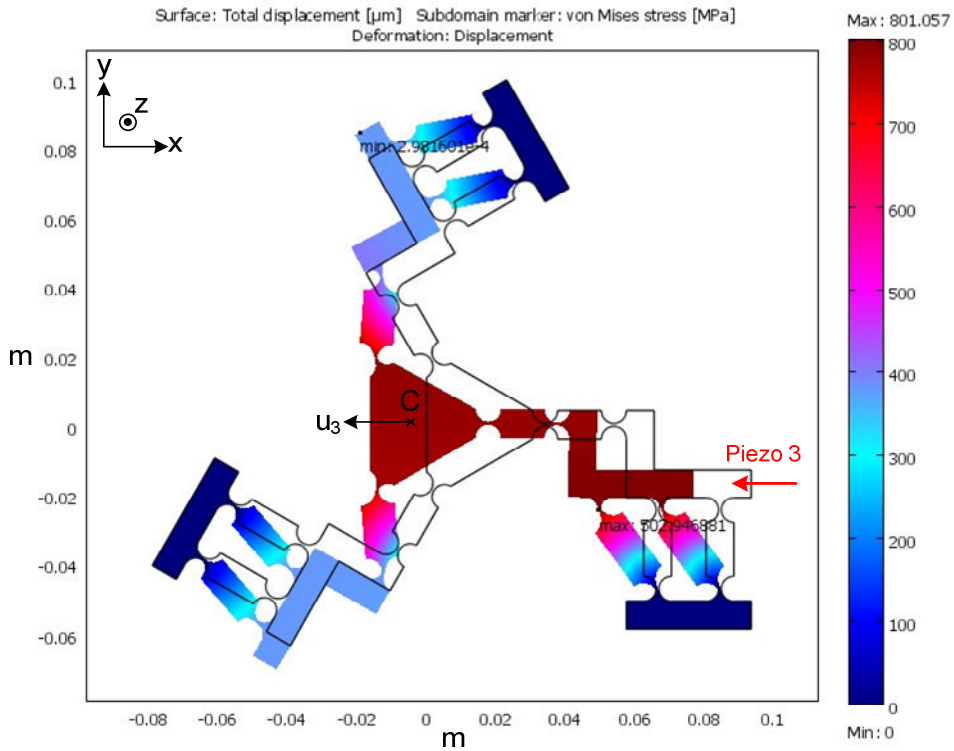
The result figures of the workspace analysis of the free 3-PRR compliant mechanism are shown in Figure 3.28. The figures of the simulations are scaled to 20:1 and the results are presented in Table 3.9. Results show us that for free 3-PRR compliant mechanism the maximum force can be applied is 212.4 N and the maximum displacements in u_1 , u_2 and u_3 directions are almost $780.65 \mu\text{m}$.



(a) Piezo 1 actuation in free 3-PRR compliant mechanism



(b) Piezo 2 actuation in free 3-PRR compliant mechanism



(c) Piezo 3 actuation in free 3-PRR compliant mechanism

Figure 3.28 Maximum displacement results of free 3-PRR compliant mechanism.

Table 3.9 Results of maximum displacement and stress of free 3-PRR compliant mechanism

Actuator	Max. Stress [MPa]	Max. Force Applied [N]	Max. Input Total Displacement [μm]	Max. Center Total Displacement [μm]
Piezo 1	502.789	212.4	800.150	780.652
Piezo 2	502.991	212.4	800.152	780.658
Piezo 3	502.945	212.4	800.145	780.656

3.3.4.2 Constrained 3-PRR Compliant Mechanism

The boundary conditions of the mechanism shown in Figure 3.29 are set as:

- The boundaries 4,5 and 6 are fixed.
- The boundaries 1,2 and 3 motion is limited by setting prescribed displacement for those boundaries because piezoelectric actuators will be fixed there which wont allow them to move backwards from the actuation direction.
- Point forces have been applied in the middle of the boundaries 1,2 and 3 in order to represent the piezoelectric actuator forces.

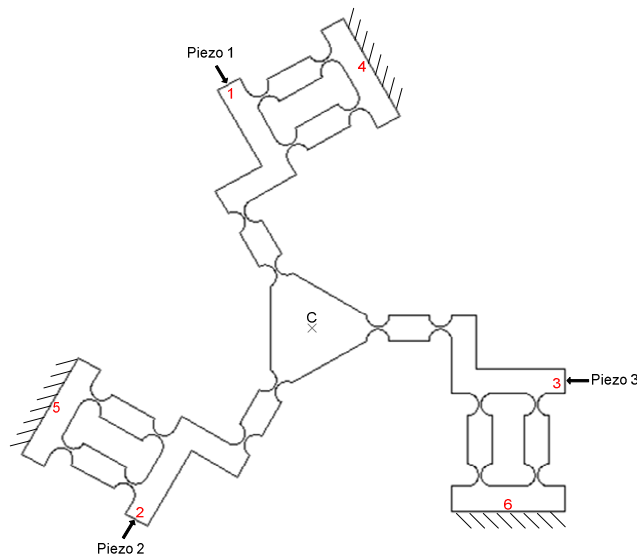
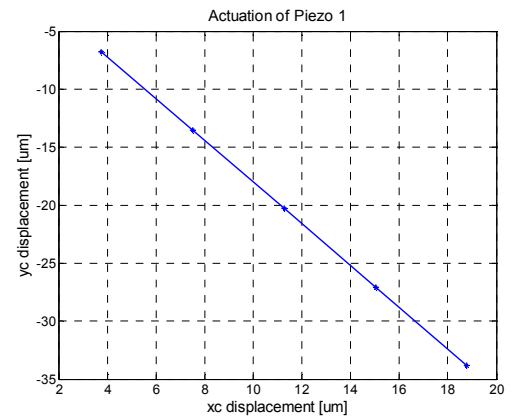
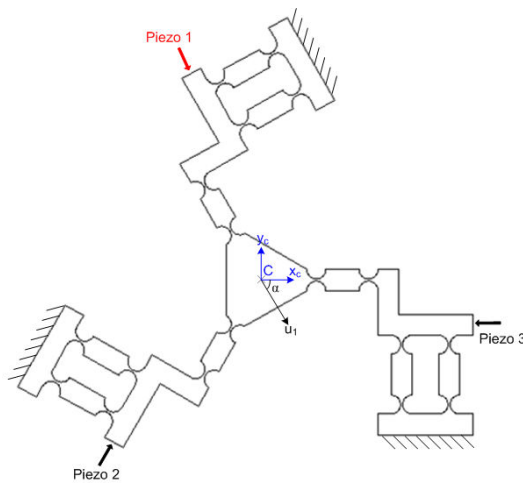


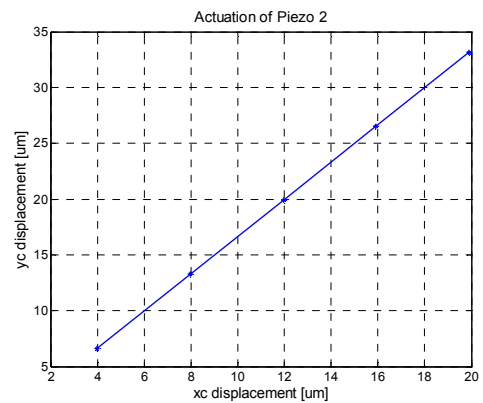
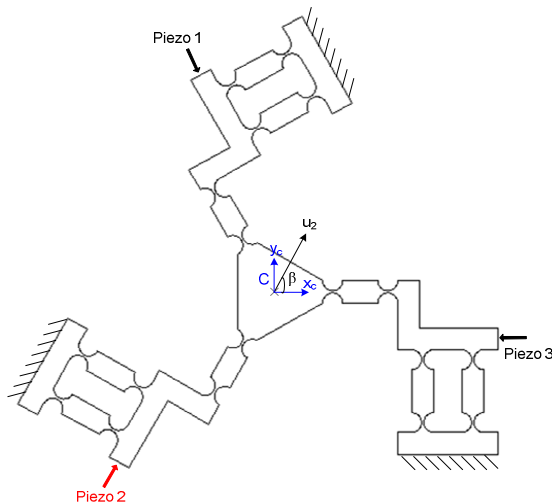
Figure 3.29 Boundary conditions of constrained 3-PRR mechanism.

24N, 48N, 72N, 96N and 120N forces are applied as point forces respectively for representing the piezoelectric actuation. The red colored piezos represents the actuated

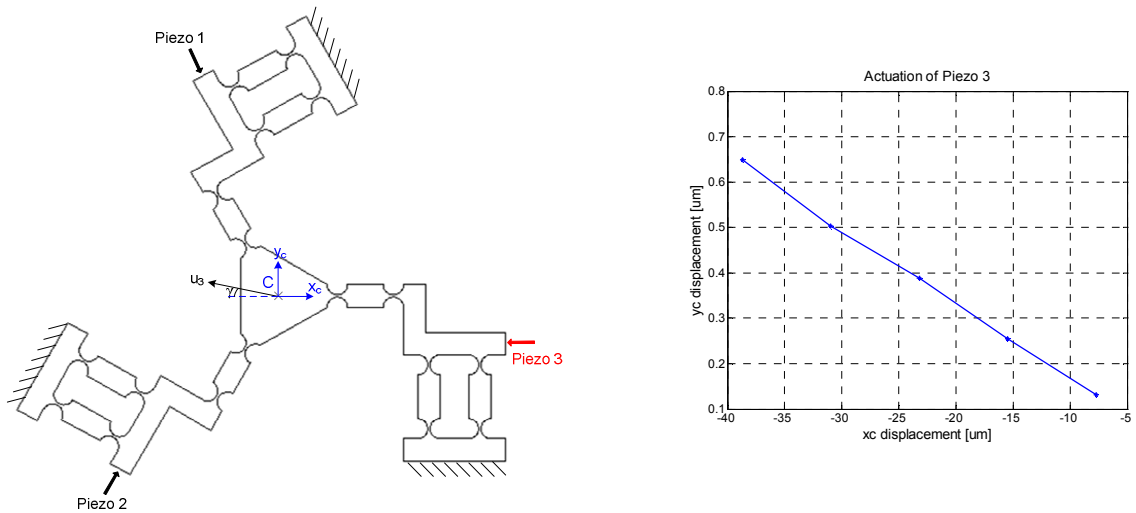
piezoelectric actuators while the other piezoelectric actuators are just attached and constrained the mechanism. When only Piezo 1 is actuated the displacement vector of the center point C is presented as u_1 vector with the angle of α as shown in Figure 3.30a, when only Piezo 2 is actuated the displacement vector of the center point C is presented as u_2 vector with the angle of β as shown in Figure 3.30b and lastly when only Piezo 3 is actuated the displacement vector of the center point C is presented as u_3 vector with the angle of γ as shown in Figure 3.30c. The results of displacements at point C for piezo actuations are also shown in Figure 3.30 as displacement plots in x direction, x_c , versus displacements in y direction, y_c for every force applied in every case.



(a) Piezo 1 is actuated for constrained 3-PRR compliant mechanism



(b) Piezo 2 is actuated for constrained 3-PRR compliant mechanism

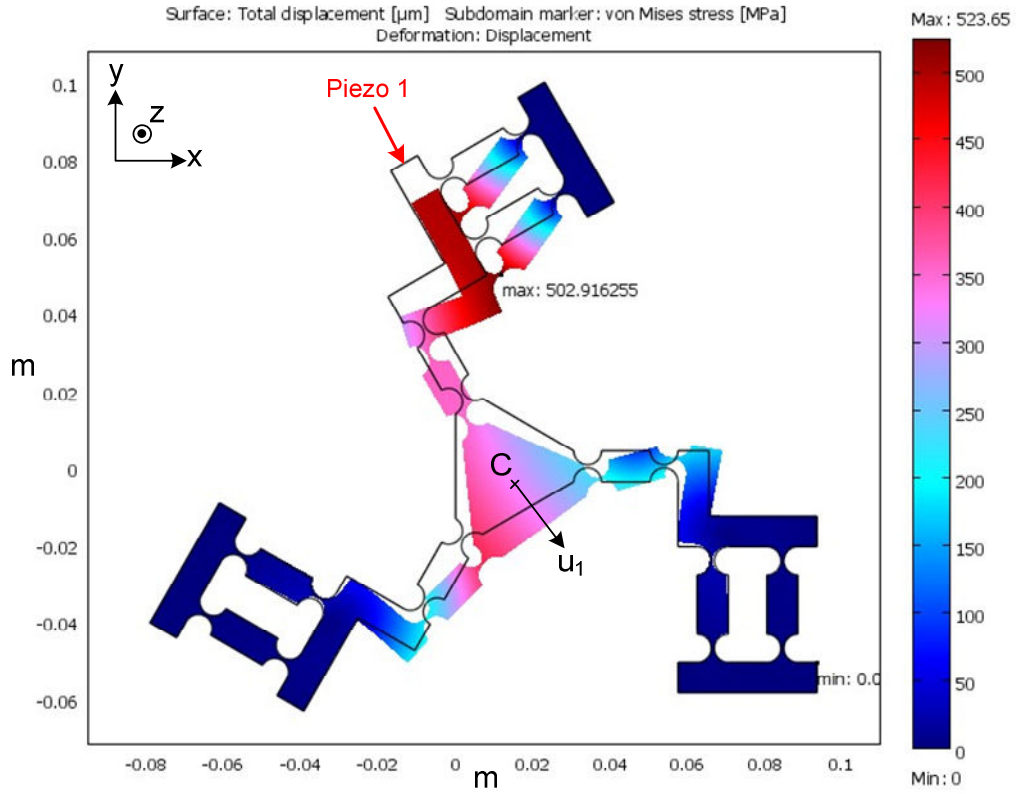


(c) Piezo 3 is actuated for constrained 3-PRR compliant mechanism

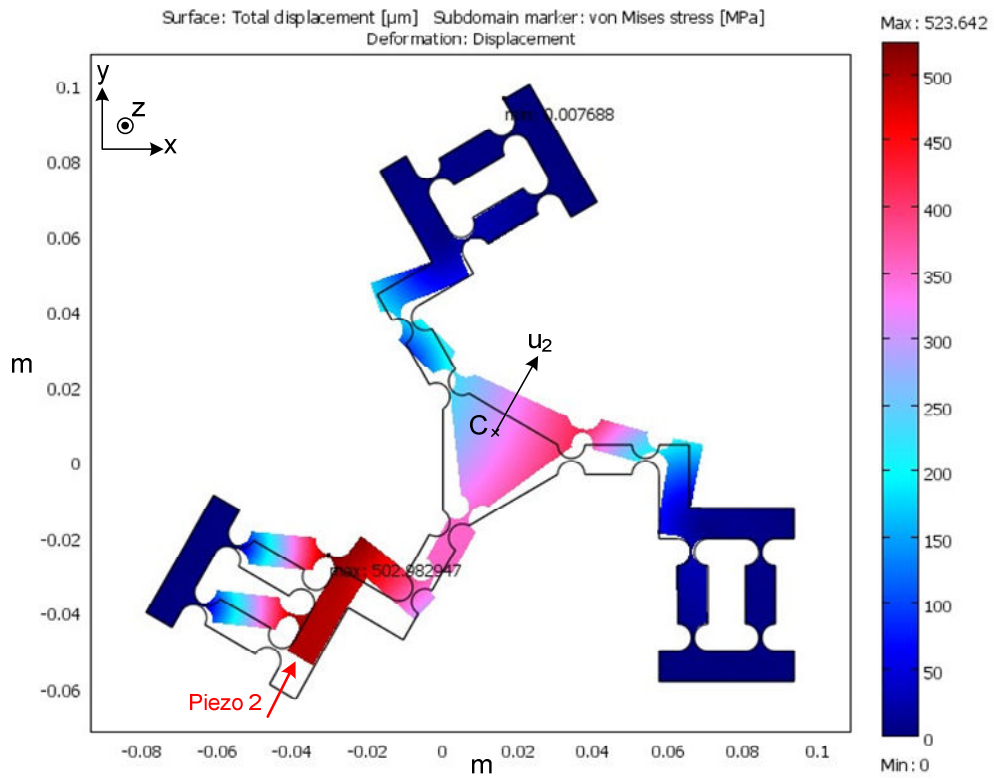
Figure 3.30 Center displacements of 3-PRR compliant mechanism.

The results in Figure 3.30a shows that when only Piezo 1 is applied to the mechanism, the center of the mechanism has displacements in u_1 direction which has 60.96° angle (α) with the x axis. When only Piezo 2 is applied to the mechanism the center displacements are in the direction of u_2 which has an angle (β) of 59.04° with the x axis and finally when Piezo 3 is applied to the mechanism the center displacements are in u_3 direction which has an angle (γ) of 1.79° with the x axis.

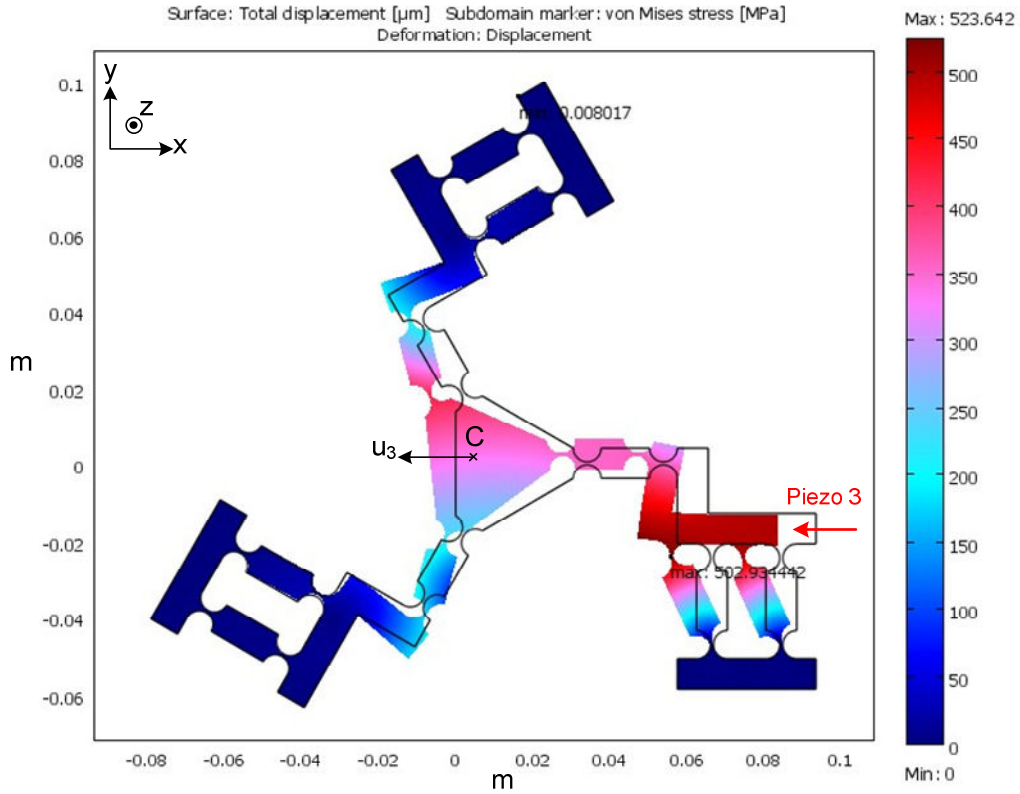
The result figures of the workspace analysis of the constrained 3-PRR compliant mechanism is shown in Figure 3.31. The figures of the simulations are scaled to 50:1 and the results are presented in Table 3.10. Results show us that for free 3-PRR compliant mechanism the maximum force can be applied is 996.8 N and the maximum displacements in u_1 , u_2 and u_3 directions are almost $323.3 \mu\text{m}$.



(a) Piezo 1 actuation in constrained 3-PRR compliant mechanism



(b) Piezo 2 actuation in constrained 3-PRR compliant mechanism



(c) Piezo 3 actuation in constrained 3-PRR compliant mechanism

Figure 3.31 Maximum displacement results for constrained 3-PRR compliant mechanism.

Table 3.10 Results of maximum displacement and stress of constrained 3-PRR compliant mechanism

Actuator	Max. Stress [MPa]	Max. Force Applied [N]	Max. Input Total Displacement [μm]	Max. Center Total Displacement [μm]
Piezo 1	502.916	996.8	501.350	323.351
Piezo 2	502.983	996.8	501.383	323.379
Piezo 3	502.934	996.8	501.384	323.397

The resonance frequency of the stage is examined by making the modal analysis with FEA. First three natural frequencies are taken into account for the analysis and the mode shapes are illustrated in Figure 3.32. The first two natural frequencies are 367.906225 Hz and 367.907129 Hz. They are almost identical and their mode shapes are translations on x-y plane as presented in Figure 3.32a and in Figure 3.32b respectively. Third mode shape is rotational as seen in Figure 3.32c which has a natural

frequency of almost 3.17 times the translational ones (1168.880755 Hz). The results show us that the designed 3-PRR compliant mechanism can be used in high frequency operations where micromotion positioning is needed.

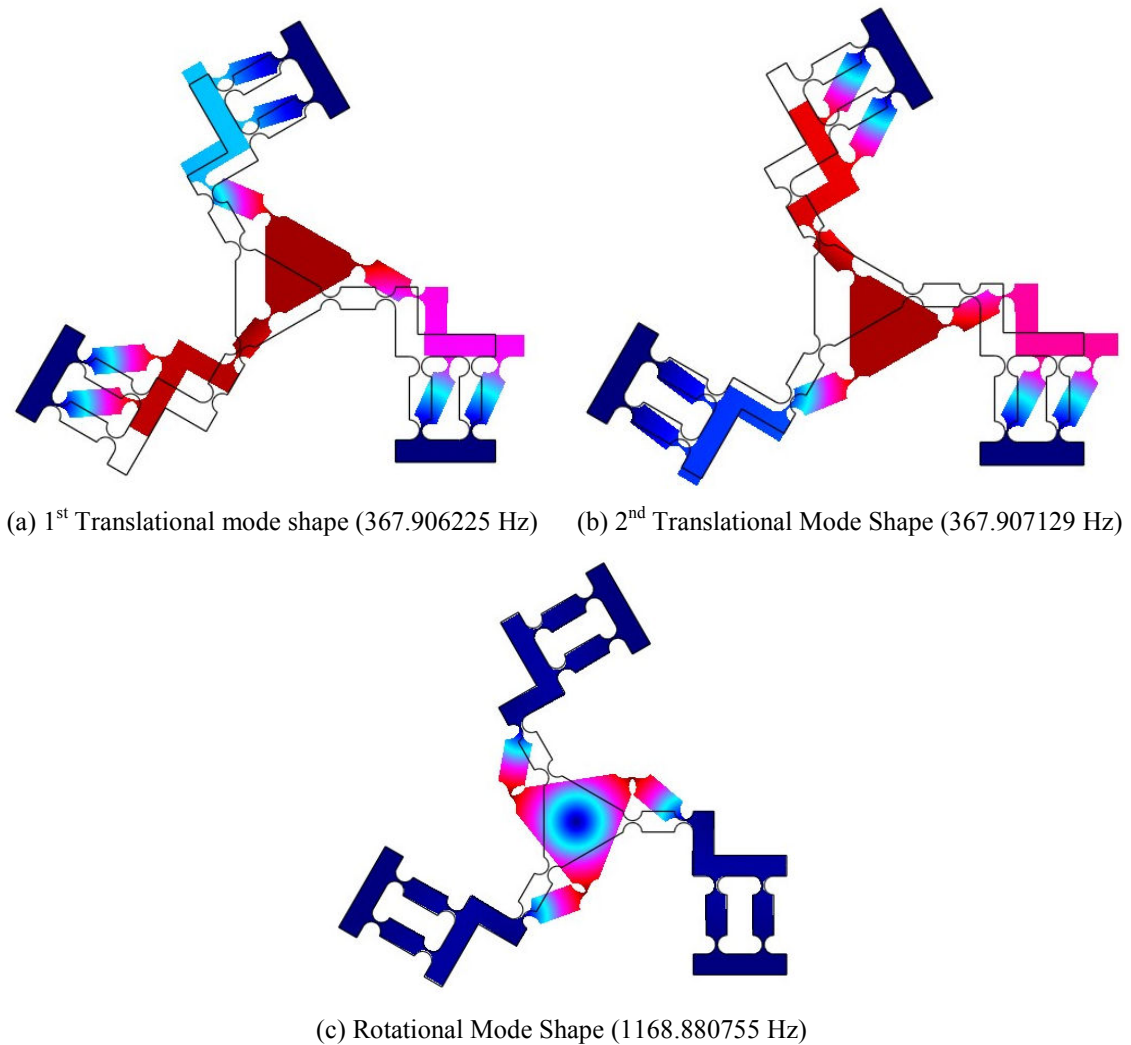


Figure 3.32 Mode shapes of 3-PRR compliant mechanism.

3.4 Comparison of 3-RRR and 3-PRR Mechanism

3-RRR and 3-PRR compliant mechanisms are designed by using right circular flexure hinges with same geometric parameters and the forces are applied at the same distances from the center of the stage to make a performance comparison. The comparisons are different for free and constrained cases of the compliant mechanisms.

3-PRR compliant mechanisms maximum range ($\approx 780.7\mu\text{m}$) is bigger than 3-RRR compliant mechanisms ($\approx 625.9\mu\text{m}$) for the free case. 3-PRR compliant mechanism allows a lot more force being applied. However when the mechanisms are constrained

by assembling the all actuators 3-RRR compliant mechanism has a little bit bigger maximum range ($\approx 352.5\mu\text{m}$) than 3-PRR has ($\approx 323.4\mu\text{m}$) this is because the mechanism is constrained and reaction forces/moments are coming from the supported sides of the mechanism which lowers the maximum range vale of the mechanisms. The translational modes of the 3-PRR compliant mechanism are bigger than 3-RRR compliant mechanism where as the rotational mode of the 3-RRR mechanism is a little bit bigger.

1 N force is applied for every piezoelectric actuator individually for free and constrained cases of 3-RRR and 3-PRR complaint mechanisms and the displacement results at the center of the triangular stage are presented in Table 3.11. For the free case 3-RRR compliant mechanism is more flexible than the 3-PRR compliant mechanism and for the constrained case 3-PRR is more flexible than 3-RRR compliant mechanism.

Table 3.11 Free and constrained compliant mechanism displacement results comparison

Forces	Free		Constrained	
	x_c [μm]	y_c [μm]	x_c [μm]	y_c [μm]
	3-RRR Compliant Mechanism		3-RRR Compliant Mechanism	
$F_1=1\text{N}$	2.233908	-3.96593	0.10027	-0.1773
$F_2=1\text{N}$	2.317616	3.917585	0.10357	0.17551
$F_3=1\text{N}$	-4.55153	0.048357	-0.2037	1.94E-03
	3-PRR Compliant Mechanism		3-PRR Compliant Mechanism	
$F_1=1\text{N}$	1.781824	-3.21459	0.157531	-0.28384
$F_2=1\text{N}$	1.893011	3.150424	0.166926	0.278567
$F_3=1\text{N}$	-3.67484	0.064175	-0.32481	0.005365

When forces coming from the edges of the triangular stage are not coinciding at the center of the stage the triangular stage starts to rotate and there are inequalities at the motion of each direction. As shown in Table 3.11 for each actuation type and cases the displacements at each u_1 , u_2 and u_3 direction are not equal. So we have assigned points P_1 , P_2 and P_3 at the edges of the triangle as shown in Figure 3.33 to analyze the coming forces directions and where all forces coincides on the triangular stage.

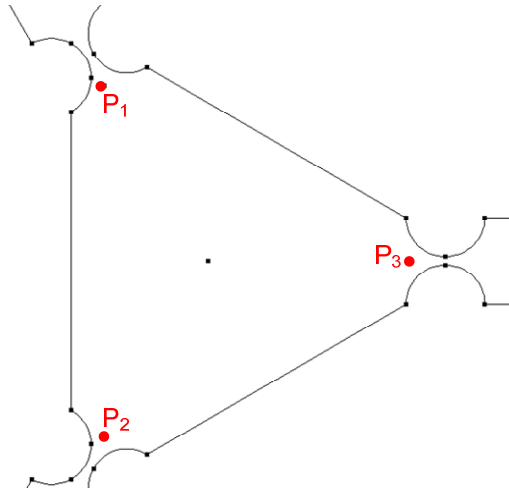
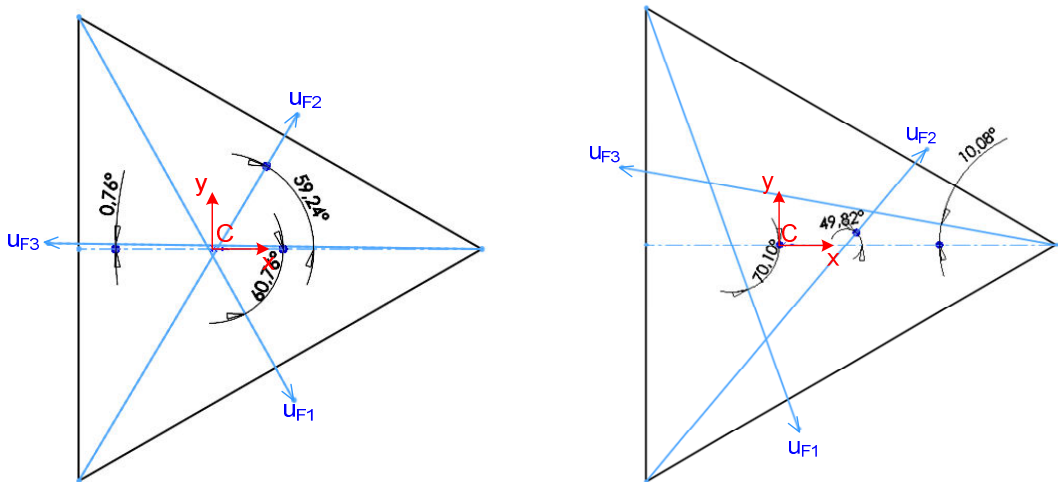


Figure 3.33 Assigned points for triangular stage

The direction of the forces coming from the edges of the triangular stage u_{F1} , u_{F2} and u_{F3} are presented in Figure 3.34 for free and constrained versions of 3-RRR and 3-PRR compliant mechanisms. As it's examined from the figures the free configuration of compliant mechanisms forces almost coincides at the center of the stage but when the mechanisms are constrained they are apart from each other causing moments acting on the stage which results center motions not parallel to the applied forces. 3-PRR compliant mechanism let bigger moments than 3-RRR compliant mechanism.



(a) Free 3-RRR compliant mechanism

(b) Constrained 3-RRR compliant mechanism

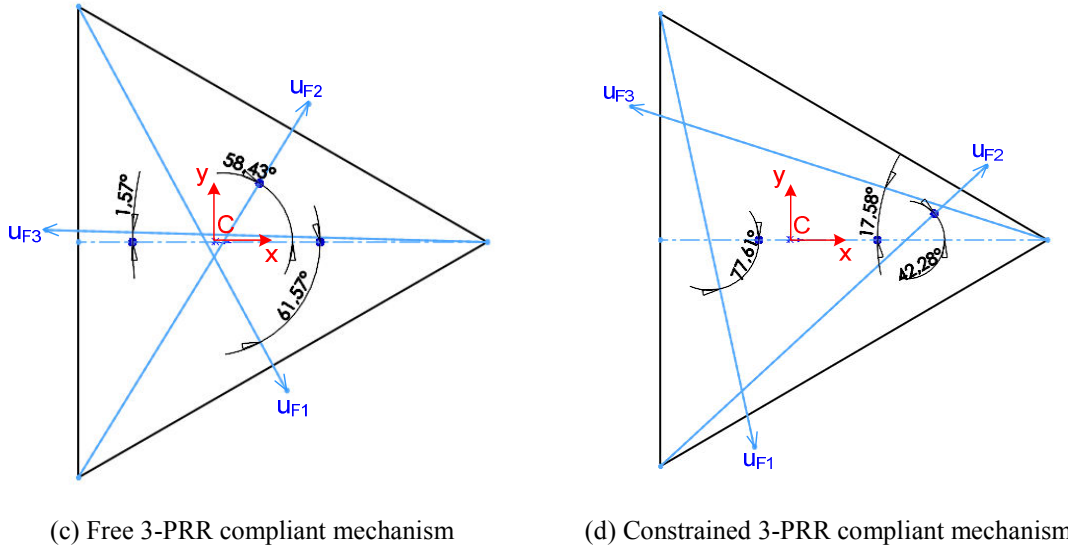


Figure 3.34 Direction of forces results for compliant mechanisms.

To summary, 3-PRR mechanism improves the range of the mechanism, the translational modes whereas it causes more rotation than 3-RRR mechanism. In the next sections we will deal with this rotation problem and we will try to control the center position of the mechanism.

3.5 Conclusion and Comments

We have designed 3-RRR and 3-PRR compliant mechanisms with right circular flexure hinges by analyzing in Finite Element Analysis software called COMSOL. The reason of using right circular hinges is explained by the stress distribution of the various circular flexure hinges and we have seen that right circular flexure hinges are the best type of flexure among the analyzed flexures because the stress is located mostly on the thinnest part of the flexures which means that the flexure bends at a certain point so eliminates the parasitic motions mostly. Right circular flexure hinges have the least range but we are dealing with small motions ($<40 \mu\text{m}$) so right circular flexure hinges are chosen for our design. The parameters of the right circular flexure hinges the thinnest part of the flexure, “t”, and the overall thickness, “b”, are selected from FEA analysis of various selection of parameters. The analysis showed us that there is an inverse asymptotical relationship between the “t”, “b” values and the maximum stress, displacement. We need enough flexibility for providing enough displacement and we need our mechanism to be stiff enough not to go under plastic deformation. That’s why

with considering of the capability of our Wire EDM manufacturing we have selected the “b” and “t” values.

3-RRR and 3-PRR compliant mechanisms are examined with the selected parameters. The aims of these analyses are to find the provided maximum displacement at the center of the stage, the motion directions for the center of the stage and the frequency modes of the mechanism. The analyses are done for two cases. Firstly the mechanisms are only fixed from the fixture links and the other links are set free. Secondly the mechanisms are fixed from the fixture links and the links that are used to actuate the mechanism are constrained by assigning a prescribed displacement defining that there are piezoelectric actuators assembled to the mechanism and they prevent the motion of the links in pull direction of the piezoelectric actuators. These analysis will show us how far we are from the analysis of the mechanisms and we will realize the manufacturing and assembling errors that will lead us to design a control methodology to kill those disturbances and find an answer to the question “Can we use non-ideal compliant mechanisms for high precision positioning?”

Finally we have compared the two structures that we have designed in terms of providing motions, achievable workspaces and frequency modes. We have found out that 3-PRR mechanism improves the range of the mechanism, the translational resonance mode whereas it causes more rotation than 3-RRR mechanism. The mechanism is stiffer but open to parasitic motions. In the next sections we will deal with this rotation problem and we will try to control the center position of the mechanism.

4 COMPLIANCE MODELING OF THE FLEXURE HINGES

Flexure modeling is the major problem while designing compliant mechanisms. There are many modeling techniques in the literature. The major ones are Classical Analytical Method, 2D Finite element method, Linear Scheme Method and Assumed mode method etc.

The model of a flexure based mechanism should be simple enough to calculate the behavior of the flexure and accurate enough to be used as a tool for design. Thus, Pseudo-Rigid-Body-Model (PRBM) [6] in which flexure hinges are treated as torsional springs and the compliant mechanism is treated as an ordinary rigid body mechanism is mainly used. By using this technique we can easily use our knowledge about rigid mechanisms modeling. The calculation of spring stiffnesses of the flexure hinges determines the precision of the model. Figure 4.1 shows the flexure hinge represented by in-plane torsional springs for in-plane motion. In this section we will compare the analytical calculation to compliance calculation results with the finite element analysis. We will try to find the best calculation method while designing the circular flexure to see whether the geometric and material parameters are good enough to be used in the compliant mechanism that we design for a specific application. In other words we should be sure that the flexure hinge bends sufficiently enough while it is not in the plastic region. Moreover, the calculation method should be simple enough to be used in practice.

The analytical calculation methods have been extensively compared by T.F. Lu et al. [70] for varying “ R/t ” values of a flexure hinge. But we will also look at the results for varying “ b ” (the width of the flexure) parameters which is not studied in the literature yet to see whether “ t ” (the shortest distance of the flexure) or “ b ” parameter would have more influence on the compliances of flexures. This study will guide for the selection of parameters in the design of compliant mechanisms.

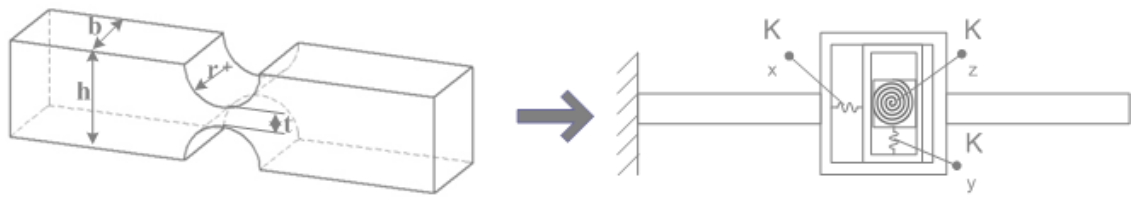


Figure 4.1 Circular flexure hinge and its PRBM.

4.1 Basic concepts of circular flexure hinges

Stiffness is the parameter that shows the resistance of a flexural structure to bending. It gives the relationship between the load and the deflection that occurs due to load. The stiffness of a flexural structure depends on both material and geometric properties. Compliance is the inverse of the stiffness, and it is the most important parameter to assess the behavior of flexural elements. The load that is applied to the flexure is generally known, and the displacement is typically the unknown parameter. Expressions were derived in terms of applied forces and moments.

There are two types of compliances: in-plane compliances and out-of-plane compliances. In this thesis we will work on in-plane compliant stiffnesses because we will mostly deal with planar compliant mechanisms that have three in-plane degrees of freedoms (DOFs). Two of them are the translational DOFs in the x and y axes, while one of them is the rotational DOF which is about the z axis. Thus, our in-plane compliances will be $\Delta x/F_x$, $\Delta y/F_y$ and $\Delta \alpha_z/M_z$. Other compliances, which are $\Delta \alpha_x/M_x$, $\Delta \alpha_y/M_y$ and $\Delta z/F_z$, represent the unwanted (parasitic) motions of the flexure.

The important characteristic geometric parameters of a circular hinge are shown in Figure 4.2. “r” is the radius of the circular hinge, “t” is the shortest distance between the circumferences of two notches, “h” is the thickness, and “b” is the width of the flexure. The material of the flexures is assumed to be an ideal linear elastic material. The important material parameters of the flexures are the modulus of elasticity “E”, shear modulus “G” and Poisson’s ratio “ ν ”.

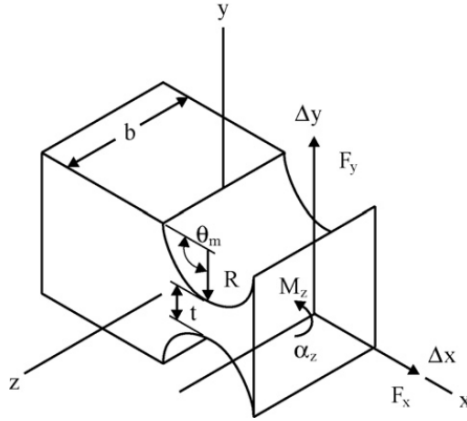


Figure 4.2 Flexure hinge coordinate frame [70].

4.2 Compliance Calculation Methods

The analytical compliance calculations are based on Castigliano's displacement theorem (2nd theorem) which allows us to calculate the linear and angular deformations of elastic bodies under loading and supporting conditions. According to Castigliano's 2nd theorem the linear displacement (u_i) and the angular deformation (θ_i) at a point i can be expressed in terms of force (F_i) and moment (M_i) acting on it as follows [8]:

$$u_i = \frac{\partial U}{\partial F_i} \quad (4.1)$$

$$\theta_i = \frac{\partial U}{\partial M_i} \quad (4.2)$$

where U is the total strain energy for an elastic member and can be written as:

$$U = U_{bending} + U_{shearing} + U_{axial} + U_{torsion} \quad (4.3)$$

$$U_{bending} = \int_L \frac{M_y^2}{2EI_y} ds + \int_L \frac{M_z^2}{2EI_z} ds \quad (4.4)$$

$$U_{shearing} = \int_L \frac{\alpha V_y^2}{2GA} ds + \int_L \frac{\alpha V_z^2}{2GA} ds \quad (4.5)$$

$$U_{axial} = \int_L \frac{N_x^2}{2EA} ds \quad (4.6)$$

$$U_{torsion} = \int_L \frac{M_x^2}{2GJ} ds \quad (4.7)$$

In general total strain energy can be written as the following equation for a point i [8]:

$$\{u_i\} = [C_i]\{L_i\} \quad (4.8)$$

where $\{u_i\}$ is the deformation vector which consists of linear and angular deformations, $\{L_i\}$ is the load vector which consists of forces and moments and $[C_i]$ is the compliance matrix whose inverse is the stiffness matrix. The first predictions have been made based on the theory presented by Paros and Weisbord [71]. Accordingly, the in-plane full compliance equations are expressed as:

$$\begin{aligned} \frac{\alpha_z}{M_z} = \frac{3}{2EbR^2} \left[\frac{1}{2\beta + \beta^2} \right] & \left\{ \left[\frac{1 + \beta}{\gamma^2} + \frac{3 + 2\beta + \beta^2}{\gamma(2\beta + \beta^2)} \right] \left[\sqrt{1 - (1 + \beta - \gamma)^2} \right] \right. \\ & \left. + \left[\frac{6(1 + \beta)}{(2\beta + \beta^2)^{3/2}} \right] \left[\tan^{-1} \left(\sqrt{\frac{2 + \beta}{\beta}} \frac{(\gamma - \beta)}{\sqrt{1 - (1 + \beta - \gamma)^2}} \right) \right] \right\} \end{aligned} \quad (4.9)$$

$$\begin{aligned} \frac{\Delta y}{F_y} = R^2 \sin^2 \theta_m \left(\frac{\alpha_z}{M_z} \right) \\ - \frac{3}{2Eb} \left\{ \left[\frac{1 + \beta}{(1 + \beta - \cos \theta_m)^2} \frac{2 + \frac{(1 + \beta)^2}{(2\beta + \beta^2)}}{(1 + \beta - \cos \theta_m)} \right] \sin \theta_m \right. \\ \left. + \left[\frac{4(1 + \beta)}{\sqrt{2\beta + \beta^2}} - \frac{2(1 + \beta)}{(2\beta + \beta^2)^{3/2}} \right] \tan^{-1} \sqrt{\frac{2 + \beta}{\beta}} \tan \frac{\theta_m}{2} - (2\theta_m) \right\} \end{aligned} \quad (4.10)$$

$$\begin{aligned} \frac{\Delta x}{F_x} = \frac{1}{Eb} \left[-2 \tan^{-1} \frac{(\gamma - \beta)}{\sqrt{1 - (1 + \beta - \gamma)^2}} \right. \\ \left. + \frac{2(1 + \beta)}{\sqrt{2\beta + \beta^2}} \tan^{-1} \left(\sqrt{\frac{2 + \beta}{\beta}} \frac{(\gamma - \beta)}{\sqrt{1 - (1 + \beta - \gamma)^2}} \right) \right] \end{aligned} \quad (4.11)$$

where $\beta = t/2R$, $\gamma = h/2R$ and $\theta_m = \pi/2$.

The simplified versions of Paros and Weisbord [71] equations are given as:

$$\frac{\Delta \alpha_z}{M_z} \approx \frac{9\pi R^{1/2}}{2Ebt^{5/2}} \quad (4.12)$$

$$\frac{\Delta y}{F_y} \approx \frac{9\pi}{2Eb} \left(\frac{R}{t}\right)^{5/2} \quad (4.13)$$

$$\frac{\Delta x}{F_x} \approx \frac{1}{Eb} \left[\pi \left(\frac{R}{t}\right)^{1/2} - 2.57 \right] \quad (4.14)$$

The in-plane compliance equations for Wu and Lobontiu's [72] are as follows:

$$\begin{aligned} \frac{\Delta \alpha_z}{M_z} = & \frac{24r^2}{Ebt^3(2R+t)(4R+t)^3} [t(4R+t)(6R^2 + 4Rt + t^2)] \\ & + 6r(2R+t)^2 \sqrt{t(4R+t)} \arctan \sqrt{1 + \frac{4R}{t}} \end{aligned} \quad (4.15)$$

$$\begin{aligned} & \frac{\Delta y}{F_y} \\ & = \frac{3}{4Eb(2R+t)} \left\{ 2(2+\pi)R + \pi t + \frac{8r^3(44R^2 + 28rt) + 5t^2}{t^2(4R+t)^2} \right\} \\ & + \frac{(2R+t)\sqrt{t(4R+t)} [-80r^4 + 24R^3t + 8(3+2\pi)R^2t^2 + 4(1+2\pi)Rt^3 + \pi t]}{\sqrt{t^5(4R+t)^5}} \\ & - \frac{8(2R+t)^4(-6R^2 + 4Rt + t^2)}{\sqrt{t^5(4R+t)^5}} \arctan \sqrt{1 + \frac{4R}{t}} \\ & \frac{\Delta x}{F_x} = \frac{1}{Eb} \left[\frac{2(2R+t)}{\sqrt{t(4R+t)}} \left(\arctan \sqrt{1 + \frac{4R}{t}} \right) - \frac{\pi}{2} \right] \end{aligned} \quad (4.16)$$

$$\quad (4.17)$$

Schotborgh [68] have presented dimensionless design graphs for circular flexure hinges where graphs are constructed by curve-fitting the results obtained from Finite Element Analysis. The in-plane compliance equations are given as:

$$\frac{\alpha_z}{M_z} = \left\{ \frac{Ebt^2}{12} \left[-0.0089 + 1.3556 \sqrt{\frac{t}{2R}} - 0.5227 \left(\frac{t}{2R}\right) \right] \right\}^{-1} \quad (4.18)$$

$$\frac{\Delta y}{F_y} = \left\{ Eb \left[0.0040 - 0.0727 \sqrt{\frac{t}{2R}} + 0.3417 \left(\frac{t}{2R}\right) \right] \right\}^{-1} \quad (4.19)$$

$$\frac{\Delta x}{F_x} = \left\{ Eb \left[0.0010 + 0.4256 \sqrt{\frac{t}{2R}} + 0.0824 \left(\frac{t}{2R}\right) \right] \right\}^{-1} \quad (4.20)$$

4.3 Numerical of Circular Flexure Hinge

The commercial Multiphysics Analysis software called COMSOL Multiphysics 3.5a is used for modeling a circular flexure hinge. The circular flexure hinge is modeled by using triangular plane stress elements, which have 2 degrees of freedom. 2D triangular plane stress elements are preferred for predicting the stiffness values of a flexure hinge instead of plane strain elements because Schotborgh [68] has proven that plain stress elements make safer estimations. Mapped meshing technique is used to control the distribution of number of elements. The number of elements is increased on the boundaries which are near the hinge until the results are converged to some number. These critical locations places are important because they will have the highest stress values. The flexure hinge's material that is used is Aluminum 7075 and necessary material properties that is used in the analysis are displayed in Table 4.1

Table 4.1 Material properties of AL7075

Modulus of Elasticity (E) [Pa]	Poisson's ratio (ν)	Density (ρ) [kg/m ³]
71.7e9	0.33	2810

In the literature the numerical calculations are always done for the displacement at point A as shown in Figure 4.3-4.5. We need pure moment in z axis (M_z), translational (F_y), and longitudinal (F_x) forces to calculate the in-plane stiffnesses of the flexure hinge. We have applied unit moment, unit translational and unit longitudinal forces to calculate the in-plane compliances of the flexure. The following sections discuss how we have applied the loads to our design.

4.3.1 Boundary Conditions

- Applying only unit moment M_z :

Two F_x forces in the opposite direction are applied at the end of the flexure part as shown in Figure 4.3. The necessary magnitude of the F_x forces that we should give for having a unit moment is calculated as follows:

$$M_z = 2 \cdot F_x \cdot \frac{h}{2} \quad (4.21)$$

$$F_x = \frac{M_x}{h} = \frac{1}{h} \quad (4.22)$$

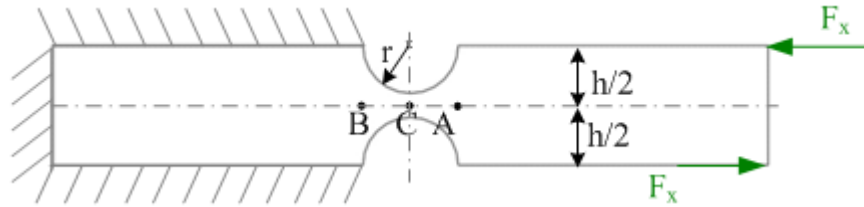


Figure 4.3 Applying moment (M_z).

- Applying only translational unit force F_y :

After applying a unit F_y force two F_x forces in the opposite direction are applied to kill the moment effect of F_y as shown in Figure 4.4. The magnitudes of the F_x forces is calculated as follows:

$$F_y \cdot L = 2 \cdot F_x \cdot \frac{h}{2} \quad (4.23)$$

$$F_x = F_y \cdot \frac{L}{h} = 1 \cdot \frac{L}{h} \quad (4.24)$$

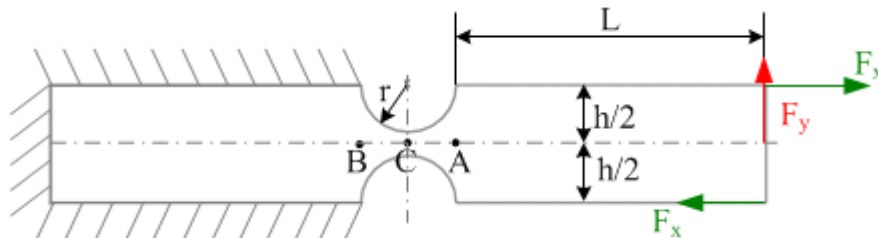


Figure 4.4 Applying translational force (F_y).

- Applying only longitudinal unit force F_x :

A unit F_x force is simply applied as shown in Figure 4.5.

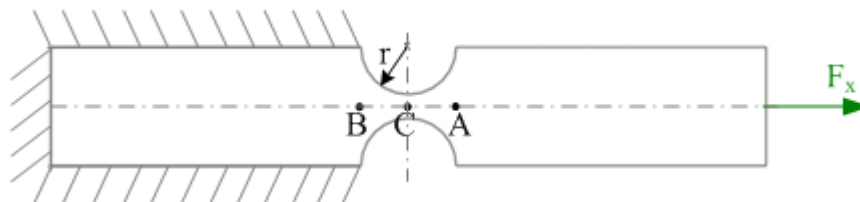


Figure 4.5 Applying longitudinal force (F_x).

4.3.2 Meshing

Mapped mesh technique is used while meshing the part. 2D triangular plane stress elements have been used as mentioned before. The aim is to find minimum number of elements that will assure convergence of the results. After trying different number of elements for the boundaries of the part and looking at the results, the minimum number of elements is found as 3070 number of elements. 1st and 5th boundaries have 10 number of elements, while 2nd, 8th, 4th and 6th boundaries have 30 number of elements. Finally 3rd, and 7th boundaries have 60 elements. The meshed flexure hinge is shown in Figure 4.6. The in-plane compliance results are shown in Table 4.2.

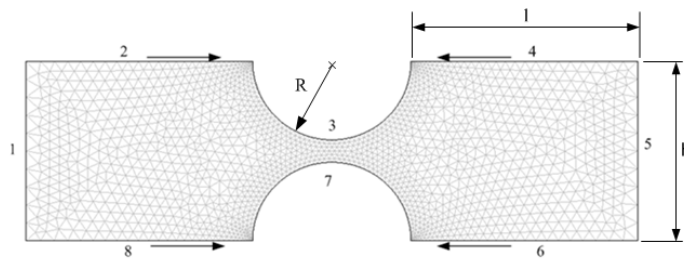


Figure 4.6 The meshed part analyzed using finite element method.

4.4 Results and Comparison of The Methods

The geometric properties of our design as follows: $R= 3.5$ mm, $l=10$ mm and $h=8$ mm. In Table 4.2 the FEA and the analytical results are shown for in plane compliances. As seen from Table 4.3 % errors compared to FEA results are presented. The highlighted errors are the smallest errors among the methods and they will be selected for the compliance calculations.

Table 4.2 Compliance results of FEA and 4 kinds of analytic calculation methods

	$\Delta\alpha_z/M_z$ [rad/Nm]	$\Delta y/F_y$ [$\mu\text{m}/\text{N}$]	$\Delta x/F_x$ [$\mu\text{m}/\text{N}$]
FEA	0.039483	0.541093	0.005617
Paros and Weisbord	0.0386	0.47348	0.004707
Paros and Weisbord (simplified)	0.0369	0.45187	0.0046128
Wu and Lobontiu	0.0355	0.4659	0.0054039
Schotborgh	0.0547	0.055048	0.0080325

Table 4.3 Compliance errors of analytic methods compared to FEA

	%error for $\Delta\alpha_z/M_z$	%error for $\Delta y/F_y$	% error for $\Delta x/F_x$
Paros and Weisbord	%2.236	%12.496	%16.201
Paros and Weisbord (simplified)	%6.542	%16.489	%17.878
Wu and Lobontiu	%10.088	%13.897	%3.794
Schotborgh	%38.541	%89.827	%45.430

The compliance results are shown in Figures 4.7-4.9 for “b” values changing from 5 mm to 15 mm. Accordingly, Paros and Weisbord calculation method [71] gives the closest compliance values in z directions to FEA results for all width values in Figure 4.7. Simplified version of this method [71] also gives reasonable predictions and it can be used for the calculation of compliance in z direction. Wu and Lonontiu's [72] calculation method gives the best compliance results in x direction when compared to FEA for all width values as shown in Figure 4.8. Other methods are a bit far away from the FEA results. Schotborgh calculation method [68] for the compliance in y direction is very far away from FEA results as shown in Figure 4.9. The closest method to FEA is Paros and Weisbord's method [71] followed by Wu and Lobontiu's method [72]. Wu and Lobontiu's method [72] is better than the simplified version of Paros and Weisbord's [71] for every width value.

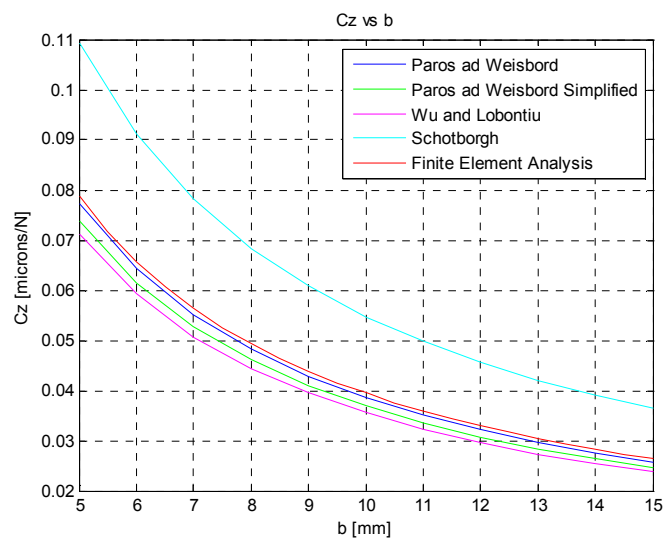


Figure 4.7 $\Delta\alpha_z/M_z$ compliance results for varying width “b”.

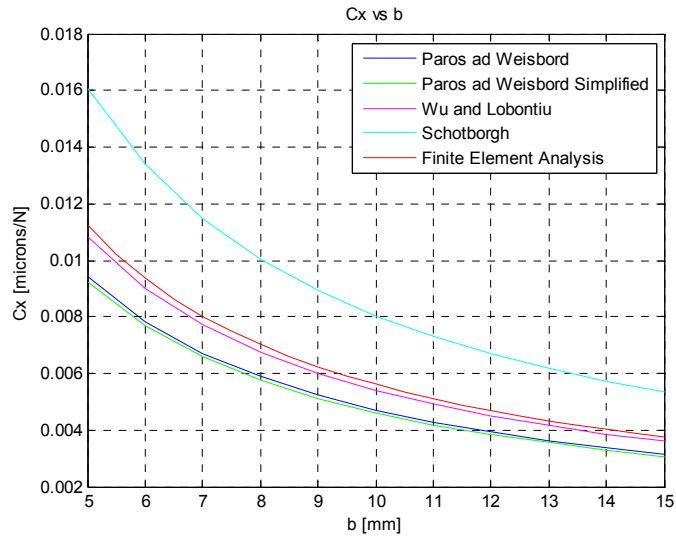


Figure 4.8 $\Delta x/F_x$ compliance results for varying width “b”.

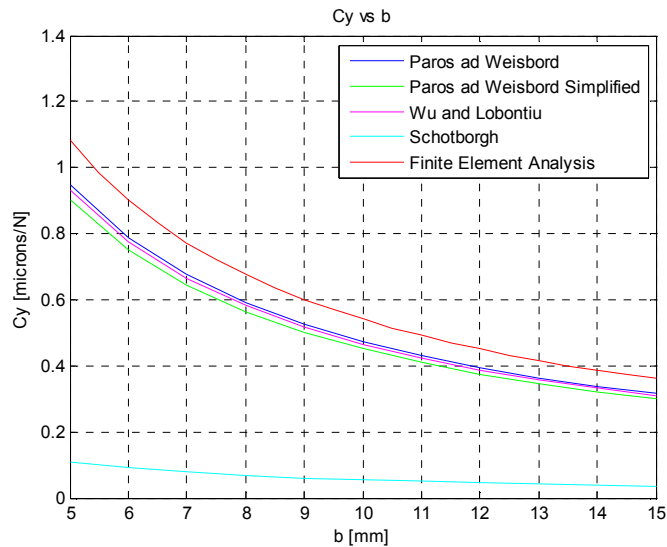


Figure 4.9 $\Delta y/F_y$ compliance results for varying width “b”.

After analyzing the effects of the width “b”, the shortest distance “t” of the hinge is varied from 0.4mm to 4mm by changing the radius of the hinge. The width of the flexure “b” is taken as constant 10 mm, while the height of the flexure “h” is taken as 8mm. It could be inferred that when the “t” parameter of the flexure is changed the hinge radius of the flexure is also changed. An extensive study is performed for “R/t” parameter by T.F. Lu et al. in [70]. Here we also want to see the effects of “t” parameter for a constant height to be able to make a comparison between “b” and “t” parameters. The compliance results for FEA and other methods are presented in Figures 4.10-4.13.

The rotational compliance in z direction found using Paros and Weisbord's method [71] is the closest to FEA until the shortest distance of the flexure hinge reaches

3 mm as shown in Figure 4.10. Beyond this value, Wu and Lobontiu's method [72] is a little bit better than the Paros and Weisbord's [71] but in general this method can be taken for the rotational compliance in z direction

When looking at Figure 4.11 we can see that Schotborgh calculation method [68] can't be used until a certain “t” value which is 1.5 mm because of the difference of his hinge types which as not a right circular flexure hinge that we used as explained in [70]. Paros and Weisbord's method's [71] results are the closest results to FEA until “t” is equal to 1.1 mm. Beyond this value, Wu and Lobontiu's method [72] starts to provide closer results wrt FEA as shown in Figure 4.12

In Figure 4.13, it can be seen that for the varying “t” values in the processes of calculating the compliance in x direction Wu and Lobontiu's method [72] is the closest one to FEA method until “t” is 3.1 mm. Beyond this value, Paros and Weisbord's method [71] starts to be the closest one to FEA. Moreover, it can be stated that the simplified version of Paros and Weisbord [71] is also close to the FEA results for thin “t” values ($t < 1$ mm). The simplified version cannot be used for $t > 1$ mm.

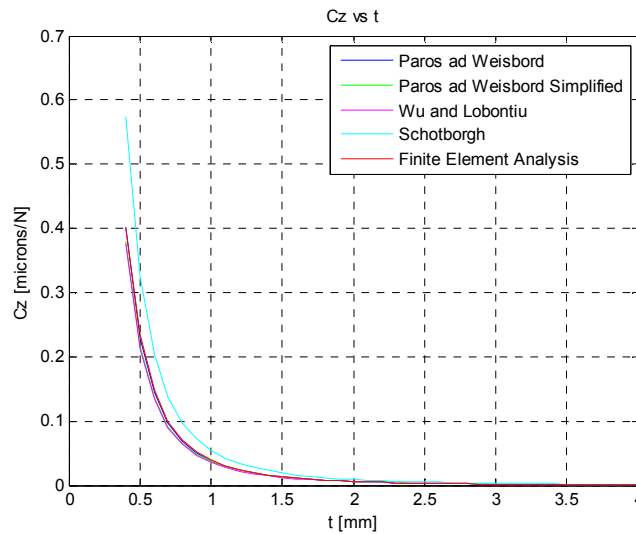


Figure 4.10 $\Delta\alpha_z/M_z$ compliance results for varying shortest distance “t” of the flexure.

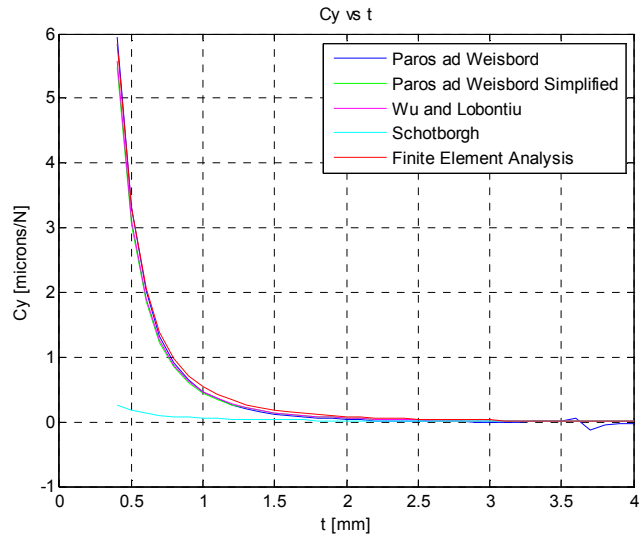


Figure 4.11 $\Delta y/F_y$ compliance results for varying shortest distance “t” of the flexure.

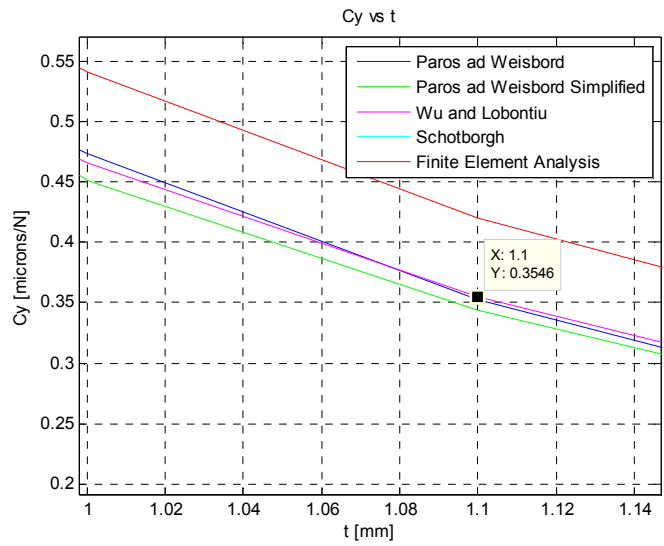


Figure 4.12 $\Delta y/F_y$ compliance results for varying shortest distance “t” of the flexure (zoomed around $t=1.1$ mm).

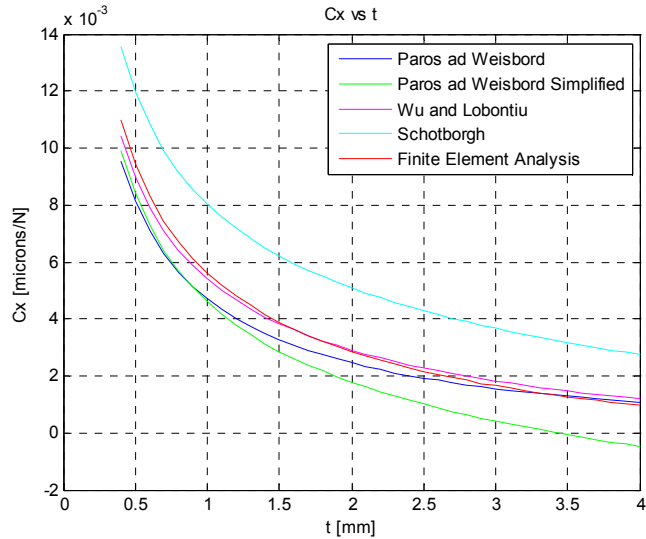


Figure 4.13 $\Delta x/F_x$ compliance results for varying shortest distance “t” of the flexure.

We can also see the effects of “b” and “t” on the compliances by examining the above figures. The in-plane compliance in x direction (C_x) is decreasing, while the thickness and the width of the flexure increase. When we fit a linear line to the graphs the slope of C_x decreases faster as “t” is increases. Thus, we can say that C_x mostly depends on “t”. The in-plane compliance in y direction (C_y) also decreases, as the thickness and the width of the flexure increases. C_y decreases faster as “t” increases up to a value (1 mm), beyond which the slope of the curve decreases and C_y starts to depend mostly on “b”. Finally, the in-plane rotational compliance in z direction (C_z) also decreases, as the thickness and the width of the flexure increases. The behavior of C_z is similar to C_y .

4.5 Conclusion and Comments

The calculation methods of in-plane x, y translational compliances and z rotational compliance of a certain circular flexure hinge are presented and the methods are compared using the finite element method. Based on the results, Schotborgh method [68] can only be used for the rotational compliance in z direction while the translational compliances in x and y directions has bigger errors compared to other methods because of the difference of his hinge models. Paros and Weisboard’s calculations [71] give the best translational compliance in y direction and rotational compliance in z direction, and

finally, the translational compliance in x direction can be most accurately calculated by the Wu and Lobontiu's method [72].

The compliance calculation methods are also compared to the finite element analysis (FEA) for varying geometric parameters “b” (the width of the flexure) and “t” (the shortest distance of the flexure). These analyses give us the selectable calculation methods for certain “b” and “t” parameters. Besides, they show which geometric parameter (b or t) has more influence on in which direction of compliances. C_x mostly depends on “t”. C_y decreases faster as “t” increases until 1 mm, beyond which the slope of the curve decreases and C_y starts to depend mostly on “b”. The behavior of C_z is similar to C_y . Thus, this work gives us the advantage of selecting the right calculation methods and geometric parameters for designing flexure based mechanisms.

5 KINETOSTATIC MODELING OF 3-PRR COMPLIANT MECHANISM

The modeling of the 3-PRR compliant stages are obtained by using Kinetostatic modeling technique. This method is firstly presented by V. Krovi et al. in [73] then by Lu Tien-Fu et. al. in [61] and is used for calculations for four-bar compliant mechanisms and 3-RRR compliant mechanisms with different link angles. These studies have claimed that this method provides better prediction of the rotational motion when compared to Pseudo Rigid Body Method. Moreover Kinetostatic model is a simple closed form model that does not require a lot of computational efforts to solve. Therefore, we have chosen this method to apply it to the designed 3-PRR compliant mechanism to see whether it can be used for fast computation of the kinetostatic parameters of our compliant mechanism.

Kinetostatic modeling method combines compliances of the flexures with the kinematics of the compliant mechanism and gives the advantage of having knowledge about the kinematics and force design criteria of the stage. In PRBM technique only $\Delta\alpha_z/M_z$ compliance is used for flexure hinges by treating flexures to have one DOF motion capability, which decrease the accuracy of the model but in Kinetostatic Modeling all in-plane compliances, $\Delta x/F_x$, $\Delta y/F_y$ and $\Delta\alpha_z/M_z$, are taken into account, which will give us more accurate results. Mainly, the choice of flexure hinge compliance calculation method affects the accuracy of the results. Therefore, we will use the proper calculation method to calculate the compliance of the flexure hinge as we compared in Section 4. The choice of the flexure hinge compliance has minimal effect on the Position Jacobian of the mechanism because it only depends on the kinematics of the mechanism. And we will use this method to compute the Jacobian and compliance that relates the output displacements to the input forces of the stage to be used in our dynamic model.

The kinetostatic model is composed of 4 compliance matrices as in Eqn. 5.1 which relates the output and input displacements to the input and output forces/moments.

$$\begin{bmatrix} \mathbf{U}_o \\ \mathbf{U}_{in} \end{bmatrix} = \underbrace{\begin{bmatrix} \mathbf{C}_{o,F_o} & \mathbf{C}_{o,F_{in}} \\ \mathbf{C}_{in,F_o} & \mathbf{C}_{in,F_{in}} \end{bmatrix}}_{\mathbf{C}} \begin{bmatrix} \mathbf{F}_o \\ \mathbf{F}_{in} \end{bmatrix} \quad (5.1)$$

\mathbf{U}_o is the output displacement matrix of the stage which are Δx_o , Δy_o and $\Delta \alpha_o$.

\mathbf{U}_{in} is the input displacement matrix which are given by the piezos connected to the tabs of the mechanism.

\mathbf{F}_o is the output force matrix in Eqn. 5.2 acting on point O which is the center of the stage.

$$\mathbf{F}_o = [F_{ox} \quad F_{oy} \quad M_{oz}]^T \quad (5.2)$$

\mathbf{F}_{in} is the input force matrix in Eqn. 5.3 acting on the tabs of the mechanism

$$\mathbf{F}_{in} = [F_{in1} \quad F_{in2} \quad F_{in3}]^T \quad (5.3)$$

\mathbf{C} is the compliance matrix that composed of compliances that relates output forces to output displacements, \mathbf{C}_{o,F_o} , input forces to output displacements, $\mathbf{C}_{o,F_{in}}$, output forces to input displacements, \mathbf{C}_{in,F_o} , and input forces to input displacements, $\mathbf{C}_{in,F_{in}}$.

5.1 3-PRR Kinetostatic Modeling

3-PRR compliant mechanism is modeled by first modeling only one PRR limb. Then found compliance results are transformed in the other two limbs by using transformation matrices. The assigned coordinate frames, forces and moments acting on the circular flexure hinges are shown in Figure 5.1, and the necessary measurements are presented in Figure 5.2.

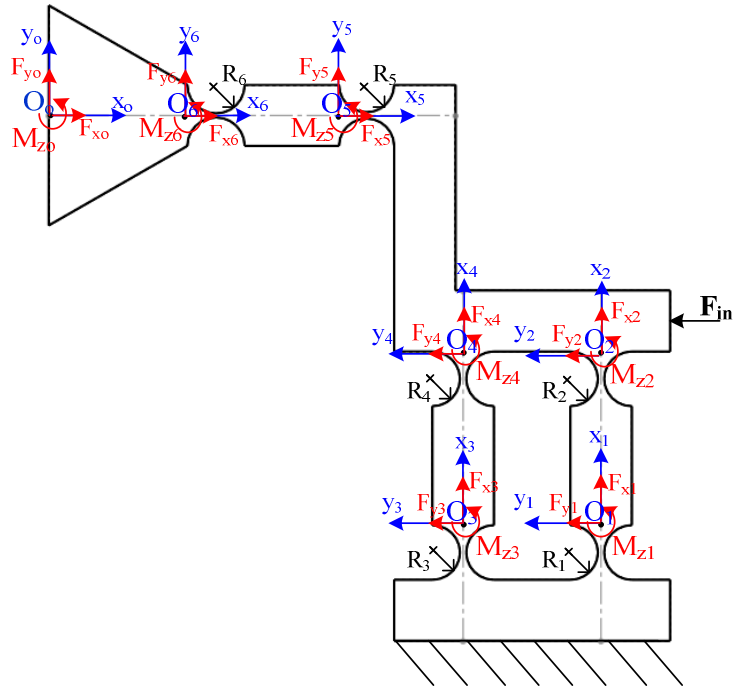


Figure 5.1 Assigned coordinate frames and acting forces/moments.

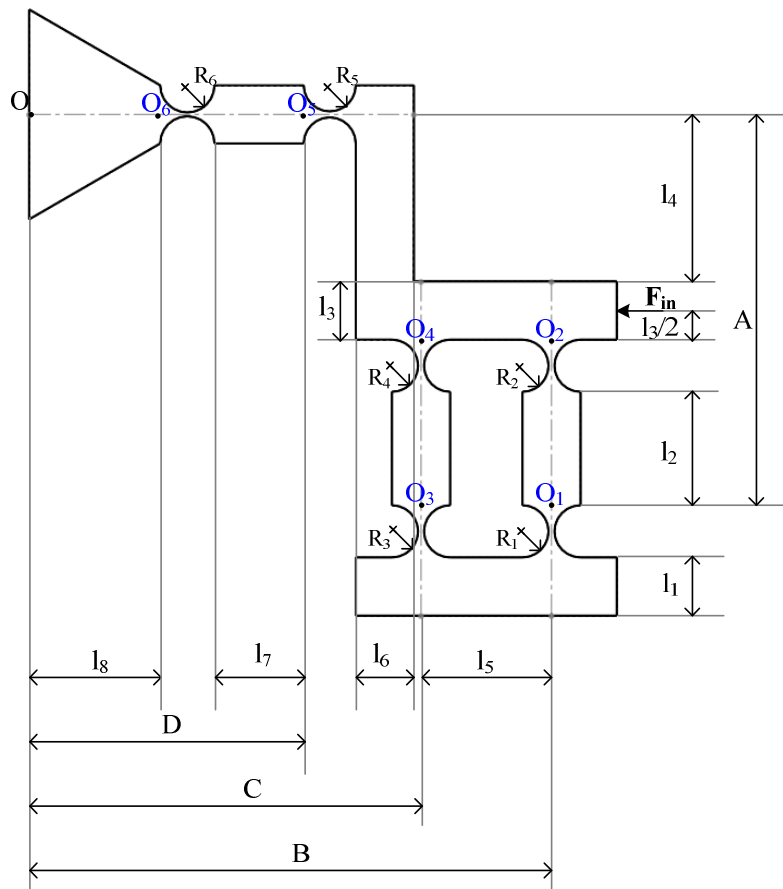


Figure 5.2 Measurements of a PRR link.

5.1.1 Derivation of $C_{o,Fo}$

The procedure for deriving full $C_{o,Fo}$ matrix for a PRR link is the same for all hinges. Hinge 1 will be derived in detail to be as an example and the acting forces of other hinges will be presented.

Hinge 1

We will calculate the output compliance matrix of flexure hinge 1 with respect to point “o” caused by F_{ox} , F_{oy} and M_{oz} [61].

$$C_{h1} = \begin{bmatrix} \frac{\partial \Delta x_o^1}{\partial F_{ox}} & \frac{\partial \Delta x_o^1}{\partial F_{oy}} & \frac{\partial \Delta x_o^1}{\partial M_{oz}} \\ \frac{\partial \Delta y_o^1}{\partial F_{ox}} & \frac{\partial \Delta y_o^1}{\partial F_{oy}} & \frac{\partial \Delta y_o^1}{\partial M_{oz}} \\ \frac{\partial \Delta \alpha_o^1}{\partial F_{ox}} & \frac{\partial \Delta \alpha_o^1}{\partial F_{oy}} & \frac{\partial \Delta \alpha_o^1}{\partial M_{oz}} \end{bmatrix} \quad (5.4)$$

The forces and moments acting on Hinge 1 are as follows:

$$F_{1x} = F_{oy} \quad (5.5)$$

$$F_{1y} = F_{in} - F_{ox} \quad (5.6)$$

$$M_{1z} = \left(\frac{l_3}{2} + 2R_2 + l_2 \right) F_{in} - AF_{ox} - BF_{oy} + M_{oz} \quad (5.7)$$

The compliances are computed by defining the translational and rotational displacements and taking the derivatives of the displacements with respect to output forces as moments as follows:

- Calculating the compliances $\partial \alpha_o^1 / \partial F_{ox}$, $\partial \alpha_o^1 / \partial F_{oy}$, $\partial \alpha_o^1 / \partial M_{oz}$

The rotational displacement about z-axis $\Delta \alpha_1^1$ at point 1 respect to 1 coordinate frame:

$$\Delta \alpha_1^1 = \left[\frac{\Delta \alpha_z}{M_z} \right]_1 \cdot M_{1z} + \left[\frac{\Delta \alpha_z}{M_z} \right]_1 \cdot F_{1y} R_1 \quad (5.8)$$

Where $\left[\frac{\Delta \alpha_z}{M_z} \right]_1$ is the rotational compliance of hinge 1. The rotational displacement about z axis at point “o”, $\Delta \alpha_o^1$ is the same as the $\Delta \alpha_1^1$ rotational displacement. Thus, the compliance results are the same as the derivatives of $\Delta \alpha_1^1$:

$$\frac{\partial \Delta \alpha_o^1}{\partial F_{ox}} = - \left[\frac{\Delta \alpha_z}{M_z} \right]_1 \cdot (A + R_1) \quad (5.9)$$

$$\frac{\partial \Delta \alpha_o^1}{\partial F_{oy}} = - \left[\frac{\Delta \alpha_z}{M_z} \right]_1 \cdot B \quad (5.10)$$

$$\frac{\partial \Delta \alpha_o^1}{\partial M_{oz}} = \left[\frac{\Delta \alpha_z}{M_z} \right]_1 \quad (5.11)$$

➤ Calculating the compliances $\partial y_o^1 / \partial F_{ox}$, $\partial y_o^1 / \partial F_{oy}$, $\partial y_o^1 / \partial M_{oz}$

The translational displacement about y-axis Δy_1^1 at point 1 respect to 1 coordinate frame is given at:

$$\Delta y_1^1 = \left[\frac{\Delta y}{F_y} \right]_1 \cdot F_{1y} + \left[\frac{\Delta y}{M_z} \right]_1 \cdot M_{1z} R_1 \quad (5.12)$$

The translational displacement about the y-axis at point 1, Δy_1^1 compliances caused by F_{ox} , F_{oy} and M_{oz} are calculated as follows:

$$\frac{\partial \Delta y_1^1}{\partial F_{ox}} = - \left[\frac{\Delta y}{F_y} \right]_1 - \left[\frac{\Delta \alpha_z}{M_z} \right]_1 \cdot A R_1 \quad (5.13)$$

$$\frac{\partial \Delta y_1^1}{\partial F_{oy}} = - \left[\frac{\Delta \alpha_z}{M_z} \right]_1 \cdot B R_1 \quad (5.14)$$

$$\frac{\partial \Delta y_1^1}{\partial M_{oz}} = \left[\frac{\Delta \alpha_z}{M_z} \right]_1 \cdot R_1 \quad (5.15)$$

The translational displacement about y-axis at point “o”, Δy_o^1 , is the summation of Δy_1^1 and the displacement caused by the rotational motion of the assumed link having a measurement of A shown in Figure 5.2:

$$\Delta y_o^1 = \Delta y_1^1 + A \cdot \Delta \alpha_o^1 \quad (5.16)$$

The translational displacement Δy_o^1 compliances caused by F_{ox} , F_{oy} and M_{oz} are calculated as follows:

$$\begin{aligned} \frac{\partial \Delta y_o^1}{\partial F_{ox}} &= \frac{\partial \Delta y_1^1}{\partial F_{ox}} + A \cdot \frac{\partial \Delta \alpha_o^1}{\partial F_{ox}} \\ &= - \left[\frac{\Delta y}{F_y} \right]_1 - \left[\frac{\Delta \alpha_z}{M_z} \right]_1 \cdot A R_1 + A \left(- \left[\frac{\Delta \alpha_z}{M_z} \right]_1 \cdot (A + R_1) \right) \end{aligned} \quad (5.17)$$

$$= - \left[\frac{\Delta y}{F_y} \right]_1 - [A R_1 + A(A + R_1)] \left[\frac{\Delta \alpha_z}{M_z} \right]_1$$

$$\begin{aligned} \frac{\partial \Delta y_o^1}{\partial F_{oy}} &= \frac{\partial \Delta y_1^1}{\partial F_{oy}} + A \cdot \frac{\partial \Delta \alpha_o^1}{\partial F_{oy}} \\ &= - \left[\frac{\Delta \alpha_z}{M_z} \right]_1 \cdot B R_1 - A \left[\frac{\Delta \alpha_z}{M_z} \right]_1 \cdot B \end{aligned} \quad (5.18)$$

$$= -B(R_1 + A) \left[\frac{\Delta \alpha_z}{M_z} \right]_1$$

$$\begin{aligned}
\frac{\partial \Delta y_o^1}{\partial M_{oz}} &= \frac{\partial \Delta y_1^1}{\partial M_{oz}} + A \cdot \frac{\partial \Delta \alpha_o^1}{\partial M_{oz}} \\
&= \left[\frac{\Delta \alpha_z}{M_z} \right]_1 \cdot R_1 + A \left[\frac{\Delta \alpha_z}{M_z} \right]_1 \\
&= (R_1 + A) \cdot \left[\frac{\Delta \alpha_z}{M_z} \right]_1
\end{aligned} \tag{5.19}$$

➤ Calculating the compliances $\partial x_o^1 / \partial F_{ox}$, $\partial x_o^1 / \partial F_{oy}$, $\partial x_o^1 / \partial M_{oz}$

The translational displacement about y-axis Δx_1^1 at point 1 respect to 1 coordinate frame:

$$\Delta x_1^1 = \left[\frac{\Delta x}{F_x} \right]_1 \cdot F_{1x} \tag{5.20}$$

The translational displacement on the x-axis at point 1, Δx_1^1 compliances caused by F_{ox} , F_{oy} and M_{oz} is calculated as follows:

$$\frac{\partial \Delta x_1^1}{\partial F_{ox}} = 0 \tag{5.21}$$

$$\frac{\partial \Delta x_1^1}{\partial F_{oy}} = \left[\frac{\Delta x}{F_x} \right]_1 \tag{5.22}$$

$$\frac{\partial \Delta x_1^1}{\partial M_{oz}} = 0 \tag{5.23}$$

The translational displacement Δx_o^1 at point “o” is the summation of displacement Δx_1^1 at point 1 and the displacement in x direction caused by the rotational motion of the assumed link having a displacement of A shown in Figure 5.2:

$$\Delta x_o^1 = \Delta x_1^1 + \underbrace{[A - A \cos \Delta \alpha_o^1]}_{\approx 0} \tag{5.24}$$

The second term of the summation in Eqn. 5.24 is very small so we can take it as 0 and the translational displacement Δx_o^1 becomes equal to the translational displacement Δx_1^1 . Thus, the compliances of the Δx_o^1 displacement are the same as Δx_1^1 :

$$\frac{\partial \Delta x_o^1}{\partial F_{ox}} = 0 \tag{5.25}$$

$$\frac{\partial \Delta x_o^1}{\partial F_{oy}} = \left[\frac{\Delta x}{F_x} \right]_1 \tag{5.26}$$

$$\frac{\partial \Delta x_o^1}{\partial M_{oz}} = 0 \tag{5.27}$$

The compliance calculations for other hinges are similar to hinge 1. Only the forces acting on the hinges and calculation of displacements with respect to “o” point are presented.

Hinge 2

The output compliance matrix of flexure hinge 2 with respect to point “o” caused by F_{ox} , F_{oy} and M_{oz} is in Eqn. 5.28. The values of the matrix are calculated as we have shown for Hinge 1:

$$C_{h2} = \begin{bmatrix} \frac{\partial \Delta x_o^2}{\partial F_{ox}} & \frac{\partial \Delta x_o^2}{\partial F_{oy}} & \frac{\partial \Delta x_o^2}{\partial M_{oz}} \\ \frac{\partial \Delta y_o^2}{\partial F_{ox}} & \frac{\partial \Delta y_o^2}{\partial F_{oy}} & \frac{\partial \Delta y_o^2}{\partial M_{oz}} \\ \frac{\partial \Delta \alpha_o^2}{\partial F_{ox}} & \frac{\partial \Delta \alpha_o^2}{\partial F_{oy}} & \frac{\partial \Delta \alpha_o^2}{\partial M_{oz}} \end{bmatrix} \quad (5.28)$$

The forces and moments acting on Hinge 2 are as follows:

$$F_{2x} = F_{oy} \quad (5.29)$$

$$F_{2y} = F_{in} - F_{ox} \quad (5.30)$$

$$M_{2z} = \left(\frac{l_3}{2}\right) F_{in} - (l_3 + l_4) F_{ox} - B F_{oy} + M_{oz} \quad (5.31)$$

The translational and rotational displacements of Hinge 2 with respect to “o” coordinate frame are defined as in equations below:

$$\Delta \alpha_2^2 = \left[\frac{\Delta \alpha_z}{M_z} \right]_2 \cdot M_{2z} + \left[\frac{\Delta \alpha_z}{M_z} \right]_2 \cdot F_{2y} R_2 \quad (5.32)$$

$$\Delta \alpha_o^2 = \Delta \alpha_2^2 \quad (5.33)$$

$$\Delta y_2^2 = \left[\frac{\Delta y}{F_y} \right]_2 \cdot F_{2y} + \left[\frac{\Delta y}{M_z} \right]_2 \cdot M_{2z} R_2 \quad (5.34)$$

$$\Delta y_o^2 = \Delta y_2^2 + (l_3 + l_4) \cdot \Delta \alpha_o^2 \quad (5.35)$$

$$\Delta x_2^2 = \left[\frac{\Delta x}{F_x} \right]_2 \cdot F_{2x} \quad (5.36)$$

$$\Delta x_o^2 = \Delta x_2^2 + \underbrace{[(l_3 + l_4) - (l_3 + l_4) \cos \Delta \alpha_o^2]}_{\approx 0} \quad (5.37)$$

Hinge 3

The output compliance matrix of flexure hinge 3 with respect to point “o” caused by F_{ox} , F_{oy} and M_{oz} is expressed as:

$$C_{h3} = \begin{bmatrix} \frac{\partial \Delta x_o^3}{\partial F_{ox}} & \frac{\partial \Delta x_o^3}{\partial F_{oy}} & \frac{\partial \Delta x_o^3}{\partial M_{oz}} \\ \frac{\partial \Delta y_o^3}{\partial F_{ox}} & \frac{\partial \Delta y_o^3}{\partial F_{oy}} & \frac{\partial \Delta y_o^3}{\partial M_{oz}} \\ \frac{\partial \Delta \alpha_o^3}{\partial F_{ox}} & \frac{\partial \Delta \alpha_o^3}{\partial F_{oy}} & \frac{\partial \Delta \alpha_o^3}{\partial M_{oz}} \end{bmatrix} \quad (5.38)$$

The forces and moments acting on Hinge 3 are as follows:

$$F_{3x} = F_{oy} \quad (5.39)$$

$$F_{3y} = F_{in} - F_{ox} \quad (5.40)$$

$$M_{3z} = \left(\frac{l_3}{2} + 2R_4 + l_3 \right) F_{in} - AF_{ox} - CF_{oy} + M_{oz} \quad (5.41)$$

The translational and rotational displacements of Hinge 3 with respect to “o” coordinate frame are defined as:

$$\Delta \alpha_3^3 = \left[\frac{\Delta \alpha_z}{M_z} \right]_3 \cdot M_{3z} + \left[\frac{\Delta \alpha_z}{M_z} \right]_3 \cdot F_{3y} R_3 \quad (5.42)$$

$$\Delta \alpha_o^3 = \Delta \alpha_3^3 \quad (5.43)$$

$$\Delta y_3^3 = \left[\frac{\Delta y}{F_y} \right]_3 \cdot F_{3y} + \left[\frac{\Delta y}{M_z} \right]_3 \cdot M_{3z} R_3 \quad (5.44)$$

$$\Delta y_o^3 = \Delta y_3^3 + A \cdot \Delta \alpha_o^3 \quad (5.45)$$

$$\Delta x_3^3 = \left[\frac{\Delta x}{F_x} \right]_3 \cdot F_{3x} \quad (5.46)$$

$$\Delta x_o^3 = \Delta x_3^3 + \underbrace{[A - A \cos \Delta \alpha_o^3]}_{\approx 0} \quad (5.47)$$

Hinge 4

The output compliance matrix of flexure hinge 4 with respect to point “o” caused by F_{ox} , F_{oy} and M_{oz} is given as:

$$C_{h4} = \begin{bmatrix} \frac{\partial \Delta x_o^4}{\partial F_{ox}} & \frac{\partial \Delta x_o^4}{\partial F_{oy}} & \frac{\partial \Delta x_o^4}{\partial M_{oz}} \\ \frac{\partial \Delta y_o^4}{\partial F_{ox}} & \frac{\partial \Delta y_o^4}{\partial F_{oy}} & \frac{\partial \Delta y_o^4}{\partial M_{oz}} \\ \frac{\partial \Delta \alpha_o^4}{\partial F_{ox}} & \frac{\partial \Delta \alpha_o^4}{\partial F_{oy}} & \frac{\partial \Delta \alpha_o^4}{\partial M_{oz}} \end{bmatrix} \quad (5.48)$$

The forces and moments acting on Hinge 4:

$$F_{4x} = F_{oy} \quad (5.49)$$

$$F_{4y} = F_{in} - F_{ox} \quad (5.50)$$

$$M_{4z} = \left(\frac{l_3}{2} \right) F_{in} - (l_3 + l_4) F_{ox} - CF_{oy} + M_{oz} \quad (5.51)$$

The translational and rotational displacements of Hinge 4 with respect to “o” coordinate frame are defined as in equations below:

$$\Delta\alpha_4^4 = \left[\frac{\Delta\alpha_z}{M_z} \right]_4 \cdot M_{4z} + \left[\frac{\Delta\alpha_z}{M_z} \right]_4 \cdot F_{4y}R_4 \quad (5.52)$$

$$\Delta\alpha_o^4 = \Delta\alpha_4^4 \quad (5.53)$$

$$\Delta y_4^4 = \left[\frac{\Delta y}{F_y} \right]_4 \cdot F_{4y} + \left[\frac{\Delta y}{M_z} \right]_4 \cdot M_{4z}R_4 \quad (5.54)$$

$$\Delta y_o^4 = \Delta y_4^4 + (l_3 + l_4) \cdot \Delta\alpha_o^4 \quad (5.55)$$

$$\Delta x_4^4 = \left[\frac{\Delta x}{F_x} \right]_4 \cdot F_{4x} \quad (5.56)$$

$$\Delta x_o^4 = \Delta x_4^4 + \underbrace{[(l_3 + l_4) - (l_3 + l_4) \cos \Delta\alpha_o^4]}_{\approx 0} \quad (5.57)$$

Hinge 5

The output compliance matrix of flexure hinge 5 with respect to point “o” caused by F_{ox} , F_{oy} and M_{oz} is given as:

$$C_{h5} = \begin{bmatrix} \frac{\partial \Delta x_o^5}{\partial F_{ox}} & \frac{\partial \Delta x_o^5}{\partial F_{oy}} & \frac{\partial \Delta x_o^5}{\partial M_{oz}} \\ \frac{\partial \Delta y_o^5}{\partial F_{ox}} & \frac{\partial \Delta y_o^5}{\partial F_{oy}} & \frac{\partial \Delta y_o^5}{\partial M_{oz}} \\ \frac{\partial \Delta \alpha_o^5}{\partial F_{ox}} & \frac{\partial \Delta \alpha_o^5}{\partial F_{oy}} & \frac{\partial \Delta \alpha_o^5}{\partial M_{oz}} \end{bmatrix} \quad (5.58)$$

The forces and moments acting on Hinge 5 are expressed as:

$$F_{5x} = F_{ox} \quad (5.59)$$

$$F_{5y} = F_{oy} \quad (5.60)$$

$$M_{5z} = -DF_{oy} + M_{oz} \quad (5.61)$$

The translational and rotational displacements of Hinge 5 with respect to “o” coordinate frame are defined as:

$$\Delta\alpha_5^5 = \left[\frac{\Delta\alpha_z}{M_z} \right]_5 \cdot M_{5z} + \left[\frac{\Delta\alpha_z}{M_z} \right]_5 \cdot F_{5y}R_5 \quad (5.62)$$

$$\Delta\alpha_o^5 = \Delta\alpha_5^5 \quad (5.63)$$

$$\Delta y_5^5 = \left[\frac{\Delta y}{F_y} \right]_5 \cdot F_{5y} + \left[\frac{\Delta y}{M_z} \right]_5 \cdot M_{5z}R_5 \quad (5.64)$$

$$\Delta y_o^5 = \Delta y_5^5 + D \cdot \Delta\alpha_o^5 \quad (5.65)$$

$$\Delta x_5^5 = \left[\frac{\Delta x}{F_x} \right]_5 \cdot F_{5x} \quad (5.66)$$

$$\Delta x_o^5 = \Delta x_5^5 + \underbrace{[(D) - (D) \cos \Delta \alpha_o^5]}_{\approx 0} \quad (5.67)$$

Hinge 6

The output compliance matrix of flexure hinge 6 with respect to point “o” caused by F_{ox} , F_{oy} and M_{oz} is expressed as:

$$C_{h6} = \begin{bmatrix} \frac{\partial \Delta x_o^6}{\partial F_{ox}} & \frac{\partial \Delta x_o^6}{\partial F_{oy}} & \frac{\partial \Delta x_o^6}{\partial M_{oz}} \\ \frac{\partial \Delta y_o^6}{\partial F_{ox}} & \frac{\partial \Delta y_o^6}{\partial F_{oy}} & \frac{\partial \Delta y_o^6}{\partial M_{oz}} \\ \frac{\partial \Delta \alpha_o^6}{\partial F_{ox}} & \frac{\partial \Delta \alpha_o^6}{\partial F_{oy}} & \frac{\partial \Delta \alpha_o^6}{\partial M_{oz}} \end{bmatrix} \quad (5.68)$$

The forces and moments acting on Hinge 5 are as follows:

$$F_{6x} = F_{ox} \quad (5.69)$$

$$F_{6y} = F_{oy} \quad (5.70)$$

$$M_{6z} = -l_8 F_{oy} + M_{oz} \quad (5.71)$$

The translational and rotational displacements of Hinge 2 with respect to “o” coordinate frame are defined as:

$$\Delta \alpha_6^6 = \left[\frac{\Delta \alpha_z}{M_z} \right]_6 \cdot M_{6z} + \left[\frac{\Delta \alpha_z}{M_z} \right]_6 \cdot F_{6y} R_6 \quad (5.72)$$

$$\Delta \alpha_o^6 = \Delta \alpha_6^6 \quad (5.73)$$

$$\Delta y_6^6 = \left[\frac{\Delta y}{F_y} \right]_6 \cdot F_{6y} + \left[\frac{\Delta y}{M_z} \right]_6 \cdot M_{6z} R_6 \quad (5.74)$$

$$\Delta y_o^6 = \Delta y_6^6 + l_8 \cdot \Delta \alpha_o^6 \quad (5.75)$$

$$\Delta x_6^6 = \left[\frac{\Delta x}{F_x} \right]_6 \cdot F_{6x} \quad (5.76)$$

$$\Delta x_o^6 = \Delta x_6^6 + \underbrace{[(l_8) - (l_8) \cos \Delta \alpha_o^6]}_{\approx 0} \quad (5.77)$$

The PRR link is composed of two parallel links and a link connected in serial to the parallel link. In order to compute the full $C_{o,Fo}$ compliance matrix we will use the equivalent spring constant calculation method. When the links with hinges are connected in parallel the equivalent compliance is calculated in Eqn. 5.78 and when the links with hinges are connected in serial the equivalent compliance is calculated as:

$$1/C_{eq} = 1/C_1 + 1/C_2 \quad (5.78)$$

$$C_{eq} = C_1 + C_2 \quad (5.79)$$

According to the calculation of equivalent compliances, first, the equivalent compliance of the prismatic joint is calculated. As it is shown in Figure 5.1, hinge 1's, hinge 2's, hinge 3's and hinge 4's assigned coordinates frames are rotated around 90° from the O coordinate frame so that C_{h1} , C_{h2} , C_{h3} and C_{h4} compliance matrices should be rotated by 90° before calculations. The transformation matrix is T_1 shown in Eqn. 5.80, and the rotated compliances are calculated as follows:

$$T_1 = \begin{bmatrix} \cos(\pi/2) & -\sin(\pi/2) & 0 \\ \sin(\pi/2) & \cos(\pi/2) & 0 \\ 0 & 0 & 1 \end{bmatrix} \quad (5.80)$$

$$C'_{h1} = T_1 \cdot C_{h1} \quad (5.81)$$

$$C'_{h2} = T_1 \cdot C_{h2} \quad (5.82)$$

$$C'_{h3} = T_1 \cdot C_{h3} \quad (5.83)$$

$$C'_{h4} = T_1 \cdot C_{h4} \quad (5.84)$$

The links that form the PRR link have the compliances in the following form:

$$C_{L_{1o},F_o} = C'_{h1} + C'_{h2} \quad (5.85)$$

$$C_{L_{2o},F_o} = C'_{h3} + C'_{h4} \quad (5.86)$$

$$C_{L_{3o},F_o} = C_{h5} + C_{h6} \quad (5.87)$$

The prismatic joint's compliance is composed of the links 1 and 2 and they are connected in parallel so the prismatic joint compliance can be expressed as:

$$C_{P_{1o},F_o} = [C_{L_{1o},F_o}^{-1} + C_{L_{2o},F_o}^{-1}]^{-1} \quad (5.88)$$

The prismatic joint and the third link, which is composed of flexure hinges 5 and 6, are connected in series as shown in Figure 5.1 so the compliance that relates the output forces/moments and output displacements of a PRR link becomes:

$$C_{T_1,F_o} = C_{P_{1o},F_o} + C_{L_{3o},F_o} \quad (5.89)$$

The other two PRR links are the rotated version of calculated PRR link of 120° and -120°. The compliances of the other PRR links can be calculated by using T_2 and T_3 transformation matrices as follows:

$$T_2 = \begin{bmatrix} \cos(2\pi/3) & -\sin(2\pi/3) & 0 \\ \sin(2\pi/3) & \cos(2\pi/3) & 0 \\ 0 & 0 & 1 \end{bmatrix} \quad (5.90)$$

$$T_3 = \begin{bmatrix} \cos(-2\pi/3) & -\sin(-2\pi/3) & 0 \\ \sin(-2\pi/3) & \cos(-2\pi/3) & 0 \\ 0 & 0 & 1 \end{bmatrix} \quad (5.91)$$

The displacements at point "o" caused by the two PRR links can be calculated as:

$$U_{T_2, F_0} = \underbrace{T_2 C_{T_1, F_0} T_2^T}_{C_{T_2, F_0}} F_0 \quad (5.92)$$

$$U_{T_3, F_0} = \underbrace{T_3 C_{T_1, F_0} T_3^T}_{C_{T_3, F_0}} F_0 \quad (5.93)$$

$$C_{T_2, F_0} = T_2 C_{T_1, F_0} T_2^T \quad (5.94)$$

$$C_{T_3, F_0} = T_3 C_{T_1, F_0} T_3^T \quad (5.95)$$

The three PRR links are connected in parallel. The compliance matrix C_{o, F_0} is calculated by the equivalent compliance rule as:

$$C_{o, F_0} = (C_{T_1, F_0}^{-1} + C_{T_2, F_0}^{-1} + C_{T_3, F_0}^{-1})^{-1} \quad (5.96)$$

By using C_{o, F_0} compliance matrix and applied output forces/moments we can easily find the output displacements of the stage as:

$$\begin{bmatrix} \Delta x_o \\ \Delta y_o \\ \Delta \alpha_o \end{bmatrix} = C_{o, F_0} \begin{bmatrix} F_{ox} \\ F_{oy} \\ M_{oz} \end{bmatrix} \quad (5.97)$$

5.1.2 Derivation of $C_{o, F_{in}}$ and C_{in, F_0}

The compliance matrix gives us the relationship between the output displacements of point ‘‘o’’ and the input forces F_{1in} , F_{2in} and F_{3in} actuated by the piezo actuators. The compliance matrix is calculated with the same method used for C_{o, F_0} compliance. The first PRR link’s $C_{o, F_{in}}$ and C_{in, F_0} compliance will be found and the other two PRR links will be calculated by using the transformation matrices. Finally, using equivalent compliance method $C_{o, F_{in}}$ and C_{in, F_0} compliance matrices of the 3PRR mechanism will be found [61].

The input forces are acting on the prismatic joints of PRR links so Hinges 1, 2, 3 and 4 will be taken into account for the computation.

Hinge 1

$$C_{H1, F_0} = \begin{bmatrix} \frac{\partial \Delta x_o^1}{\partial F_{1in}} & \frac{\partial \Delta y_o^1}{\partial F_{1in}} & \frac{\partial \Delta \alpha_o^1}{\partial F_{1in}} \end{bmatrix}^T \quad (5.98)$$

Calculating the compliances $\partial \Delta x_o^1 / \partial F_{1in}$, $\partial \Delta y_o^1 / \partial F_{1in}$ and $\partial \Delta \alpha_o^1 / \partial F_{1in}$ are calculated by using the defined acting forces on the hinge 1 and the displacements defined by the forces as:

$$\frac{\partial \Delta \alpha_o^1}{\partial F_{1in}} = \begin{bmatrix} \Delta \alpha_z \\ M_z \end{bmatrix}_1 \cdot \left(\frac{l_3}{2} + 2R_2 + l_2 + R_1 \right) \quad (5.99)$$

$$\begin{aligned} \frac{\partial \Delta y_0^1}{\partial F_{1in}} &= \left[\frac{\Delta y}{F_y} \right]_1 + \left[\frac{\Delta \alpha_z}{M_z} \right]_1 \cdot \left(\frac{l_3}{2} + 2R_2 + l_2 \right) R_1 \\ &+ \left[\frac{\Delta \alpha_z}{M_z} \right]_1 \cdot A \left(\frac{l_3}{2} + 2R_2 + l_2 + R_1 \right) \end{aligned} \quad (5.100)$$

$$\frac{\partial \Delta x_0^1}{\partial F_{1in}} = 0 \quad (5.101)$$

Hinge 2

$$C_{H2_0, F_0} = \left[\frac{\partial \Delta x_0^2}{\partial F_{1in}} \quad \frac{\partial \Delta y_0^2}{\partial F_{1in}} \quad \frac{\partial \Delta \alpha_0^2}{\partial F_{1in}} \right]^T \quad (5.102)$$

Calculating the compliances $\partial \Delta x_0^2 / \partial F_{1in}$, $\partial \Delta y_0^2 / \partial F_{1in}$ and $\partial \Delta \alpha_0^2 / \partial F_{1in}$ are calculated by using the defined acting forces on the hinge 2 and the displacements defined by the forces as:

$$\frac{\partial \Delta \alpha_0^2}{\partial F_{1in}} = \left[\frac{\Delta \alpha_z}{M_z} \right]_2 \cdot \left(\frac{l_3}{2} + R_2 \right) \quad (5.103)$$

$$\frac{\partial \Delta y_0^2}{\partial F_{1in}} = \left[\frac{\Delta y}{F_y} \right]_2 + \left[\frac{\Delta \alpha_z}{M_z} \right]_2 \cdot \left(\frac{l_3}{2} \right) R_2 + \left[\frac{\Delta \alpha_z}{M_z} \right]_2 \cdot (l_3 + l_4) \left(\frac{l_3}{2} + R_2 \right) \quad (5.104)$$

$$\frac{\partial \Delta x_0^2}{\partial F_{1in}} = 0 \quad (5.105)$$

Hinge 3

$$C_{H3_0, F_0} = \left[\frac{\partial \Delta x_0^3}{\partial F_{1in}} \quad \frac{\partial \Delta y_0^3}{\partial F_{1in}} \quad \frac{\partial \Delta \alpha_0^3}{\partial F_{1in}} \right]^T \quad (5.106)$$

Calculating the compliances $\partial \Delta x_0^3 / \partial F_{1in}$, $\partial \Delta y_0^3 / \partial F_{1in}$ and $\partial \Delta \alpha_0^3 / \partial F_{1in}$ are calculated by using the defined acting forces on the hinge 3 and the displacements defined by the forces as:

$$\frac{\partial \Delta \alpha_0^3}{\partial F_{1in}} = \left[\frac{\Delta \alpha_z}{M_z} \right]_3 \cdot \left(\left(\frac{l_3}{2} + 2R_4 + l_3 \right) + R_3 \right) \quad (5.107)$$

$$\begin{aligned} \frac{\partial \Delta y_0^3}{\partial F_{1in}} &= \left[\frac{\Delta y}{F_y} \right]_3 + \left[\frac{\Delta \alpha_z}{M_z} \right]_3 \cdot \left(\frac{l_3}{2} + 2R_4 + l_3 \right) R_3 \\ &+ \left[\frac{\Delta \alpha_z}{M_z} \right]_3 \cdot A \left(\left(\frac{l_3}{2} + 2R_4 + l_3 \right) + R_3 \right) \end{aligned} \quad (5.108)$$

$$\frac{\partial \Delta x_0^3}{\partial F_{1in}} = 0 \quad (5.109)$$

Hinge 4

$$C_{H4_o, F_o} = \left[\frac{\partial \Delta x_o^4}{\partial F_{1in}} \quad \frac{\partial \Delta y_o^4}{\partial F_{1in}} \quad \frac{\partial \Delta \alpha_o^4}{\partial F_{1in}} \right]^T \quad (5.110)$$

Calculating the compliances $\partial \Delta x_o^4 / \partial F_{1in}$, $\partial \Delta y_o^4 / \partial F_{1in}$ and $\partial \Delta \alpha_o^4 / \partial F_{1in}$ are calculated by using the defined acting forces on the hinge 4 and the displacements defined by the forces as:

$$\frac{\partial \Delta \alpha_o^4}{\partial F_{1in}} = \left[\frac{\Delta \alpha_z}{M_z} \right]_4 \cdot \left(\frac{l_3}{2} + R_4 \right) \quad (5.111)$$

$$\frac{\partial \Delta y_o^4}{\partial F_{1in}} = \left[\frac{\Delta y}{F_y} \right]_4 + \left[\frac{\Delta \alpha_z}{M_z} \right]_4 \cdot \left(\frac{l_3}{2} \right) R_4 + \left[\frac{\Delta \alpha_z}{M_z} \right]_4 \cdot (l_3 + l_4) \left(\frac{l_3}{2} + R_4 \right) \quad (5.112)$$

$$\frac{\partial \Delta x_o^4}{\partial F_{1in}} = 0 \quad (5.113)$$

If we use the equivalent stiffness rule the links of the prismatic joints will have the compliances as:

$$C_{L_{10}, F_{in}} = C_{H_{10}, F_{in}} + C_{H_{20}, F_{in}} \quad (5.114)$$

$$C_{L_{20}, F_{in}} = C_{H_{30}, F_{in}} + C_{H_{40}, F_{in}} \quad (5.115)$$

$$C_{P_{10}, F_{in}} = \left[C_{L_{10}, F_{in}}^{-1} + C_{L_{20}, F_{in}}^{-1} \right]^{-1} \quad (5.116)$$

The output displacement of the PRR link can be written in terms of input force F_{in} in Eqn. 117 and in terms of output force matrix F_o :

$$U_{P_{10}} = C_{P_{10}, F_{in}} F_{in} \quad (5.117)$$

$$U_{P_{10}} = C_{P_{10}, F_o} F_o \quad (5.118)$$

When F_{in} is the unit force the equivalent output force can be calculated as follows:

$$F_{P_{10}eqv} = inv(C_{P_{10}, F_o}) \cdot C_{P_{10}, F_{in}} \quad (5.119)$$

The $C_{o, F_{1in}}$ compliance caused by F_{1in} from prismatic joint 1 can be calculated as in Eqn. (5.120). Again by using the transformation matrices T2 and T3 that are presented while calculating C_{o, F_o} the $C_{o, F_{1in}}$ and $C_{o, F_{2in}}$ compliances can be calculated as:

$$C_{o, F_{1in}} = C_{o, F_o} \cdot F_{P_{10}eqv} \quad (5.120)$$

$$C_{o, F_{2in}} = T_2 \cdot C_{o, F_{1in}} \quad (5.121)$$

$$C_{o, F_{3in}} = T_3 \cdot C_{o, F_{1in}} \quad (5.122)$$

The full $C_{o, F_{in}}$ compliance matrix of 3PRR compliance stage is given as:

$$C_{o, F_{in}} = \begin{bmatrix} C_{o, F_{1in}} & C_{o, F_{2in}} & C_{o, F_{3in}} \end{bmatrix} \quad (5.123)$$

C_{in,F_o} is the transpose of the $C_{o,Fin}$ so it can be written as:

$$C_{in,F_o} = [C_{o,Fin}]^T \quad (5.124)$$

5.1.3 Derivation of $C_{in,Fin}$

$C_{in,Fin}$ compliance matrix relates the input displacement and the input forces acting on the mechanism and it is in the form of:

$$C_{in,Fin} = [C_{in,F_{1in}} \quad C_{in,F_{2in}} \quad C_{in,F_{3in}}] \quad (5.125)$$

When a unit force is applied the $C_{in,Fin}$ will be equal to the input displacements and F_{1in} will be equal to equivalent output force so it can be written as:

$$C_{in,F_{1in}} = C_{in,F_o} \cdot F_{P_{1oeqv}} \quad (5.126)$$

For the other prismatic joints using transformation matrices the following expressions could be written:

$$C_{in,F_{2in}} = C_{in,F_o} \cdot T_2 \cdot F_{P_{1oeqv}} \quad (5.127)$$

$$C_{in,F_{3in}} = C_{in,F_o} \cdot T_3 \cdot F_{P_{1oeqv}} \quad (5.128)$$

5.1.4 The Jacobian matrix of 3 PRR compliant mechanism:

The Jacobian matrix gives us the relationship between the input displacement and output displacement of the stage and it can be found by using the compliances of the mechanism when there is no external forces, $F_o=0$, as follows:

$$U_{in} = C_{in,Fin} \cdot F_{in} \quad (5.129)$$

$$F_{in} = inv(C_{in,Fin}) \cdot U_{in} \quad (5.130)$$

$$U_o = C_{o,Fin} \cdot F_{in} \quad (5.131)$$

$$U_o = \underbrace{C_{o,Fin} \cdot inv(C_{in,Fin})}_{Jacobian} \cdot U_{in} \quad (5.132)$$

$$J = C_{o,Fin} \cdot inv(C_{in,Fin}) \quad (5.133)$$

5.2 The Results and Comparison with FEA

The in-plane compliances ($\Delta\alpha_z/M_z$, $\Delta y/F_y$ and $\Delta x/F_x$) are calculated by using the material properties and geometric properties of the circular flexure hinges that are

presented in Table 5.1. In Section 4 we have analyzed the methods for finding the best calculation method for the in-plane compliances and the results state that Paros and Weisboard's calculations give the best translational compliance in y direction, $\Delta y/F_y$, and rotational compliance in z direction, $\Delta\alpha_z/M_z$, and finally, the translational compliance in x direction, $\Delta x/F_x$, can be most accurately calculated by the Wu and Lobontiu's method. The compliance results are presented in Table 5.2. All hinges have the same geometric properties ($R_1=R_2=R_3=R_4=R_5=R_6$) so the calculated in-plane compliances for all hinges are also the same. The link lengths of the 3-PRR compliant mechanism are shown in Table 5.3. The kinetostatic compliance method results are presented in Table 5.4.

Table 5.1 Material and Geometric Properties of Circular Flexure Hinges

Radius of Hinges (R) [mm]	Width of the Hinges (b) [mm]	Minimum thickness of the hinges (t) [mm]	Modulus of Elasticity (E) [N/mm ²]	Poisson's ratio (v)
3.6	10	0.8	71.7e3	0.33

Table 5.2 Calculated In-Plane Compliances of Circular Flexure Hinges

$\Delta x/F_x$ [$\mu\text{m}/\text{N}$]	$\Delta y/F_y$ [$\mu\text{m}/\text{N}$]	$\Delta\alpha_z/M_z$ [rad/Nm]
0.006418110	0.9103117	0.06889

Table 5.3 Link Length of 3-PRR Compliant Mechanism

l1 [mm]	l2 [mm]	l3 [mm]	l4 [mm]	l5 [mm]	l6 [mm]	l7 [mm]	l8 [mm]
8	15.6	8	10	18	8	12.6	11.07
A [mm]	B [mm]	C [mm]	D [mm]				
51.87	64.47	46.47	30.87				

Table 5.4 Compliance Results for 3-PRR Compliant Mechanism

Compliances and Jacobian	Results
$C_{o,Fo}$ $[\mu\text{m}/\text{N}, \text{rad}/\text{N}, \mu\text{m}/\text{Nmm}, \mu\text{rad}/\text{Nmm}]$	$\begin{bmatrix} 3.145 & 1.479 & 0 \\ 1.479 & 3.145 & 0 \\ 0 & 0 & 22900 \end{bmatrix}$
$C_{o,Fin}$ $[\mu\text{m}/\text{N}, \mu\text{rad}/\text{N}]$	$\begin{bmatrix} -3.422 & 1.781 & 1.641 \\ 0.081 & 2.923 & -3.004 \\ -217.015 & -217.015 & -217.015 \end{bmatrix}$
$C_{in,Fin}$ $[\mu\text{m}/\text{N}]$	$\begin{bmatrix} 3.093 & -0.0621 & -0.0621 \\ -0.0621 & 3.093 & -0.0621 \\ -0.0621 & -0.0621 & 3.093 \end{bmatrix}$
J	$\begin{bmatrix} -1.103 & 0.574 & 0.529 \\ 0.026 & 0.942 & -0.969 \\ 74.445 & 74.445 & 74.445 \end{bmatrix}$

$C_{o,Fin}$ and Jacobian of the 3-PRR compliant mechanism are the most important results because they can be useful while computing the dynamics and kinematics of the mechanism while providing the position control of the stage. Because of this the kinetostatic method results of $C_{o,Fin}$ compliance and Jacobian of 3-PRR compliant mechanism are compared with the Finite Element Analysis. The procedure of the Finite Element Analysis by using COMSOL Multiphysics 3.5a software has been explained in Section 4. Unit forces have been applied to free 3-PRR compliant mechanism as shown in Figure 5.3. The unit forces F_1 , F_2 and F_3 are applied individually, and the displacement at point C and the rotation of the triangular stage are examined. The displacements at points 1, 2 and 3 have also been measured for the calculating the Jacobian matrix of the stage. The displacement results of FEA and Kinetostatic method are presented in Table 5.5 when unit forces are applied and the Jacobian matrix results are shown in Table 5.6

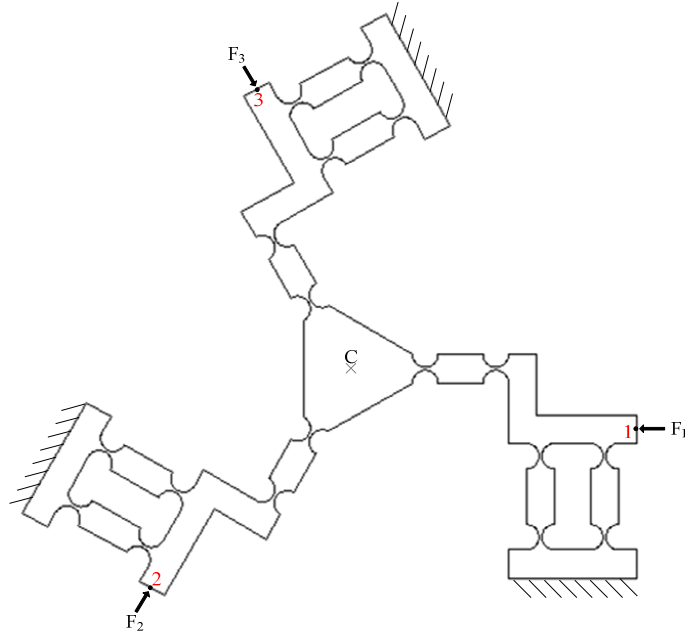


Figure 5.3 Boundary conditions of 3-PRR compliant mechanism for FEA.

Table 5.5 The $C_0 F_{in}$ compliance matrix results of FEA and kinetostatic method

Forces	Finite Element Analysis			Kinetostatic Method		
	Δx_c [μm]	Δy_c [μm]	$\Delta \alpha_c$ [μrad]	Δx_c [μm]	Δy_c [μm]	$\Delta \alpha_c$ [μrad]
$F_1=1$ N	-3.67484	0.065175	-254.5	-3.422	0.081	-217.015
$F_2=1$ N	1.893011	3.150424	-254.5	1.781	2.923	-217.015
$F_3=1$ N	1.781824	-3.21459	-254.5	1.641	-3.004	-217.015

Table 5.6 Jacobian matrix results of FEA and kinetostatic method

Finite Element Analysis Jacobian Matrix	Kinetostatic Method Jacobian Matrix
J_{FEA} $= \begin{bmatrix} -0.97549 & 0.503504 & 0.472986 \\ 0.017035 & 0.836286 & -0.8533 \\ -67.5578 & -67.5578 & -67.5578 \end{bmatrix}$	$J_{Analytical}$ $= \begin{bmatrix} -1.103 & 0.574 & 0.529 \\ 0.026 & 0.942 & -0.969 \\ -74.445 & -74.445 & -74.445 \end{bmatrix}$

The % errors of $C_0 F_{in}$ and Jacobian matrices when compared to the Finite element Analysis are shown in Table 5.7 and Eqn. 5.134, respectively. According to the results the $C_0 F_{in}$ compliance matrix the angular displacement of the stage has the most error which is almost 15% and the error for displacements in x-y axes is between 8-9%

except the displacement in y direction for F_1 . This is because of the small values of displacements in that direction compared to the other directions as shown in Table 5.5. The Jacobian error is greater than $C_{o,Fin}$, which is expected because it is composed of $C_{in,Fin}$ and $C_{o,Fin}$ compliances. This means that we also have errors while calculating $C_{in,Fin}$ compared to FEA results. The huge error at the 2nd row 1st column of $J_{\%error}$ has the same reason of F_1 force direction which provides smaller displacement when compared with the other directions.

Table 5.7 % errors of computed $C_{o,Fin}$

Forces	% error Δx_c	% error Δy_c [μm]	%error $\Delta \alpha_c$
$F_1=1$ N	6.875	24.488	14.728
$F_2=1$ N	5.898	7.214	14.728
$F_3=1$ N	7.913	6.542	14.728

$$J_{\%error} = \begin{bmatrix} -13.115 & -14.074 & -11.855 \\ -53.57 & -12.703 & -13.522 \\ -10.193 & -10.193 & -10.193 \end{bmatrix} \quad (5.134)$$

The errors are identical when we look at our error results while computing the in-plane compliances of the flexure hinges which are presented in Table 3.3. With this technique we do not calculate the bending effects of the links connected to the flexure hinges, which are also calculated with Finite element analysis.

5.3 Dynamics of the Compliant Mechanisms

3-PRR mechanism decouples the stiffness between the actuators and the output motion of the end-effector, which is the center of the triangular stage. Therefore, we can have three independent single input (F_i) single output (u_i) systems, which will ease the computation of controlling the system. As shown in Figure 5.4 we have used the mass-spring model for calculating the dynamics of the mechanism in each actuation direction u_1 , u_2 and u_3 .

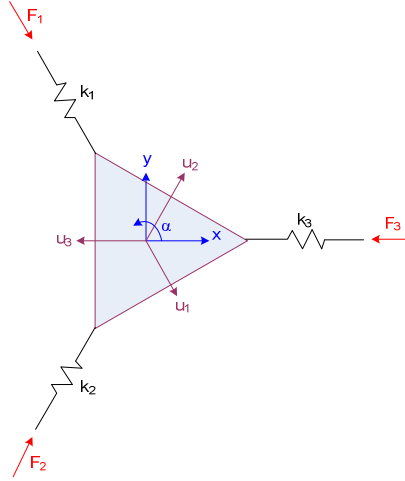


Figure 5.4 The mass-spring model of compliant mechanism.

We can simply write the dynamics of the three mass-spring systems, which generates the dynamics of the 3-PRR compliant mechanism by using the $C_{o,F_{in}}$ and Jacobian matrices calculated with kinetostatic modeling technique. The mass-spring model for each direction can be written as follows

$$M_i \ddot{u}_i + K_i u_i = F_i \quad (5.134)$$

M_i is the mass matrix, K_i is the stiffness matrix, and F_i is the force matrix where $i=1,2$ and 3 represent each actuation direction. By using the compliance $C_{o,F_{in}}$ and Jacobian matrices we can compute the stiffness matrix K_i . $C_{o,F_{in}}$ compliance matrix relates the input forces to the output displacements Δx , Δy and $\Delta \alpha$. The inverse of computed Jacobian matrix, \mathbf{J} , can be used for transforming the output displacements to the displacements in actuation directions which are u_1 , u_2 and u_3 . The corresponding scheme is given as:

$$\begin{bmatrix} \Delta x \\ \Delta y \\ \Delta \alpha \end{bmatrix} = C_{o,F_{in}} \cdot \begin{bmatrix} F_1 \\ F_2 \\ F_3 \end{bmatrix} \quad (5.135)$$

$$\begin{bmatrix} F_1 \\ F_2 \\ F_3 \end{bmatrix} = C_{o,F_{in}}^{-1} \cdot \begin{bmatrix} \Delta x \\ \Delta y \\ \Delta \alpha \end{bmatrix} \quad (5.136)$$

$$\begin{bmatrix} \Delta x \\ \Delta y \\ \Delta \alpha \end{bmatrix} = \mathbf{J} \cdot \begin{bmatrix} u_1 \\ u_2 \\ u_3 \end{bmatrix} \quad (5.137)$$

$$\begin{bmatrix} F_1 \\ F_2 \\ F_3 \end{bmatrix} = \underbrace{C_{o,F_{in}}^{-1} \cdot \mathbf{J}}_K \cdot \begin{bmatrix} u_1 \\ u_2 \\ u_3 \end{bmatrix} \quad (5.138)$$

By reorganizing the mass-spring systems, the dynamics of the mechanism can be written as in eqn. (5.139)

$$\begin{bmatrix} m & 0 & 0 \\ 0 & m & 0 \\ 0 & 0 & m \end{bmatrix} \cdot \begin{bmatrix} \ddot{u}_1 \\ \ddot{u}_2 \\ \ddot{u}_3 \end{bmatrix} + \mathbf{C}_{o,F_{in}}^{-1} \cdot \mathbf{J} \cdot \begin{bmatrix} u_1 \\ u_2 \\ u_3 \end{bmatrix} = \begin{bmatrix} F_1 \\ F_2 \\ F_3 \end{bmatrix} \quad (5.139)$$

The mass matrix \mathbf{M} for 3-PRR compliant mechanism is given as:

$$\mathbf{M} = \begin{bmatrix} 0.05 & 0 & 0 \\ 0 & 0.05 & 0 \\ 0 & 0 & 0.05 \end{bmatrix} [\text{kg}] \quad (5.140)$$

The computed \mathbf{K} matrix for our 3-PRR compliant mechanism becomes:

$$\mathbf{K} = \begin{bmatrix} 0.1 & -0.22 & -0.22 \\ -0.22 & 0.1 & -0.22 \\ -0.22 & -0.22 & 0.1 \end{bmatrix} [\text{N}/\mu\text{m}] \quad (5.141)$$

The mode equation of the mechanism based on the vibration theory can be written as:

$$(\mathbf{K} - \omega_j^2 \mathbf{M}) \Phi_j = 0 \quad (5.142)$$

Where Φ_j is the eigenvector representing the mode shapes and j representing the mode numbers. ω_j^2 describes the corresponding natural cyclic frequency, and it can be obtained by solving the characteristic equation as follows:

$$|\mathbf{K} - \omega_j^2 \mathbf{M}| = 0 \quad (5.143)$$

If we define an \mathbf{A} matrix as in Eqn. 5.144 we find the ω_j^2 by calculating the eigenvalues of matrix \mathbf{A} . From the relation $\omega = 2\pi f$ we can calculate the natural frequencies as:

$$\mathbf{A} = \mathbf{M}^{-1} \mathbf{K} \quad (5.144)$$

$$\omega_j^2 = \text{eig}(\mathbf{A}) \quad (5.145)$$

$$f_j = \frac{\omega_j}{2\pi} \quad (5.146)$$

We have calculated the first mode natural frequency of the 3-PRR compliant mechanism as 404 Hz, while The FEA result was 367.9 Hz resulting a difference of 9.8% for calculating the natural frequency of the mechanism by using the compliance and jacobian matrices that we have calculated from Kinetostatic Method.

5.4 Conclusion and Comments

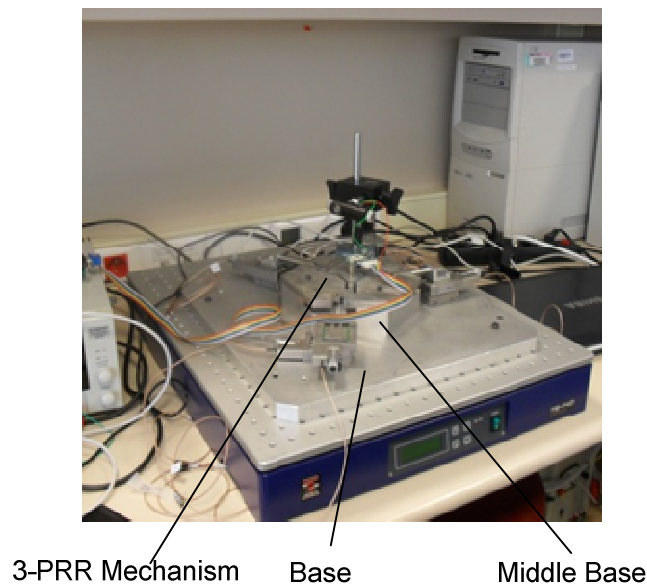
Kinetostatic method, which combines the kinematics and static of the compliant mechanisms has been used to provide an easier and faster calculation method compared to Finite Element Analysis. We have applied this method only for our 3-PRR compliant mechanism because this method has been applied in previous studies on 3-RRR compliant mechanism with different links configuration. The method depends on the compliance calculations as we have analyzed in the previous section. We have compared the $C_{o,Fin}$ matrix results with Finite Element Analysis the angular displacement of the stage has the largest error which is almost 15% and the error for displacements in x-y axes is between 8-9%. In the Jacobian matrix errors are between almost 13-15%. The errors are because of the compliance calculation errors that we have seen in Section 4 and we have taken the links as rigid ones, whereas in FEA the links also bending effects are taken into consideration. After by using $C_{o,Fin}$ compliance matrix and Jacobian matrix we have defined mass-spring systems for each actuation direction. We have calculated the stiffness matrix and finally we obtained the natural frequency of the mechanism, which is close to Finite Element Analysis results with the error of 9.8%. We can conclude that the Kinetostatic model should be improved to be used instead of FEA while designing. The bending effects of the links can be taken into account to improve the results.

6 EXPERIMENTAL SETUP AND PERFORMANCE RESULTS

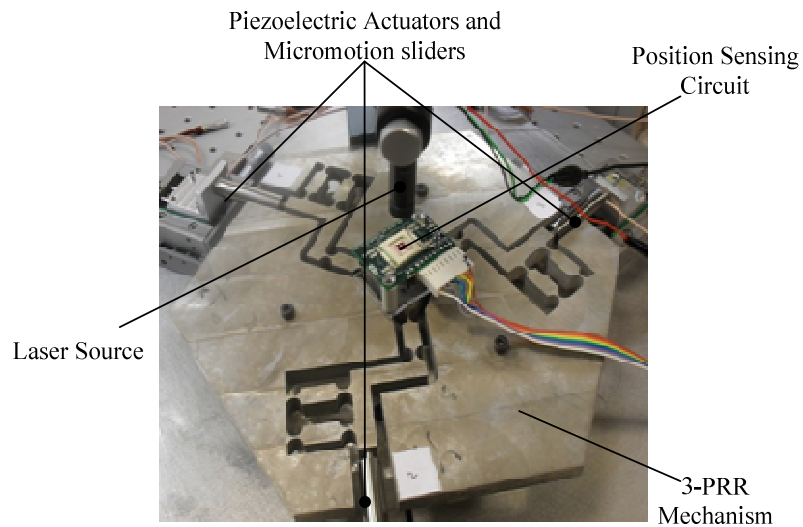
This section presents the experimental setup that is built for our 3-RRR and 3-PRR compliant micropositioning stages. The parts that are designed for assembling the piezoelectric actuators and the measurement system with the stages are explained in detail. The results of the performances of these stages are also examined by comparing the FEA and Kinetostatic modeling results to each other.

6.1 The Experimental Setup

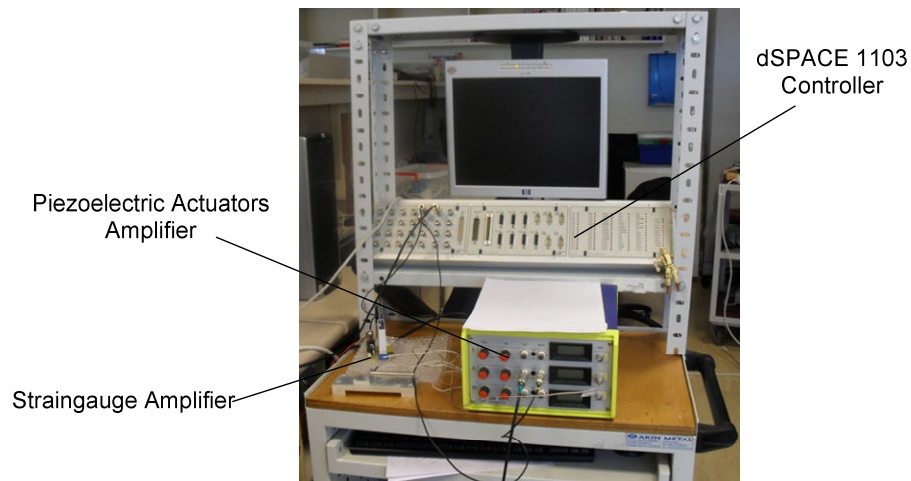
The experimental setup shown in Figure 6.1 is composed of mechanical parts and electronic equipments. The designed mechanical parts are the mechanisms, three piezoelectric actuators, a base table, three sliding stages with micrometers, a laser position sensor and a middle base. The electronic equipments are dSPACE 1103 controller, piezoelectric actuators amplifier, the stain gauge amplifier and the electronic circuit of laser positioning sensing diode.



(a)



(b)



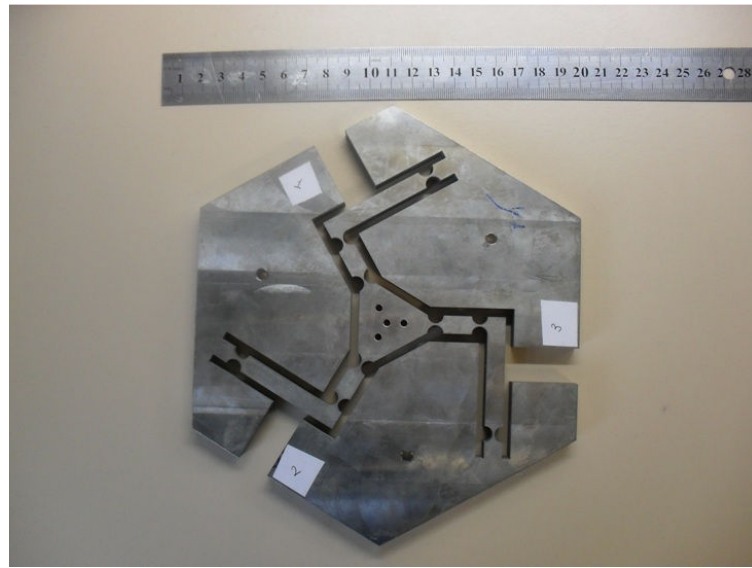
(c)

Figure 6.1 Full experimental setup photos.

6.1.1 Manufactured Compliant Mechanisms

Designed 3-RRR and 3-PRR compliant micropositioning stages are manufactured by using Wire Electrical Discharge Machining (Wire EDM) technique which uses electrical discharges to cut the desired shape from the material. The electrical discharge is created between an electrode and the workpiece. While spark is jumping across the gap between the electrode and the workpiece, the material is removed and the desired 2D shape is cut. The accuracy of this machining technique is high when compared to CNC machining and other traditional machining techniques. This process can also make sharp inside corners and thin walls. Because of these advantages, Wire EDM is a

common technique for manufacturing compliant mechanisms. Manufactured 3-RRR and 3-PRR compliant mechanisms are shown respectively in Figures 6.2a and b.



(a) 3-RRR compliant mechanism



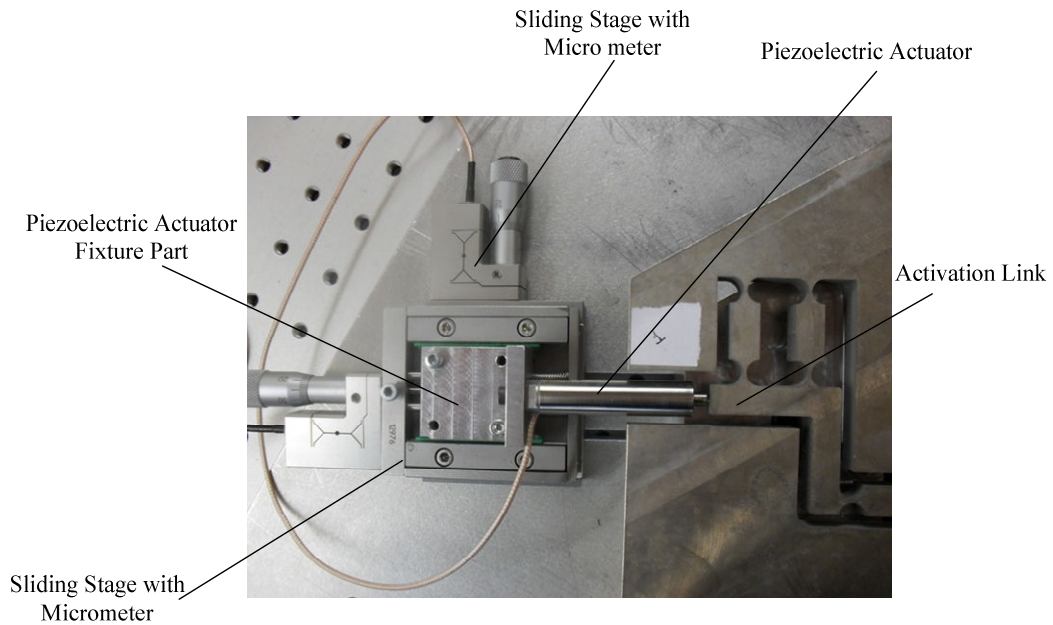
(b) 3-PRR compliant mechanism

Figure 6.2 Manufactured compliant mechanisms using wire EDM.

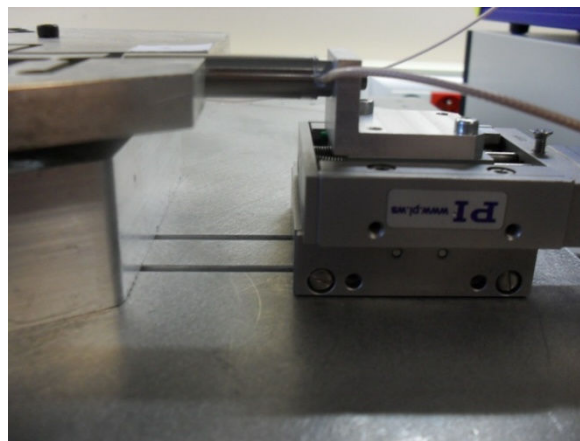
6.1.2 Designed and Manufactured Other Mechanical Parts

We have three kinds of piezoelectric actuators with different lengths available to be used as actuators with our designed compliant mechanisms. Thus our setup should give us the flexibility of changing the compliant mechanisms and the piezoelectric actuators. Therefore, PI's M-332 miniature translation stages with P-853 piezoelectric micrometer drives are used for positioning and preloading the piezoelectric actuators

with different sizes. These miniature translation stages allow positioning manually by using its micrometer drive with a range of 18 mm. A piezoelectric actuator fixing part is designed to assemble on top of the stages and 6 stages are put in such a way that (shown in Figure 6.3) the condition of the piezoelectric actuators can be adjusted in x and y directions according to the activation link of the mechanisms so that we can drive the flexible joints correctly and preload the mechanism. Thus, each activation link has 2 stages in x and y directions and an actuator fixing part at the top of the stages.



(a)



(b)

Figure 6.3 Miniature translation stages for piezoelectric actuator positioning.

The lengths of our piezoelectric actuators are 19 mm, 46 mm and 64 mm. The ranges of the translation stages are not enough, a base stage for fixing the translational stage according to the piezoelectric actuators that we can use is designed by drilling key holes as shown in Figure 6.4a which enables positioning of the translational stages as shown in Figure 6.4b. Necessary holes are also drilled for fixing the base on top of the vibration isolation table and assemble of the stage fixture base. A middle base in Figure 6.4c is designed for assembling the compliant mechanism as shown in Figure 6.4d.

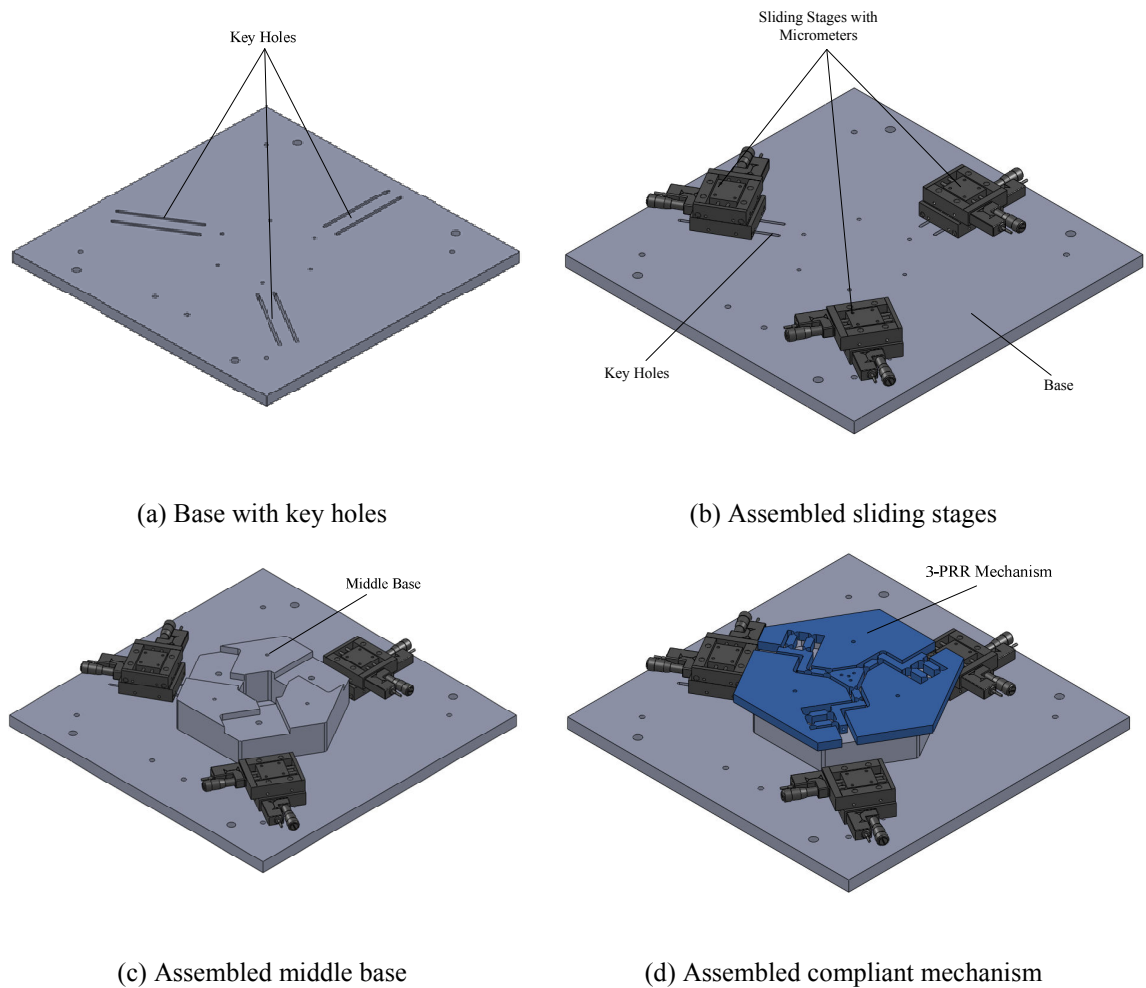
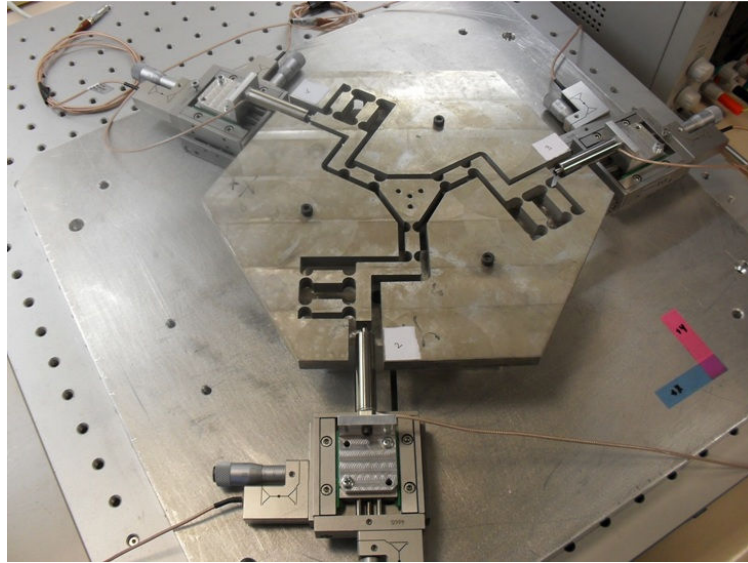
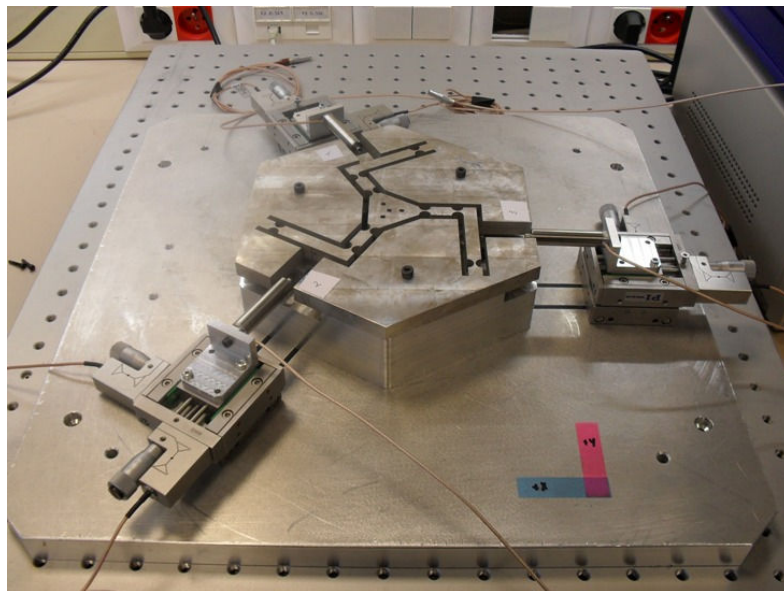


Figure 6.4 Designed parts for the assembly of the setup.

All these necessary parts are manufactured by CNC milling technique, and Aluminum 7075 is used as substrate material. The assembled setup with 3-PRR compliant stage is presented in Figure 6.5a and by adjusting the translation sliding stages manually 3-RRR compliant stage is assembled as shown in Figure 6.5b.



(a) 3-PRR Compliant Mechanism



(b) 3-RRR Compliant Mechanism

Figure 6.5 Assembling of manufactured parts of experimental setup.

A part for measurement has also been designed as shown in Figure 6.6 to assemble the dual position sensing diode on a PCB that will be presented in the next section. The part is designed in such a way that the optical center of the board coincides with the triangular center of the stages. The used material is plexiglass.

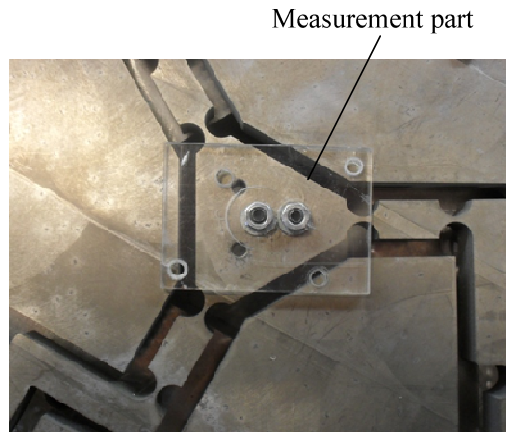


Figure 6.6 Measurement part.

6.1.3 Piezoelectric Actuators

The piezoelectric actuators (Figure 6.7) are Piezomechanik's low voltage actuators with preloading casings. Maximum force generation of these piezoelectric actuators is 800 N. The types of actuators, their properties in the datasheets and the ones having strain gauge embedded to measure the displacements are presented in Table 6.1. The piezoelectric actuators have semibipolar -30 V/ +150 V activation and unipolar 0 V/+150V activation. The first max. stroke value is for semibipolar activation, and the second max. stroke value is for unipolar activation. In our experiments unipolar activation has been used by limiting the voltage input to the actuator.

Table 6.1 Piezoelectric Actuator Datasheet Properties

Type	Max. Stroke [μm]	Length [mm]	Capacitance [nF]	Stiffness [N/ μm]	Resonance frequency [kHz]	Measurement
PSt 150/5/7 VS10	13/9	19	350	50	40	Yes
PSt 150/5/40 VS10	55/40	46	1600	12	20	No
PSt 150/5/60 VS10	80/60	64	2400	8	15	Yes

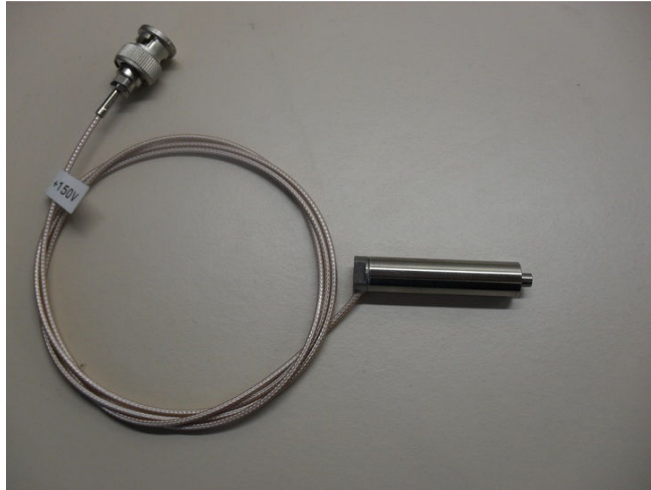


Figure 6.7 Piezoelectric actuator.

6.1.4 Measurements, Amplifiers and Control Unit

The position measurement of the compliant mechanism is performed by using a laser source and Silicon Sensor's DL16 dual position sensing diode on 7PCBA3 PCB board. The PSD and the PCB board are assembled as shown in Figure 6.8. The position sensing diode has a 4 mm x 4 mm and 16 mm² active area. The resolution the PSD is 0.06 μm with a spot diameter of 0.5 mm. The PCB has sum and difference amplifiers to provide the bipolar analog voltage outputs, which are taken for the X and Y position of the light spot coming from the laser source on the diode.

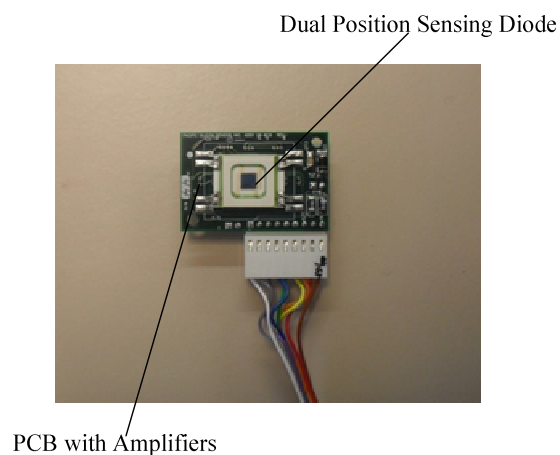


Figure 6.8 Dual position sensor on PCB.

The dual position measurement sensor is mounted as shown in Figure 6.9a on the triangular stage of the compliant mechanisms by using the designed part as explained

earlier (Figure 6.6). The laser source is mounted on the top of the mechanism as presented in Figure 6.9b by using holders.

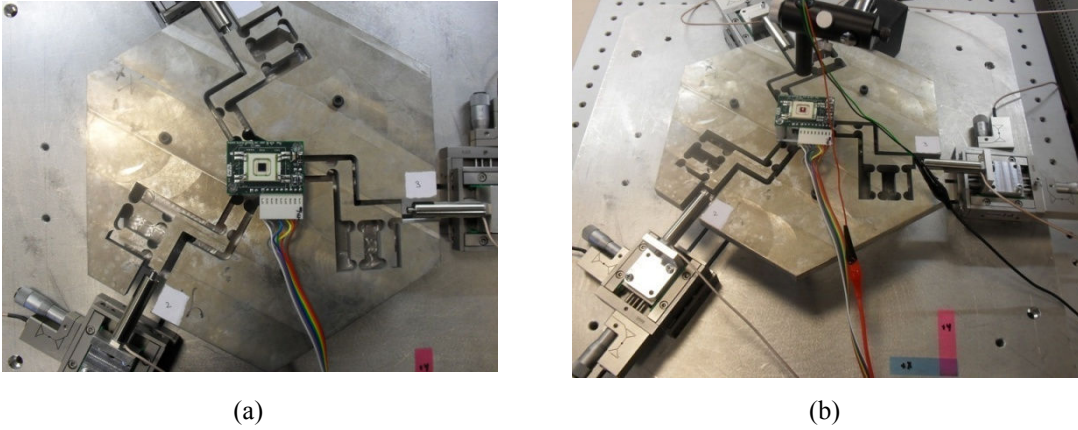


Figure 6.9 Mounted dual position measurement with laser source.

Before taking measurements from the center of the compliant stages we have built a small setup shown in Figure 6.10 to find a conversion between the displacement values and the output voltages. Firstly we have designed a butterworth filter having two degrees in denominator and zero degree in the numerator. The sample time of running the laser sensor is 10^{-4} s so the sample frequency f_s is 10^4 Hz and the cut off frequency f_c is taken as 20 Hz. The natural frequency will be calculated as:

$$\omega_n = 2 \frac{f}{f_s} \Rightarrow \omega_n = 2000 \quad (6.1)$$

The general filter transfer function in z domain is:

$$\frac{Y(z)}{U(z)} = \frac{b_0 + b_1z^{-1} + b_2z^{-2} + \dots + b_nz^{-n}}{1 + a_1z^{-1} + a_2z^{-2} + \dots + a_mz^{-m}} \quad (6.2)$$

We have taken $n=0$ and $m=2$ and calculated b and a values by using *maxflat* function in MATLAB as:

$$b_0 = 3.930e-5$$

$$a_1 = -1.991$$

$$a_2 = 9.912e-1$$

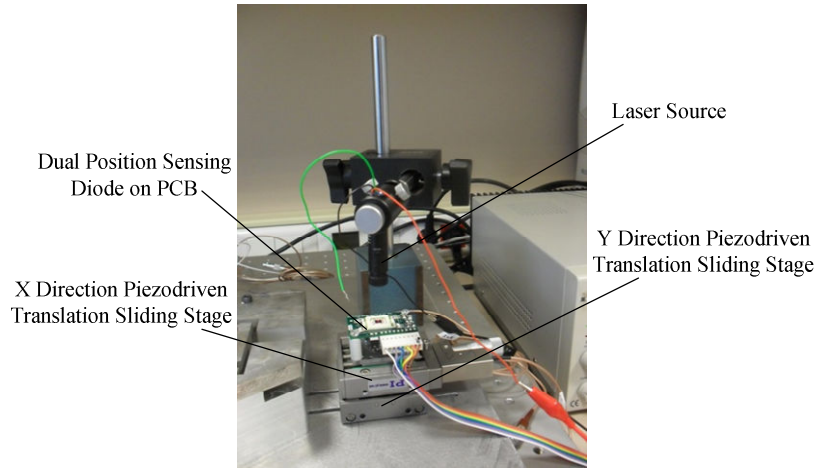


Figure 6.10 Laser calibration setup.

After designing a filter for the output of our measurements the stages are driven manually, and PI's piezoelectric actuator P-854 is used for finding a conversion number between the output voltage and displacement. 500 μm , 1000 μm and 1500 μm displacement are manually provided for both X and Y axes. Also, using the amplifier the piezoelectric actuators are actuated to have 25 μm displacement in X and Y directions. We have repeated these experiments many times. When Y sample stage's piezoelectric actuator has its maximum stroke of 25 μm the example graph for Y voltage output shown in Figure 6.11a, and the X output voltage shown in Figure 6.11b. The difference voltage for the y 25 μm motion corresponds to 0.00176 V output. Thus, the sensor will have conversion of $1.4239\text{e}+4$ $\mu\text{m}/\text{V}$. We have used this conversion number for our compliant mechanisms triangular stage center displacement measurements.

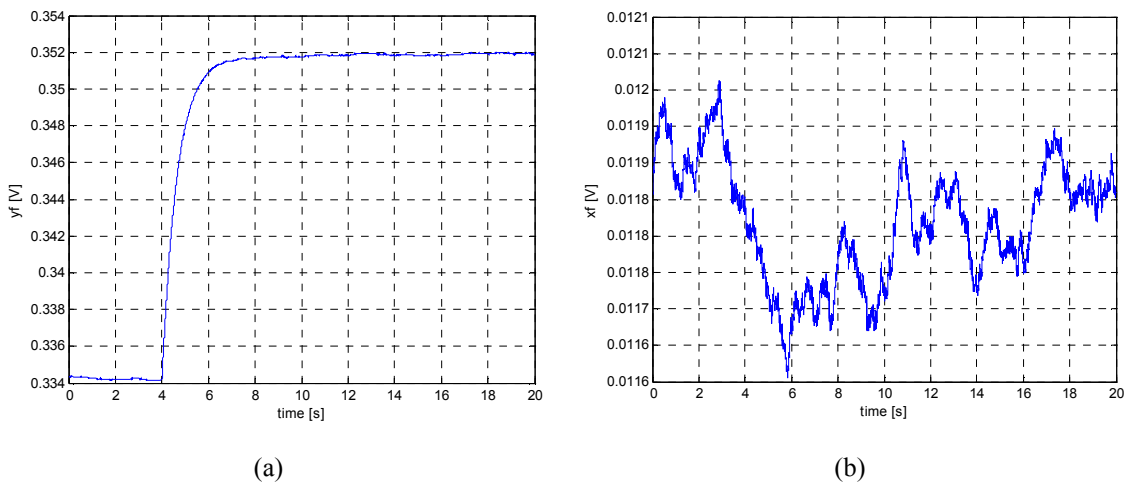
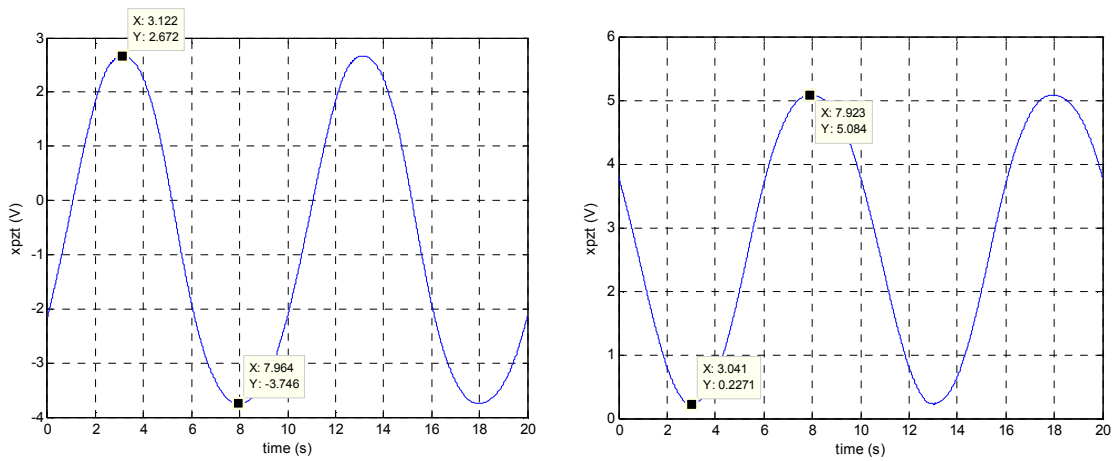


Figure 6.11 (a) Filtered output Y voltage, (b) Filtered output X voltage.

Piezomechanik's analog amplifier SVR 150/3 is used for actuating the piezoelectric actuators. The amplifier allows semibipolar -30 V / 150 V actuation by amplifying the input voltage coming from the controller, and it has 3 independent channels that allows us to amplify 3 piezoelectric actuators at the same time. The maximum amplifying gain is 30.

Dataforth's SCM5B38-05D strain gauge input module is used for half bridge circuit of the strain gauge to amplify and measure the output voltage. The signal conditioning product has the input range of -20mV to +20mV, and its sensitivity is 2mV/V, while its output range is -10V to +10V. A conversion parameter between the strain gauge output voltage and the displacement of the piezoelectric actuator is found by giving the maximum stroke for PST 150/5/80 VS10 type piezoelectric actuator. The piezoelectric actuator is both driven by unipolar and bipolar actuation. Figure 6.12a shows the output voltage for max. unipolar actuation. The difference between the max and min values of the strain gauge output is 6.412V. The max stroke for the bipolar actuation is 80 μm . Thus, for 1 μm actuation 80.015 mV is the output voltage. The conversion value from voltage to displacement is 12.477 $\mu\text{m}/\text{V}$. Figure 6.12b shows the output voltage for max. bipolar actuation. The difference between the min and max output voltage values taken from the strain gauge circuit is 4.857 V. The max stroke for the unipolar actuation is 60 μm . Thus, 1 μm displacement corresponds to 80.955 mV output voltage. The conversion value from voltage to displacement is 12.353 $\mu\text{m}/\text{V}$.



(a) Max. bipolar actuation of PEA

(b) Max. unipolar actuation of PEA

Figure 6.12 Strain gauge amplifier output voltages of PEA.

The controller board that is used for controlling and doing the experiments is dSPACE DS1103 controller board. ControlDesk software environment which allows C language is used for coding. The connections of dSPACE are shown in Figure 6.13. The measurement outputs from strain gauge amplifiers or dual positioning sensors are connected to dSPACE by using analog-to-digital connections (ADCs), and the necessary outputs coming from the dSPACE to the piezoelectric actuator amplifiers inputs are through digital-to-analog connections (DACs).

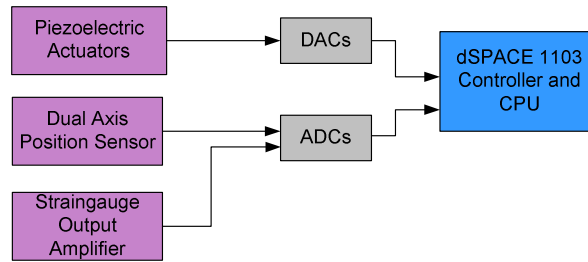


Figure 6.13 Connections of dSPACE with measurements and amplifiers.

6.2 3-RRR Performance Results

The experiments are performed for 3-RRR Compliant micromotion stage by actuating the piezoelectric actuators and examining the end-effector motion, which is measured by the dual position sensing detector. The used piezoelectric actuator is PSt 150/5/40 having 40 μm maximum stroke with unipolar actuation. The direction of the u_1 , u_2 and u_3 vectors shown in Figure 6.14 and the workspace of the 3-RRR compliant mechanism are determined. As in the finite element analysis the experiments are done in two ways. Firstly, only the actuators in action are assembled to the stage. Secondly, all actuators are assembled to the stage even though they are not actuated all the time.

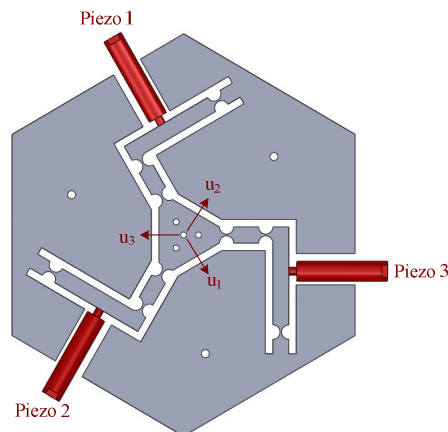
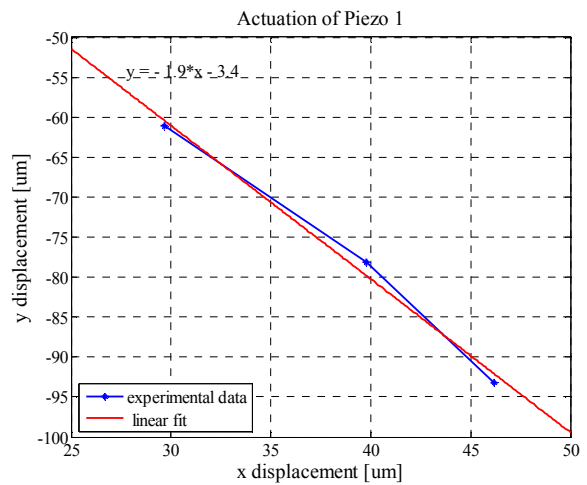
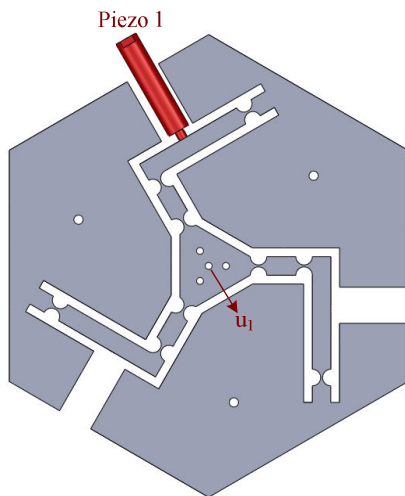
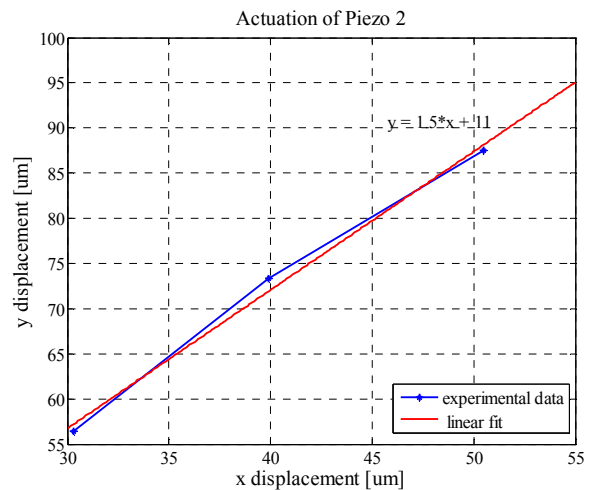
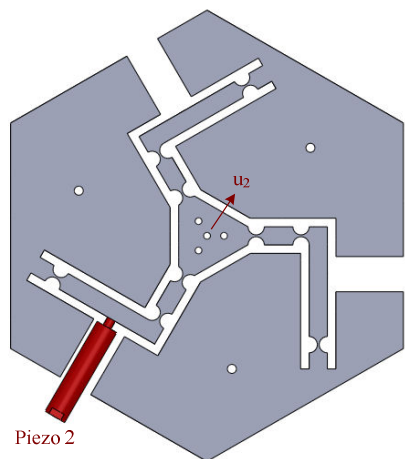


Figure 6.14 Motion vectors of PEAs in 3-RRR compliant mechanism.

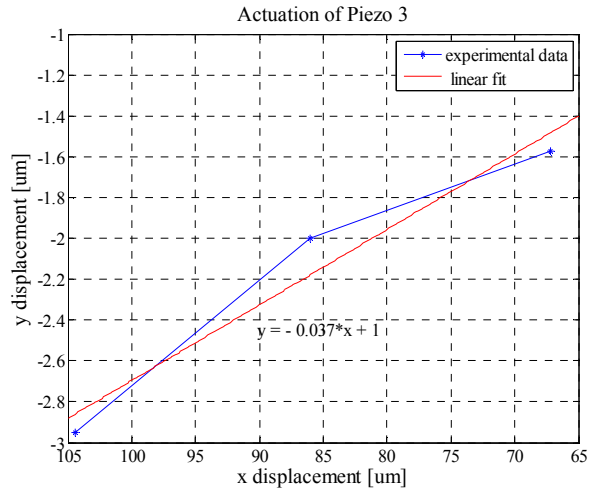
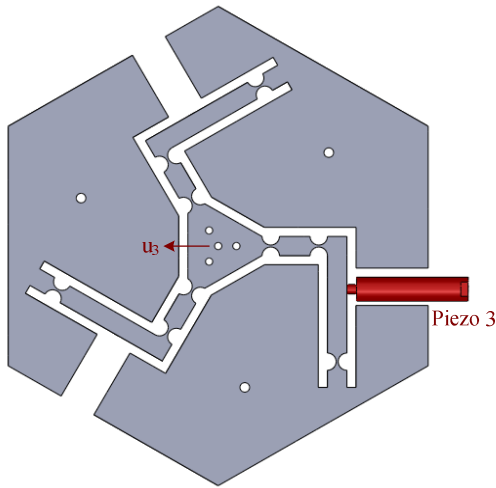
Piezo 1 is actuated while other piezoelectric actuators are not connected to the mechanism. Respectively 90 V, 120 V and 150 V are supplied to the piezoelectric actuator, and the end-effector motion in X and Y axis is shown in Figure 6.15a. After that only Piezo 2 is actuated with the same amount of voltages, the results are presented in Figure 6.15b. Lastly, Piezo 3 is actuated in the same way. The results of Piezo 3 are shown in Figure 6.15c. In micropositioning of flexure based mechanism the small displacements are almost linear so a linear curve is fit for the results to estimate the direction of the vectors. According to the slope of the motion vector u_1 has a slope of -62.493° , u_2 has a slope of 56.88° , and u_3 has a slope of 2.117° with X axis.



(a)



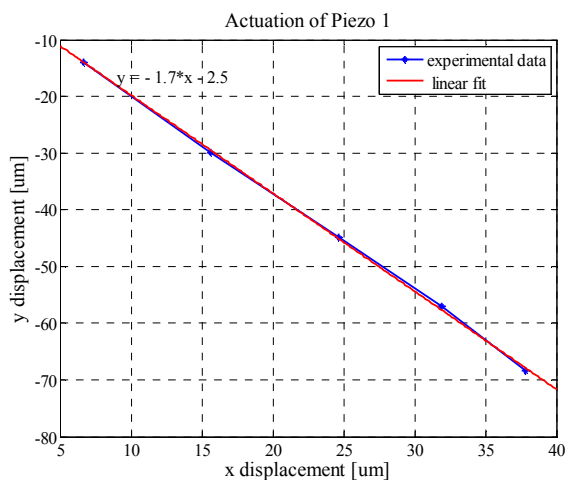
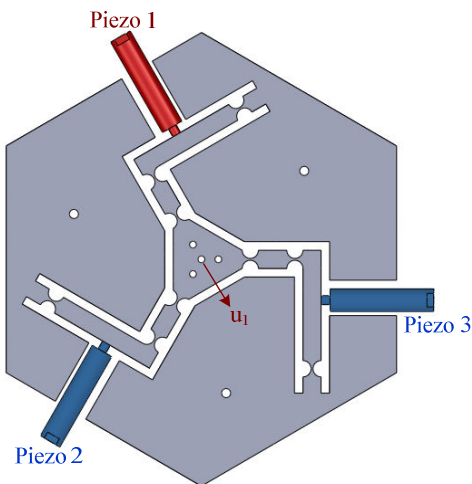
(b)



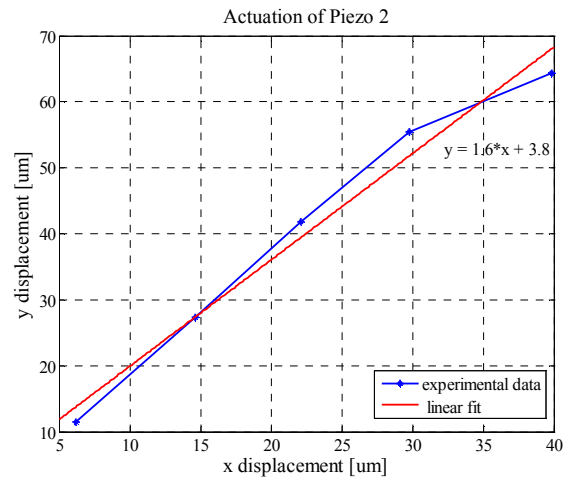
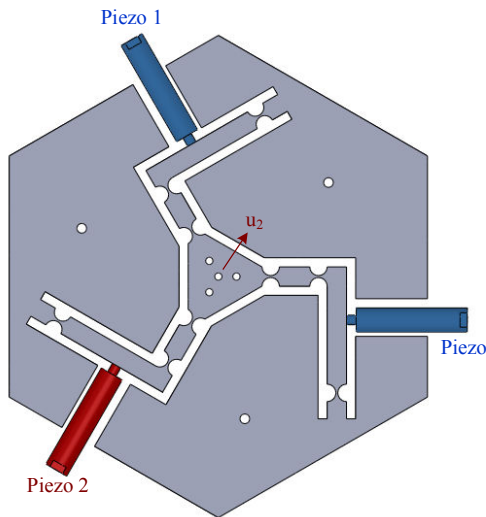
(c)

Figure 6.15 3-RRR compliant mechanism experiment displacement results when only 1 PEA is assembled.

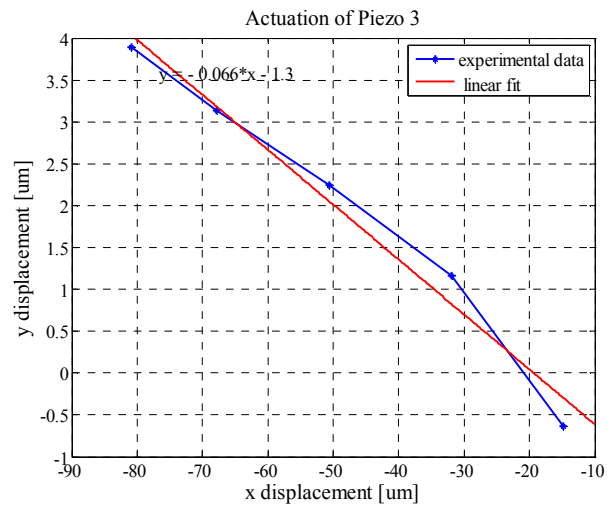
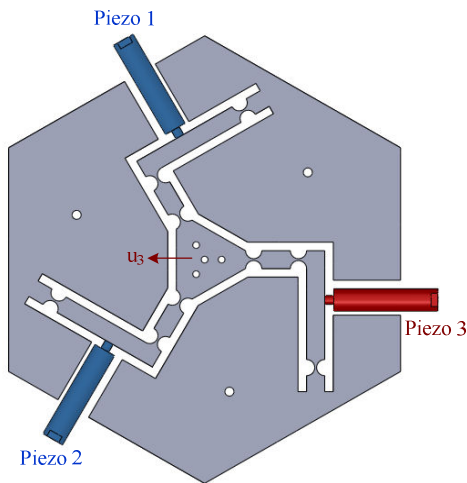
The same experiments are performed but all actuators are assembled to the mechanism as shown in Figure 6.16. The blue piezoelectric actuators are the ones that are not active and the red ones are the ones that are actuated. 30 V, 60 V, 90 V, 120 V and 150 V are supplied to the piezoelectric actuator and the end-effector motions in X and Y axes are examined. Linear curves are fit to the graphs to estimate the slope of the motions. Only Piezo 1 is actuated in Figure 6.16a, and the motion vector u_1 has a slope of -59.96° , Piezo 2 is actuated in Figure 6.16b, and the slope of the motion vector u_2 has a slope of 58.2° . Finally, in Figure 6.16c only Piezo 3 is actuated and the slope of its motion vector u_3 is -3.75° .



(a)



(b)



(c)

Figure 6.16 3-RRR compliant mechanism experiment displacement results for all PEAs are assembled.

The workspace of 3-RRR compliant mechanism is determined by giving the maximum strokes to the piezoelectric actuators as shown in Table 6.2. All piezoelectric actuators are assembled and ready to actuate the mechanism. The results for maximum X and Y displacement values for the given inputs are presented in Table 6.3. The shape of the workspace is drawn in Figure 6.17. The shape of the workspace of 3-RRR compliant mechanism is a hexagonal but not equilateral, and the motion vectors u_1 , u_2 and u_3 are not parallel to the forces that are applied from piezoelectric actuators.

Table 6.2 Workspace actuation and results of 3-RRR compliant mechanism

Piezo 1 [μm]	Piezo 2 [μm]	Piezo 3 [μm]	X_{max} [μm]	Y_{max} [μm]	U_{max} [μm]
40	0	0	37.805393	-68.408752	78.160124
0	40	0	39.825641	64.309138	75.642229
0	0	40	-80.938537	1.885379	80.960493
40	40	0	74.4646596	-2.753272	74.515542
0	40	40	-35.804950	62.234008	71.798789
40	0	40	-42.991442	-65.471842	78.325131
40	40	40	-5.174028	0.138919	5.175893

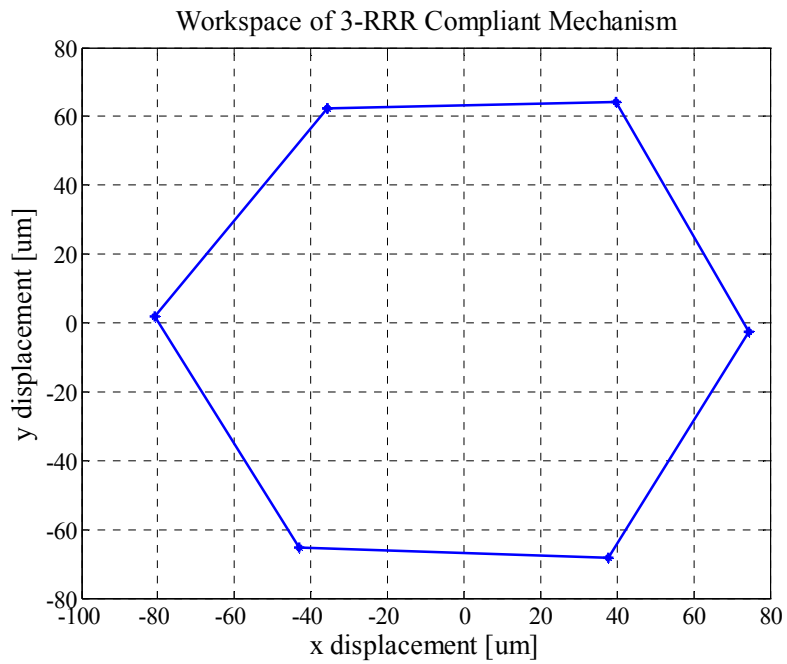


Figure 6.17 Workspace of 3-RRR compliant mechanism.

6.3 3-PRR Performance Results

The same experiments as in 3-RRR stage are repeated for our designed 3-PRR compliant micropositioning stage by actuating the piezoelectric actuators and examining the end-effector motion. The direction of the u_1 , u_2 and u_3 vectors are shown in Figure 6.18 and the workspace of the 3-PRR compliant mechanism is determined. Firstly, only the actuators in action are assembled to the stage. Secondly, all actuators are assembled to the stage even though they are not actuated at the same time.

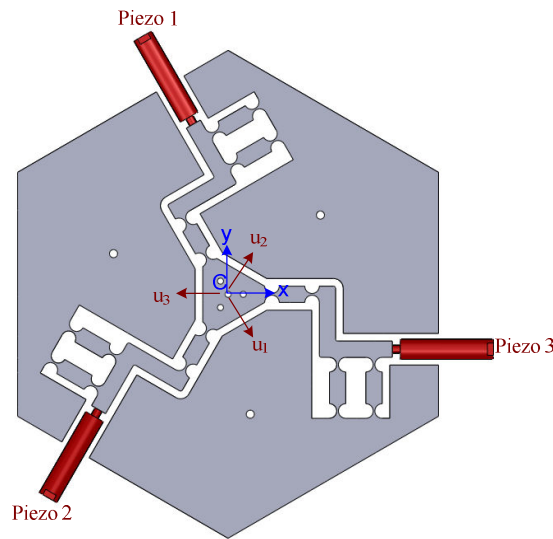
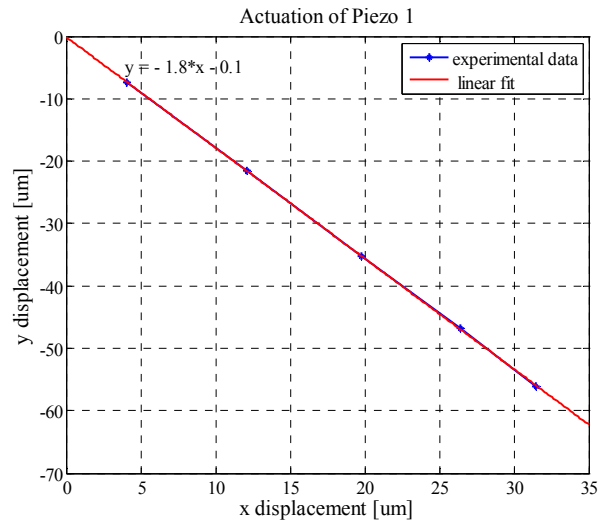
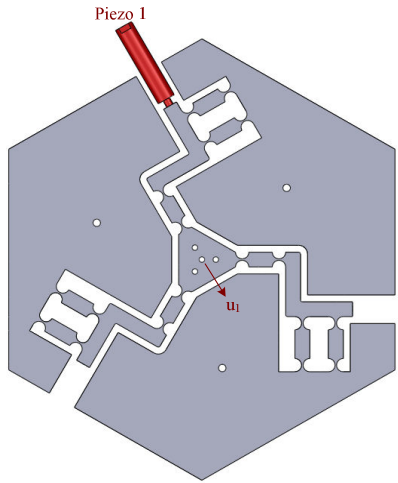
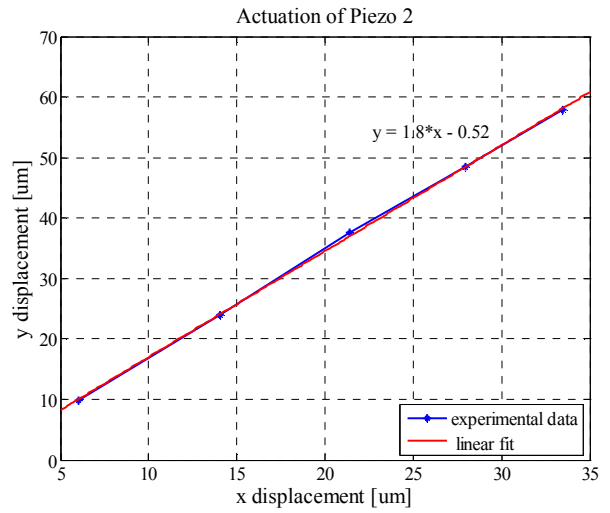
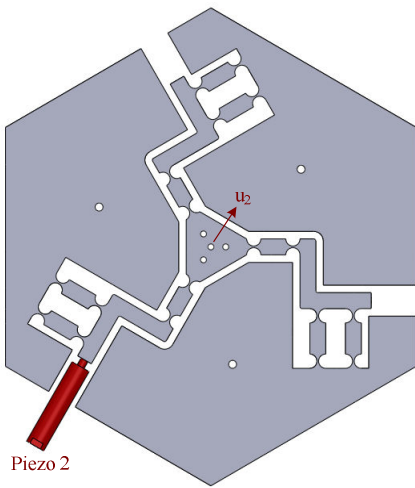


Figure 6.18 Motion vectors of PEAs in 3-PRR compliant mechanism.

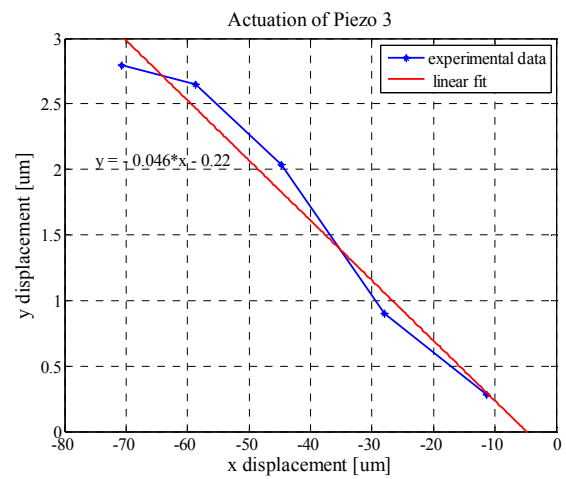
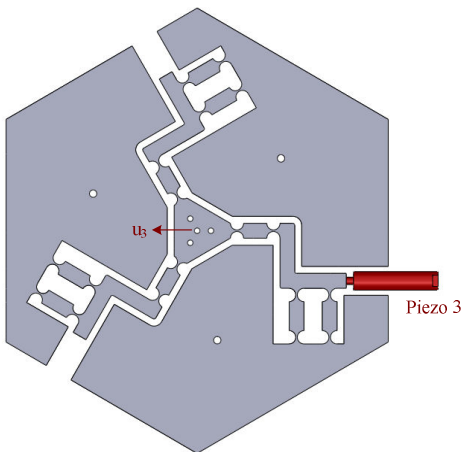
Piezo 1 is actuated when other piezoelectric actuators are not connected to the mechanism. 30 V, 60 V, 90 V, 120 V and 150 V are supplied to the piezoelectric actuator and the end-effector motion in X and Y axis is shown in Figure 6.19a. After that only Piezo 2 is actuated with the same amount of voltages, and the results are presented in Figure 6.19b. Lastly, Piezo 3 is actuated in the same way. The results of Piezo 3 are shown in Figure 6.19c. In micropositioning of flexure based mechanism the small displacements are almost linear so a linear curve would be a good fit to the results to estimate the direction of the vectors. According to the slope of the motion vector u_1 has a slope of -60.60° , u_2 has a slope of 60.29° , and u_3 has a slope of -2.62° with X axis. The angles of the motion vectors are better than the 3-RRR compliant mechanism results, which are presented in Figure 6.15.



(a)



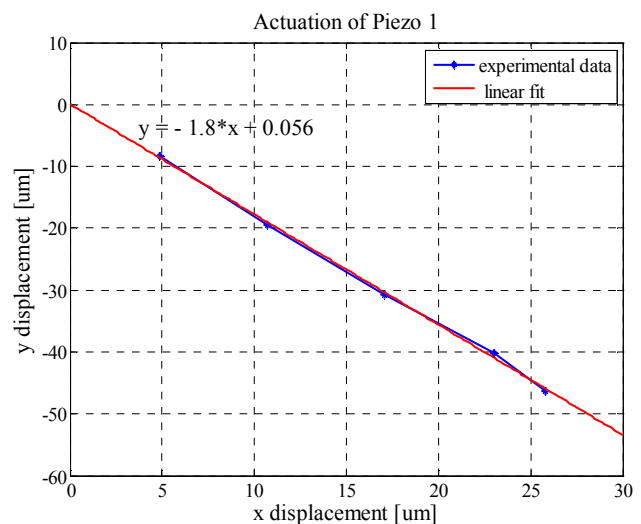
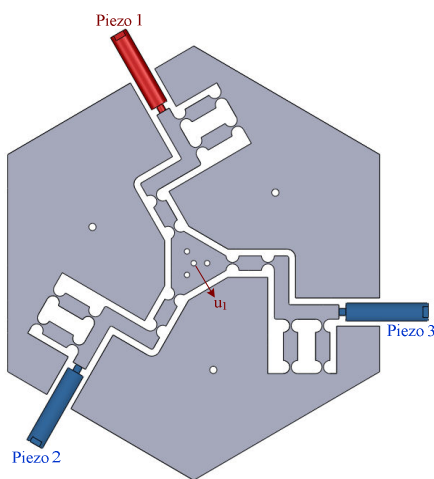
(b)



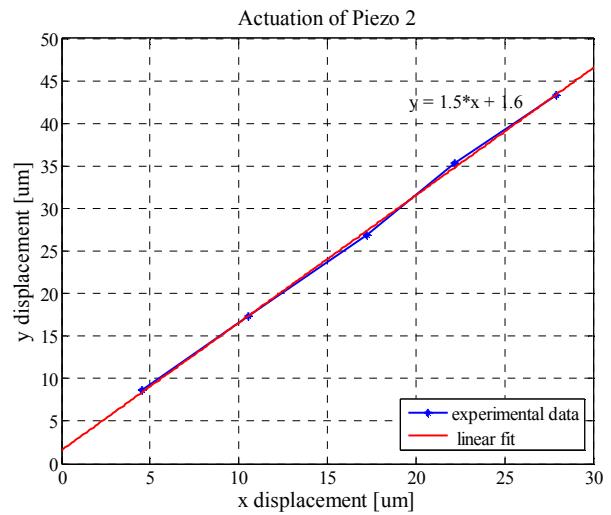
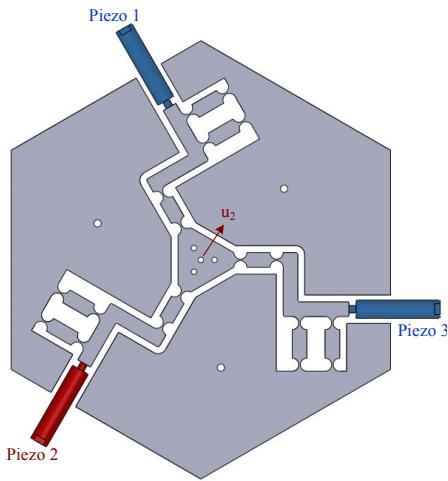
(c)

Figure 6.19 3-PRR Compliant mechanism experiment displacement results when only 1 PEA is assembled.

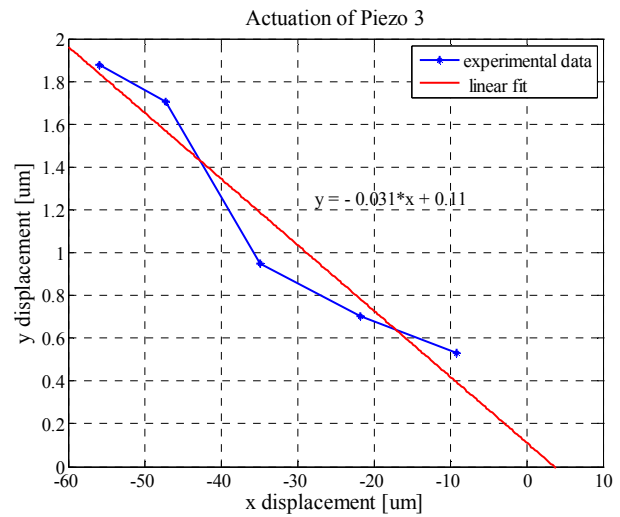
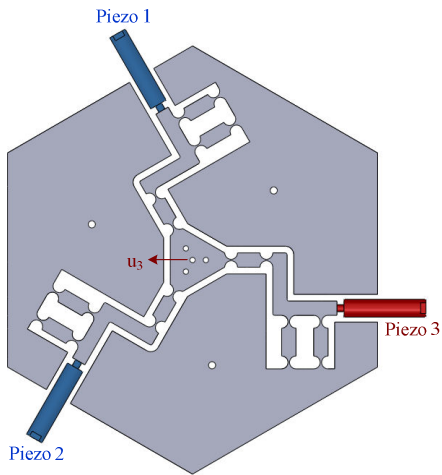
The same experiments for 3-PRR compliant mechanism are performed for all actuators assembled to the mechanism as shown in Figure 6.20. The blue piezoelectric actuators are the ones that are not active while the red ones are the ones that are actuated. 30 V, 60 V, 90 V, 120 V and 150 V are supplied to the piezoelectric actuator and the resulting end-effector motions in X and Y axes are examined. Linear curves provide a good fit for the graphs to estimate the slope of the motions. When Piezo 1 is only actuated in Figure 6.20a, and the motion vector u_1 has a slope of -60.7° , Piezo 2 is actuated in Figure 6.20b, and the slope of the motion vector u_2 has a slope of 56.27° . Finally, in Figure 6.20c only Piezo 3 is actuated, and the slope of its motion vector u_3 is -1.766° . When all actuators are connected and preloaded only the direction of the u_3 vector is better than 3-RRR compliant mechanism results, which are presented in Figure 6.16. The other two motion vectors are shifted more with respect to the piezoelectric forces that are applied to the mechanism due to the manufacturing and assembling errors.



(a)



(b)



(c)

Figure 6.20 3-PRR Compliant mechanism experiments for all PEAs are assembled.

The workspace of 3-PRR compliant mechanism is determined by giving the maximum strokes to the piezoelectric actuators and taking the X and Y measurements when all piezoelectric actuators are assembled to the mechanism as shown in Table 6.2. The shape of the workspace is drawn in Figure 6.17, which is a distorted hexagonal and is more shifted than the 3-RRR results shown in Figure 6.17.

Table 6.3 Workspace results

Piezo 1 [μm]	Piezo 2 [μm]	Piezo 3 [μm]	X_{max} [μm]	Y_{max} [μm]	U_{max} [μm]
40	0	0	25.807	-46.357	53.0560
0	40	0	27.887	43.314	51.515
0	0	40	-55.861	1.876	55.893
40	40	0	53.320	-3.484	53.434
0	40	40	-29.161	45.169	53.764
40	0	40	-30.367	-41.609	51.512
40	40	40	-4.931	-5.880	7.673

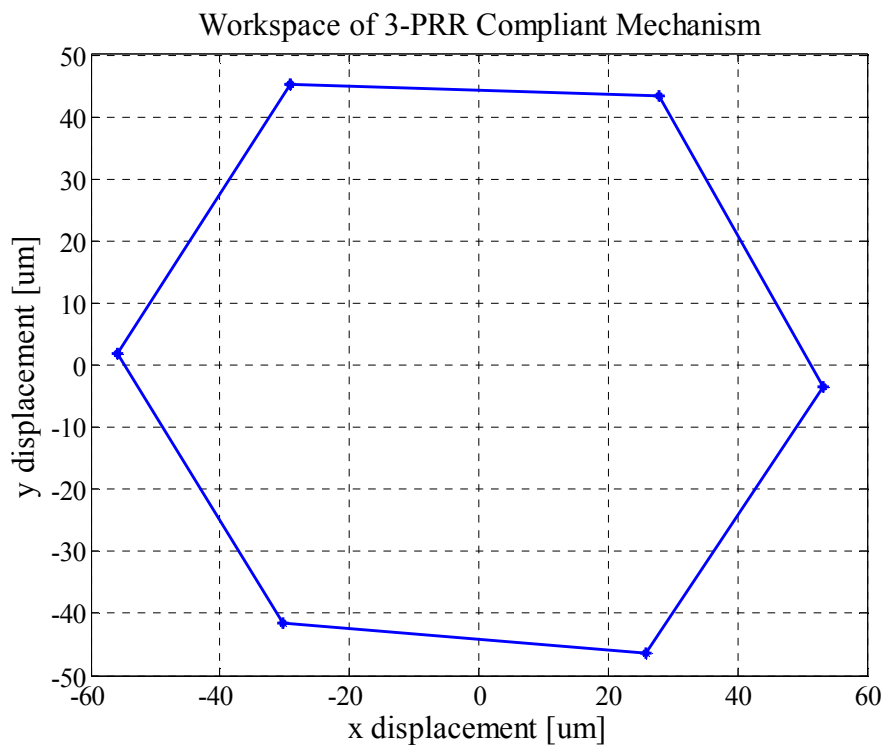


Figure 6.21 Workspace of 3-PRR compliant mechanism.

6.4 Comparison of 3-RRR and 3-PRR Compliant Mechanisms

The performance experiments of 3-RRR and 3-PRR compliant mechanisms show us that when all piezoelectric actuators are not assembled to the mechanism 3-PRR mechanism's motion vectors are close to the actuation vectors so the shape of the workspace is almost an equilateral hexagonal. This means that when only the piezoelectric actuator, which will actuate the mechanism, is only connected and preloaded the 3-PRR compliant mechanism gives us better results when we only control the position of the piezoelectric actuator without having an end-effector measurement. However, when all piezoelectric actuators are connected, which is the practical case, 3-PRR mechanism results more shifted motion vectors than 3-RRR compliant mechanism because of the moment creation when the other links are supported even though they are not in action. There can be also more manufacturing and assembling errors.

When the workspaces of 3-PRR and 3-RRR compliant mechanisms are compared 3-RRR compliant mechanism has the largest strokes in every motion direction for both of the cases (when all piezoelectric actuators are connected or only the piezoelectric actuator in action is connected). This is because of the amplification of the input stroke in 3-RRR mechanism is more but when we analyze both mechanisms we see that the stress is distributed in 3-PRR mechanism more evenly than 3-RRR mechanism, so that 3-PRR mechanism can be exposed to higher force amplitudes than the 3-RRR mechanism. Thus, the workspace of 3-PRR mechanism can be bigger. This means that we can use piezoelectric actuator having bigger maximum strokes and applying bigger forces for 3-PRR mechanism, whereas 3-RRR mechanism will deform in plastic region earlier than 3-PRR mechanism.

6.5 Comparison with FEA

The experimental results of 3-RRR and 3-PRR compliant mechanisms are compared with the Finite element analysis of the mechanisms to see how far we are from the ideal system. The errors that we obtained from manufacturing and assembly errors can be seen easily with this comparison. We have used PSt 150/5/60 VS10 piezoelectric actuator having 60 μm max. stroke for unipolar actuation with strain gauge

measurement to have the information about input displacement to compare the results with FEA.

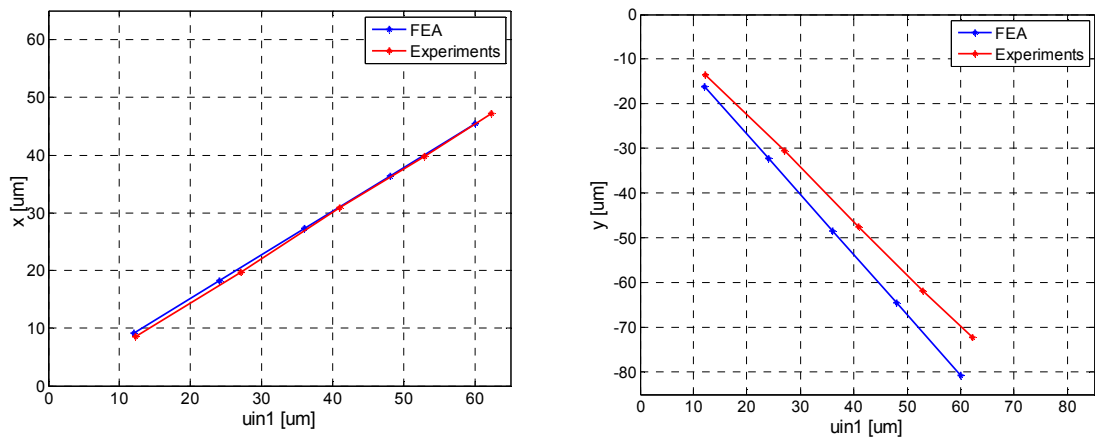
6.5.1 3-RRR Compliant Mechanism

12, 24, 36, 48 and 60 μm input displacements are given to each of the piezoelectric actuators, respectively. All piezoelectric actuators are assembled to the mechanism, and they are all preloaded ready to drive the link that they are connected to.

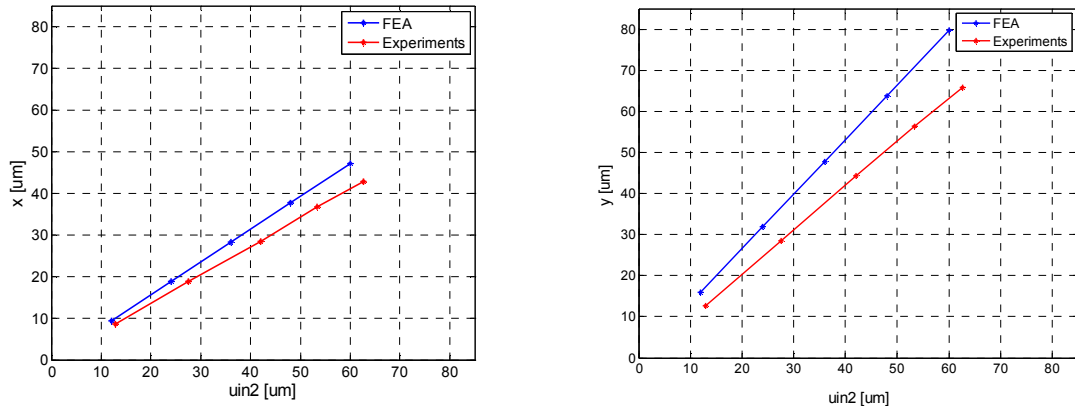
The results, which present the x-y displacements for each u_{in1} , u_{in2} and u_{in3} input displacements, are shown in Figure 6.22. The % errors of x-y axes when compared to FEA for each input are presented in Table 6.4. There is a large y motion in the manufactured mechanism, whereas in FEA results the y motion is very small when only piezo 3 is actuated. The resulting motions in the other directions have errors up to 21% when looking at the results. Thus, we need to eliminate these errors by control methods.

Table 6.4 % errors compared to FEA for 3-PRR

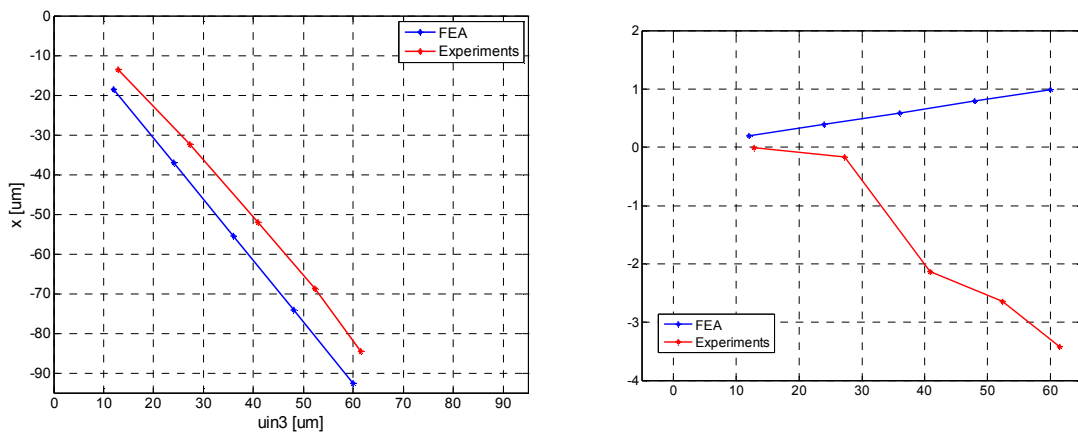
u_{in1}		u_{in2}		u_{in3}	
% error for x	% error for y	% error for x	% error for y	% error for x	% error for y
-0.088	13.75	12.87	20.95	10.86	4.39e2



(a) Results for u_{in1}



(b) Results for u_{in2}



(c) Results for u_{in3}

Figure 6.22 Comparison of experimental and FEA results of 3-RRR compliant mechanism.

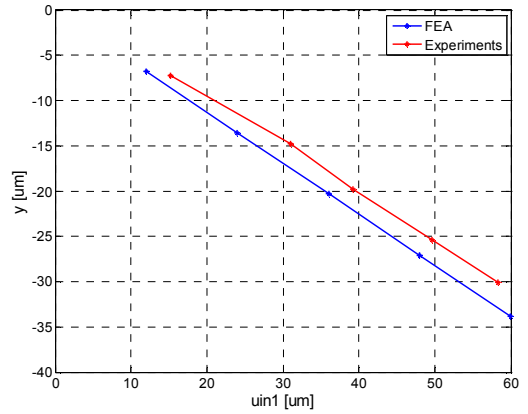
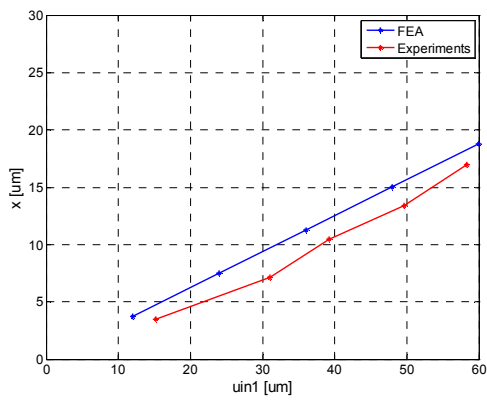
6.5.2 3-PRR Compliant Mechanism

12, 24, 36, 48 and 60 μm input displacements are given to each of the piezoelectric actuators, respectively. All piezoelectric actuators are assembled to the mechanism, and they are all preloaded ready to drive the link that they are connected to.

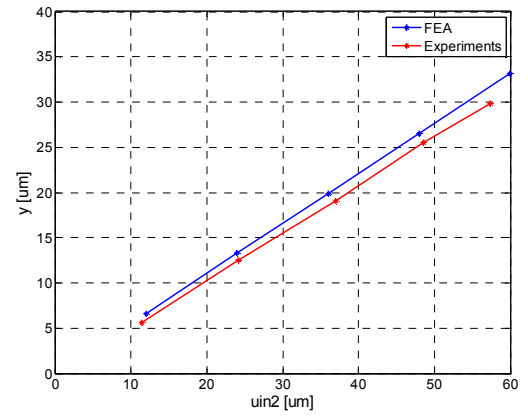
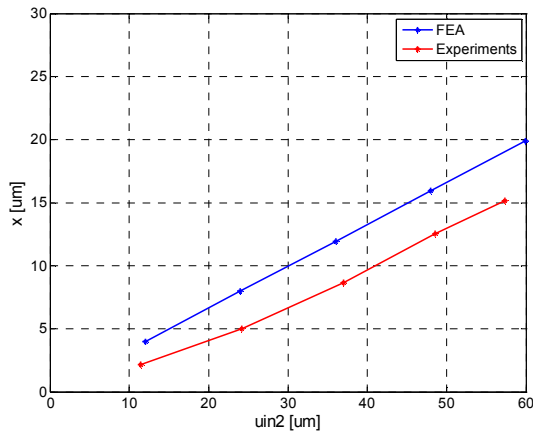
The results, which present the x-y displacements for each u_{in1} , u_{in2} and u_{in3} input displacements, are shown in Figure 6.23. The % errors in x-y axes when compared to FEA for each input are presented in Table 6.5. The manufactured 3-PRR mechanism has errors up to 20% when looking at the results. Thus, we need to eliminate these errors by control methods.

Table 6.5 % errors compared to FEA for 3-PRR

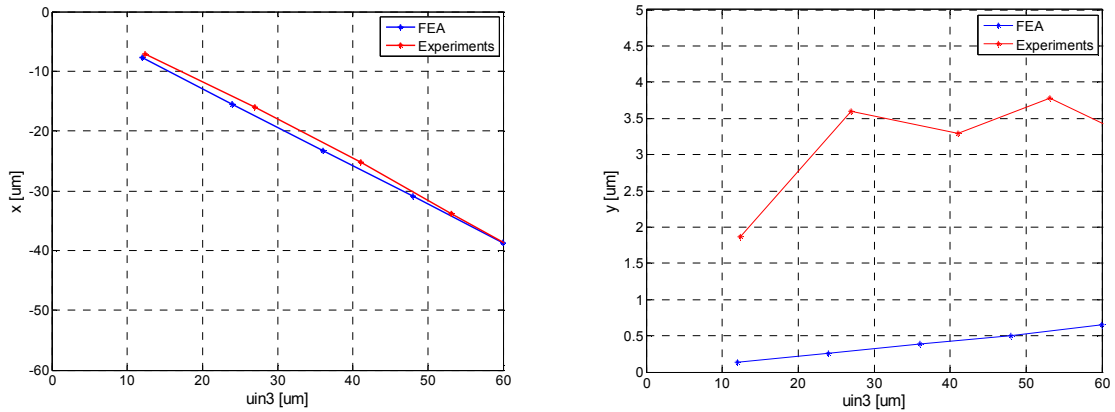
u_{in1}		u_{in2}		u_{in3}	
% error for x	% error for y	% error for x	% error for y	% error for x	% error for y
7.086	8.402	20.25	5.873	-0.25	-3.986



(a) Results for u_{in1}



(b) Results for u_{in2}



(c) Results for u_{in3}

Figure 6.23 Comparison of experimental and FEA results of 3-PRR compliant mechanism.

6.6 Conclusion and Comments

The experimental setup is explained in detail. The calibrations of dual positioning sensor and strain gauge measurements are presented. The experiments are performed for 3-RRR and 3-PRR compliant mechanism to see the amplitude and direction of motion at the center of the stage by using dual position sensor. As in Finite element analysis the experiments are done for two cases. First, one piezoelectric actuator is assembled to the mechanism and preloaded. Secondly, all of the piezoelectric actuators are connected to the mechanism and preloaded to be ready to drive the links. Finally, by giving the maximum stroke from the piezoelectric actuators which is $40 \mu\text{m}$ we have obtained the workspaces of the mechanisms.

After, we have compared the experimental results of 3-RRR and 3-PRR compliant mechanisms to each other. When only the piezoelectric actuator, which will actuate the mechanism, is only connected and preloaded the 3-PRR compliant mechanism gives us better results because the motion vectors are almost parallel to the direction of the actuation forces. However when all piezoelectric actuators are connected, which is the practical case, 3-PRR mechanism results in more shifted motion vectors than 3-RRR compliant mechanism because of the moment creation when the other links are supported even though they are not in action. There can also be some manufacturing and assembling errors. The workspace of 3-RRR compliant mechanism is bigger than the 3-PRR compliant mechanism because it is more flexible.

The experimental results are compared with the Finite element results to see how far we are from the ideal cases. All piezoelectric actuators are connected to the mechanism and preloaded. PSt 150/5/60 VS10 piezoelectric actuator having 60 μm max. stroke for unipolar actuation with strain gauge measurement is used to have the information about input displacement to compare FEA results. The results showed us that manufactured mechanisms are not close to the ideal actuated mechanisms implying that we need to have a control method to eliminate those errors and make our mechanisms to be useful as a high precision positioning stage.

7 PIEZOELECTRIC ACTUATOR MODELING AND CONTROL

Certain crystals are found to be electrically polarized when mechanical strain is applied. This effect is called “piezoelectric effect”. Similarly when an electric field applied to the piezoelectric material, it deforms and this effect is called “the inverse piezoelectric effect”. These effects are proportional to mechanical strain and electric field which implies that compressive and tensile stresses have opposite polarity. In 1940’s during World War I piezoelectricity has been used commercially in ultrasonic submarine detectors. Since then many researches have been made to fabricate and use piezoelectric materials [5].

The piezoelectric effect has been used for measurement of pressure, force, movement, strain, vibration to electric signals etc. The inverse piezoelectric effect has been used for actuation especially in micro/nano technology because of the deformation of the material when electric field is applied. Piezoelectric actuators have been selected for our application because of the advantages that they have as follows:

- Possibility of being in small size,
- Having picometer positioning resolution,
- Commercially available,
- Producing low heat in low frequencies,
- Enough knowledge is known for controlling the piezoelectric actuators,
- Availability to be used in high frequencies,
- Providing smooth and continuous motion with no friction effect.

On the contrary piezoelectric actuators have some disadvantages. The main disadvantage is that they have hysteresis behavior in voltage/displacement or force/displacement relations while operating. However, this hysteresis effect can be modeled and it can be eliminated by applying closed loop control methods with observers.

7.1 Modeling of Piezoelectric Actuators

We have modeled the piezoelectric actuators by using Goldfarb and Celonovic proposed model in [74], which consists of an electrical and a mechanical part. Different nonlinear models can be embedded to the model for modeling the behavior of hysteresis effect of the piezoelectric actuators.

Piezoelectric actuators electromechanical lumped model can be represented by the Eqns. 7.1-7.6. v is the total voltage across the actuator, v_p is the piezoelectric voltage and v_h is the hysteresis voltage. T is the electromechanical transformation ratio that connects electrical part to mechanical part of the model. q is the total charge in the actuator, q_p is the charge transduced due to mechanical motion, H is the hysteresis function that depends on q , F_p is the force of the piezoelectric effect and F_{ext} is the external force on the actuator. According to Eqn. 7.6, u is the displacement, m_p , c_p and k_p are the equivalent mass, damping and stiffness of the piezoelectric actuator respectively. F_c is the control force while F_{dis} is the disturbance force.

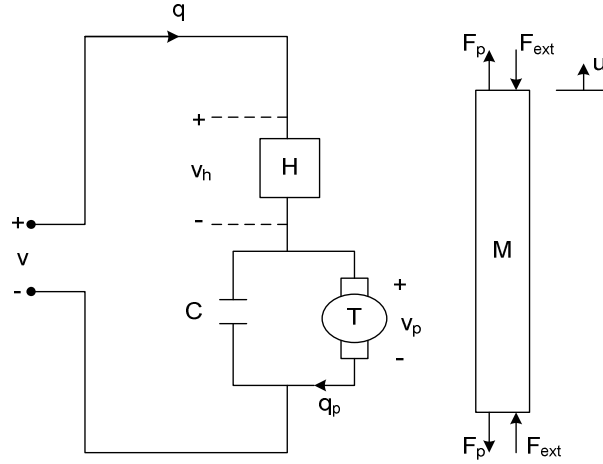


Figure 7.1 Piezoelectric actuator model [74]

$$v_p = v - v_h \quad (7.1)$$

$$v_h = H(q) \quad (7.2)$$

$$q = C v_p + q_p \quad (7.3)$$

$$q_p = T u \quad (7.4)$$

$$F_p = T v_p \quad (7.5)$$

$$m_p \ddot{u} + c_p \dot{u} + k_p u = \underbrace{T v}_{F_c} - \underbrace{T v_h - F_{ext}}_{F_{dis}} \quad (7.6)$$

The lumped parameters m_p , c_p and k_p can be calculated according to Eqns. 7.7-7.9 by using the piezoelectric ceramic material properties like elastic modulus E , viscosity η , mass density ρ and geometric properties like length L and cross sectional area A of the piezostack:

$$m_p = \rho AL \quad (7.7)$$

$$c_p = \frac{\eta A}{L} \quad (7.8)$$

$$k_p = \frac{EA}{L} \quad (7.9)$$

The material properties of piezoelectric material (PZT - lead zirconate titanate) are presented on Table 7.1.

Table 7.1 Material properties of PZT

Elastic Modulus, E	Viscosity, η	Density, ρ
$6.6 \cdot 10^{10} \text{ N/m}^2$	10 mPa.s	7800 kg/m^3

7.1.1 Hysteresis Model

The used piezoelectric actuator model in Eqn. 7.6 needs information about hysteresis v_h . Thus, we need a hysteresis model. We have used Coleman and Hodgdon's [75] proposed hysteresis model based on magnetic hysteresis and it has been proven in [76] that the hysteresis model is also suitable for electrical hysteresis modeling.

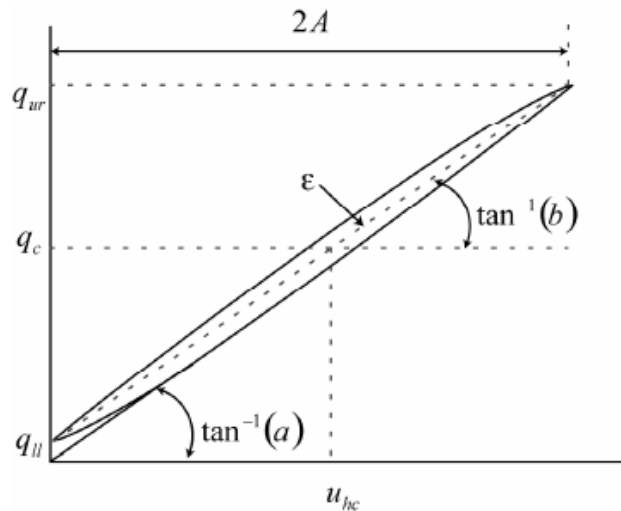


Figure 7.2 Hysteresis loop and its parameters [77].

According to the selected hysteresis model the relationship between the hysteresis voltage v_h and charge q in the actuator is expressed as:

$$\dot{q} = \alpha \cdot |v_h \cdot (f(v_h) - v_h)| + v_h \cdot g(v_h) \quad (7.10)$$

$$f(v_h) = a_h \cdot v_h \quad (7.11)$$

$$g(v_h) = b_h \quad (7.12)$$

α is a constant and $f(v_h)$ and $g(v_h)$ are the functions that shape the hysteresis loop, and they are chosen as in Eqns. 7.11 and 7.12 where a and b are the constants. In Figure 7.2 a hysteresis loop is shown, and v_{hc} is the average voltage is applied to the actuator by the sinusoidal input, q_{hc} is the corresponding average charge to v_{hc} and determines the center point of the hysteresis loop, which is $f(v_{hc})$. The average slope of the loop is determined by $g(v_{hc})$. The shape functions are defined in Eqns. 7.11 and 7.12.

The center point and the average slope of the hysteresis loop in Figure 7.2 can be calculated as follows:

$$q_c = a_h v_{hc} \quad (7.13)$$

$$q_{ur} - q_{ll} = b_h \cdot 2A \quad (7.14)$$

q_{ur} is the upper right and q_{ll} is the lower left hand side points of the hysteresis loop and A is the input amplitude.

α parameter can be obtained by using a relation of the hysteresis loop, ε , which is derived for small amplitude of the sinusoidal input as:

$$\varepsilon = \frac{4}{3} \cdot (a_h - b_h) \cdot \alpha \cdot A^3 \quad (7.15)$$

The behavior of the piezoelectric actuator should be analyzed to find the constants a_h , b_h and α by applying small amplitude, moderate frequency sinusoidal input as $v = \tilde{v} + A \cdot \sin(\omega \cdot t)$ where \tilde{v} is the offset, A is the amplitude and ω is the angular frequency.

7.1.2 Simulation of the Model

The model of the piezoelectric actuator has been simulated by using MATLAB/Simulink. The block diagram of the model is presented in Figure 7.3. Piezomechanik's PSt 150/5/60 VS10 strain gauge embedded to piezoelectric actuators are chosen for the simulation and experiments. The parameters of the piezoelectric actuator are shown in Table 7.2. The linear model parameters m_p , c_p and k_p are found by

using the material properties and datasheet parameters of the piezoelectric actuator. The hysteresis parameters a_h and b_h are taken from K. Abidi [77].

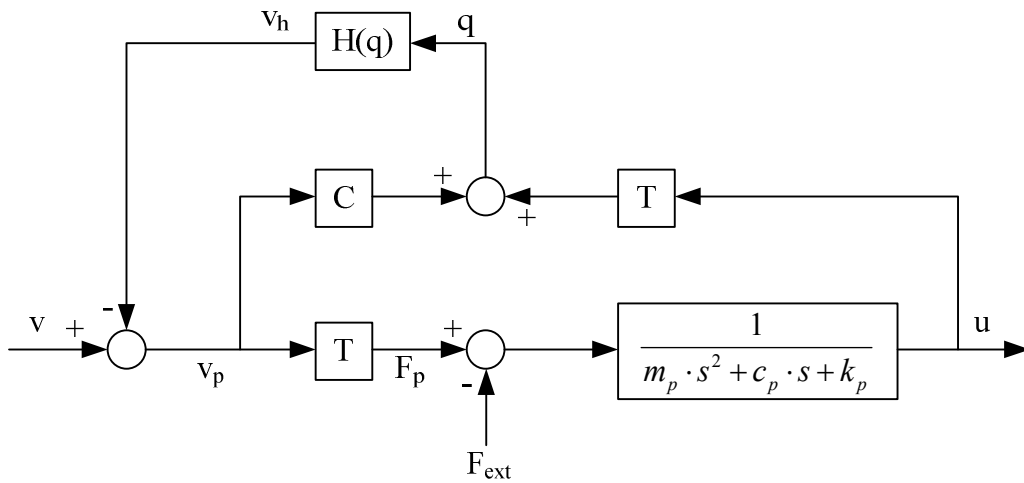


Figure 7.3 Block diagram of PEA model with hysteresis.

Table 7.2 PSt 150/5/60 VS10 Piezoelectric actuator parameters

Parameter	Value
m_p	$9.24 \cdot 10^{-4}$ kg
c_p	685 Ns/m
k_p	$8 \cdot 10^6$ N/m
T	4.8 N/V
C	2.4 mF
a_h	5
b_h	4.5
α	1.8

The piezoelectric actuator is simulated by applying 0V-150V sinusoidal input to have the unipolar maximum stroke which is 60 μm for the selected piezoelectric actuator. $v = 75 + 75\sin(0.2\pi t)$ is applied, and the position result of the piezoelectric actuator is presented in Figure 7.4. The error of the simulation results is 0.7878 μm . We can see the hysteresis effect of the piezoelectric actuator with the input piezo voltage v_p shown in Figure 7.5

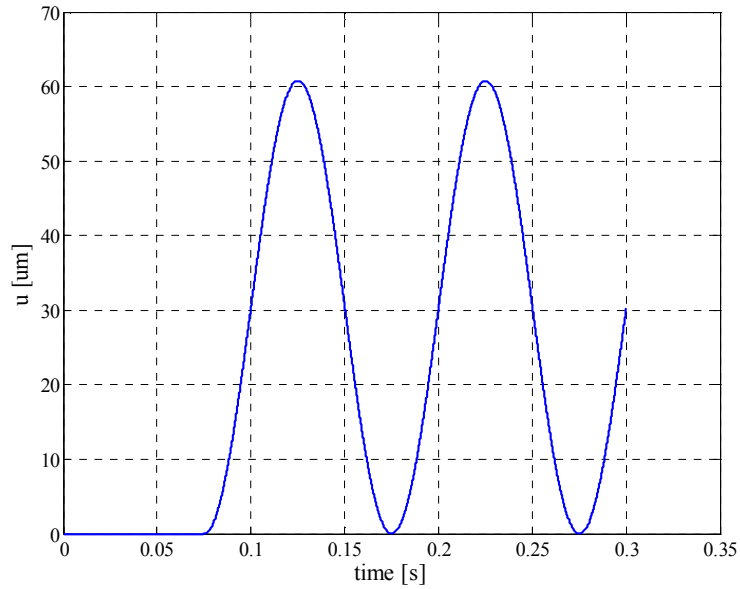


Figure 7.4 The displacement result of simulated PEA.

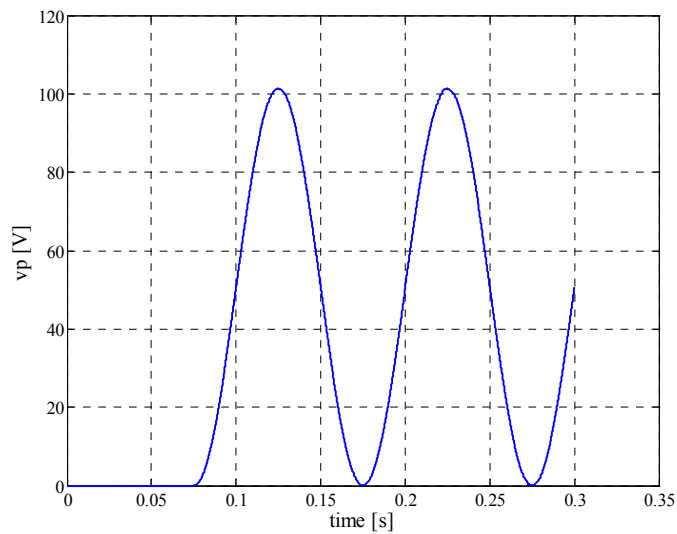


Figure 7.5 The input piezo voltage result of simulated PEA.

7.2 Sliding Mode Control with Disturbance Observer

The Piezoelectric actuators (PEA) should be control accurate enough to be used in high precision systems. The stable control of manipulator positions are based on model based control system analysis and design but hysteresis and uncertain disturbances cause an obstacle to control the piezoelectric actuators. Sliding Mode Control technique is a robust control to eliminate the uncertainties of the model and disturbances like

hysteresis because of this advantage SMC used in nonlinear systems. In this work we have used Sliding mode Control for position control of the piezoelectric actuator which has a second order electromechanical system with lumped model parameters (m_p, c_p, k_p) . The input of the system is voltage and output is the position of the piezoelectric actuator. We have also a Disturbance Observer with Sliding Mode Controller to eliminate the all uncertainties in the system by modeling the piezoelectric actuator with nominal parameters (m_n, c_n, k_n) .

7.2.1 Sliding Mode Observer for PEA

We are able to eliminate disturbances by modeling an observer so that a linear model is defined by using nominal parameters of actuator as in Eqn. 7.6. The displacement u for every piezo actuator can be measured by using laser position sensor and taking the inverse of the transformation matrix. The supply voltage is also measurable. The linear model of the piezoelectric actuator is expressed as:

$$m_n \ddot{u} + c_n \dot{u} + k_n u = T_n v - F_d \quad (7.16)$$

We can define F_d as the sum of hysteresis force, external force and the uncertainties in the plant parameters, which are Δm , Δc , Δk and ΔT . These parameters are assumed as bounded and continuous:

$$F_d = T_n v_h + F_{ext} + \Delta T(v + v_h) + \Delta m \ddot{u} + \Delta c \dot{u} + \Delta k u \quad (7.17)$$

The observer can be designed as a position tracking system, in which F_d is replaced with an observer control $T_n v_{obsx}$ because u and v_{in} can be measured and the observer transfer function is written as:

$$m_n \ddot{\hat{u}} + c_n \dot{\hat{u}} + k_n \hat{u} = T_n v_{in} - T_n v_{obs} \quad (7.18)$$

\hat{u} is the estimated position, v_{in} is the plant control input, v_{obs} is the observer control input, where $\hat{u} \rightarrow u$, $F_d = T_n v_{obs}$. A sliding manifold is selected for that purpose which is $\sigma = \dot{u} - \dot{\hat{u}} + C_{obs}(u - \hat{u})$. The Lyapunov function which will provide stability is taken as $v_L = \sigma^2/2$ which is positive definite and the derivative of Lyapunov function is taken as $-D_{obs}\sigma^2$, which is negative definite. We will get Eqn. 7.19 by equating the above results and simplifying:

$$L = \sigma \dot{\sigma} = -D_{obs}\sigma^2 \Rightarrow \dot{\sigma} + D_{obs}\sigma = 0 \quad (7.19)$$

If we insert sliding mode manifold into the Eqn. 7.19:

$$(\ddot{u} - \ddot{\hat{u}}) + (C_{obs} + D_{obs})(\dot{u} - \dot{\hat{u}}) + C_{obs}D_{obs}(u - \hat{u}) = 0 \quad (7.20)$$

When we subtract the equations (7.18) from (7.17) and insert the result into the above equation (7.20) we can find the equivalent control v_{ceq} which keep system motion in manifold $\sigma + \dot{\sigma} = 0$.

$$v_{ceq} = \frac{1}{T_n} \{F_d + [c_n - m_n(C_{obs} + D_{obs})](\dot{u} - \dot{\hat{u}})[k_n - m_n C_{obs} D_{obs}](u - \hat{u})\} \quad (7.21)$$

Eqn. 7.21 tells us that when $\sigma \rightarrow 0$ then $u \rightarrow 0$ and $T_n v_{ceq} \rightarrow F_d$. For the implementations discrete form of sliding mode control is used as:

$$v_{(k)} = v_{(k-1)} + K_{obs} \left(D_{obs} \sigma_{(k)} + \frac{\sigma_{(k)} - \sigma_{(k-1)}}{dT} \right) \quad (7.22)$$

K_{obs} is a design parameter that optimize the controller and dT is the sampling interval for discrete time control. The system and the observer can be summarized as in Eqns. 7.23-7.25:

$$m_n \ddot{u} + c_n \dot{u} + k_n u = T v_{in} - F_d \quad (7.23)$$

$$m_n \ddot{\hat{u}} + c_n \dot{\hat{u}} + k_n \hat{u} = T_n v_{in} - T_n v_{obsc} \quad (7.24)$$

$$v_{in} = v_c + \frac{\alpha}{T_n} v_{obsc} \quad (7.25)$$

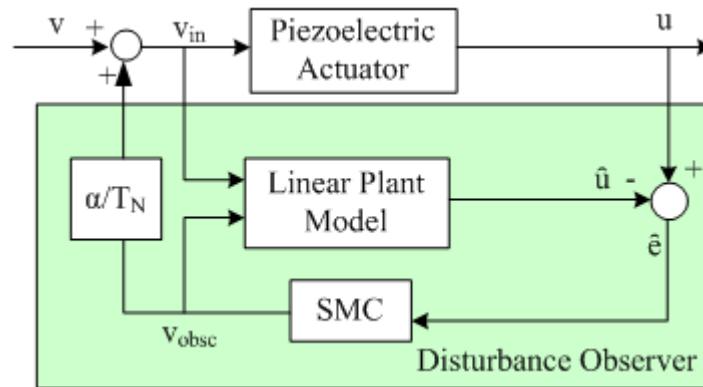


Figure 7.6 Block diagram of disturbance observer with sliding mode controller.

In Figure 7.6 the block diagram of disturbance observer with sliding mode controller is presented where v is the voltage that is given to the system, v_{obsc} is the observer control voltage, v_{in} is the calculated input voltage, u is the displacement of the piezoelectric actuator, \hat{u} is the estimated displacement and \hat{e} is the estimation error.

v_{obsc} can be obtained from Eqns. 7.23-7.25 as follows:

$$v_{obsc} = \frac{T_n F_d - T_n \Delta T_n u_0}{T_n + \alpha \Delta T_n} \quad (7.26)$$

where $\Delta T_n = T - T_n$ if Eqn. 7.26 is plugged in Eqn. 7.23:

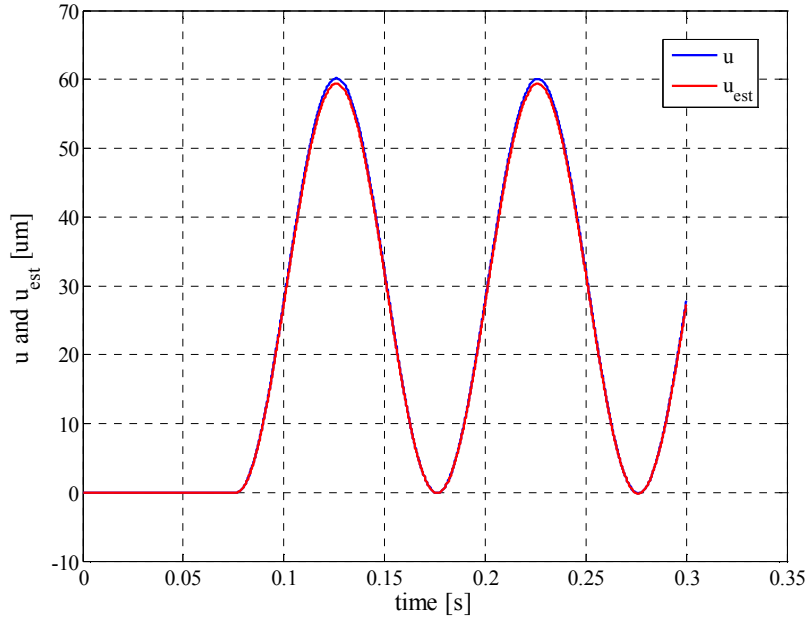
$$m_n \ddot{u} + c_n \dot{u} + k_n u = \frac{T_n}{T_n + \alpha \Delta T_n} + \frac{\alpha T_n - (T_n + \alpha \Delta T_n)}{T_n + \alpha \Delta T_n} F_d \quad (7.27)$$

From Eqn. 7.27 we can conclude that when $\alpha \rightarrow 1$ then we obtain:

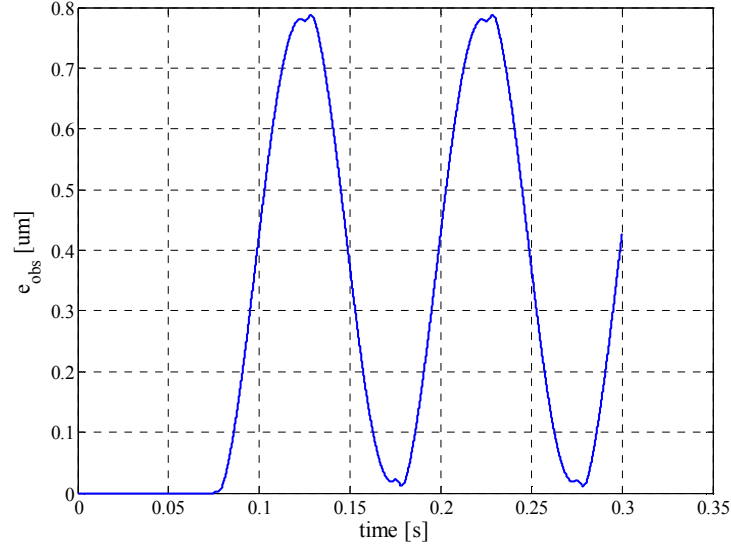
$$m_n \ddot{u} + c_n \dot{u} + k_n u = T_n u_0 \quad (7.28)$$

Therefore, the system should be compensated by designing a closed loop controller based on this model. The proposed controller will be explained in the following section.

The block diagram for the observer is built in Simulink as shown in Figure 7.6. The piezoelectric actuator plant is taken from Figure 7.3. The nominal parameters are set as shown in Table 7.2. The observer is compensated and the observer control parameters are set as $K_{\text{obs}}=0.00008$, $D_{\text{obs}}=500$, $C_{\text{obs}}=2$. The results for the case $v = 75 + 75\sin(20\pi t)$ is applied are presented in Figure 7.7.



(a)



(b)

Figure 7.7 Simulation results for sliding mode observer of PEA.

7.2.2 Position Control with Sliding Mode Control

A closed loop control is applied for the position control of the piezoelectric actuator. The position measurement of piezoelectric actuator is obtained by using strain gauge which is embedded within the piezoelectric actuator. The sliding manifold for the position control is selected to be as in Eqn. 7.26 and when the sliding manifold is reached the closed loop control showed in Eqn. 7.27 and the system is described as:

$$\sigma_x = (\dot{u}_{ref} - \dot{u}) + C_x(u_{ref} - u) \quad (7.26)$$

$$v_{(k)} = v_{(k-1)} + K_{ux} \left(D_x \sigma_{x(k)} + \frac{\sigma_{x(k)} - \sigma_{x(k-1)}}{dT} \right) \quad (7.27)$$

$$(\ddot{u}_{ref} - \ddot{u}) + (C_x + D_x)(\dot{u}_{ref} - \dot{u}) + C_x D_x (u_{ref} - u) = 0 \quad (7.28)$$

In Figure 7.8 the block diagram for position control with sliding mode controller is added to the disturbance observer system presented in Figure 7.6.

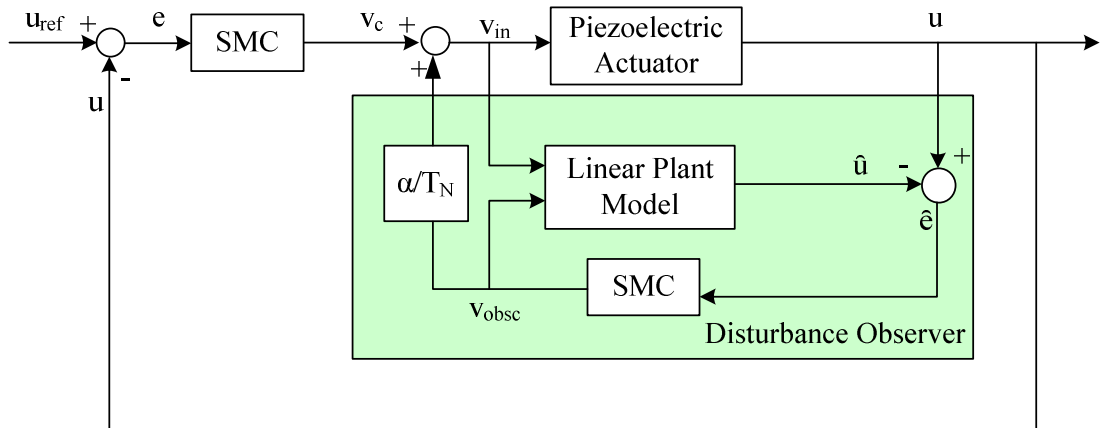


Figure 7.8 Block diagram of position control with sliding mode controller.

7.3 Implementation of Position Control with Disturbance Observer for PEA

The setup for implementing the proposed position control of PEA is presented in Figure 7.8. dSPACE 1103 Controller is used for the control implementation, and the proposed control methodology is coded in C. The sampling time for computing is 0.0001 sec. Piezomechanik's PSt 150/5/60 VS10 with strain gauge embedded for position measurement is used. The measurement is taken from strain gauge measurement which is connected to Dataforth's SCM5B38-05D for amplifying the voltage. The voltage is converted to position after the calibration as explained in section 6.1.4. The position value is sent through DAC to DS1103. The coded control method calculates the necessary input voltage v_{in} for the PEA and it is sent through ADC to Piezoelectric Amplifier to amplify the needed voltage to provide the amplified voltage value to PEA.

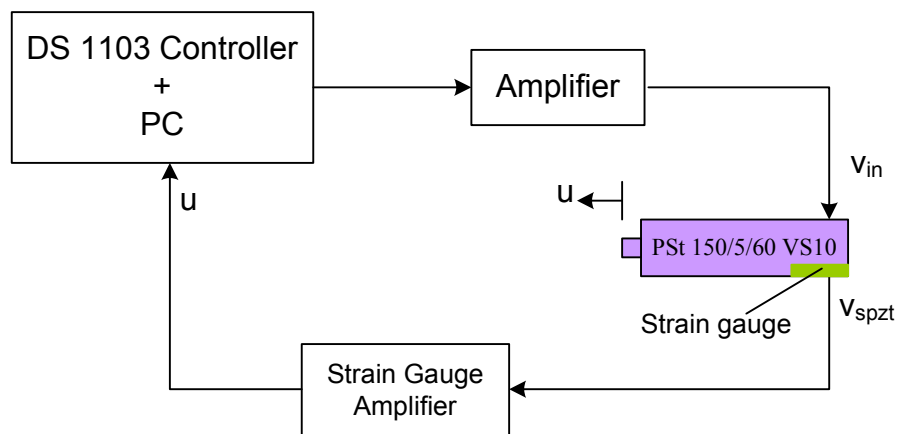
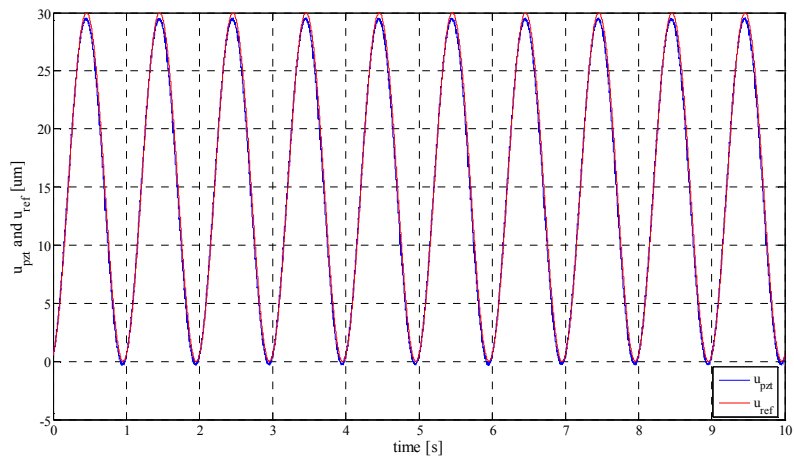


Figure 7.9 The Setup for implementation of position control of PEA.

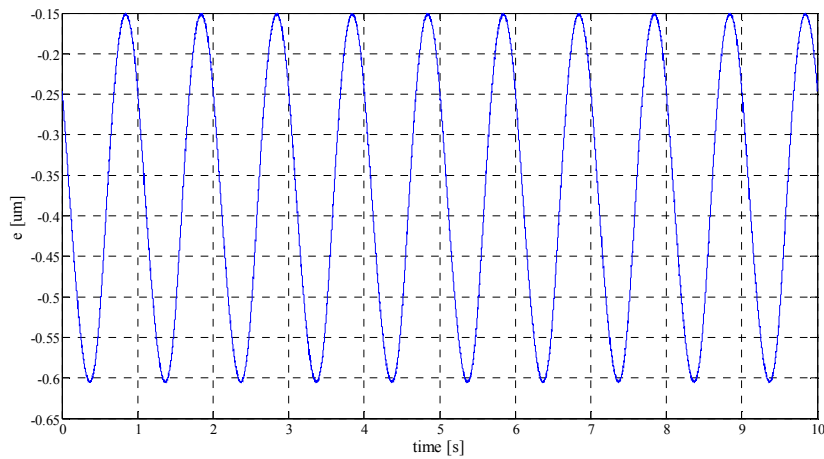
The experiments are performed to see the effect of using observer for position control of the piezo electric actuator. First v_{obs} is set as 0, and the PEA is controlled only with Sliding Mode Controller. Then v_{obs} is also calculated, and PEA is controlled with disturbance observer.

7.3.1 Position Control of PEA Without Observer

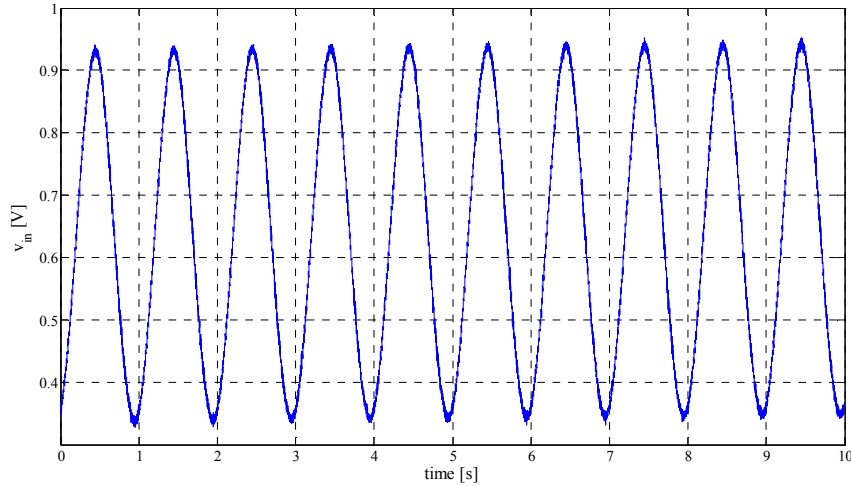
The reference position for the PEA is set to $u = 15 + 15 \sin(2\pi t)$ to examine the sinusoidal behavior of the PEA. The SMC controller parameters are set to $K_x=0.001$, $C_x=80000$ and $D_x=0.0001$. The results are presented in Figure 7.10. The reference and measured position values of PEA are presented in Figure 7.10a. The position tracking error as shown in Figure 7.10b is between $-0.65 \mu\text{m}$ and $-0.15 \mu\text{m}$. The v_{in} value shown in Figure 7.10c is the calculated input voltage for PEA and it is not amplified.



(a)



(b)



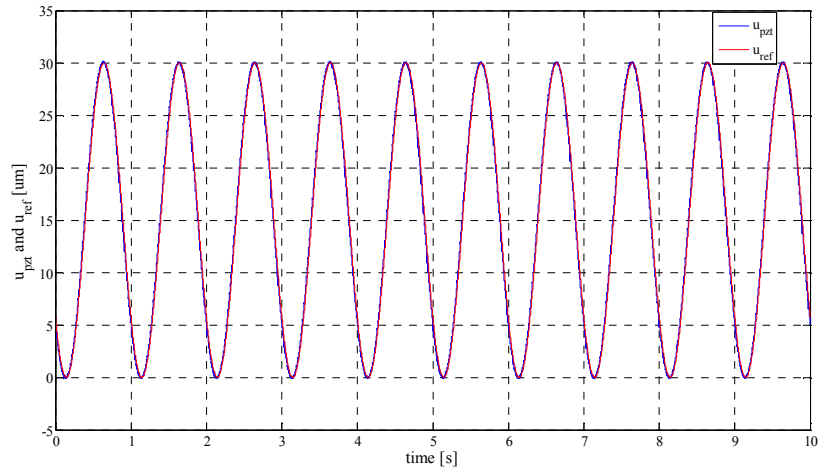
(c)

Figure 7.10 Results of position control of PEA without observer.

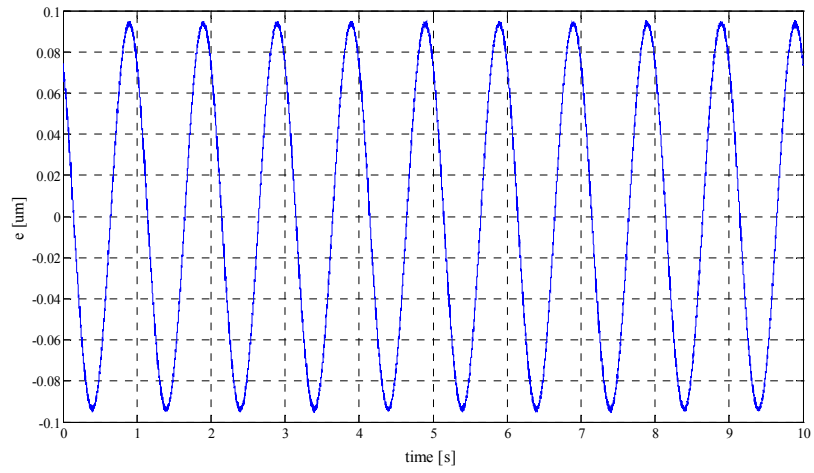
We have made the position control of the PEA having errors between $-0.15 \mu\text{m}$ and $-0.6 \mu\text{m}$ without using disturbance observer. The error we have is big for micro motion applications therefore, we need to use an observer to lower the errors.

7.3.2 Position Control of PEA With Observer

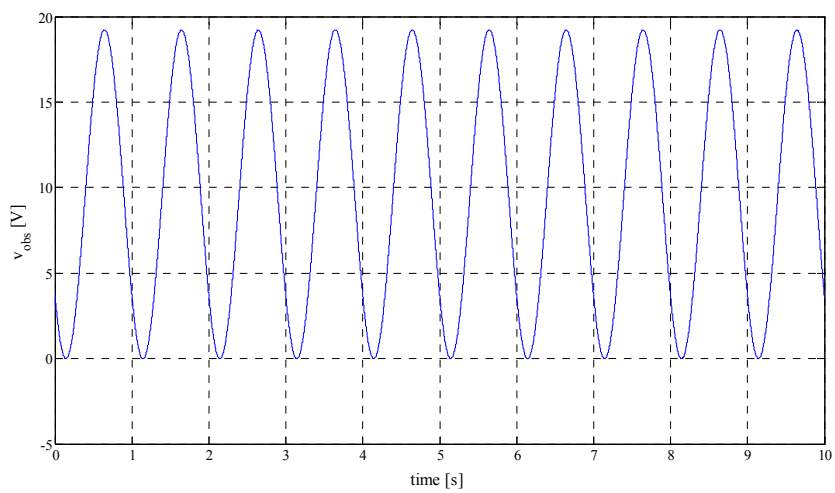
The same experiment is performed for PEA with observer by setting the reference position as $u = 15 + 15\sin(2\pi t)$. The SMC controller parameters are the same, which are $K_x=0.0009$, $C_x=80000$ and $D_x=1000$. The Sliding mode observer parameters are tuned as $K_{obs} = 0.00008$, $C_{obs}=0.001$ and $D_{obs}=8000$. The results are presented in Figure 7.11. The reference and measured position values of PEA are presented in Figure 7.11a. The position tracking error as shown in Figure 7.11b is between $0.01 \mu\text{m}$ and $-0.3 \mu\text{m}$. The voltage calculated with sliding mode observer v_{obs} is shown in Figure 7.11c. The v_{in} value is shown in Figure 7.11d and is the calculated input voltage for PEA and it is not amplified.



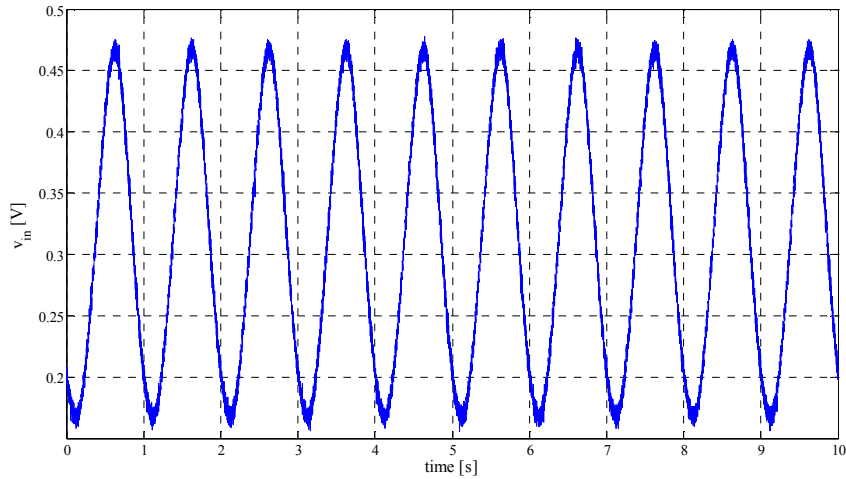
(a)



(b)



(c)



(d)

Figure 7.11 Results of position control of PEA with observer.

We have succeeded to make the position control of the PEA having errors between $0.1 \mu\text{m}$ and $-0.09 \mu\text{m}$ with disturbance observer so we can say that we have eliminated the disturbances by using the disturbance observer.

7.4 Conclusion and Comments

Before making the position control of the compliant mechanisms the position control of the piezoelectric actuator is accomplished by using sliding mode control with observer. We have seen the advantage of using observer by making experiments with and without using it. Finally, we can conclude that by using observer the disturbances which are uncertainties, and hysteresis of PEA can be eliminated because the position tracking error is decreased when compared the results with the without observer position control results.

8 POSITION CONTROL OF COMPLIANT MECHANISMS

The position control of the 3-RRR and 3-PRR mechanisms is needed to be used as positioning stages because of the unwanted motions due to manufacturing and assembling errors, moreover the forces acting on the mechanisms are not coinciding at the center of the triangular stages as shown in Section 3, which causes an unwanted rotation causing parasitic errors. We have proposed that these unwanted motions can be eliminated by using a control method based on sliding mode control with modeling a appropriate disturbance observer.

The unwanted motions of the mechanisms are examined experimentally in Section 6. We have observed that the kinematics calculated with the kinetostatic model and finite element analysis do not match with experimental results because our mechanism and setup is not ideal. Thus, with the computed models we can not make the position control of the mechanisms by only controlling the piezoelectric actuators as we have succeed in Section 7 so that we have asked ourselves whether we can fix this problem with a different control methodology.

In the previous section we have only controlled piezoelectric actuators' motion by taking measurement from the strain gauge embedded on the piezo stack. We have seen that sliding mode controller with disturbance observer gave us better results than without using observer. We have implemented the same piezoelectric actuator control to our 3-RRR mechanism by combining the three piezoelectric actuators' models with kinematic relation that is obtained experimentally. Instead of strain gauge measurement we have used dual laser position measurement and converted the x-y motions of the triangular stage to the motions of piezoelectric actuators tips. The reference is set for the x-y motion of the stage and similarly the reference positions for piezoelectric actuators are calculated by using the experimentally obtained transformation matrix.

The position control of 3-PRR compliant mechanism is examined more in detail than 3-RRR compliant mechanism to enhance the position errors that we got from our position control experiments for 3-RRR compliant mechanism. First open loop control

for the piezoelectric actuators is implemented. Thereafter, the same control methodology which is used in 3-RRR compliant mechanism's position control, is used to check for the closed loop control advantage. Then the advantage of redundant system for high precision positioning is analyzed by controlling two piezoelectric actuators for x-y motion. The results are compared with the control of three piezoelectric actuators for x-y motion and the advantage of redundant mechanism is discussed. Finally, the models for each position direction are experimentally extracted by using "System Identification Toolbox" in MATLAB. Instead of using piezoelectric actuators nominal plant for disturbance observer these extracted models are used as linear nominal models for the mechanism motions. The observer control parameters and the position control parameters are tuned to have better results than the previous control method based on only piezoelectric actuator model.

8.1 Position Control of 3-RRR Mechanism

PSt 150/5/40 VS10 piezoelectric actuators which have maximum stroke of $40\ \mu\text{m}$ for unipolar actuation are used. The direction of the motion vectors at the center of the mechanism, which are u_1 , u_2 and u_3 , are experimentally determined to have the kinematics of the mechanism shown in Figure 8.1. After calibration of laser position sensor, we have applied 30, 60, 90, 120 and 150 Volts to the piezoelectric actuators individually when all the piezoelectric actuators are assembled to the mechanism and preloaded before starting actuation.

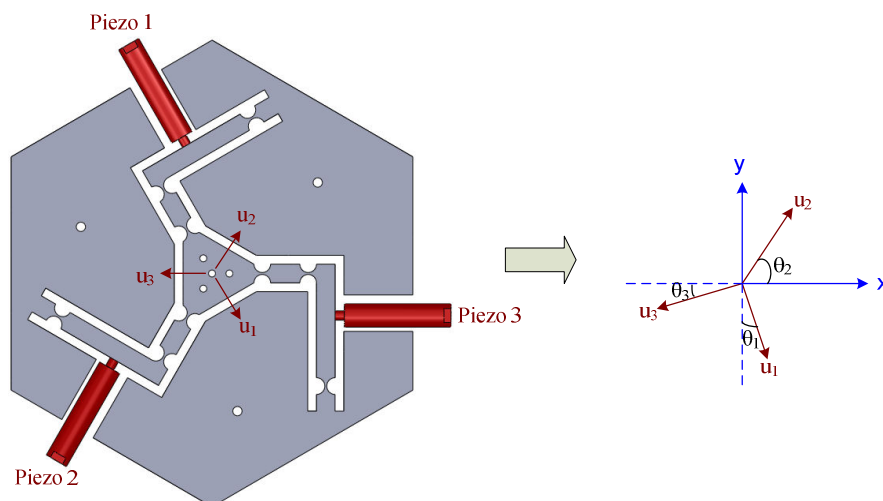


Figure 8.1 Motion vectors of 3-RRR compliant mechanism.

After actuating all piezoelectric actuators individually the transformation matrix \mathbf{A} , which relates the motions u_1 , u_2 and u_3 to x-y motion of the end-effector, is determined using Eqn. 8.1. The results of the experiments are presented in Section 6.2 which are $\theta_1=26^\circ$, $\theta_2=25^\circ$ and $\theta_3=1.5^\circ$.

$$\begin{bmatrix} x \\ y \end{bmatrix} = \underbrace{\begin{bmatrix} \sin(\theta_1) & \cos(\theta_2) & -\cos(\theta_3) \\ -\cos(\theta_1) & \sin(\theta_2) & -\sin(\theta_3) \end{bmatrix}}_{\mathbf{A}} \cdot \begin{bmatrix} u_1 \\ u_2 \\ u_3 \end{bmatrix} \quad (8.1)$$

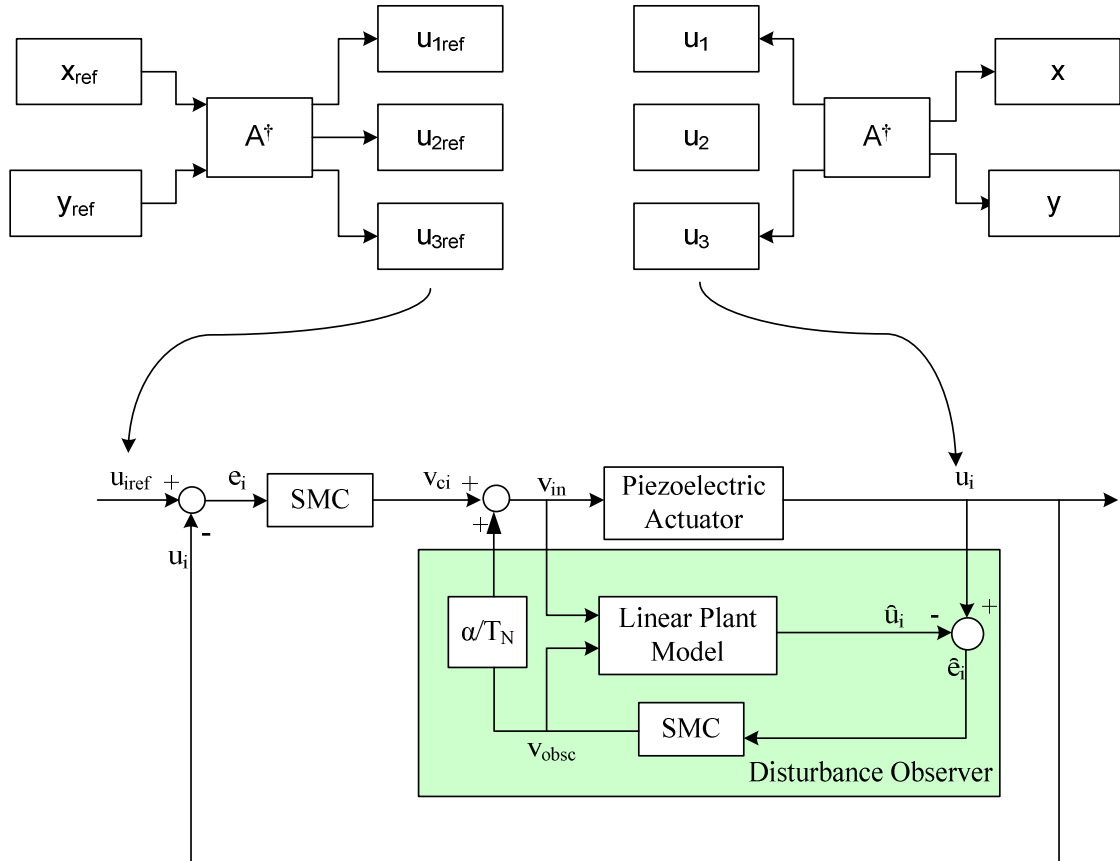


Figure 8.2 Block diagram of the position control of compliant mechanism.

As we have mentioned earlier in Section 3 3-RRR kinematic structure decouples the stiffness between the actuators so that it gives us the advantage of controlling the actuators separately. This means that we can have three independent single input single output (SISO) controllers for this kind of mechanism. The control methodology based on the control of piezoelectric actuators is explained in Figure 8.2. The references of piezoelectric actuators are calculated by multiplying the pseudo inverse of \mathbf{A} matrix in Eqn. 8.1 with the x-y references of the end-effector. Similarly the measured x-y motions using the dual position sensor assembled on the end-effector is multiplied with the pseudo inverse of \mathbf{A} matrix and the motions of piezoelectric actuators u_1 , u_2 and u_3 are

found. The control scheme is explained in Section 7.2. The necessary transformations and control method calculations are coded in C. The sampling time for computing is 100 μ sec which is necessary time for the calculations in dSPACE. The nominal parameters of used PSt 150/5/40 VS10 Piezoelectric actuators are shown in Table 8.1. The sliding mode observer parameters and the sliding mode control for position parameters are presented in Table 8.2. All calculations are done in SI unit system.

Table 8.1 Nominal parameters of PSt 150/5/40 VS10 Piezoelectric Actuator

Parameter	Value
m_n	$6.16 \cdot 10^{-4}$ kg
c_n	1027.5 Ns/m
k_n	$12 \cdot 10^6$ N/m
T	3.1 N/V
α	0.05

Table 8.2 The control parameters of 3-RRR mechanism

Sliding Mode Observer Parameters		Sliding Mode Control for Position Parameters	
K_{obs}	0.000008	K_x	0.005
C_{obs}	10	C_x	80000
D_{obs}	200	D_x	0.0001

Circular references with different diameters are given to the mechanism by giving the x_{ref} and y_{ref} as in Eqn. 8.2-8.3:

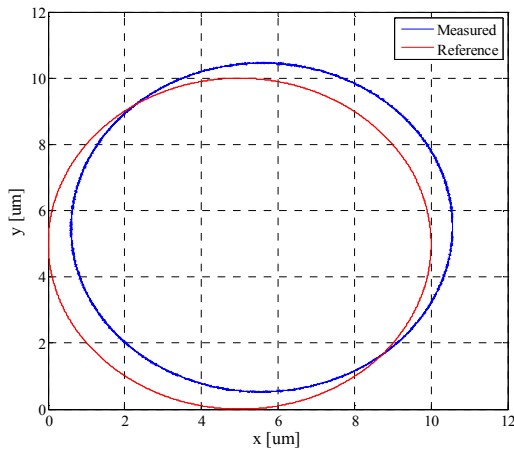
$$x_{ref} = Amp + Amp \sin(2\pi ft) \quad (8.2)$$

$$y_{ref} = Amp + Amp \cos(2\pi ft) \quad (8.3)$$

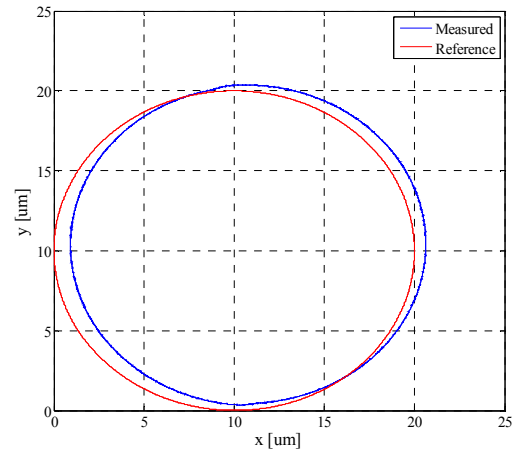
The position control results are presented in Figure 8.3 for different circular references with changing ‘‘Amp’’ parameter representing the radius of the circles, varied from 5 μ m to 30 μ m. The frequency (f) of the reference is set as 0.1 Hz. The center motion of the stage is shifted to the left with respect to the given references.

The x and y motion results and the errors in x and y directions are presented in Figure 8.4 when the radius of the reference circle is 30 μ m. As shown in Figure 8.4 b and 8.d the errors in x and y direction have jumps. This is because the voltage input to

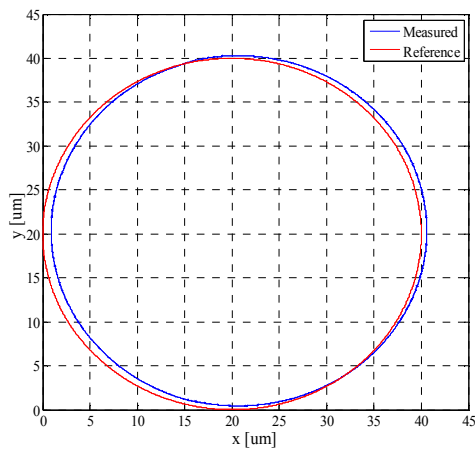
the piezoelectric actuators is saturated between 0-150V not allowing negative values of voltages. The piezoelectric actuators are not fixed to the mechanism; they are just preloaded before actuation and can not pull back the links. This situation can be fixed by having a better observer and tuning the parameters.



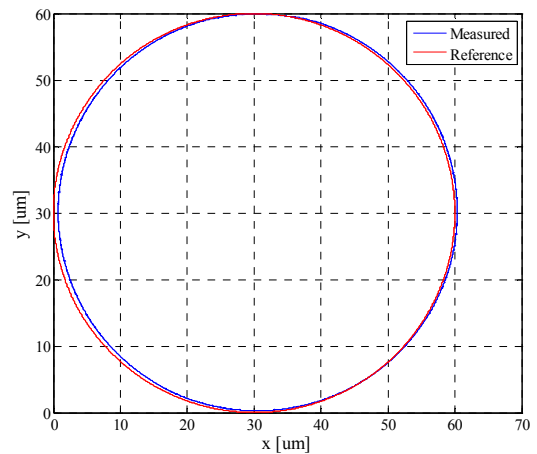
(a) Radius of 5 μm for reference



(b) Radius of 10 μm for reference

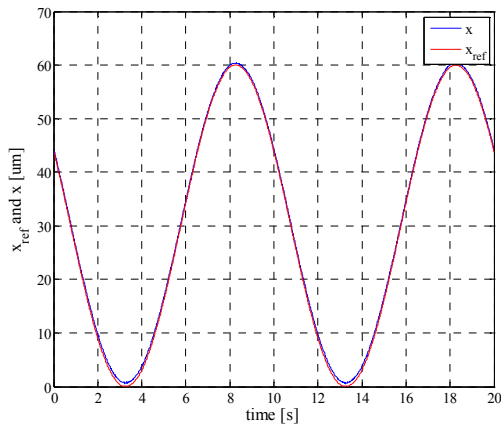


(c) Radius of 20 μm for reference

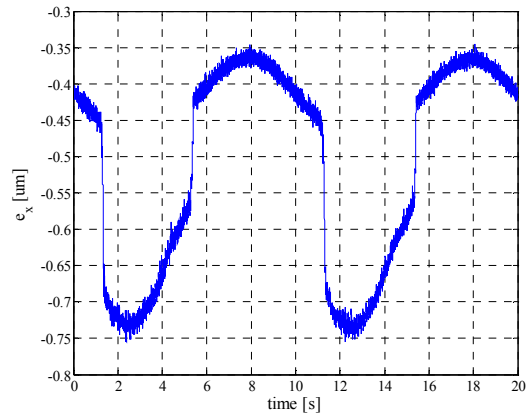


(d) Radius of 30 μm for reference

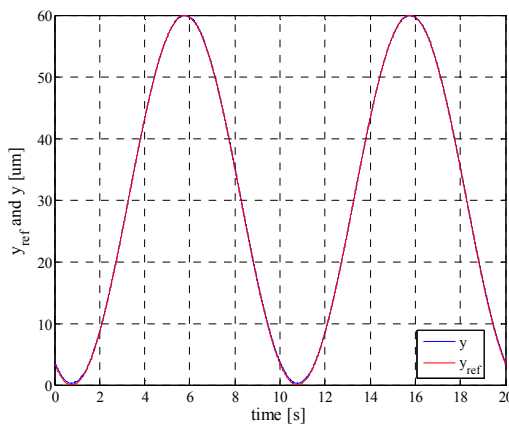
Figure 8.3 Position control results of 3-RRR compliant mechanism.



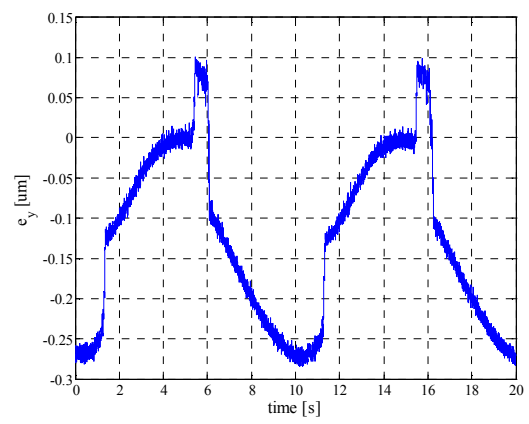
(a)



(b)



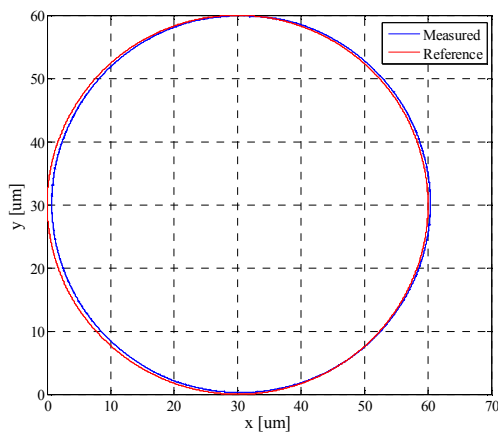
(c)



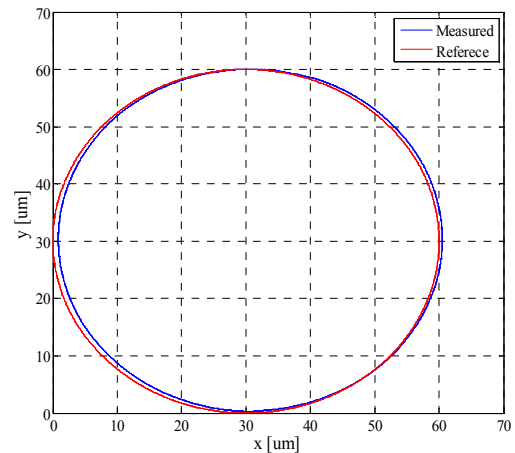
(d)

Figure 8.4 x and y position results when the Radius of reference circle is 30 μm .

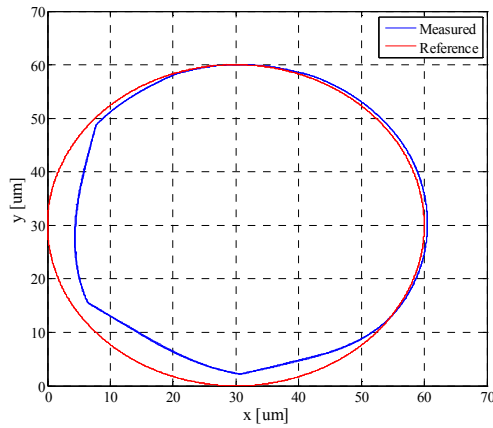
The frequency of the reference circle is increased to 0.2 Hz and 0.3 Hz when the radius is kept constant to 30 μm . The results are shown in Figure 8.5. We can see that when the reference is fast the system can not compute fast enough and the errors increase.



(a) Results of 0.1 Hz



(b) Results of 0.2 Hz



(c) Results of 0.3 Hz

Figure 8.5 Position control results for references having different frequencies.

8.2 Position Control of 3-PRR Mechanism

The position control of 3-PRR compliant mechanism is examined in detail in this section. First, the position control of the compliant mechanism is performed by using a simple PID controller which is common for position control in the literature. Then open loop control by using piezoelectric actuator model is applied to 3-PRR compliant mechanism to compare the results with closed loop control. Thereafter, the closed loop control is applied first to the non-redundant 3-PRR mechanism by using only two actuators for position control in X-Y axes. All three actuators are activated for position control of the 3-RRR compliant mechanism, and the results are compared with the non-redundant case. Finally, the models for each actuation direction are extracted from the experiments of 3-PRR compliant mechanism, and they are used as nominal models of the system instead of piezoelectric actuator models for disturbance observer.

8.2.1 Position Control with Piezoelectric Actuator Models

The direction of the displacement vectors from the PEAs which are u_1 , u_2 and u_3 shown in Figure 8.6 are determined experimentally to have the kinematics of the mechanism. After calibration of laser position sensor, we have applied 30, 60, 90, 120 and 150 Volts to the piezoelectric actuators when all the piezoelectric actuators are assembled to the mechanism and preloaded before starting actuation.

The transformation matrix \mathbf{A} which relates the motions u_1 , u_2 and u_3 to x-y motion of the end-effector can be written as in Eqn. 8.4:

$$\begin{bmatrix} x \\ y \end{bmatrix} = \underbrace{\begin{bmatrix} \sin(\theta_1) & \cos(\theta_2) & -\cos(\theta_3) \\ -\cos(\theta_1) & \sin(\theta_2) & \sin(\theta_3) \end{bmatrix}}_{\mathbf{A}} \cdot \begin{bmatrix} u_1 \\ u_2 \\ u_3 \end{bmatrix} \quad (8.4)$$

The angles of the direction of the u vectors are found as $\theta_1=25^\circ$, $\theta_2=26^\circ$ and $\theta_3=1.5^\circ$.

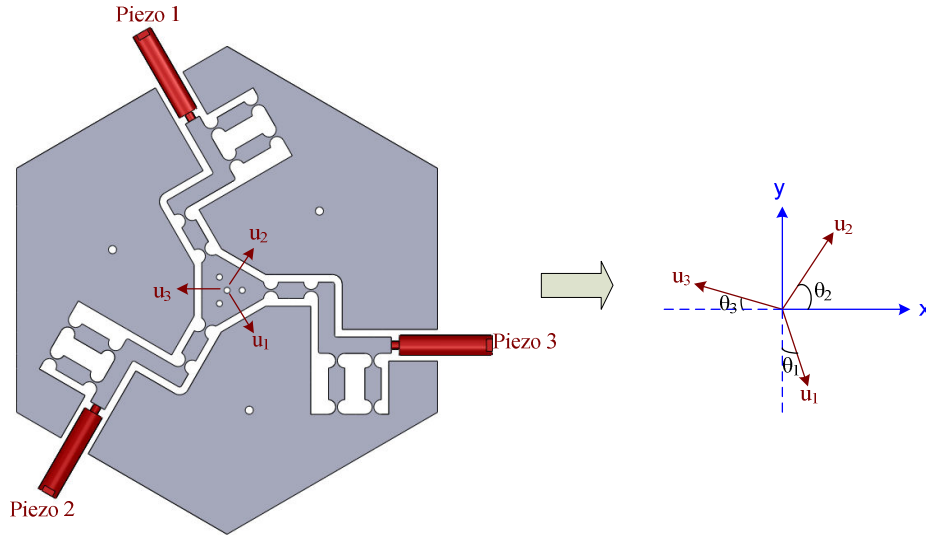


Figure 8.6 Motion vectors of 3-PRR compliant mechanism.

The same position control methodology shown in Figure 8.2 is applied to 3-PRR compliant mechanism by using the pseudo inverse of \mathbf{A} matrix in eqn. (8.4). The necessary transformations and control method calculations are coded in C. The needed sampling time for computing is 100 μ sec. The same sliding mode observer parameters and the sliding mode control for position parameters which are presented in Table 8.2, are used for the experiments

8.2.2 PID Control Results

We have implemented simple PID control as presented in the block diagram shown in Figure 8.7 to compare the results with the proposed control methodology. By using the pseudo inverse of the transformation matrix, \mathbf{A} , we have made the position control of each piezoelectric actuator by using discretized PID controller as follows:

$$v(t) = K_p \cdot e(t) + K_i \int_0^t e(t)dt + K_d \frac{de(t)}{dt} \quad (8.5)$$

$$e_i(t) = u_{iref}(t) - u_i(t) \quad (8.6)$$

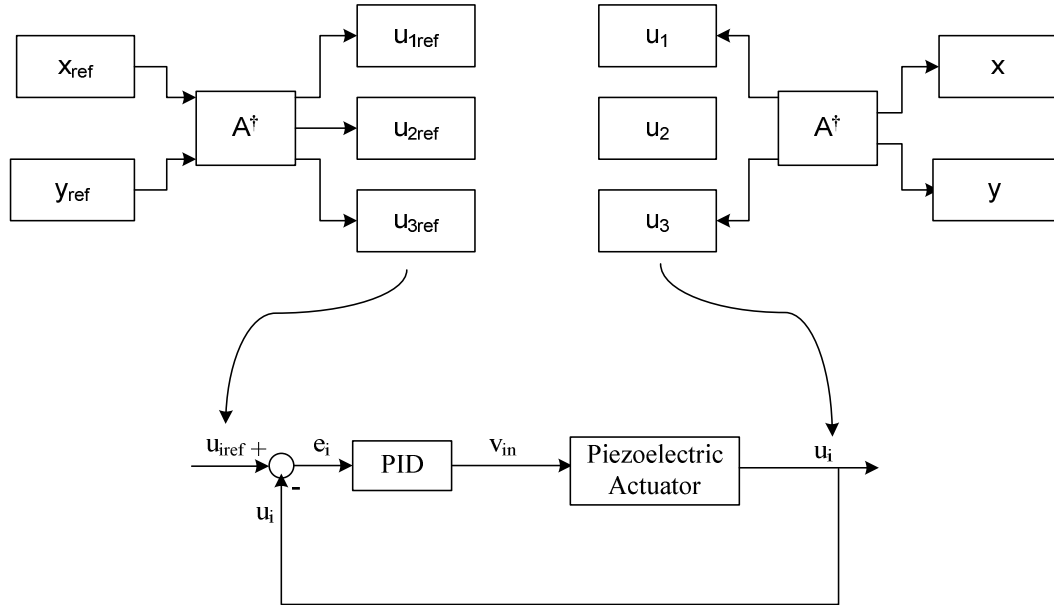
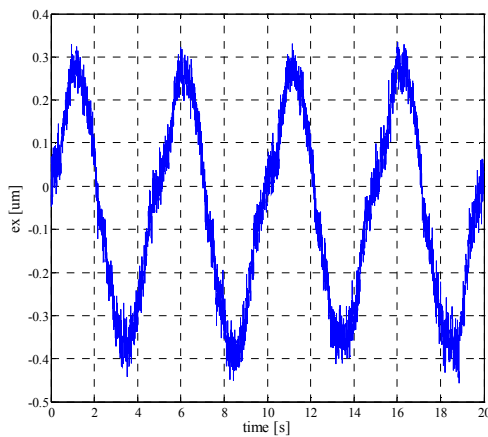
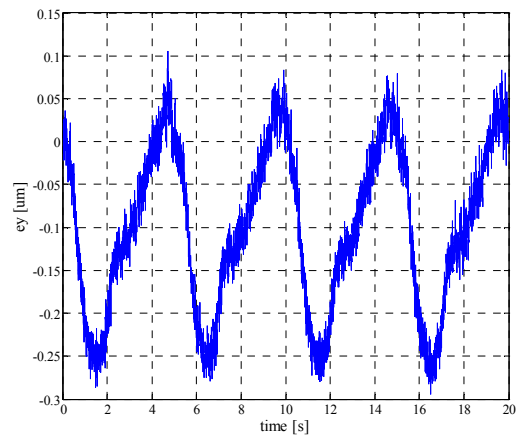


Figure 8.7 Block diagram of the PID position control of compliant mechanism.

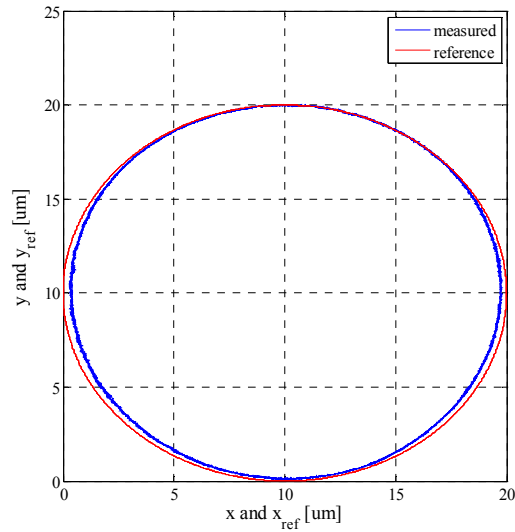
A circular trajectory having 20 μm diameter of circle is given as a reference to the mechanism by setting references as $x_{ref} = 10 + 10 \sin(0.2\pi t)$ and $y_{ref} = 10 + 10 \cos(0.2\pi t)$. The errors in x direction and y direction are shown in Figures 8.8a and 8.8b. The x-y motion is presented in Figure 8c. ($K_p = 0.005$, $K_i = 0.0001$, $K_d = 0.0001$) The results show us that the error in x direction is between 0.3 μm and -0.4 μm , while the error in y direction is between 0.1 μm and -0.25 μm .



(a) Errors in x direction



(b) Errors in y direction



(c) End-effector motion

Figure 8.8 Results of PID position control for 3-PRR compliant mechanism

8.2.3 Open Loop Control with PEA Models

Inverse of the linear model of the plant is used for estimating the necessary voltage input to the piezoelectric actuators as shown in Figure 8.9. Again a circular trajectory having $20\mu\text{m}$ diameter of circle is given as the reference. The errors in x direction and y direction are shown in Figures 8.10a and 8.10b. The x - y motion is presented in Figure 8.10c.

It can be seen from the results that open loop control with the inverse of linear models of the piezoelectric actuators does not have enough accuracy for the end-effector motion of our flexure based mechanism. The error in x direction is between $3\mu\text{m}$ and $-8\mu\text{m}$, while the error in y direction is between $2\mu\text{m}$ and $-8\mu\text{m}$. When we look at the motion result we can examine that the reference trajectory is shifted and it is not in a circular shape.

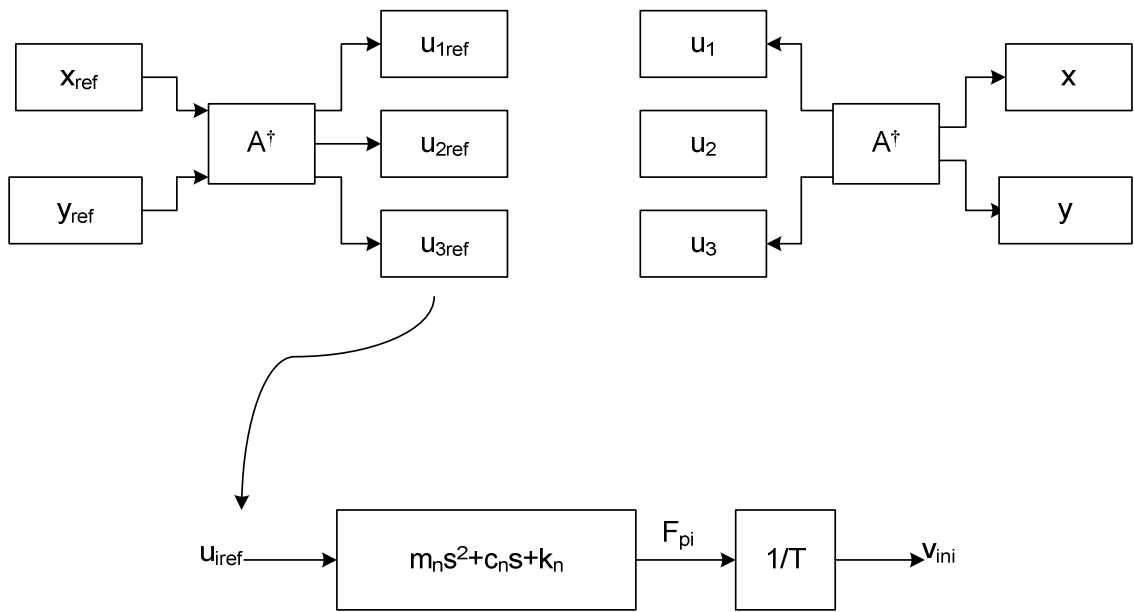


Figure 8.9 Open loop control block diagram.

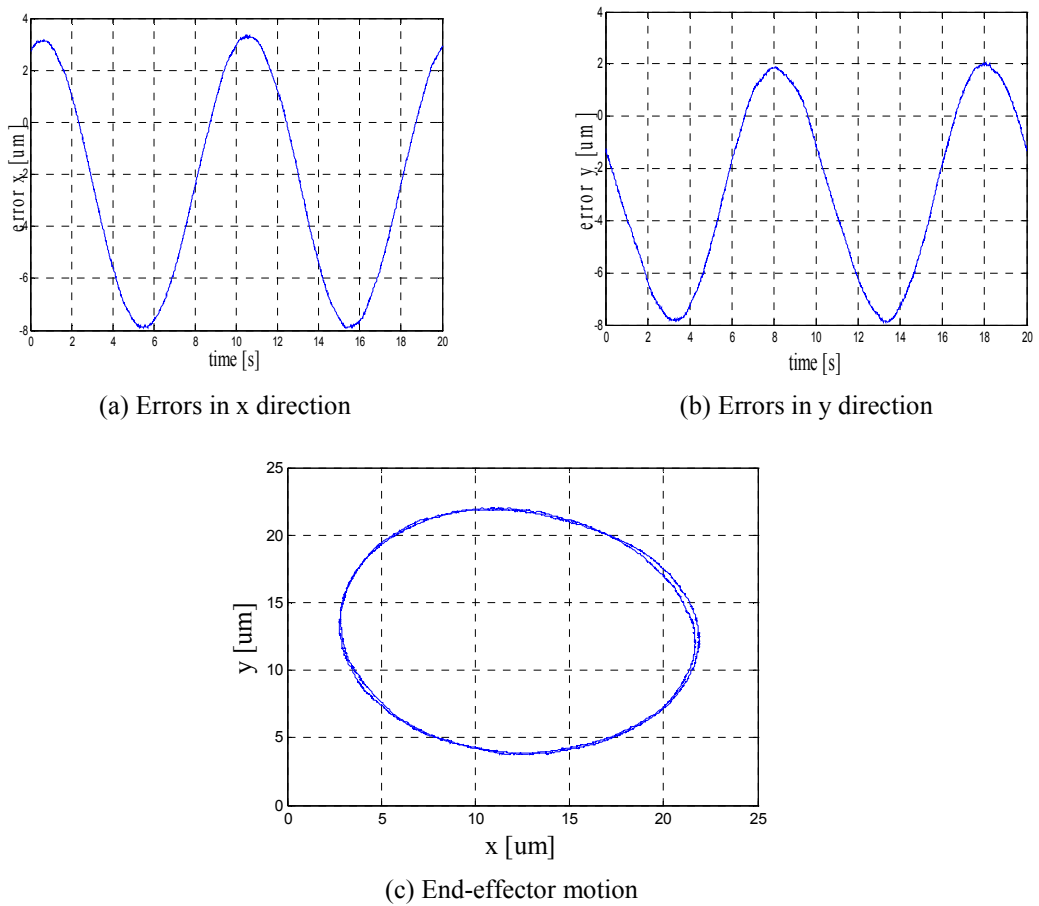


Figure 8.10 Results of open loop control for 3-PRR compliant mechanism.

8.2.4 Closed Loop Control

Closed loop control is applied to the mechanism, and the block diagram of each of the piezoelectric actuator is shown in Figure 8.2. The linear model with the nominal parameters as presented in Table 8.1 is used for the observer with sliding mode control to kill the hysteresis and unwanted disturbances of the system, and another sliding mode control is used for tracking the reference positions. As in open loop control the necessary reference positions of piezoelectric actuators for tracking reference x-y motion is calculated by using pseudo inverse of transformation matrix A . First, 2 piezoelectric actuators (the 2nd and 3rd ones according to the Figure 8.11) are in action while the other piezo (the 1st one) is attached to the mechanism as a rigid support. Then all of the actuators are in action and controlled with the same manner. The sampling time is taken as 100 μ sec.

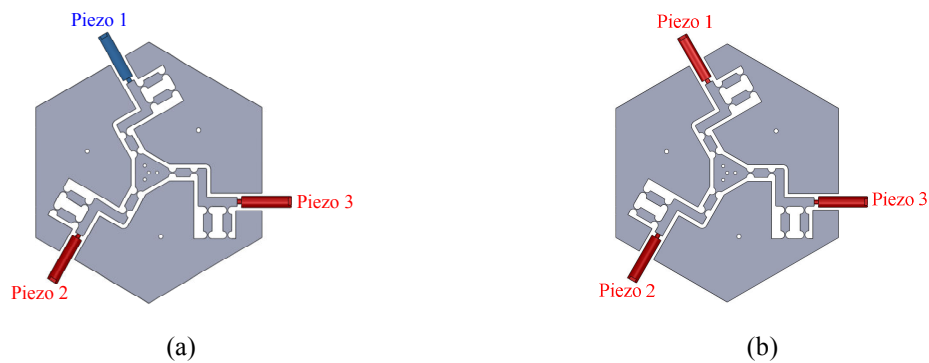


Figure 8.11 (a) 2 PEAs are activated, (b) 3 PEAs are activated.

8.2.4.1 Non-Redundant Control Results

The errors in x direction as shown in Figure 8.12a are between 0.05 μ m and 0.55 μ m and the errors in y direction shown in Figure 8.12b are between 0.05 μ m and 0.5 μ m. The measured x-y motion of the end-effector is presented in Figure 8.12c. The errors are smaller than open loop control of 3 piezoelectric actuators but there is still a shift from the reference trajectory.

The control outputs (piezoelectric inputs), which are amplified 30 times by the piezo amplifier, are shown in Figures 8.13a and 8.13b for two piezoelectric actuators. As seen from figures, the actuators are at almost their maximum stroke, which

corresponds to 150V. Especially the piezoelectric actuator that creates u_2 displacement vector reaches to 150V.

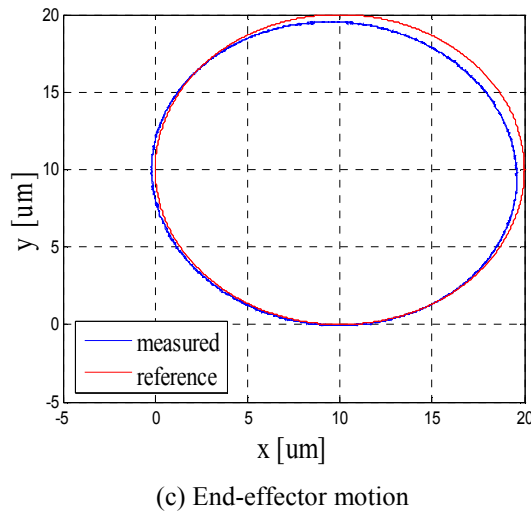
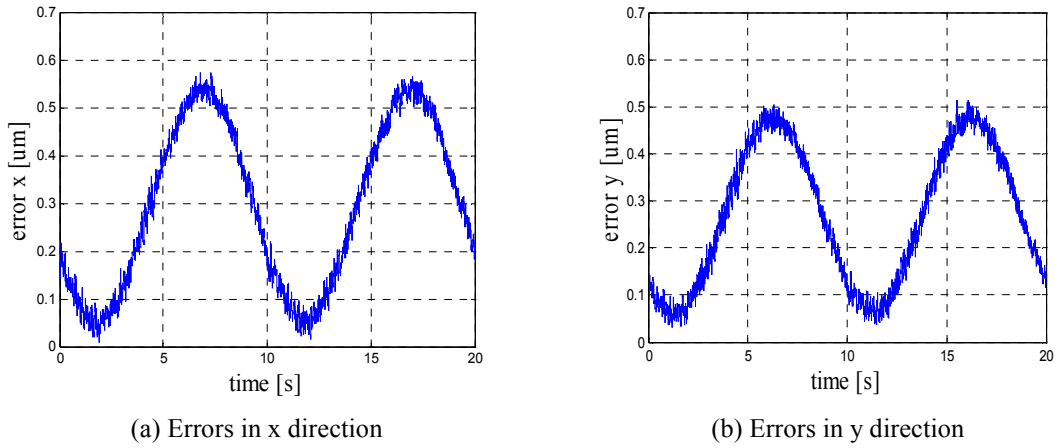


Figure 8.12 . Position control results of 3-PRR compliant mechanism for non-redundant case.

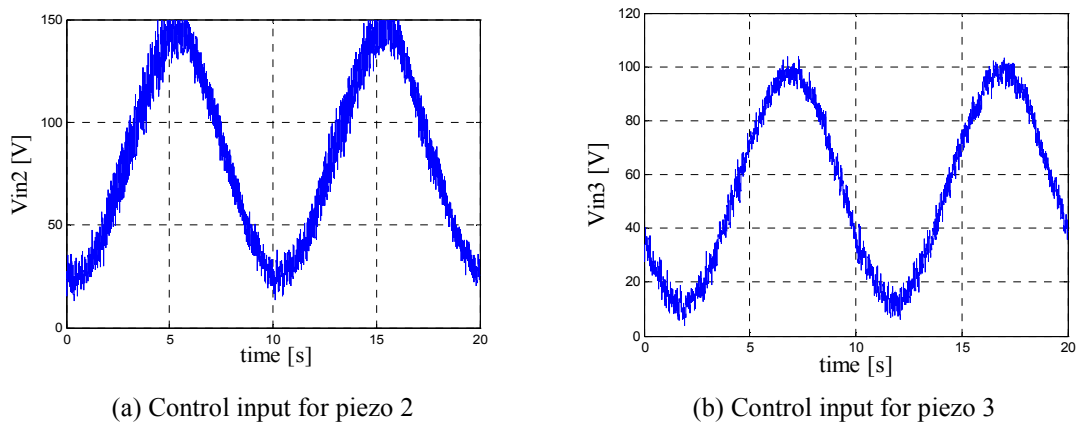


Figure 8.13 Control inputs for non-redundant case.

8.2.4.2 Redundant Control Results

The position control experiments are performed for the redundant case of the mechanism in which all three piezoelectric actuators are controlled.

The errors in x direction is between $-0.15 \mu\text{m}$ and $0.25 \mu\text{m}$ as shown in Figure 8.14a while the errors in y direction is between $0.06 \mu\text{m}$ and $0.25 \mu\text{m}$ as shown in Figure 8.14b. x-y motion results compared with the reference motion shown in Figure 8.14c.

The control outputs for piezoelectric actuators which are amplified by 30 with the amplifier of the piezoelectric actuators, are shown in Figures 8.15a, b and c. The voltages are not close to their maximum voltage (150 V). Thus, this means that the redundancy allows us to extend the workspace when compared to the results of 2 actuators results.

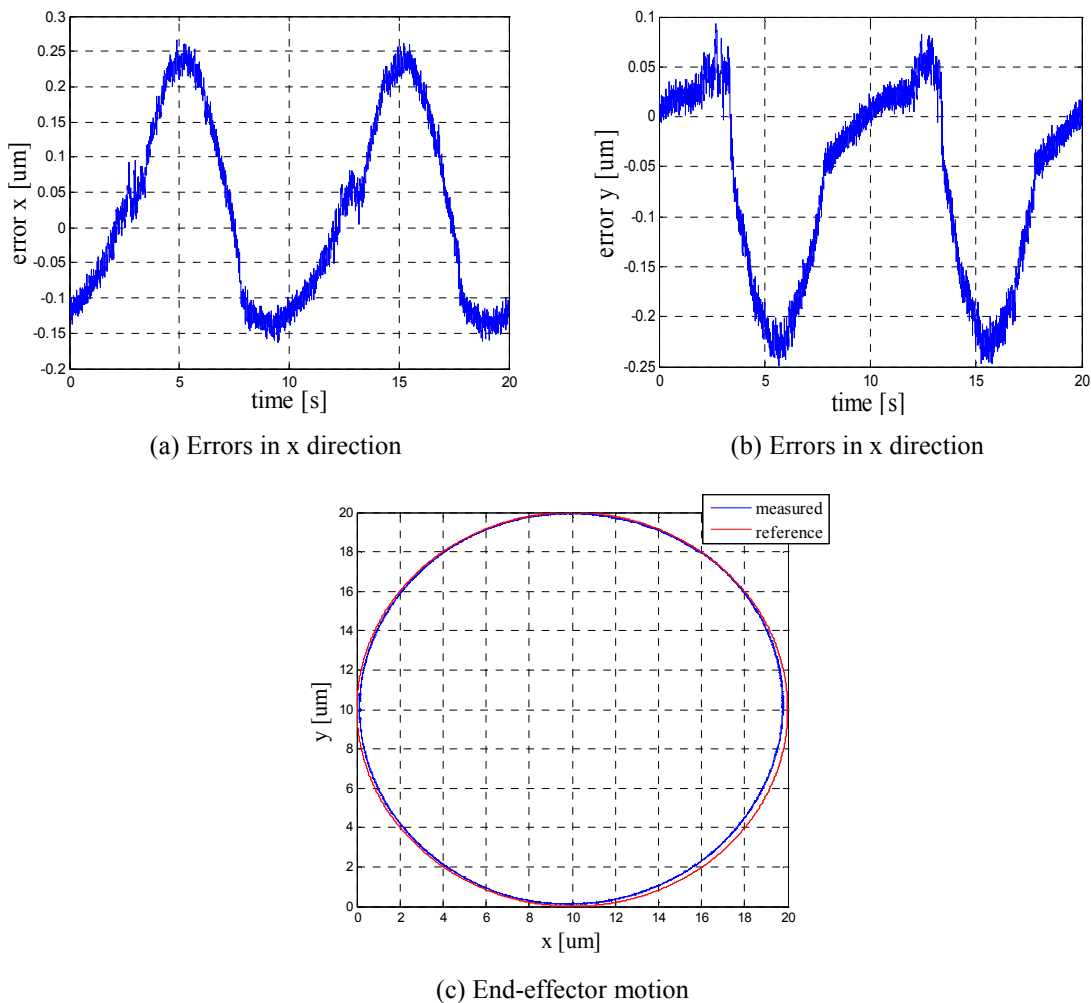
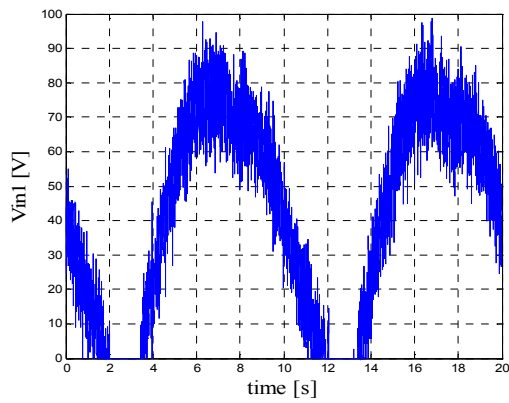
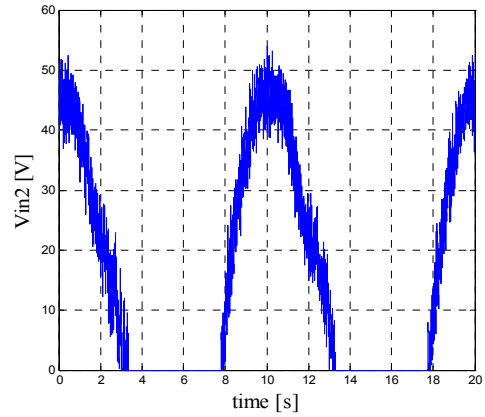


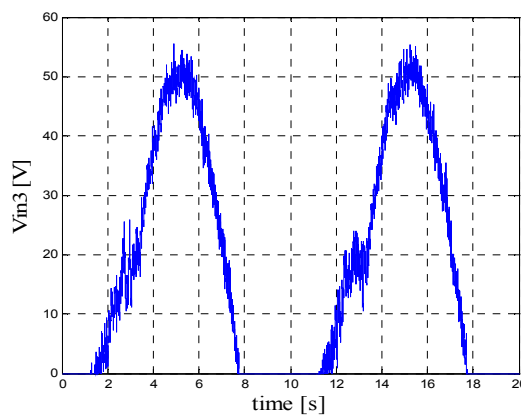
Figure 8.14 Position control results of 3-PRR compliant mechanism for redundant case.



(a) Control input for piezo 1



(b) Control input for piezo 2



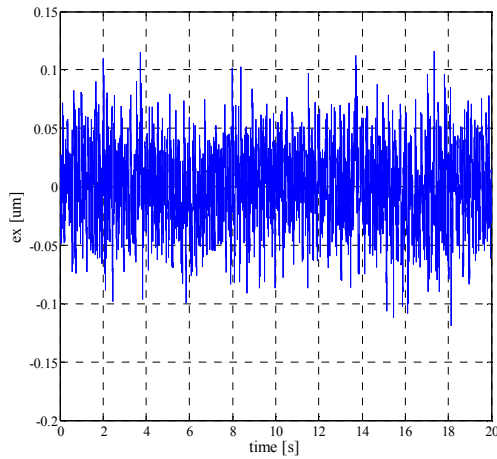
(c) Control input for piezo 3

Figure 8.15 Control inputs for redundant case.

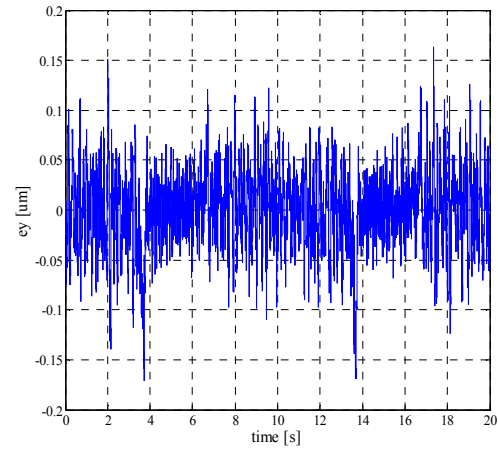
Table 8.3 Tuned SMC disturbance observer and SMC position controller parameters

Sliding Mode Observer Parameters		Sliding Mode Control for Position Parameters	
K_{obs}	0.000002	K_x	0.02
C_{obs}	1	C_x	40
D_{obs}	50	D_x	3000

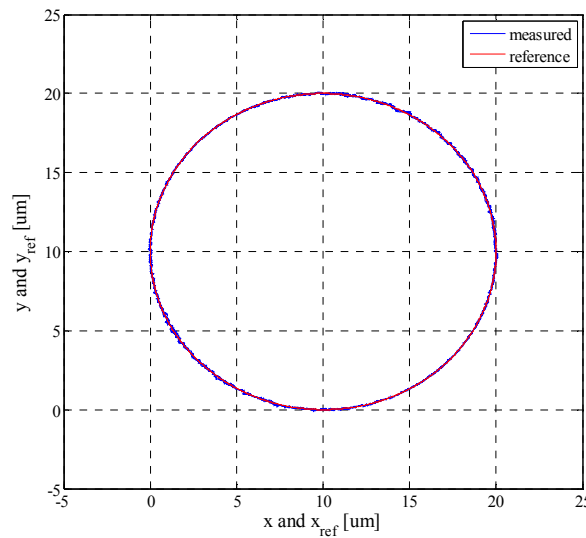
The control parameters are tuned (Table 8.3) and the new results for the same reference are presented in Figure 16. It can be seen that the errors in x direction is decreased to $\pm 0.12 \mu\text{m}$ while the errors in y direction are decreased between $0.17 \mu\text{m}$ and $-0.13 \mu\text{m}$.



(a) Errors in x direction



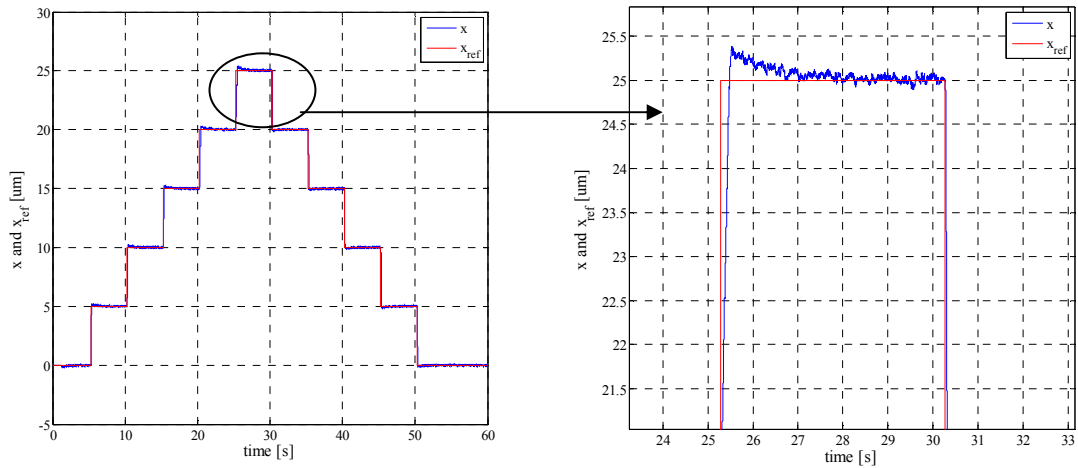
(b) Errors in y direction



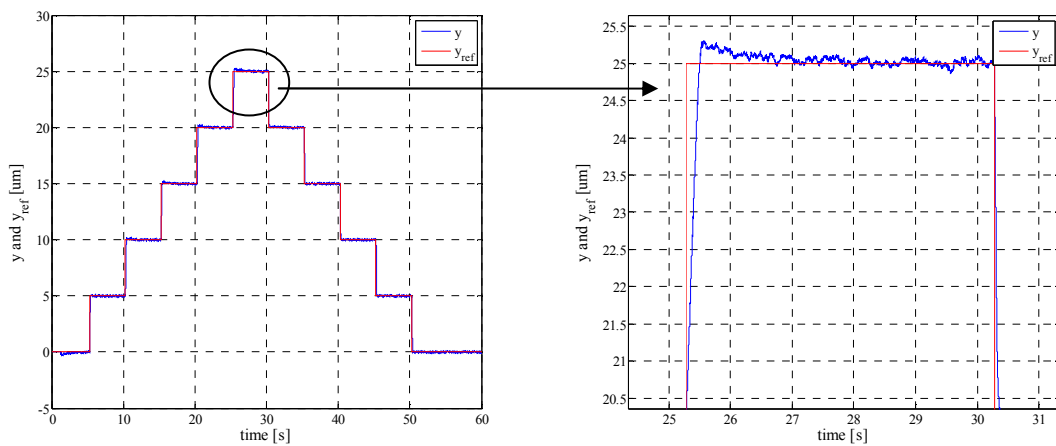
(c) End-effector motion

Figure 8.16 Position control results of 3-PRR compliant mechanisms with tuned parameters.

Stepwise motion is generated by giving x and y motion references having $5 \mu\text{m}$ steps for each 5 seconds as shown in Figure 8.17 to see the behavior of the positioner for step responses. If we look close, we can see that we have overshoots in x and y directions and small vibrations due to measurement which has a 2nd order filter.



(a) Step references in x direction



(b) Step references in y direction

Figure 8.17 Step responses with $5\mu\text{m}$ steps in x and y directions using position control with PEA models.

8.2.5 Experimental Modeling of 3-PRR Compliant Mechanisms

The models separately for u_1 , u_2 and u_3 motion of the 3-PRR compliant mechanism are experimentally extracted. Each piezoelectric actuator is actuated by applying a step voltage of 120 V and the end-effector position is measured from dual position sensor in x and y axes by using the pseudo inverse matrix \mathbf{A} . The x-y position measurement is converted to the positions in u_1 , u_2 and u_3 directions. The step input results for each actuation are used for estimating the models for each actuation. The “System Identification Toolbox” is used in MATLAB by giving the input results as the applied voltage and the output results, which are the motions in u_1 , u_2 and u_3 directions.

The three models are estimated by selecting the transfer function as a second order transfer function in the form of Eqn. 8.7:

$$G(s) = \frac{T_{p1}}{(1 + T_{p2} \cdot s)(1 + T_{p3} \cdot s)} \quad (8.7)$$

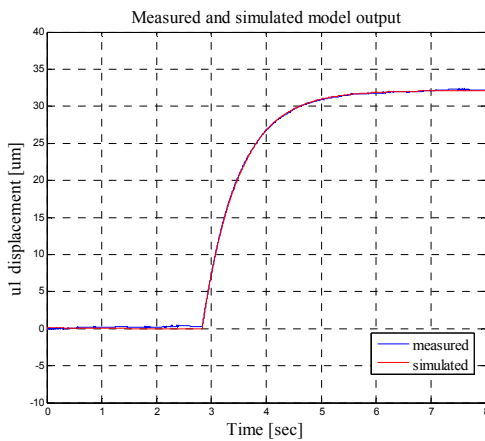
The estimated transfer functions step responses with 120 V applied and the experimental data for the same step responses for each direction is presented in Figure 8.18. The step responses are slow when compared to piezoelectric actuator step response is because of the limitation in measurement taken from the laser position sensor. In order to get reasonable data from the measurements we have used a second order filter as explained in section 6.1.4 and the filter makes the system slow.

The estimated transfer functions $G_1(s)$, $G_2(s)$ and $G_3(s)$ could represent the experimental data. (respectively %98.92, % 99.44 and % 99.78) .

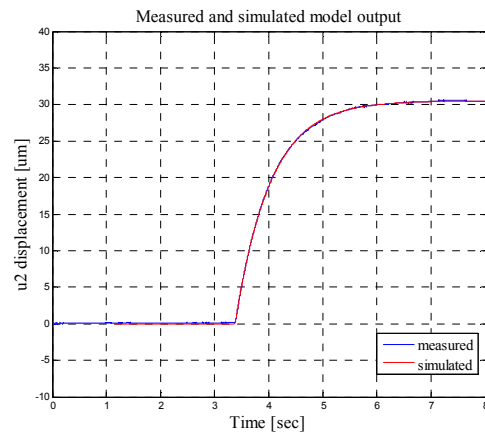
The results for model estimations are presented in Table 8.3

Table 8.4 Estimated transfer functions parameters

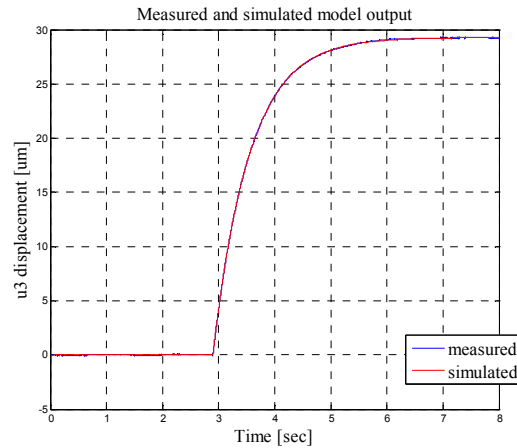
Parameters	$G_1(s) = \frac{U_1(s)}{V_1(s)}$	$G_2(s) = \frac{U_2(s)}{V_2(s)}$	$G_3(s) = \frac{U_3(s)}{V_3(s)}$
T_{p1}	80.262	76.305	73.218
T_{p2}	0.65557	0.65228	0.65349
T_{p3}	0.001	0.0034021	0.0038507



(a) Step response of u_1 direction



(b) Step response of u_2 direction



(c) Step response of u_3 direction

Figure 8.18 Experimental models and experiments results for step responses 3-PRR compliant mechanism.

The transfer functions for each direction is different as seen from the estimated parameters in Table 8.4. This means that the behavior of the mechanism for each actuation direction is different due to manufacturing and assembling errors. It would be better to use these estimated models instead of using the same linear piezoelectric models for each direction.

8.2.5.1 Position Control Results with Experimental Models

The experimentally estimated transfer functions are used as nominal transfer functions for every motion direction instead of piezoelectric actuator models in Eqn. 7.18 as shown in Figure 8.19. A circle with diameter of $20 \mu\text{m}$ is given as a reference and the Sliding Mode Control Parameters and Disturbance Observer Parameters are adjusted as presented in Table 8.3. The errors in x and in y directions due to changed control parameters are presented in Figures 8.20a and 8.20b which show that the errors are lowered almost to the accuracy of the used position sensing device, which is $0.06 \mu\text{m}$. The center of the stage tracks the reference as shown in Figure 8.20c. The errors shown in Figure 8.20 are due to measurement disturbances. This means that we have succeeded to provide position control of our compliant mechanism in the accuracy of the measurement by using experimental model results instead of piezoelectric actuator model.

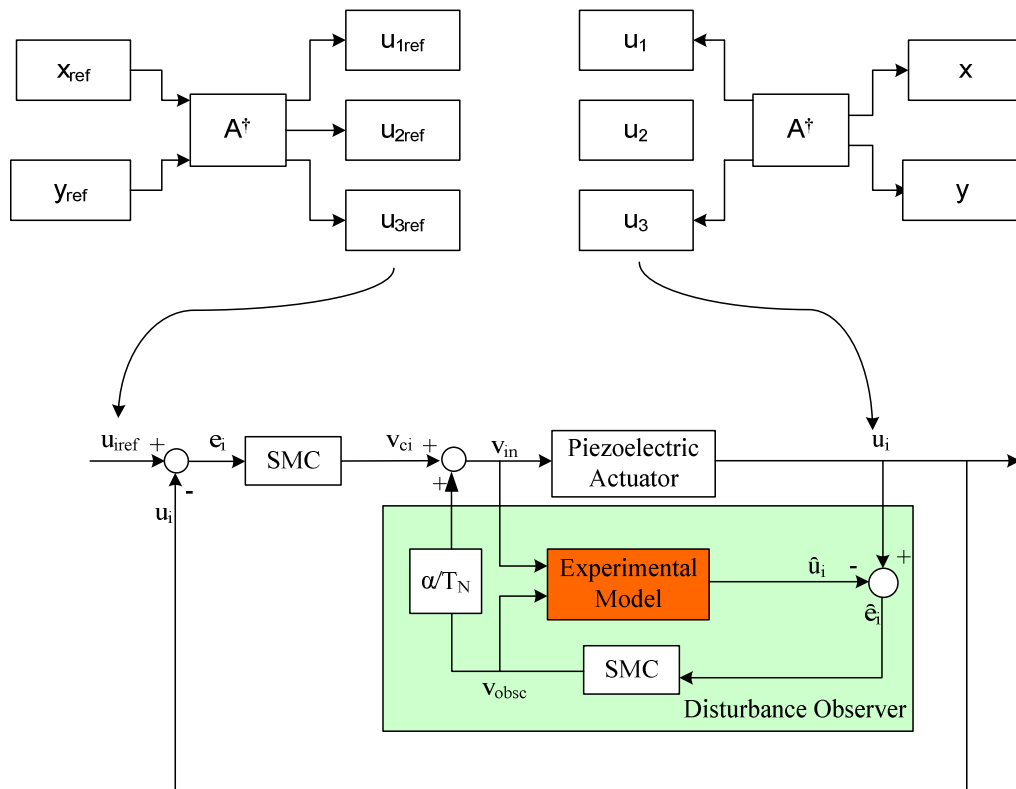
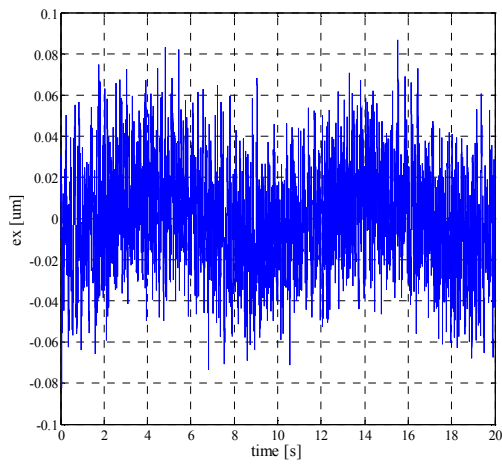
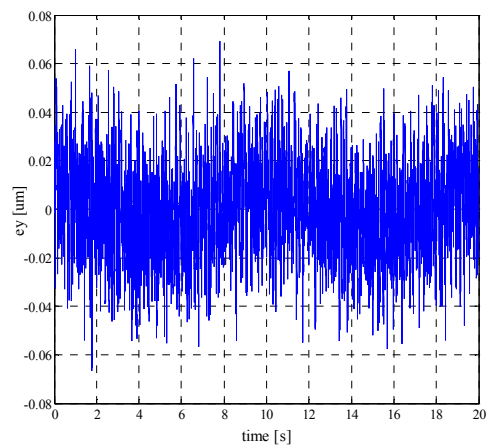


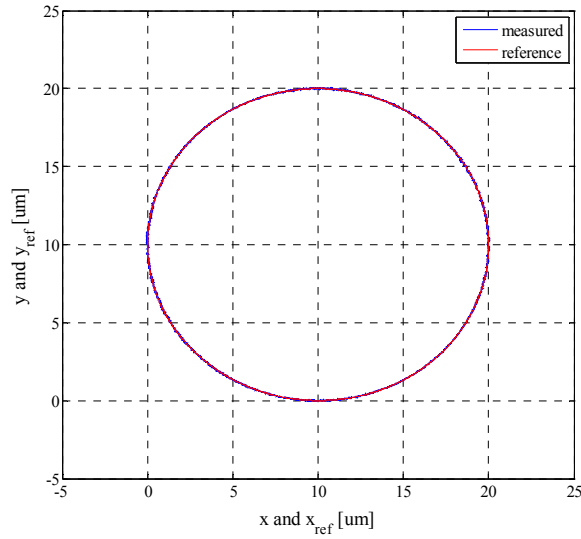
Figure 8.19 Sliding mode position control with experimental model based disturbance observer.



(a) Errors in x direction



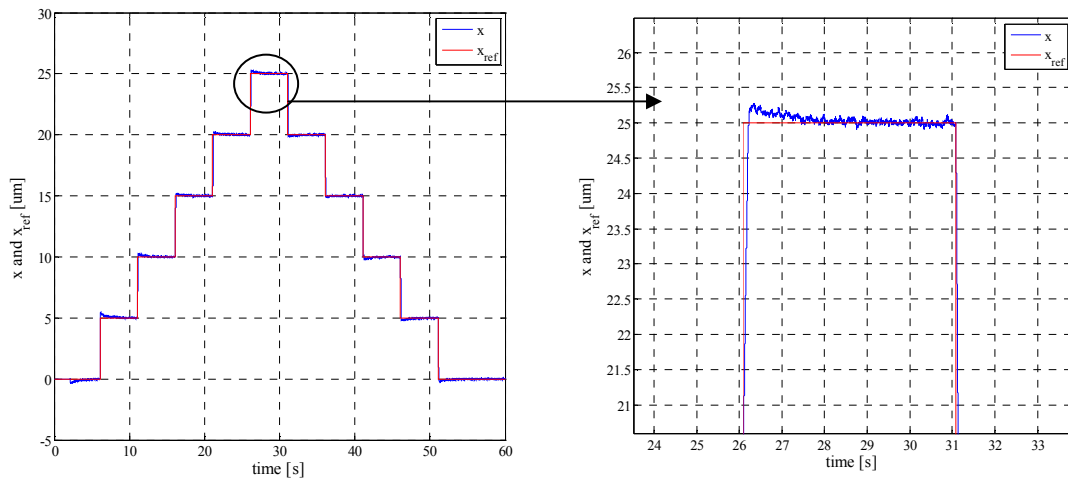
(b) Errors in y direction



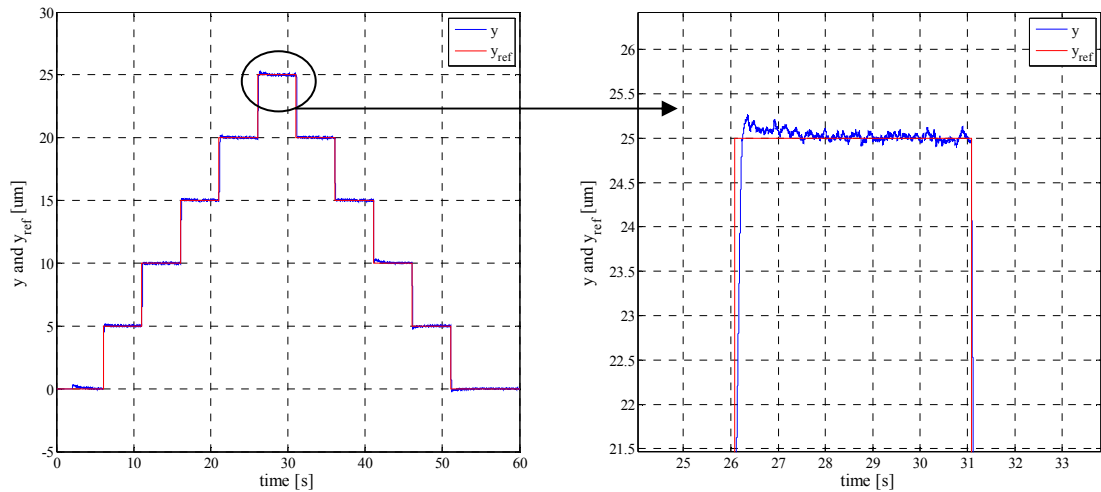
(c) End-effector motion

Figure 8.20 Position control using experimental models results of 3-PRR compliant mechanism.

Stepwise motion is generated by giving x and y motion references having $5 \mu\text{m}$ steps for each 5 seconds as shown in Figure 8.21 to see the behavior of the positioner to step responses. If we look closely for the same control parameters we can see that we have overshoots in x and y directions, which are lower than the results, where PEA models are used instead of experimental models shown in Figure 8.17.



(a) Step references in x direction



(b) Step references in y direction

Figure 8.21 Step responses with $5\mu\text{m}$ steps in x and y directions using position control with experimental models.

8.3 Conclusion and Comments

We have examined the position control of compliant mechanisms in this section and conclude with a control methodology based on sliding mode control with observer by using experimental 2^{nd} order transfer functions in each direction of motion provided from the piezoelectric actuators.

First by using the transformation matrix the piezoelectric actuators motion u_1 , u_2 and u_3 is obtained by using experimental data the position control is made only by using the position control of piezoelectric actuator based on the linear model of the actuators for the disturbance observer. For the 3-RRR compliant mechanism the position error in x direction is between $-0.35\ \mu\text{m}$ and $0.7\ \mu\text{m}$, the error in y direction is between $-0.7\ \mu\text{m}$ and $0.1\ \mu\text{m}$. We have seen that when the frequency of the circular reference increases the errors get bigger due to lack of computing performance of dSPACE 1103.

Different types of control methodologies have been applied to 3-PRR compliant micropositioning stage. The error results are shown in Table 8.5. First simple PID control is applied and the parameters are tuned. Then open loop control by using piezoelectric actuator is applied and gave us bad results which shows us that there are unpredictable motions in our mechanism. Then we have applied the same control methodology that is used for 3-RRR compliant mechanism. The benefit of redundancy

of the compliant mechanism is also presented by only actuating 2 piezoelectric actuators in 3-PRR compliant mechanism. The results showed us that the workspace is decreased as we have expected and besides the position errors get bigger which is between 0.05 μm and 0.55 μm for x direction and between 0.05 μm and 0.5 for y direction. We have tuned the control parameters of SMC with DOB by using PEA models and decreased the errors $\pm 0.12 \mu\text{m}$ for x direction and between 0.17 μm and -0.13 μm for y direction. We have also observed the stepwise motion of the mechanism which have small overshoots.

Table 8.5 Errors in x and y direction for 3-PRR compliant microposition stage with different control types

Control Type	Error in x direction [μm]	Error in y direction [μm]
PID	0.3 μm and -0.4 μm	0.1 μm and -0.25 μm
Open Loop with PEA Model	3 μm and -8 μm	2 μm and -8 μm
SMC with DOB by using PEA Models	$\pm 0.12 \mu\text{m}$	0.17 μm and -0.13 μm
SMC with DOB by using Experimental Models	$\pm 0.06 \mu\text{m}$	$\pm 0.06 \mu\text{m}$

Finally we have designed a different control method based on SMC with observer by using extracted experimental transfer functions in each actuation direction for the 3-PRR compliant mechanism. The extracted transfer functions also show that for each direction of motion the behavior of the mechanism is different due to nonlinearities based on manufacturing, assembling errors. The models are put as linear models instead of piezoelectric actuators linear transfer function based on nominal parameters. The observer and control parameters are used as the same as the tuned versions using PEA models. We have succeeded to lower the position errors down to $\pm 0.06 \mu\text{m}$, which is the accuracy of the dual laser position sensor. Stepwise motion is also given as the reference for the new proposed control method, and it is seen that we have less overshoots than the previous controller using PEA models.

9 CONCLUSION AND FUTURE WORK

In this thesis, compliant mechanisms based on 3-RRR and 3-PRR kinematic structures have been designed as fine positioning stages for X-Y positioning and came up with a methodology of control to overcome the problems that are brought by unpredictable behaviors and manufacturing/ assembling errors.

The decided compliant mechanism should be stiff enough for parasitic motions and flexible enough to provide motion at least 40 μm in X-Y directions which is the maximum stroke of our piezoelectric actuators. We have chosen to have a triangular stage as the end-effector having three actuation points coming from the edges of the triangle. Having 3 actuators for x-y motion will give us a redundant system which will improve the range capability and improve our control methodology. The first compliant stage is based on rigid 3-RRR kinematic structure having right flexure hinges as revolute joints. Then 3-PRR compliant stages are designed to improve the stiffness of the stage by having linear spring parallelogram mechanism as prismatic joints. Besides providing redundancy to be used as only x-y positioning another reason to select this kinematic structure is that these kinematic structures decouple the stiffness between the actuators so it gives the advantage of controlling the actuators separately. So we can use 3 independent single input single output (SISO) controllers.

The selection of right circular flexure joint type is made with the results of Finite Element Analysis using COMSOL software. The stress distributions and displacements of different kinds of flexures are examined and it's concluded that the right circular flexure hinges are the best choice among the elliptical ones because the stress is located mostly on the small area of the thinnest part of the flexure which means that the flexure bends at a certain point so eliminates the parasitic motions mostly. Although Right circular flexure hinges have the least range but we are dealing with small motions (<40 μm) so right circular flexure hinges are chosen for our design. The parameters of the right circular flexure hinges the thinnest part of the flexure, "t", and the overall thickness, "b", are selected from FEA analysis of various selection of parameters. The

analysis showed us that there is an inverse asymptotical relationship between the “t”, “b” values and the maximum stress, displacement. We need enough flexibility for providing enough displacement and we need our mechanism to be stiff enough not to go under plastic deformation. That’s why with considering of the capability of our Wire EDM manufacturing we have selected the “b” and “t” values.

3-RRR and 3-PRR compliant mechanisms are examined with the selected parameters. The aims of these analyses are to find the provided maximum displacement at the center of the stage, the motion directions for the center of the stage and the natural frequencies of the mechanism. The analyses are done for two cases. Firstly the mechanisms are only fixed from the fixture links and the other links are set free. Secondly the mechanisms are fixed from the fixture links and the links that are used to actuate the mechanism are constrained by assigning a prescribed displacement defining that there are piezoelectric actuators assembled to the mechanism and they prevent the motion of the links in pull direction of the piezoelectric actuators. We have compared the two structures that we have designed in terms of providing motions, achievable workspaces and frequency modes. We have found out that 3-PRR mechanism improves the range of the mechanism, the translational resonance mode whereas it causes more rotation than 3-RRR mechanism.

After making computations by using Finite element analysis software we have searched for a method to model the behavior of compliant mechanisms. The model of a flexure based mechanism should be simple enough to calculate the behavior of the flexure and accurate enough to be used as a tool for design. Thus, Pseudo-Rigid-Body-Model (PRBM) [6] in which flexure hinges are treated as torsional springs and the compliant mechanism is treated as an ordinary rigid body mechanism is mainly used. Firstly, the calculation methods of in-plane x, y translational compliances and z rotational compliance of a certain circular flexure hinge that we have used in the design of compliant mechanisms are examined. The methods are compared with the finite element analysis. We have found out that Schotborgh method can only be used for the rotational compliance in z direction, the translational compliances in x and y directions has bigger errors compared to other methods because of the difference of his hinge models. Paros and Weisboard’s calculations give the best translational compliance in y direction and rotational compliance in z direction and finally the translational compliance in x direction can be most accurately calculated by the Wu and Lobontiu’s method. The compliance calculation methods are also compared with the finite element

analysis (FEA) for varying geometric parameters “b” (the width of the flexure) and “t” (the shortest distance of the flexure). These analyses give us the selectable calculation methods for certain “b” and “t” parameters besides they show which geometric parameter (b or t) have more influence on in which direction of compliances. Thus this work gives us the advantage of selecting the right calculation methods and geometric parameters for designing flexure based mechanisms.

The compliances of the flexure hinges are combined with the kinematic of the mechanisms by applying kinetostatic method which provides an easier and faster calculation method than FEA. We have applied this method only for our 3-PRR compliant mechanism. The method depends on the compliance calculations which we have found the best calculation method for translation in x and y direction and rotational in z direction. We have compared the $C_{o,Fin}$ matrix results with Finite Element Analysis the angular displacement of the stage has the most error which is almost %15 and the error for displacements in x-y axes is between 8-9%. The Jacobian matrix has errors between almost %13-15. Then by using $C_{o,Fin}$ compliance matrix and Jacobian matrix we have defined mass-spring systems for each actuation direction. We have calculated the stiffness matrix and finally we have got the natural frequency of the mechanism which is close to Finite Element Results with the error of %9.8. The errors are because the compliance calculation errors that we have seen in Section 4 and we have taken the links as rigid whereas in FEA the links are also bending which affects the results. So if the links are taken as beams and if the deflections of the beams are calculated the modeling results are expected to be improved.

We have made the performance experiments of 3-RRR and 3-PRR compliant mechanisms as we have analyzed in Finite element analysis. We have compared the experimental results of 3-RRR and 3-PRR compliant mechanisms. When only the piezoelectric actuator which will actuate the mechanism is only connected and preloaded the 3-PRR compliant mechanism give us better results because the motion vectors are almost parallel to the direction of the actuation forces. However when all piezoelectric actuators are connected, which is the practical case, 3-PRR mechanism results more shifted motion vectors than 3-RRR compliant mechanism because of the moment creation when the other links are supported even though they are not in action. There can also be more manufacturing and assembling errors. The workspace of 3-RRR compliant mechanism is bigger than the 3-PRR compliant mechanism because it's more flexible. . The experimental results are compared with the Finite element results to see

how far we are from the ideal cases. All piezoelectric actuators are connected to the mechanism and preloaded. PSt 150/5/60 VS10 piezoelectric actuator having maximum stroke of 60 μm for unipolar actuation with strain gauge measurement is used to have the information about input displacement to compare FEA results. The results showed us that manufactured mechanisms are not close to the ideal actuated mechanisms. That's why we need to have a control method to eliminate those errors and make our mechanisms to be useful as a high precision positioning stage.

Before making the position control of the compliant mechanisms the position control of the piezoelectric actuator is done by using sliding mode control with observer. We have seen the advantage of using observer by making experiments with and without using it. Finally, we can conclude that by using observer the disturbances which are uncertainties, hysteresis of PEA can be eliminated because the position tracking error is decreased when compared the results with the without observer position control results.

We have examined the position control of compliant mechanisms and conclude with a control methodology based on sliding mode control with observer by using experimental 2nd order transfer functions in each direction of motion provided from the piezoelectric actuators. First by using the transformation matrix between the center of the stage of motion in x-y axes and the piezoelectric actuators motion u_1 , u_2 and u_3 is found by using experimental data the position control is made only by using the position control of piezoelectric actuator based on the linear model of the actuators for the disturbance observer. We have set a reference circular path having a diameter of 20 μm for all control implementations. For the 3-RRR compliant mechanism the position error in x direction is between -0.35 μm and 0.7 μm , the error in y direction is between -0.7 μm and 0.1 μm . The same control methodology is applied to 3-PRR compliant mechanism with the errors between -0.15 μm and 0.25 μm for x direction and the errors between 0.06 μm and 0.25 μm for y direction. We have also seen that when the frequency of the circular reference increases the errors get bigger due to lack of computing performance of dSPACE 1103. The benefit of redundancy of the compliant mechanism is also presented by only actuating 2 piezoelectric actuators in 3-PRR compliant mechanism. The results showed us that the workspace is decreased as we have expected and besides the position errors get bigger which is between 0.05 μm and 0.55 μm for X direction and between 0.05 μm and 0.5 for Y direction. We have tuned the parameters for SMC with Disturbance observer based on SMC by using PEA

models for redundant 3-PRR compliant mechanism and we have succeeded to lower the errors the errors in x direction to $\pm 0.12 \mu\text{m}$ and the errors in y direction between $0.17 \mu\text{m}$ and $-0.13 \mu\text{m}$.

Finally we have designed a different control method based on SMC with observer by using extracted experimental transfer functions in each actuation direction for the 3-PRR compliant mechanism. The extracted transfer functions also show that for each direction of motion the behavior of the mechanism is different due to nonlinearities based on manufacturing, assembling errors. The models are put as linear models instead of piezoelectric actuators linear transfer function based on nominal parameters. The observer and control parameters are selected same as we have tuned for the 3-PRR compliant stage position control. At the end we have observed that the position errors are almost decreased to $\pm 0.06 \mu\text{m}$ which is the accuracy of the dual laser position sensor that we have used. We have also given stepwise path as reference to see the step response of the 3-PRR compliant stage which has control methods based on PEA model and Experimental model. We have observed that there are a little bit overshoots due to parameters set and the filter that we have used for the measurement but the new control method based on experimental model lowered the overshoots for the same control parameters. Therefore, we can conclude that we have succeeded to design a better control methodology to lower the position errors to the accuracy of measurement.

9.1 Contributions

The contributions of this thesis can be stated as follows:

- We have come up with a design methodology as shown in Figure 9.1. After defining the limitations of compliant micro positioning stage a proper kinematic structure is selected. Then flexible joints are designed for providing the behaviour of kinematic structure. The important parameters like the link lengths, thickness, width etc. are determined by using FEA or Kinetostatic model solutions. The results should coincide with the limitations that are defined. Experiments are done and compared with the ideal case that is simulated if the results are not matching we can design a control methodology to get rid of the uncertainties in the mechanism.
- The in-plane compliance calculation methods have been compared in terms of the thinnest part “t” of the flexure but we have also compared the in-plane compliance

methods in terms of overall thickness “b” of the flexure hinges. This gives us the advantage of selecting the most proper calculation method for our flexure hinges.

- 3-PRR compliant mechanism is designed which is stiffer than 3-RRR compliant mechanism which has higher translational frequencies and makes the system more resistive to parasitic motions because of the used prismatic joint.

- We have designed a control methodology which is based on Sliding mode control with observer based on Sliding mode control by using the experimental models and task space measurement. The control methodology gives us the advantage of controlling the compliant mechanism with manufacturing, assembling errors and other uncertainties when compared with the ideal designed mechanism. The x-y position errors are in the accuracy of the used laser position sensing device so we can say that our control is successful.

- The proposed design procedure for compliant mechanisms are presented in blocks as shown Figure 9.1. Firstly, according to the determined limitations a kinematic structure is selected for the necessary application and the rigid joints of selected kinematic structure are replaced by the flexible joints. Necessary parameters are chosen according to the Finite element analysis and modeling technique that is used. If the stage doesn't provide the limitations for our application then we go back to the selecting the kinematic structure block to reshape our mechanism by changing the kinematic structure, flexible joints or the necessary design parameters. Else, we go on with the manufactured compliant mechanism and start to make experiments to validate the theoretical results. Finally, if the experiments are compatible with the experimental results we succeed to design our compliant mechanism. Otherwise, we will try to design a control methodology to get rid of the manufacture and assembly errors that cause unexpected results when compared to the ideal case. With the elimination of errors we can succeed to have a compliant mechanism that provides our limitations properly.

9.2 Future Work

The future work related to this work can be listed as follows:

- The modeling of compliant mechanisms can be improved by taken into account the out of plane flexure compliances which are the rotation about x axis $\Delta\alpha_x/M_x$, the rotation about y axis $\Delta\alpha_y/M_y$ and the translational displacement in z axis $\Delta z/F_z$.

- 3-D Finite element models can be generated to compare the out of plane compliance results of compliant mechanisms.

- The links connecting the flexure hinges can be taken as Euler Bernoulli beams so that the deflection of the beams can also be taken into account for modeling the compliant mechanisms.

- A different type of measurement can be used so that the rotation of the stage or the motion at z axis can be measured. The measurement can be a capacitive measurement system.

- The rotation of the stage can also be controlled by using the feedback of measurement.

- The stage can be used for micropositioning applications that are in Microsystems Laboratory (Microassembly Workstation, Laser Micromachining Unit, Microfactory System).

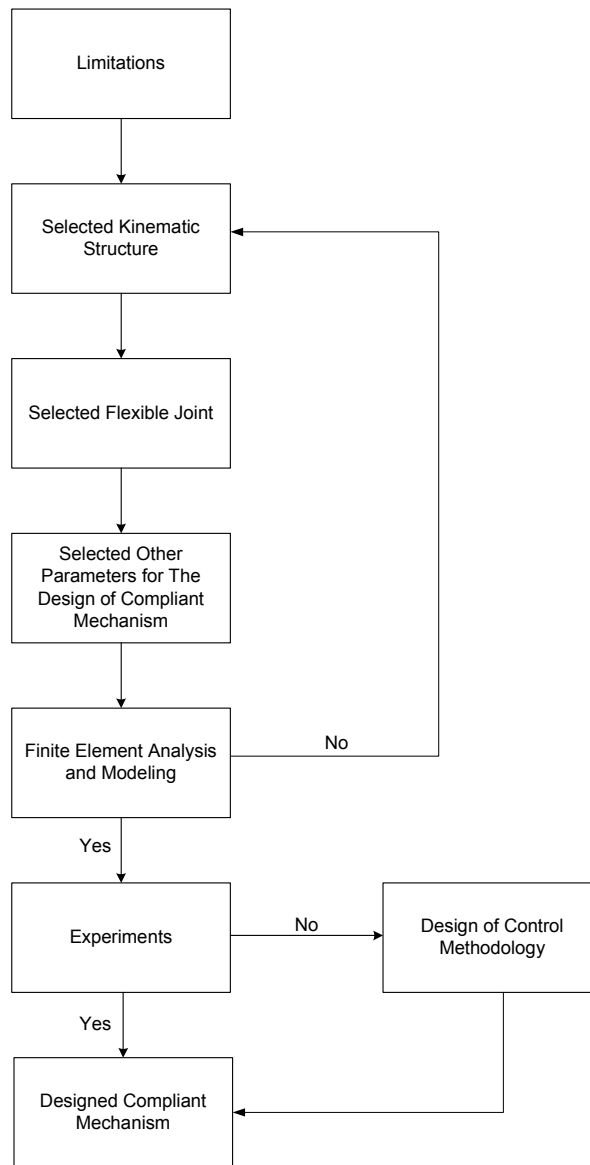


Figure 9.1 Design path of compliant mechanisms.

10 REFERENCES

- [1] A. H. Slocum, *Precision Machine Design*. New Jersey, USA: Prentice Hall, 1992.
- [2] D.G.Chetwynd S.T. Smith, *Foundations of Ultraprecision Mechanism Design*. North Carolina, USA: CRC Press, 1994.
- [3] Edin Golubovic, "Design and realization of laser micromachining system," Sabanci University, Master Thesis 2011.
- [4] Emrah Deniz Kunt, "Design and realization of a microassembly workstation," Sabanci University, Master Thesis 2006.
- [5] Henk van der Wulp, *Piezo-driven stages for nanopositioning with extreme stability*. Delft: Delft University Press, 1997.
- [6] L. L. Howell, *Compliant Mechanisms*.: Wiley, 2001.
- [7] R. C. Tjiptoprodjo, W. J. Zhang, G. S. Yang P.R. Ouyang, "Micro-motion devices technology: The state of arts review," *International Journal of Advanced Manufacturing Technology*, vol. 38, pp. 463-478, August 2008.
- [8] Nicolae Lobontiu, *Compliant Mechanisms: Design of Flexure Hinges*. CRC Press, 2003.
- [9] Robert L. Norton, *Machine Design*, 2nd ed. United States of America: Prentice-Hall Inc., 2000.
- [10] E. Teague F. Scire, "Piezodriven 50-um range stage with subnanometer resolution," *Review of Scientific Instruments*, vol. 49, no. 12, pp. 1735-1740.
- [11] B. N. Damazo, R. Silver, H. Zhou J.D. Gilsinn, "A macro-micro motion system for a scanning tunneling microscope," , 2002.
- [12] S. Avadhanula, R.E. Groff, R.S. Fearing A.M.Hoover, "A rapidly prototyped 2-axis positioning stage for microassembly using large displacement compliant mechanisms," , Orlando, 2006.

- [13] G. H. Kim, K. R. Cha S. H. Jeong, "A study on optical device alignment system using ultra precision multi-axis stage," *Journal of Materials Processing Technology*, vol. 187-188, pp. 65–68, June 2007.
- [14] Qingsong Xo Yangming Li, "Design and Analysis of a Totally Decoupled Flexure-Based XY Parallel Micromanipulator," *Transactions on Robotics*, vol. 25, pp. 645-567, June 2009.
- [15] Jingyan Dong Sebastian Polit, "Development of a High-Bandwidth XY Nanopositioning Stage for High-Rate Micro-/Nanomanufacturing," *IEEE/ASME Transactions On Mechatronics*, vol. 16, no. 4, pp. 724-733 , August 2010.
- [16] T. Ono, M. Esashi M.F.M. Sabri, "A large displacement piezodriven silicon XY-microstage," pp. 2405-2408, 2009.
- [17] B. Shirinzadeh, D. Zhang Y. Tiana, "A flexure-based mechanism and control methodology for ultra-precision turning operation," *Precision Engineering*, vol. 33, no. 2, pp. 160-166, April 2009.
- [18] A. H. Slocum S. Awtar, "A large range XY Flexure Stage for Nanopositioning," Montpellier, France, 2005.
- [19] Alexander H. Slocum Shorya Awtar, "Constraint-based Design of Parallel Kinematic XY Flexure Mechanisms," *Precision Engineering*, vol. 129, pp. 1-33, August 2007.
- [20] C. Chang, T. Ono, M. Esashi D. Zhang, "A piezodriven XY-microstage for multiprobe nanorecording," *Sensors and Actuators A: Physical*, vol. 108, no. 1-3, pp. 230–233, November 2003.
- [21] Emilio Carlos, Nelli Silva Guilherme Aires Loberto, "Development of a XY Piezoelectric Nanopositioner," *Mechatronics*, vol. 1, pp. 662-671, 2004.
- [22] J.J. Lee, S. Hata K.B. Choi, "A piezo-driven compliant stage with double mechanical amplification mechanisms arranged in parallel," *Sensors and Actuators A: Physical*, vol. 161, no. 1-2, pp. 173-181, June 2010.
- [23] I-Ming Chen Huy-Hoang Pham, "Evaluation of resolution of flexure parallel mechanisms for ultraprecision manipulation," *Review of Scientific Instruments*, vol. 75, no. 9, pp. 3016-3024, September 2004.
- [24] I-Ming Chen Huy Hoang Pham, "Kinematics, Workspace and Static Analyses of 2-DOF Flexure Parallel Mechanism," 2002.

- [25] W. J. Zhang, M. M. Gupta P. R. Ouyang, "A New Compliant Mechanical Amplifier Based on a Symmetric Five-Bar Topology," *Journal of Mechanical Design*, vol. 130, no. 10, pp. 104501-05, October 2008.
- [26] B. Shirinzadeh, D. Zhang Y. Tian, "Design and dynamics of a 3-DOF flexure-based parallel mechanism for micro/nano manipulation," *Microelectronic Engineering*, vol. 87, no. 2, pp. 230–241, February 2010.
- [27] Daniel C. Handley, Yuen Kuan Yong, Craig Eales Tien-Fu Lu, "A three-DOF compliant micromotion stage with flexure hinges," *Industrial Robot: An International Journal*, vol. 31, no. 4, pp. 355 - 361, 2004.
- [28] W. Szyszkowski, W.J. Zhang B. Zettl, "Accurate low DOF modeling of a planar compliant mechanism with flexure hinges: the equivalent beam methodology," *Precision Engineering*, vol. 29, no. 2, pp. 237–245, April 2005.
- [29] J. Zou, L. G. Watson, W. Zhao, G. H. Zong, S. S. Bi W. J. Zhang¹, "The Constant-Jacobian Method for Kinematics of a Three-DOF Planar Micro-Motion Stage," *Journal of Robotic Systems*, vol. 19, no. 2, pp. 63-72, February 2002.
- [30] Tien-Fu Lu, Daniel C. Handley Yuen Kuan Yong, "Loop Closure Theory in Deriving Linear and Simple Kinematic Model for a 3 DOF Parallel Micromanipulator," , Perth, 2003.
- [31] Tien-Fu Lu, J. Minase Y. K. Yong, "Trajectory Following with a three-DOF Micro-motion Stage," , Auckland, 2006.
- [32] D.C. Handley, Yuen Kuan Yong Tien-Fu Lu, "Position Control of a 3 DOF Compliant Micro Motion Stage," , 2004.
- [33] Chung Kai Tseng, Hon Chan Chien Shuo Hung Chang, "An ultra-precision XYThetaz piezo-micropositioner. II. Experiment and performance," *Ultrasonics, Ferroelectrics and Frequency Control*, vol. 46, no. 4, pp. 906 - 912, July 1999.
- [34] Rong Liu, Yue-min Wu, Long Shi, Guang-hua Zong Dai-hong Chao, "Manufacturing error analysis of compliant 3-DOF microrobot," *Frontiers of Mechanical Engineering in China*, vol. 1, no. 3, pp. 299-304, 2006.
- [35] Zhaoying Zhou Yingfei Wu, "An XY θ mechanism actuated by one actuator," *Mechanism and Machine Theory*, vol. 39, no. 10, pp. 1101-1110, October 2004.

- [36] Yangmin Li Yuan Yun, "Design and analysis of a novel 6-DOF redundant actuated parallel robot with compliant hinges for high precision positioning," *Nonlinear Dynamics*, vol. 61, no. 4, pp. 829-845, 2010.
- [37] Zong Guanghua, Liu Rong Chao Daihong, "Design of a 6-DOF Compliant Manipulator Based on Serial-Parallel Architecture," , Monterey, 2005.
- [38] Martin L Culpepper Shih-chi Chen, "Design of a six-axis micro-scale nanopositioner — uHexFlex," *Precision Engineering*, vol. 30, pp. 314-324, July 2996.
- [39] Dan Zhang, Zhongzhe Chi, Qunjun Song, Yunjian Ge, Yu Ge Qiaokang Liang, "Six-DOF micro-manipulator based on compliant parallel mechanism with integrated force sensor," *Robotics and Computer-Integrated Manufacturing*, vol. 27, no. 1, pp. 124-134, February 2011.
- [40] Stefano Bottinelli, Jean March Breguet, Reymond Clavel Jean-Philippe Bacher, "Delta: A New Ultra-high Precision Micro-robot," *APII-JESA*, vol. 36, pp. 1263-1275, 2002.
- [41] Regamey Yves-Julien, Fracheboud Maurice, Clavel Reymond Pham Patric, "Orion MinAngle: A flexure-based, double-tilting parallel kinematics for ultra-high precision applications requiring high angles of rotation," , Tokyo, 2005.
- [42] I-Ming Chen Huy-Hoang Pham, "Design and Modeling of a Selective-Actuation XYZ Flexure Parallel Mechanism," , 2004.
- [43] Lining Sun, Zhijiang Du Wei Dong, "Stiffness research on a high-precision, large-workspace parallel mechanism with compliant joints," *Precision Engineering*, vol. 32, no. 3, pp. 222–231, July 2008.
- [44] Qingsong Xu and Yangmin Li, "Mechanical Design of Compliant Parallel Micromanipulators for Nano Scale Manipulation," Zhuhai, 2006.
- [45] Gordon Anderson Martin L. Culpepper, "Design of a low-cost nano-manipulator which utilizes a monolithic, spatial compliant mechanism," *Precision Engineering*, vol. 28, no. 4, pp. 469–482, October 2004.
- [46] Jingyan Dong, Placid M. Ferreira Qing Yao, "A novel parallel-kinematics mechanisms for integrated, multi-axis nanopositioning: Part 1. Kinematics and design for fabrication," *Precision Engineering*, vol. 32, no. 1, pp. 20-33, January 2008.

- [47] Win Tun Latt, Cheng Yap Shee, Wei Tech Ang U-Xuan Tan, "Design and development of a low-cost flexure-based hand-held mechanism for micromanipulation," Kobe, 2009.
- [48] S. Payandeh, A.M. Parameswaran M.C.S. Tam, "Design and development of a multiple DOF compliant robot," Seattle, 2005.
- [49] Feng Gao, Xianchao Zhao, Q. Jeffrey Ge Yi Yue, "Relationship among input-force, payload, stiffness and displacement of a 3-DOF perpendicular parallel micro-manipulator," *Mechanism and Machine Theory*, vol. 45, no. 5, pp. 756-771, May 2010.
- [50] J.Hesselbach, A.Raatz, J. Wrege, S.Soetebier, "Design and Analysis of a Macro Parallel Robot with Flexure Hinges for Micro Assembly Tasks," Paris, 2004.
- [51] A. Raatz, H. Kunzmann J. Hesselbach, "Performance of Pseudo-Elastic Flexure Hinges in Parallel Robots for Micro-Assembly Tasks," *CIRP Annals - Manufacturing Technology*, vol. 53, no. 1, pp. 329-332, 2004.
- [52] Q. Xu Y. Li, "A Totally Decoupled Piezo-Driven XYZ Flexure Parallel Micropositioning Stage for Micro/Nanomanipulation," *IEEE Transactions on Automation Science and Engineering*, vol. 8, no. 2, pp. 265-278, April 2011.
- [53] S. K. Hung, M. Y. Chen, S.T. Li, L. C. Fu C. H. Lin, "A novel high precision electromagnetic flexure-suspended positioning stage with an eddy current damper," , Seoul, 2008, pp. 771 - 776.
- [54] J. Dong, F. Pengwang, P. Ferreira D. Mukhopadhyay, "A SOI-MEMS-based 3-DOF planar parallel-kinematics nanopositioning stage," *Sensors and Actuators A: Physical*, vol. 147, no. 1, pp. 240-251, September 2008.
- [55] H. Asai, M. Kawafuku, Y. Hori M. Sasaki, "Self-Tuning Control of a Translational Flexible Arm Using Neural Networks," Nashville, 2000.
- [56] M. Scaccia, A. Di Vasta, F. Ianniello N.P. Belfiore, "Dynamic performance of micro-compliant platforms: experimental analysis," Balatonfüred, Hungary, 2006.
- [57] S. Kota Z. Li, "Dynamic Analysis of compliant mechanisms," , Montreal, Canada, 2002.
- [58] L. L. Howell, Y. Yue Y. Yu, "Dynamic modeling of compliant mechanisms based on the pseudo-rigid-body model," *Journal of Mechanical Design*, vol.

- 127, no. 4, pp. 760-765, 2005.
- [59] L. L. Howell A. J. Nielson, "An investigation of compliant micro-half-pantographs using the pseudorigid body model," *Mechanics of Structures and Machines*, vol. 29, no. 3, pp. 317-330, 2001.
- [60] A. Midha L. L. Howell, "A Loop-Closure Theory for the Analysis and Synthesis of Compliant Mechanisms," *Journal of Mechanical Design*, vol. 118, pp. 121-125, 1996.
- [61] Lu Tien-Fu Yong Yuen Kuan, "Kinetostatic modeling of 3-RRR compliant micro-motion stages with flexure hinges," *Mechanism and Machine Theory* , vol. 44, no. 6, pp. 1156-1175, 2009.
- [62] J. K. Mills B. Kang, "Dynamic modeling of structurally-flexible planar parallel manipulator," *Robotica*, vol. 20, no. 3, pp. 329-339, 2002.
- [63] Bijan Shirinzadeh Hwee Choo Liaw, "Enhanced adaptive motion tracking control of piezo-actuated flexure-based four-bar mechanisms for micro/nano manipulation," *Sensors and Actuators A: Physical*, vol. 147, no. 1, pp. 254–262, September 2008.
- [64] B. Shirinzadeh H. C. Liaw, "Neural Network Motion Tracking Control of Piezo-Actuated Flexure-Based Mechanisms for Micro-/Nanomanipulation," *IEEE/ASME Transactions on Mechatronics*, vol. 14, no. 5, pp. 517-527, October 2009.
- [65] Bijan Shirinzadeh Hwee Choo Liaw, "Robust generalised impedance control of piezo-actuated flexure-based four-bar," *Sensors and Actuators A: Physical*, vol. 148, no. 2, pp. 443-453, 2008.
- [66] Qingsong Xu Yangmin Li, "A Novel Piezoactuated XY Stage With Parallel, Decoupled, and Stacked Flexure Structure for Micro-/Nanopositioning," *IEEE Transactions on Industrial Electronics*, vol. 58, no. 8, pp. 3601-3615 , August 2011.
- [67] Qingsong Xu Yangmin Li, "Adaptive Sliding Mode Control With Perturbation Estimation and PID Sliding Surface for Motion Tracking of a Piezo-Driven Micromanipulator," *IEEE Transactions on Control Systems Technology*, vol. 18, no. 4, pp. 798-810 , July 2010.
- [68] F. G. M. Kokkeler, H. Tragter, F. J. A. M. van Houten W. O. Schotborgh,

- "Dimensionless design graphs for flexure elements and a comparison between three flexure elements," *Precision Engineering*, vol. 29, pp. 41-47, 2005.
- [69] King Tim Xu Wei, "Flexure hinges for piezoactuator displacement amplifiers: flexibility, accuracy, and stress considerations," *Precision Engineering*, vol. 19, no. 1, pp. 4-10, July 1996.
- [70] T. F. Lu and D. C. Handley Y. K. Yong, "Review of circular flexure hinge design equations and derivation of empirical formulations," *Precision Engineering*, vol. 32, no. 1, pp. 63-70, 2008.
- [71] L. Weisbord J. M. Paros, "How to design Flexure Hinges," *Journal of Machine Design*, vol. 37, pp. 151-157, November 1965.
- [72] Z. Zhou Y. Wu, "Design calculations for flexure hinges," *American Institute of Physics*, vol. 73, pp. 3101-3106, August 2002.
- [73] V. Krovi, G. Ananthasuresh, and V. Kumar, "Kinematic and Kinetostatic Synthesis of Planar Coupled Serial Chain Mechanisms," *Journal of Mechanical Design*, vol. 124, pp. 301-312, 2002.
- [74] N. Celanovic M. Goldfrab, "Modeling Piezoelectric Stack Actuators for Control of Micromanipulation," *IEEE Control Systems*, vol. 17, no. 3, pp. 69-79, June 1997.
- [75] W.L. De Koning, R. Banning H.J.M.T.S. Adriaens, "Modeling piezoelectric actuators," *Mechatronics, IEEE/ASME Transactions on*, vol. 5, no. 4, pp. 331-341, December 2000.
- [76] A. Sabanovic, S. Yesilyurt K. Abidi, "Sliding mode control based disturbance compensation and external force estimation for a piezoelectric actuator," , 2004.
- [77] Khalid Abidi, "Sliding-Mode Control For High-Precision Motion Control Systems," Sabancı Univesity, MSc. Thesis 2004.